University of Bradford eThesis

COMPUTATION OF ELECTROMAGNETIC FIELDS IN ASSEMBLAGES OF BIOLOGICAL CELLS USING A MODIFIED FINITE DIFFERENCE TIME DOMAIN SCHEME

C H SEE

Ph.D.

2007

COMPUTATION OF ELECTROMAGNETIC FIELDS IN ASSEMBLAGES OF BIOLOGICAL CELLS USING A MODIFIED FINITE DIFFERENCE TIME DOMAIN SCHEME

Computational electromagnetic methods using quasi-static approximate version of FDTD, modified Berenger absorbing boundary and Floquet periodic boundary conditions to investigate the phenomena in the interaction between EM fields and biological systems

Chan Hwang SEE
B.Eng. (First Class Honours)

Submitted for the Degree of

Doctor of Philosophy

School of Engineering, design and Technology

University of Bradford

2007

Abstract

COMPUTATION OF ELECTROMAGNETIC FIELDS IN ASSEMBLAGES OF BIOLOGICAL CELLS USING A MODIFIED FINITE DIFFERENCE TIME DOMAIN SCHEME

Computational electromagnetic methods using quasi-static approximate version of FDTD, modified Berenger absorbing boundary and Floquet periodic boundary conditions to investigate the phenomena in the interaction between EM fields and biological systems

Chan Hwang SEE

Key Words:

Finite-Difference Time Domain (FDTD); quasi-static method; Floquet Periodic Boundary Conditions; Perfect Matching layers; Computer Modelling

There is an increasing need for accurate models describing the electrical behaviour of individual biological cells exposed to electromagnetic fields. In this area of solving linear problem, the most frequently used technique for computing the EM field is the Finite-Difference Time-Domain (FDTD) method. When modelling objects that are small compared with the wavelength, for example biological cells at radio frequencies, the standard Finite-Difference Time-Domain (FDTD) method requires extremely small time-step sizes, which may lead to excessive computation times. The problem can be overcome by implementing a quasi-static approximate version of FDTD, based on transferring the working frequency to a higher frequency and scaling back to the frequency of interest after the field has been computed.

An approach to modeling and analysis of biological cells, incorporating the Hodgkin and Huxley membrane model, is presented here. Since the external medium of the biological cell is lossy material, a modified Berenger absorbing boundary condition is used to truncate the computation grid. Linear assemblages of cells are investigated and then Floquet periodic boundary conditions are imposed to imitate the effect of periodic replication of the assemblages. Thus, the analysis of a large structure of cells is made more computationally efficient than the modeling of the entire structure. The total fields of the simulated structures are shown to give reasonable and stable results at 900MHz, 1800MHz and 2450MHz. This method will facilitate deeper investigation of the phenomena in the interaction between EM fields and biological systems.

Moreover, the nonlinear response of biological cell exposed to a 0.9GHz signal was discussed on observing the second harmonic at 1.8GHz. In this, an electrical circuit model has been proposed to calibrate the performance of nonlinear RF energy conversion inside a high quality factor resonant cavity with known nonlinear device. Meanwhile, the first and second harmonic responses of the cavity due to the loading of the cavity with the lossy material will also be demonstrated. The results from proposed mathematical model, give good indication of the input power required to detect the weakly effects of the second harmonic signal prior to perform the measurement. Hence, this proposed mathematical model will assist to determine how sensitivity of the second harmonic signal can be detected by placing the required specific input power.

Table of Contents

Chapter 1: Introduction

Chapter 2: The Finite-Difference Time-domain (FDTD) Technique for Computational Electromagnetics

Chapter 3: The Lumped-Element Finite Difference Time Domain Technique (LE-FDTD) for Hybrid Electromagnetic Systems with lumped-element Modelling

Chapter 4: Quasi-Static FDTD Scheme for Electrically-Small Regions in Free Space, Lossless and Lossy Penetrable Media

Chapter 5: Computation of Electromagnetic Field inside a Tissue Using Quasi-Static and Lumped-Element FDTD Scheme

Chapter 6: Numerical and Experimental Analysis of Proposed Cylindrical Cavity For Detection of Nonlinear Response in Biological Cells Exposed to RF Energy

Chapter 7: Conclusions and Suggestions for Further Work

Author's Contribution

Acknowledgements

I would like to express my deepest appreciation and thankful to Dr. R A Abd-Alhameed and Prof. P S Excell for their invaluable guidance and constructive criticism throughout the completion of this thesis. They have been generous in their time and always a source of encouragement and inspiration. I also would like to express my sincere thanks to Prof. Y F Hu, Prof. K Horoshenkov and Prof. S Tait for their continuous encouragement and support for the last two years that will never be forgotten.

A special word of thanks to Mr. John Vaul for his help and support on insightful discussion on implementation of FDTD algorithm, and to Mr. Iftekhar Ahmed for his greatly support on the experimental work and measurements presented in this thesis.

My sincere gratitude is extended to each member of the antenna and applied electromagnetic research group and especially Mr D Zhou, Dr R Alias, Mr K. Khalil, Mr T H Lee, Mr S W J Chung, Mr M Mutardi and Dr J M Moustafa. I also wish to thank Mr A Mistry and Mr A Robinson for his constant technical support throughout my stay at University of Bradford.

Last but by no means least, I convey my warmest thanks to my parents for their endless support throughout my life and for providing me the chance to reach this far with my studies.

Acronyms

1-D	One-dimension
2-D	Two-dimension
3-D	Three-dimension
3G	Third Generation
4G	Fourth Generation
ABC	Absorbing Boundary Condition
ADI	Alternating Direction Implicit
B	Magnetic flux density
BJT	Bipolar Junction Transistor
C	Capacitance
CAD	Computer-Aided Design
CEM	Computational Electromagnetic
D	Electric flux density
E	Electric Field
EM	Electromagnetic
EMF	Electromagnetic Field
EMP	Electromagnetic Pulse
FDTD	Finite-Difference Time-Domain
FEM	Finite-Element Method
FFT	Fast Fourier Transform
FSS	Frequency Selective Surface
FVTD	Finite Volume Time Domain
GSM1800	Global System for Mobile at 1800MHz
H	Magnetic Field
HH/H&H model	Hodgkin & Huxley Model
HSDPA	High-Speed Downlink Packet Access
I	Current
IEEE	Institute of Electrical and Electronics Engineers
IFA	Incident-field array
J	Electric current density
L	Inductance
LE-FDTD	Lumped-Element FDTD
M	Magnetic current density
MM	Markov models
MMIC	Monolithic Microwave Integrate Circuit
MoM	Method of Moment
M&P	McCulloch and Pitts
MRTD	Multiresolution time-domain

PBC	Periodic Boundary Condition
PBG	Photonic Bandgap
PCB	Printed Circuit Board
PDE	Partial Differential Equation
PEC	Perfect Electric Conductor
PML	Perfectly Matched Layer
QS-FDTD	Quasi-Static FDTD
R	Resistance
RF	Radio Frequency
SAR	Specific Absorption Rate
TE	Transverse Electric
TE_z	Transverse electric relative to the z-direction (only H_z, E_x, and E_y fields are present)
TEM	Transverse Electromagnetic
TF/SF	Total-field/ Scattered-field
TM	Transverse Magnetic
TM_z	Transverse magnetic relative to the z-direction (only $\mathrm{E_z}$, $\mathrm{H_x}$, and $\mathrm{H_y}$ fields are present)
UTD	Uniform Theory of Diffraction
UWB	Ultra Wideband
V	Voltage
WiMAX	Worldwide Interoperability for Microwave Access
WWW	World Wide Web
Z	Impedance

List of Tables

List of Figures

Chapter 1

Introduction

1.1 Background and Motivations

The interest in diagnostic and therapeutic applications of RF/microwaves in Medicine and in the assessment of possible health hazards due to EM radiation have stimulated the development of research streams in both modelling and experiments for evaluating EM power deposition in the interior of the human body or biological system. In order to establish precisely the required safety standard for regulating human exposure to EM waves, different aspects of studying the problem such as tissue level, cell level and ionic level have been carried out theoretically and experimentally.

At tissue level, the EM properties that describe the biological body properties can be studied by considering the geometry structure of each tissue making up the body as a scatterer. In experimental dosimetry, tissue equivalent “phantoms” are used instead of real bodies on predicted Specific Absorption Rate (SAR) values in biological tissue during EMF exposure. Empirically based estimates of the whole-body SAR are commonly performed using Dewar flask or twin-well calorimetry [1, 2]. Localized SAR values can be determined using temperature changes measured by implanted thermal probes. SAR values could be extrapolated from these temperature changes using [3], which is based on the specific heat of the tissue. Surface SAR can be computed using the same principle with infrared thermography [4]. Due to high experimental cost, this leads to demand for efficient and accurate field modelling tools for electromagnetic (EM) scattering problems. Theoretical models are required to interpret and confirm the experiment, develop an extrapolation process, and thereby develop a radiation safety standard for human. In this research area, either numerical methods or analytical methods are used to perform the computation of the problem. Due to the complexity of the problems typically encountered, numerical methods must be used since analytical solutions (closed form solutions) are only available for a small class of problems. The most frequently used numerical technique for computing the EM field is Finite-Different Time-Domain (FDTD) [5, 6]. With this method, the power absorbed inside the head of cellular phone user, due to the field radiated by the phone antenna, has been extensively studied [7-12].

At cell level, classical cells based on shelled spheres or ellipsoids were initiated by Fricke in 1925 [13], then have been used by authors [14] for RF electromagnetic field radiation studies. For the sake of simplicity, simple analytical solutions for spherical shaped of cell exposed to plane wave are provided by authors [14]. They exclude other possible geometric configurations representing more realistic cell shapes such as cylinders, rods or ellipsoids for their analysis. Due to analytical solutions are restricted to analysis of complex structures of biological cell, hence, it appears that numerical methods can sufficiently give a precise estimation of field values in realistic cell anatomies. The most difficult part of the numerical modelling of biological cell is the huge difference that might be found between the thickness of the cell’s layer, i.e micrometer cell diameter in which the membrane thickness is nanometer. Sometimes, the range of the differences can be varied between micrometer to nanometer. Basically, a few studies have been reported in this type of modelling. The most commonly used numerical technique is Finite Element Method (FEM) with adaptive meshing, to predict the electric field distribution in various shapes of the mammalian cell model [15-17].

At microscopic level, the electrical activity of various ionic realistic models of the neuronal membrane have been developed [18-23]. These models can be further divided into two classes. The first class of neuronal models was proposed by Hodgkin & Huxley (H&H) in 1952 [19]. This type of model is an electrical equivalent circuit based on sets of nonlinear differential equations in which each equation represents an ionic current flowing through the membrane. As for second class of models, a two-state device is used to represent the neuron in which an output spike is generated when a threshold is exceeded by the input voltage. The earliest type model was developed by McCulloch and Pitts (M&P) in 1943 [18]. Over the years, several additional contributions have been invented in addition to the above two models [20-23] . Recently, efforts have been made by [24-26] to create a link between the two above-mentioned classes of models. These proposed strategies are encapsulating a large amount of single ionic channel based on Markov models (MMs) [27] into a global frame work, which simulates the behaviour of a cell membrane. At a more microscopic level, classical Langevin-Lorentz model [28] and Quantum Zeeman-Stark Model [29, 30] are developed to analyse the influence of radiofrequency electromagnetic exposure on ligand binding to hydrophobic receptor proteins.

As can be noticed, all the previous analysis of EM interaction with biological entities are only focused on one aspect of cell functions problems in which there were no research activities were devoted for EM analysis and modelling process at cellular and ionic interaction mechanisms. This gives a great motivation to the present work to be carried out.

1.2 Development History of Finite-Difference Time-Domain

The FDTD method was first proposed by Yee in 1966 [5]. It is a simple and elegant way to discretize the differential form of Maxwell's equations. Yee used centred finite-difference (central-difference) expressions for the space and time derivatives that are both simply programmed and second-order accurate in the space and time increments. In general, Yee used an electric field (E) grid which was offset both spatially and temporally from a magnetic field (H) grid to obtain update equations that yield the present fields throughout the computational domain in terms of the past fields. The update equations are used in a leap-frog scheme to incrementally march the E and H fields forward in time. After the publication of Yee, this algorithm was widely used with different application in the literature [31-35].

From 1971 to 1994, with the invention of accurate absorbing boundary conditions (ABCs) proposed by Merewether [36], Engquist and Majda [37] , Mur [38], Liao [39], Keys [40] , Higdon [41] and Berenger [42], support the FDTD techniques to solve open regions problems and enhance the feasibility study of the method for wide range of applications. It should be noted that most of these proposed absorbing boundary conditions are differential equation and nonmaterial based, except for Berenger’s

Perfectly Matched Layers (PML) ABCs which are material based. Among these proposed ABCs, it was found that Berenger's PML provides significantly better accuracy than most other ABCs [43, 44].

The significant advantages of this method can be summarised as follows:

- The method implementation is simple.
- Modularization and parallelisation of algorithm can be easily implemented on parallel computers.
- Wide band applications can be easily performed by applying a different shaped time pulses such as Gaussian pulse.

The major disadvantage of the FDTD is found in modelling curved structure in which the "staircased" problems arised [45]. This is easily demonstrated in Figure 1.1. As can seen, a dielectric sphere is modelled by small cubical cells. Note that the "staircased" error can be encountered on the edges of the sphere. In addition, FDTD also introduces some errors due to the numerical dispersion [46].

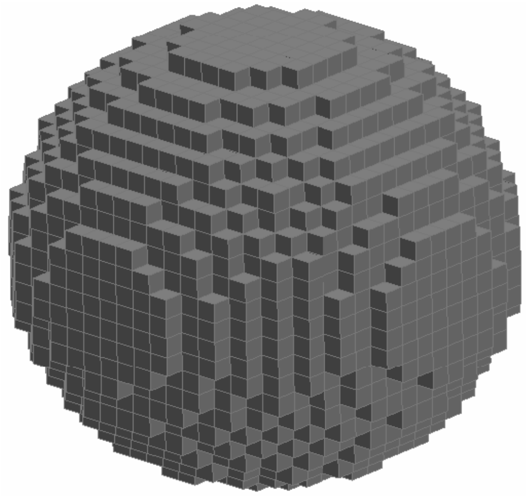

Figure 1.1: Stair-cased representation of a dielectric sphere inside FDTD computational domain.

To circumvent the limitations of FDTD, several alternative variant methods have been proposed, including Finite Volume time domain (FVTD) [47, 48] , Higher-order FDTD scheme [49, 50], Multiresolution time domain (MRTD) [51], Alternative direction implicit (ADI) [52-54], Subgridding methods [55-58] and Hybrid techniques [59-62].

1.3 State of the Art and Original Contributions

Cellular telephones and mobile wireless communication systems are being introduced into society at a very rapid rate. This has resulted in public concern about the health hazards of RF electromagnetic fields that are emitted from these devices and in turn to increase great interest of researcher to carry out a series of experiments and modelling works to understand the hazardous interaction between electromagnetic and human being. These developments contribute to establish the safety guidelines for human exposure to radio waves. As a consequence, this linear problem has been analysed thoroughly in various level of definition such as at tissue level, cell level and ionic level. In addition, the nonlinear problem on whether biological cells exhibit nonlinearity in the radiofrequency (RF) region is also justified.

The present work is devoted to modelling of the interaction between Electromagnetic (EM) fields and a cluster of biological cells. Different cell geometries were considered such as spherical, cubical and cylindrical cell. The analysis is not only involving the study of the interaction of the cells with the EM fields at tissue level, but also investigates the presence of nearby cells at the cell/sub-cell level and cellular membrane at ionic level. Moreover, the present works are further extended to find the evidences to prove and detect the nonlinear responses in biological samples in RF region.

The significant contribution of this present thesis can be summarised as follows:

1. Since the cell geometry is considerably small compared to the wavelength at the operating frequency, therefore, the analysed problem can be treated as quasi-static electromagnetic field problem. With the aim of this approximation, the frequency scaling scheme (quasi-static FDTD) which is proposed by authors [63] to solve numerical dosimetry of anatomically based model at power line frequency can be used. The present thesis successfully verifies the works of authors [63] at powerline frequency and implements the same concepts to biological cells modelling at mobile communication frequency.

2. This present thesis also verifies and clarifies the electric field distribution results of existing tissue model from paper [64]. Meanwhile, the thesis proposes the modified Perfectly Matched Layer (PML) Absorbing Boundary Condition (ABC) to replace the Mur ABC to truncate the FDTD computational domain in order to improve the accuracy of the published work in paper [64].

3. The present thesis also successfully validates the numerical results of modelling single biological equivalent spherical cell in several of penetrable media such as free space, lossless and lossy media, with the Mie series exact solution [65] at powerline and microwave frequency when it is excited by a plane wave.

4. The interaction mechanism of the biological tissue with the electromagnetic field at mobile communication frequencies such as 900MHz, 1800MHz, 2000MHz and 2400MHz are studied. The tissue was accurately modelled by using Floquet periodic theorem [66]. The boundary condition of this theorem was successfully applied on the border of a stack of spherical, cubical and cylindrical equivalent biological cells. With this boundary condition, it allows the simulation of the complete tissue at reasonable level of computational resources.

5. The present work also includes the equivalent circuit of cell's membrane developed by Hodgkin-Huxley (HH) [19] to the surface of the biological cells. This circuit was added to the cell membrane by placing the equivalent normal field component to the cell surface [67, 68].

6. Currently, there is no evidence to prove the nonlinearity hypotheses of the biological cells exposed to RF energy. The present work elucidates the implementation of doubly resonant cavity model in [69-73], to carry out a series of numerical modeling and experimental work to verify the nonlinearity hypothesis of the biological preparations.

1.4 Overview of Present Thesis

This work will propose a new approach that combines the high accuracy of the Finite-Difference Time-Domain (FDTD) method to calculate the EM field inside a biological cell and tissue. It is also comprised of electrically excitable cells, in which numerical and experimental solutions can be performed to investigate the possible RF nonlinear interactions in living cells. The study includes the application of existing Lumped-Element (LE-) and Quasi-Static (QS-) FDTD method to bioelectromagnetic problem modelling at powerline and mobile communication frequency. Following the background and motivation of the problem, the scope of the work and organisation of this present thesis will be discussed in chapter 1. It should be noted that a more detailed review of existing literature is reported in the beginning of each of the following chapters with separate references at the end of each.

Chapter 2 describes the basic principles of the FDTD algorithm which includes the derivation of update equations, parameters that control the stability and accuracy of FDTD method, the issue of introducing the electromagnetic wave excitation into the FDTD lattice, the concept of the plane wave source modelling that was implemented by applying an equivalent surface and the implementation of Berenger’s Perfectly Matched Layer (PML) absorbing boundary conditions for 2D and 3D structures. From all the aspect of FDTD that is mentioned above, a three dimensional Fortran FDTD code is developed and ready to be used as a tool to analyse the complex bioelectromagnetic problems.

Chapter 3 elucidates the fundamental principles of lumped element FDTD for hybrid EM systems with active and passive lumped-element modelling. This chapter demonstrates the conventional FDTD method and then according to the circuit theory to derive the relationships between the E and H fields and voltages and currents that are used to extend the general equations to include the active and passive lumped elements inside the FDTD lattice. Further, the update equations for passive lumped elements such as resistor and capacitor will be briefly derived respectively. Moreover, the presence of the intrinsic capacitor was also discussed in the context.

Chapter 4 introduces a Quasi-Static approximate version of FDTD for solving the problem of modelling electrically-small regions (much smaller than a wavelength).This approach is based on transferring the working frequency to a higher frequency, to reduce the number of time steps required. Then, the generated internal field at the higher frequency can be scaled back to frequency of interest. The equations of this frequency scaling approach are briefly derived and explained in this chapter. In the other hand, the formulation for plane wave solution in free space, lossless and lossy penetrable media are shown. Moreover, Mie series exact solution for describing the characteristics of electromagnetic radiation scattered by a homogenous sphere when it is excited by a plane wave will also be demonstrated. At last, in order to prove the validity of the quasi-static approach four examples of modelling the bioelectromagnetic problem with structures whose dimensions are a few wavelengths are given and the numerical results are compared with the Mie series exact solution. Numerical results were shown to be well agreed with the analytical results.

Chapter 5 is devoted to modelling of interaction between EM fields and a tissue, represented with spherical, cubical and cylindrical cells. Different EM approaches have been used to analyze this problem, in particular, the lumped-element FDTD has been implemented to model the cell's membrane represented with the Hodgkin-Huxley (HH) model and the Floquet theorem is implemented in order to mimic the infinite model of the tissue and in turn to reduce the computational time. Due to the analysed structure under consideration is considerably smaller than the wavelength of mobile communication frequency GSM900/GSM1800 and the time steps required for GSM900/GSM1800 frequency involves some millions of iterations, therefore, quasi-static FDTD is exploited to perform the computation of the analysis. The electric field distribution along the centre of the analysed structures will be shown and the implementation of LE-FDTD to model the equivalent circuit of the cell’s membrane (HH model) will be explained.

Chapter 6 demonstrates an efficient way to test the unsymmetrical nonlinear response of biological tissue samples exposed to a 0.9GHz signal to observe the existence of the second harmonic at 1.8GHz. A series of experiments and numerical modelling were carried out to calibrate the performance of nonlinear RF energy conversion inside a high quality factor resonant cavity with a known nonlinear loading device. Preliminary tests for the proposed detection systems were completed and initial obtained results from the test with biological sample will be shown and discussed.

Chapter 7 presents the conclusions and suggestions for further work on related topics.

1.5 References

[1] E.L.Hunt and R.D.Phillips, "Absolute physical dosimetry for whole animal experiments," *in Joint U.S Army/Georgia Inst. Technol. Microwave Dosimetry Workshop Dig., Washington, DC*, pp. 74-77, 1972.

[2] J.P.Padilla and R.Bixby, "Using Dewar-Flask calorimetry and rectal temperatures to determine the specific absorption rates of small rodents," *USAF School Aerospace Med., Brooks AFB, TX, USAFSAM-TF-86-3*, 1986.

[3] C.H.Durney, H.Massoudi, and M.F.Iskander, "Radiofrequency radiation dosimetry handbook," *USAF School Aerospace Med., Brooks AFB, TX, USAFSAM-TF-85-73*, 1986.

[4] A.W.Guy, M.D.Webb, and C.C.Sorensen, "Determination of power absorption in man exposed to high frequency electromagnetic fields by thermographic measurements on scale models," *IEEE Trans. Biomed. Eng.*, vol. 23, pp. 361-371, 1976.

[5] K.S.Yee, "Numerical solution of initial boundary value problems involving Maxwell's equation in isotropic media," *IEEE Trans. on Antennas Propagation*, vol. AP-14, pp. 302-307, 1966.

[6] A.Taflove and S.C.Hagness, *Computational Electrodynamics: the finite-difference time-domain method*, 2nd ed: Artech House,Inc, 2000.

[7] P.J.Dimbylow and S.M.Mann, "SAR calculations in an anatomically realistic model of the head for mobile communication transceivers at 900 MHz and 1.8GHz," *Phys.Med. Biol.*, vol. 39, pp. 1537-1553, 1994.

[8] O.P.Gandhi, G.Lazzi, and C.M.Furse, "Electromagnetic Absorption in the Human Head and Neck for Mobile Telephones at 835 and 1900 MHz," *IEEE Trans on*

MTT, vol. 44, pp. 1884-1896, 1996.

[9] A.Schiavoni, P.Bertotto, G.Richiardi, and P.Bielli, "SAR generated by commericial cellular phones - Phone modeling, head modeling and measurements," *IEEE Transactions on Microwave Theory and Techniques*, vol. 48, pp. 2064-2071, 2000.

[10] M.Martinez-Burdalo, A.A.Martin, M.Anguiano, and R.Villar, "Comparison of FDTD-calculated specific abosoption rate in adults and children when using a mobile phone at 900 and 1800 MHz," *Phys.Med. Biol.*, vol. 49, pp. 345-354, 2004.

[11] A.Hadjem, D.Lautru, C.Dale, M.F.Wong, V.F.Hanna, and J.Wiart, "Study of Specific Absoption Rate (SAR) Induced in Two Child Head Models and in Adult Heads Using Mobile Phones," *IEEE Transactions on Microwave Theory and Techniques*, vol. 53, pp. 4-11, 2005.

[12] D.M.Sullivan, D.T.Borup, and O.P.Gandhi, "Use of the Finite-Difference Time-Domain Method in Calculating EM Absorption in Human Tissues," *IEEE Trans on Biomed. Eng.*, vol. BME-34, pp. 148-157, 1987.

[13] H.Fricke, "The electric capacity of suspensions with special reference to blood," *J.Gen.Physiol.*, pp. 137-152, 1925.

[14] L.M.Liu and S.F.Cleary, "Absorbed Energy distribution from radio frequency electromagnetic radiation in a mammalian cell model: Effect of membrane-Bound water," *Bioelectromagnetics*, vol. 16, pp. 160-171, 1995.

[15] J.L.Sebastian, S.Munoz, M.Sancho, and J.M.Miranda, "Analysis of the Influence of the cell geometry orientation and cell proximity effects on the electric field distribution from direct RF exposure," *Phys.Med. Biol.*, vol. 46, pp. 213-225, 2001.

[16] S.M.S.Martin, J.L.Sebastian, M.Sancho, and J.M.Miranda, "A Study of the

electric field distribution in erythrocyte and rod shape cells from direct RF exposure," *Phys.Med. Biol.*, vol. 48, pp. 1649-1659, 2003.

[17] E.C.Fear and M.A.Stuchly, "Biological Cells with Gap Junctions in Low-Frequency Electric Fields," *IEEE Trans on Biomed. Eng.*, vol. 45, pp. 856-866, 1998.

[18] W.S.McCulloch and W.H.Pitts, "A logical calculus of ideas immanent in nervous activity," *Bll. of Math. Biophys. J.*, vol. 5, pp. 115-133, 1943.

[19] A.L.Hodgkin and A.F.Huxley, "A quantitative description of membrane current and its application to conduction and excitation in nerve," *J.Physiol.*, vol. 117, pp. 500-544, 1952.

[20] R.B.Stein, A.S.French, and A.V.Holden, "The frequency response, coherence and information capacity of two neuronal models," *Biophys. J.*, vol. 12, pp. 295-322, 1972.

[21] R.E.Plant and M.Kim, "Mathematical description of a bursting pacemaker neuron by a modification of the Hodgkin-Huxley equation," *Biophis.J.*, vol. 16, pp. 227-244, 1976.

[22] B.W.Adams and J.A.Benson, "The generation and modulation of endogenous rhythmicity in the Aplisia bursting pacemaker neurone R15," *Prog. Biophys. Molec. Bio.*, vol. 46, pp. 1-49, 1985.

[23] W.D.O'Neill, J.C.Lin, and Y.Chang, "Estimation of Verification of a Stochastic Neuron Model," *IEEE Trans on Biomed. Eng.*, vol. BME-33, pp. 654-665, 1986.

[24] P. Bernardi, G. Dinzeo, and S. Pisa, "A generalized ionic model of the neuronal membrane electrical activity," *IEEE Trans. Biomed. Eng.*, vol. 41, pp. 125-133, 1994.

[25] F.Apollonio, M.Liberti, G. d. 'Inzeo, and L.Tarricone, "Integrated Models for the Analysis of biological Effects of EM fields used for mobile Communications," *IEEE Trans on MTT*, vol. 48, pp. 2082-2093, 2000.

[26] F.Apollonio, M.Liberti, and G.D'Inzeo, "Theoretical Evaluation of GSM/UMTS Electromagnetic Fields on Neuronal Network Response," *IEEE Trans on MTT*, vol. 50, pp. 3029-3035, 2002.

[27] G.D'Inzeo, S.Pisa, and L.Tarricone, "Ionic channels gating under EM exposure: A stochastic model," *Bioelectron. Bioeng. J.*, vol. 29, pp. 290-304, 1993.

[28] S.Bruna, W.Rocchia, B.Bianco, J.J.Kaufman, and A.Chiabrera, "The state of the science for the Langevin-Lorentz model," *in 2nd World Cong. Elect. Mag. Biol. Med. Abstract Book*, pp. 375-378, 1997.

[29] A.Chiabrera, B.Bianco, E.Moggia, and J.J.Kaufman, "Zeeman-Stark modeling of the RF EMF interaction with ligand binding," *Bioelectromagnetics*, vol. 21, pp. 312-324, 2000.

[30] B.Bianco, A.Chiabrera, E.Moggia, and T.Tommasi, "Enhancement of the interaction between low-intensity RF EM fields and ligand binding due to cell basal metabolism," *Wireless Networks*, vol. 3, pp. 477-487, 1997.

[31] A.Taflove and M.E.Brodwin, "Numerical Solution of steady-state electromagnetic scattering problems using the time-dependent Maxwell's equations," *IEEE Trans. on Microwave Theory and Techniques*, vol. 23, pp. 623-630, 1975.

[32] A.Taflove and M.E.Brodwin, "Computation of the electromagnetic fields and induced temperatures within a model of the microwave-irradiated human eye," *IEEE Trans. on Microwave Theory and Techniques*, vol. 23, pp. 888-896, 1975.

[33] R.Holland, "Threde: a free-field EMP coupling and scattering code," *IEEE Trans.*

on Nuclear Science, vol. 24, pp. 2416-2421, 1977.

[34] K.S.Kunz and K.M.Lee, "A three-dimensional finite-difference solution of the external response of an aircraft to a complex transient EM environment I: The method and its implementation," *IEEE Trans. On Electromagnetic compatibility*, vol. 20, pp. 328-333, 1978.

[35] A.Taflove, "Application of the finite-difference time-domain method to sinusoidal steady-state electromagnetic penetration problems," *IEEE Trans. On Electromagnetic compatibility*, vol. 22, pp. 191-202, 1980.

[36] D.E.Merewether, "Transient currents on a body of revolution by an electromagnetic pulse," *IEEE Trans. On Electromagnetic compatibility*, vol. 13, pp. 41-44, 1971.

[37] B.Engquist and A.Majda, "Absorbing boundary conditions for the numerical simulation of waves," *Mathematics of Computation*, vol. 31, pp. 629-651, 1977.

[38] G.Mur, "Absorbing boundary conditions for the Finite-Difference Approximation of the time-domain Electromagnetic-field equations," *IEEE Trans. On Electromagnetic compatibility*, vol. EMC-23, pp. 377-382, 1981.

[39] Z.P.Liao, H.L.Wong, B.P.Yang, and Y.F.Yuan, "A Transmitting boundary for transient wave analysis," *Scientia Sinica (Series A)*, pp. 1063-1076, 1984.

[40] R.G.Keys, "Absorbing boundary conditions for acoustic media," *Geophysics*, vol. 50, pp. 892-902, 1985.

[41] R.L.Higdon, "Absorbing boundary conditions for difference approximations to the multi-dimensional wave equation," *Mathematics of Computation*, vol. 47, pp. 437-459, 1986.

[42] J.Berenger, "A perfectly matched layer for Absorption of Electromagnetic waves," *Journal of computational physics*, vol. 114, pp. 185-200, 1994.

[43] D.T.Prescott and N.V.Shuley, "Reflection Analysis of FDTD Boundary Conditions -Part II: Berenger's PML Absorbing Layers," *IEEE Trans on MTT*, vol. 45, pp. 1171-1178, 1997.

[44] D.T.Prescott and N.V.Shuley, "Reflection Analysis of FDTD Boundary Conditions - Part I: Time-Space Absorbing Boundaries," *IEEE Transactions on Microwave Theory and Techniques*, vol. 45, pp. 1162-1170, 1997.

[45] A. Akyurtlu, D. H. Werner, V. Veremey, D. J. Steich, and K. Avdin, "Staircasing errors in FDTD at an air-dielectric interface," *IEEE Microwave Guided Wave Letters*, vol. 9, pp. 444-446, 1999.

[46] J.B.Schneider and C.L.Wagner, "FDTD dispersion revisited: Faster-than-light propagation," *IEEE Microwave and Guided Wave Letters*, vol. 9, pp. 54-56, 1999.

[47] V.Shankar, A.H.Mohammadian, and W.F.Hall, "A time-domain finite-volume treatment for the maxwell's equations," *Electromagnetics*, vol. 10, pp. 127-145, 1990.

[48] N.K.Madsen and R.W.Ziolkowski, "A three-dimensional modified finite-volume technique for Maxwell's equations," *Electromagnetics*, vol. 10, pp. 147-161, 1990.

[49] K.P.Prokopidis and T.D.Tsiboukis, "Higher-order FDTD(2,4) scheme for accurate simulations in lossy dielectrics," *Electronic Letters*, vol. 39, pp. 835 - 836, 2003.

[50] T.T.Zygiridis and T.D.Tsiboukis, "Low-dispersion algorithms based on the higher order (2,4) FDTD method," *IEEE Transactions on Microwave Theory and Techniques*, vol. 52, pp. 1321 - 1327, 2004.

[51] M.Krumpholz and L.P.B.Katehi, "MRTD: New time-domain schemes based on multiresolution analysis," *IEEE Transactions on Antennas and Propagation*, vol. 44, pp. 555-572, 1996.

[52] T.Namiki, "A New FDTD algorithm based on Alternating-Direction Implicit Method," *IEEE Transactions on Microwave Theory and Techniques*, vol. 47, pp. 2003-2007, 1999.

[53] F.Zheng, Z.Chen, and J.Zhang, "Towards the development of a three-dimensional unconditionally stable finite-different time-domain method," *IEEE Transactions on Microwave Theory and Techniques*, vol. 48, pp. 1550-1558, 2000.

[54] X.T.Dong, N.V.Venkatarayalu, B.Guo, W.Y.Yin, and Y.B.Gan, "General Formulation of Unconditiionally Stable ADI-FDTD Method in Linear Dispersive Media," *IEEE Transactions on Microwave Theory and Techniques*, vol. 52, pp. 170-174, 2004.

[55] S.S.Zivanovic, K.S.Yee, and K.K.Mei, "A Subgridding Method for the Time-Domain Finite-Difference Method to Solve Maxwell's Equations," *IEEE Transaction on Microwave Theory and Techniques*, vol. 39, pp. 471-479, 1991.

[56] M.Okoniewski, E.Okoniewska, and M.A.Stuchly, "Three-Dimensional Subgridding Algorithm for FDTD," *IEEE Trans on Antennas and Propagation*, vol. 45, pp. 422-429, 1997.

[57] S.chaillou, J.Wiart, and W.Tabbara, "A Subgridding Scheme Based on Mesh Nesting For the FDTD method," *Microwave and Optical Technology Letters*, vol. 22, pp. 211-214, 1999.

[58] S-H.Sun and T.M.Charles, "A New Subgridding Scheme for Two-Dimensional FDTD and FDTD(2,4) Methods," *IEEE Transactions on Magnetics*, vol. 40, pp. 1041-1044, 2004.

[59] T. Rylander and A. Bondeson, "Application of stable FEM-FDTD hybrid to scattering problems," *IEEE Transactions on Antennas and Propagations*, vol. 50, pp. 141-144, 2002.

[60] A.Monorchio, A.R.Bretones, R. Mittra, G.Manara, and R.G.Martin, "A Hybrid Time-Domain Technique that Combines the Finite Element, Finite Difference and Method of Moment Techniques to Solve Complex Electromagnetic Problems," *IEEE Transactions on Antennas and Propagation*, vol. 52, pp. 2666-2674, 2004.

[61] X.Fierriers, J-P.Parmantier, S.Bertuol, and A.R.Ruddle, "Application of Hybrid Finite Difference/Finite Volume Method to Solve an Automotive EMC Problem," *IEEE Transactions on Electromagnetic Compatibility*, vol. 4, pp. 624-634, 2004.

[62] R.A.Abd-Alhameed, P.S.Excell, and M.A.Mangoud, "Broadband antenna response using Hybrid technique combining frequency domain MoM and FDTD," *ACES Journal*, vol. 20:1, pp. 70-77, 2005.

[63] O.P.Gandhi and J.Chen, "Numerical dosimetry at power-line frequencies using anatomically based models," *Bioelectromagnetics*, vol. 1, pp. 43-60, 1992.

[64] G.Emili, A.Schiavoni, F.L.Roselli, and R.Sorrentino, "Computation of electromagnetic field inside a tissue at mobile communications frequencies," *IEEE Trans on MTT*, vol. 51, pp. 178-186, 2003.

[65] J.R.Mautz, "Mie Series Solution for a Sphere," *IEEE Trans. on MTT*, vol. 26, pp. 375, 1978.

[66] A. Alexanian, N. J. Kolias, R. C. Compton, and R. A. York, "Three-dimensional FDTD analysis of quasi-optical arrays using Floquet boundary conditions and Berenger's PML," *IEEE Microwave and Guided Wave Letters*, vol. 6, pp. 138-140, 1996.

[67] P.Ciampolini, P.Mezzanotte, L.Roselli, D.Sereni, P.Torti, and R.Sorrentino, "Simulation of HF circuits with FDTD technique including nonideal lumped elements," *in IEEE MTT-S Int.Microwave Symp. Dig. Orlando,FL*, pp. 361-364, 1995.

[68] P.Ciampolini, P.Mezzanotte, L.Roselli, and R.Sorrentino, "Accurate and Efficient Circuit Simulation with Lumped-element FDTD technique," *IEEE Trans on MTT*, vol. 44, pp. 2207-2214, 1996.

[69] Q.Balzano and A.Sheppard, "RF Nonlinear Interactions in Living Cells –I: Nonequilibrium Thermodynamic Theory," *Bioelectromagnetics*, pp. 473-482, 2003.

[70] Q.Balzano, "RF Nonlinear Interactions in Living Cells-II: Detection Methods for Spectral Signatures," *Bioelectromagnetics*, pp. 483-488, 2003.

[71] Q.Balzano, "Proposed Test for Detection of Nonlinear Reponses in Biological Preparations Exposed to RF Energy," *Bioelectromagnetics*, pp. 278-287, 2002.

[72] I.Ahmed, P.S.Excell, and R.A.Abd-Alhameed, "Nonlinear and Demodulation Mechanisms in Biological Tissues," *Proceedings of the Seventh Informatics Workshop for Research Students, University of Bradford, UK*, pp. 115-118, March 2006.

[73] I.Ahmed, P.S.Excell, and R.A.Abd-Alhameed, "Nonlinear and demodulation mechanisms in biological tissues," *Proceedings of the eighth Informatics workshop for research students,University of Bradford, Bradford,UK*, pp. 16-19, 28 June 2007.

Chapter 2

The Finite-Difference Time-domain (FDTD) Technique for Computational Electromagnetics

2.1 Introduction

Due to the simplicity, robustness, and potential for great volumetric complexity afforded by FDTD modelling, FDTD method is arguably the most popular numerical method for the solution of problems in electromagnetics. Currently, tremendous amount of FDTD-related research activity is going intensely, hundreds of papers related to extensions and enhancements to this method are published which further extends its appeal worldwide each year. Electromagnetics research areas such as bioelectromagnetics, geophysical imaging, antennas, radars, wireless communications, high speed electronics, photonics, X-ray lithography and crystallography, have been successfully applied.

The international on-line database of the FDTD that is monthly updated can be easily found on the world-wide web [1]. This is the most complete reference for rapid tracking the FDTD-related published literatures. Besides, there were three interested books which were directly contributed to the FDTD method: Kunz and Luebbers [2] and

Taflove [3-5] .These three books may be considered the main references to recent FDTD research.

This chapter will first discuss the basic Yee's Finite Difference algorithm. Then, the stability and accuracy of this approach will be demonstrated. The introduction into the FDTD lattice of electromagnetic wave excitations appropriate for modelling engineering problems will be explained and derived. Since no computer can store unlimited amount of data, a special technique called absorbing boundary condition is applied in order to limit the solution region. The computation process is started with the excitation of a plane wave into the system and the field components are calculated at the grid mesh in discretised time steps. This process is continued until steady state has been reached. The theoretical aspects of the FDTD technique are described in the following sections. The Absorbing Boundary condition (ABC) will be reported, including the discussion of two and three dimensional Berenger's Perfectly Matched Layer (PML). Finally, a summarized conclusion of this chapter will be addressed.

2.2 FDTD Updating Equations

The FDTD method is a direct solution of Maxwell's curl equations for electric and magnetic vector fields within a finite computational domain truncated by proper boundary conditions. Consider a region of space that has materials that absorb electric or magnetic field energy, the time-dependent Maxwell's equations in differential form for a source and isotropic medium are:

$$\nabla\times \mathrm{E} = -\mu\frac{\partial \mathrm{H}}{\partial \mathrm{t}} - \sigma^{*}\mathrm{H} \tag{2.1}$$

$$\nabla\times H = \varepsilon\frac{\partial E}{\partial t} + \sigma E \tag{2.2}$$

In equations (2.1) and (2.2), σ is the electric conductivity in S/m and σ^{*} is the magnetic resistivity in Ω/m, therefore, $\sigma\,\boldsymbol{E}$ and $\sigma^{*}\boldsymbol{H}$ are the electric and magnetic losses respectively which may exist inside the medium. In cartesian coordinates, equations (2.1) and (2.2) yield the following six scalar equations:

$$\frac{\partial H_x}{\partial t} = \frac{1}{\mu}\left(\frac{\partial E_y}{\partial z} - \frac{\partial E_z}{\partial y} - \sigma^{*}H_x\right) \tag{2.3}$$

$$\frac{\partial H_y}{\partial t} = \frac{1}{\mu}\left(\frac{\partial E_z}{\partial x} - \frac{\partial E_x}{\partial z} - \sigma^{*}H_y\right) \tag{2.4}$$

$$\frac{\partial H_z}{\partial t} = \frac{1}{\mu}\left(\frac{\partial E_x}{\partial y} - \frac{\partial E_y}{\partial x} - \sigma^{*}H_z\right) \tag{2.5}$$

$$\frac{\partial E_x}{\partial t} = \frac{1}{\varepsilon}\left(\frac{\partial H_z}{\partial y} - \frac{\partial H_y}{\partial z} - \sigma\,E_x\right) \tag{2.6}$$

$$\frac{\partial E_y}{\partial t} = \frac{1}{\varepsilon}\left(\frac{\partial H_x}{\partial z} - \frac{\partial H_z}{\partial x} - \sigma\,E_y\right) \tag{2.7}$$

$$\frac{\partial E_z}{\partial t} = \frac{1}{\varepsilon}\left(\frac{\partial H_y}{\partial x} - \frac{\partial H_x}{\partial y} - \sigma E_z\right) \tag{2.8}$$

Following Yee's original notation [6], a space point in a rectangular grid is defined as:

$$(i, j, k) = (i\Delta x, j\Delta y, k\Delta z) \tag{2.9}$$

Let *F* denote any function of discrete space and time

$$F(i\Delta x, j\Delta y, k\Delta z, n\Delta t) \equiv F^{n}_{i,j,k} \tag{2.10}$$

where Δx , Δy and Δz are , respectively the grid space increments in *x, y* and *z* directions and Δt is the time increment. Using a central finite-difference approximation, space and time derivatives of *F* can be written as

$$\frac{\partial F}{\partial x} = \frac{F^{n}_{i+1/2,j,k} - F^{n}_{i-1/2,j,k}}{\Delta x} + O(\Delta x)^2 \tag{2.11}$$

$$\frac{\partial F}{\partial t} = \frac{F^{n+1/2}_{i,j,k} - F^{n-1/2}_{i,j,k}}{\Delta t} + O(\Delta t)^2 \tag{2.12}$$

In equation (2.11), $O(\Delta x)^2$ is the error term which represents all the remaining terms in a Taylor series expansion and equation (2.11) is known as a central finite difference scheme in space with second-order accuracy. Similarly, (2.12) is second-order accurate in time. Applying Yee's finite-difference scheme to (2.3):

$$\frac{H_{x\,i,j,k}^{n+1/2} - H_{x\,i,j,k}^{n-1/2}}{\Delta t} = \frac{1}{\mu_{i,j,k}} \left(\begin{array}{l} \dfrac{E_{y\,i,j,k+1/2}^{\,n} - E_{y\,i,j,k-1/2}^{\,n}}{\Delta z} \\ -\dfrac{E_{z\,i,j+1/2,k}^{\,n} - E_{y\,i,j-1/2,k}^{\,n}}{\Delta y} - \sigma^{*} H_{x\,i,j,k}^{\,n} \end{array} \right) \tag{2.13}$$

The $Hx_{i,j,k}^{n}$ field component in (2.13) is evaluated at time step *n*, but since the value of $Hx_{i,j,k}^{n}$ at time step *n* is not available, the following interpolated approximation is used:

$$H_{x\,i,j,k}^{n} = \frac{H_{x\,i,j,k}^{n+1/2} + H_{x\,i,j,k}^{n-1/2}}{2} \tag{2.14}$$

By substituting equation (2.14) in (2.13), leaving $H_{x\,i,j,k}^{n+1/2}$ on the left hand side and passing the all remaining terms to the right, assuming cubical FDTD cells are used, the finite difference updating equation for the magnetic and electric field components can be derived in the following form:

$$H_{x\,i,j,k}^{n+1/2} = D_{a,H_x}\Big|_{i,j,k} H_{x\,i,j,k}^{n-1/2} + D_{b,H_x}\Big|_{i,j,k} \left(\begin{array}{l} E_{y\,i,j,k+1/2}^{\,n} - E_{y\,i,j,k-1/2}^{\,n} \\ +E_{z\,i,j-1/2,k}^{\,n} - E_{z\,i,j+1/2,k}^{\,n} \end{array} \right) \tag{2.15}$$

$$H_{y\,i,j,k}^{n+1/2} = D_{a,H_y}\Big|_{i,j,k} H_{y\,i,j,k}^{n-1/2} + D_{b,H_y}\Big|_{i,j,k} \left(\begin{array}{l} E_{z\,i+1/2,j,k}^{\,n} - E_{z\,i-1/2,j,k}^{\,n} \\ E_{x\,i,j,k-1/2}^{\,n} - E_{x\,i,j,k+1/2}^{\,n} \end{array} \right) \tag{2.16}$$

$$H_{z\,i,j,k}^{n+1/2} = D_{a,H_z}\Big|_{i,j,k} H_{z\,i,j,k}^{n-1/2} + D_{b,H_z}\Big|_{i,j,k} \left(\begin{array}{l} E_{x\,i,j+1/2,k}^{n} - E_{x\,i,j-1/2,k}^{n} \\ + E_{y\,i-1/2,j,k}^{n} - E_{y\,i+1/2,j,k}^{n} \end{array} \right) \qquad (2.17)$$

$$E_{x\,i,j,k}^{n+1} = C_{a,E_x}\Big|_{i,j,k} E_{x\,i,j,k}^{n} + C_{b,E_x}\Big|_{i,j,k} \left(\begin{array}{l} H_{z\,i,j+1/2,k}^{n+1/2} - H_{z\,i,j-1/2,k}^{n+1/2} \\ + H_{y\,i,j,k-1/2}^{n+1/2} - H_{y\,i,j,k+1/2}^{n+1/2} \end{array} \right) \qquad (2.18)$$

$$E_{y\,i,j,k}^{n+1} = C_{a,E_y}\Big|_{i,j,k} E_{y\,i,j,k}^{n} + C_{b,E_y}\Big|_{i,j,k} \left(\begin{array}{l} H_{x\,i,j,k+1/2}^{n+1/2} - H_{x\,i,j,k-1/2}^{n+1/2} \\ + H_{z\,i-1/2,j,k}^{n+1/2} - H_{z\,i+1/2,j,k}^{n+1/2} \end{array} \right) \qquad (2.19)$$

$$E_{z\,i,j,k}^{n+1} = C_{a,E_z}\Big|_{i,j,k} E_{z\,i,j,k}^{n} + C_{b,E_z}\Big|_{i,j,k} \left(\begin{array}{l} H_{y\,i+1/2,j,k}^{n+1/2} - H_{y\,i-1/2,j,k}^{n+1/2} \\ + H_{x\,i,j-1/2,k}^{n+1/2} - H_{x\,i,j+1/2,k}^{n+1/2} \end{array} \right) \qquad (2.20)$$

where the coefficients on the left hand side are referred to as Yee's updating coefficients. The electric field coefficients can be written as follows:

$$C_a\Big|_{i,j,k} = \left(1 - \frac{\sigma_{i,j,k}\Delta t}{2\varepsilon_{i,j,k}} \right) \Bigg/ \left(1 + \frac{\sigma_{i,j,k}\Delta t}{2\varepsilon_{i,j,k}} \right) \qquad (2.21)$$

$$C_{b_m}\Big|_{i,j,k} = \left(\frac{\Delta t}{\varepsilon_{i,j,k}\Delta_m} \right) \Bigg/ \left(1 + \frac{\sigma_{i,j,k}\Delta t}{2\varepsilon_{i,j,k}} \right) \qquad (2.22)$$

and the magnetic updating coefficients are:

$$D_a\Big|_{i,j,k} = \left(1 - \frac{\sigma_{i,j,k}\Delta t}{2\mu_{i,j,k}}\right) \Bigg/ \left(1 + \frac{\sigma^{*}{}_{i,j,k}\Delta t}{2\mu_{i,j,k}}\right) \tag{2.23}$$

$$D_{b_m}\Big|_{i,j,k} = \left(\frac{\Delta t}{\mu_{i,j,k}\Delta_m}\right) \Bigg/ \left(1 + \frac{\sigma^{*}{}_{i,j,k}\Delta t}{2\mu_{i,j,k}}\right) \tag{2.24}$$

where *m* can be *x*, *y* or *z* and Δ_m is the cell size in the *m*-direction. Assuming that the structure under investigation contains different types of material (dielectric and/or magnetic), electric and magnetic field updating coefficients can easily be calculated from equations (2.21)-(2.24) before the FDTD time stepping algorithm starts.

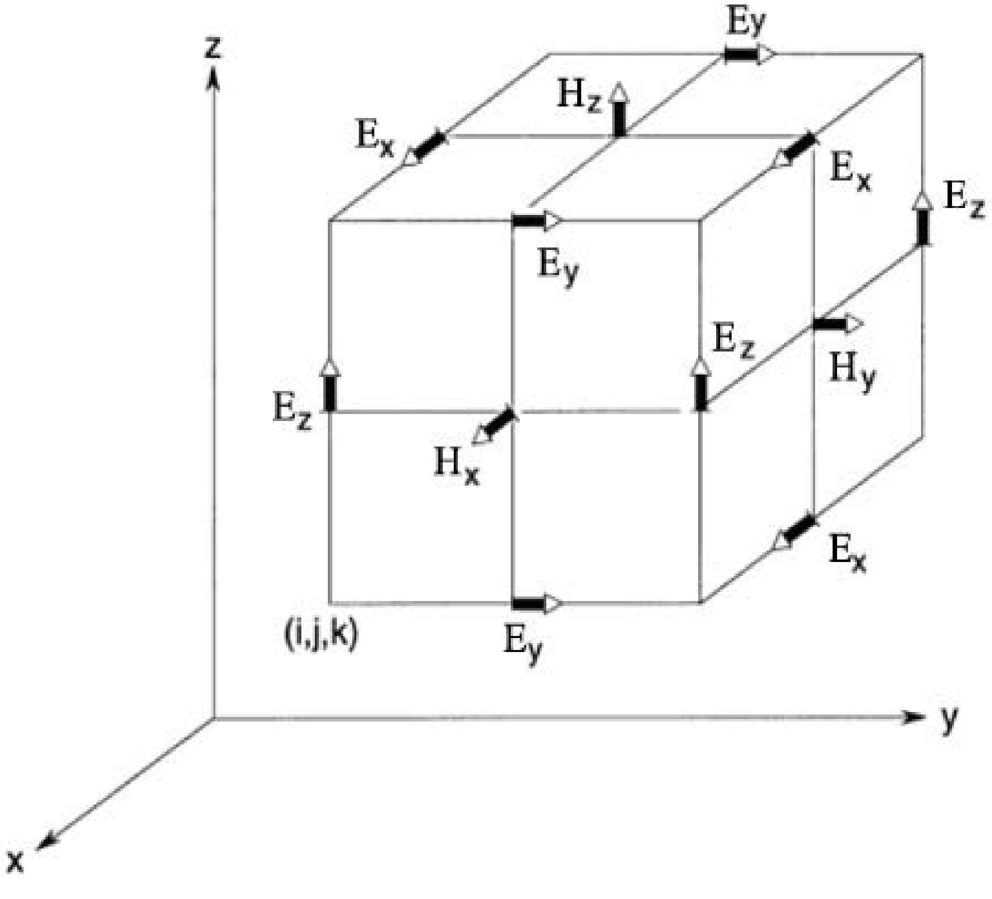

Figure 2.1: The distribution of the electric and magnetic field components on “Yee cell” or FDTD lattice [3, 5].

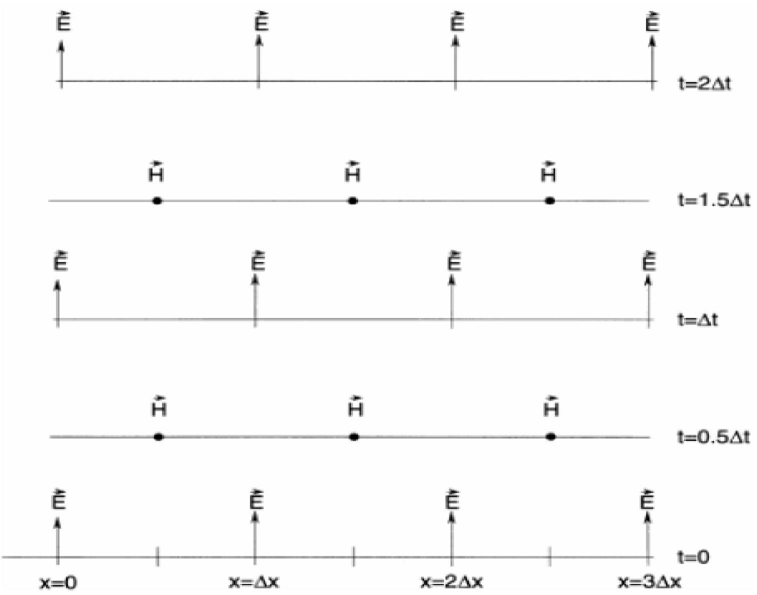

Figure 2.2: Space-time chart of the Yee algorithm in a leapfrog arrangement [3, 5].

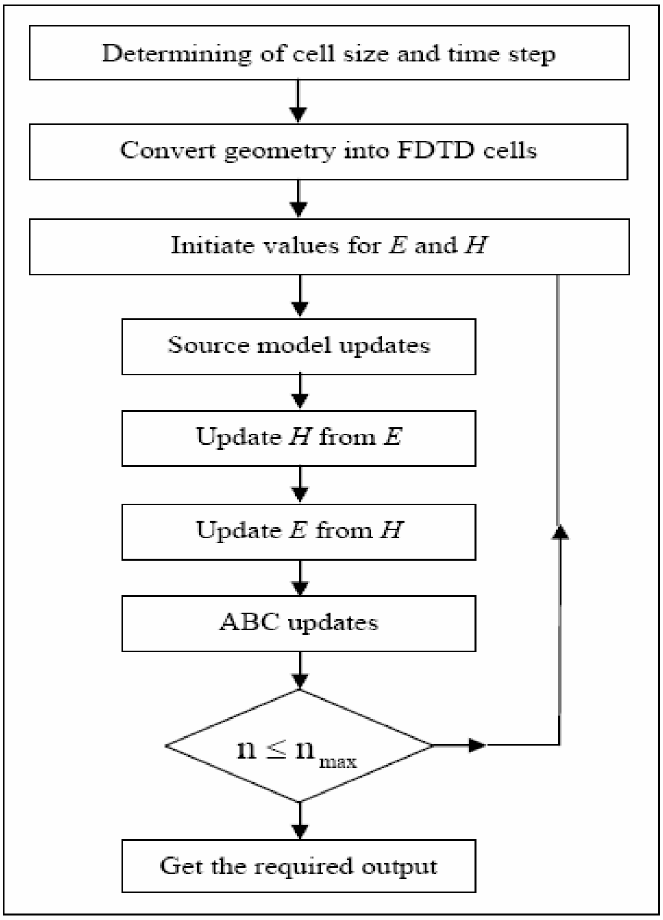

Figure 2.3: Time Stepping FDTD algorithm flow chart

The magnetic fields are located on the edges of the box and the electric fields are positioned on the faces as shown in Figure 2.1. This orientation of the fields is known as the Yee cell and is the basis for FDTD. As can be observed, the electric and magnetic field components are located half a cell from each other in Yee's cell. Each *E* or *H* component in three-dimensional space is surrounded by four circulating *H* or *E* components respectively. This configuration of the fields enables the realisation of a discretised version of Maxwell's equations. Figure 2.2 shows the electric and magnetic fields are updated using a leapfrog scheme where first the magnetic fields, then the electric field are computed at each step in time, while Figure 2.3 demonstrates the flow chart of time-stepping FDTD algorithms. From the flow chart, it can be seen that a suitable time step size should be selected properly in order to avoid the instability of the algorithms, after determining the spatial resolution based on the geometrical features and the operating frequency. It also shows a leapfrog arrangement between *E* and *H* components is used to implement the time stepping FDTD algorithm. The half-cell displacement between the *E* and *H* grids reflects the physical reality that the computer must work through them alternately.

2.3 Stability and Accuracy of the FDTD Technique

There are two significant parameters that might directly control the stability and the accuracy of FDTD technique, i.e. space resolution (grid size) Δx, $\Delta y, \Delta z$ and time resolution (time step) Δt. Due to the approximations inherent in FDTD, waves of different frequencies will propagate at slightly different speeds through the grid, this in turn causes the grid dispersion error in FDTD. This difference in propagation speed also depends on the direction of propagation relative to the grid. For accurate and stable results, the grid dispersion error must be reduced to an acceptable level. A rule of thumb sets the minimum space resolution, and thus the upper frequency limit, at less than ten cells per wavelength ($\leq \lambda/10$). Figure 2.4 depicts the fact that while increasing the grid size and direction of propagation, the numerical grid produces a certain amount of numerical dispersion error. As can be observed, when the cell size is exactly $\lambda/10$, the numerical dispersion is approximately 1%.

Once the space resolution is determined, the maximum size of the time resolution Δt immediately follows from the Courant condition [2], which sets the relation between the time and space resolution for three-dimensional FDTD as follows:

$$v_{\max}\Delta t \leq \frac{1}{\sqrt{\frac{1}{\Delta x^2}+\frac{1}{\Delta y^2}+\frac{1}{\Delta z^2}}} \tag{2.25}$$

where $v_{\max}$ is the maximum wave phase velocity in any material in the model.

For a cubic cell whose cell size is Δ, in a *d*-dimensional (*d*=1, 2 or 3) spatially homogeneous FDTD grid, equation (2.25) becomes:

$$\Delta t \leq \frac{\Delta}{v_{\max}\sqrt{d}} \tag{2.26}$$

To minimise the computer run time requirement, the time step should be chosen as large as possible yet satisfying equation (2.26). Choosing smaller time steps gives more accuracy but with longer simulation run times. In order to compromise the accuracy and the efficiency of FDTD simulation, the value of $\Delta x \,/\, (2\nu_{max})$ for time resolution is always considered in many FDTD codes that must satisfy the Courant condition.

In fact the stability also depends upon the algorithm used to model the Absorbing Boundary Conditions (ABC) to simulate the domain extension to infinity. The theoretical details of one efficient type of ABC used in the research work presented in this thesis will be given in section 2.5.

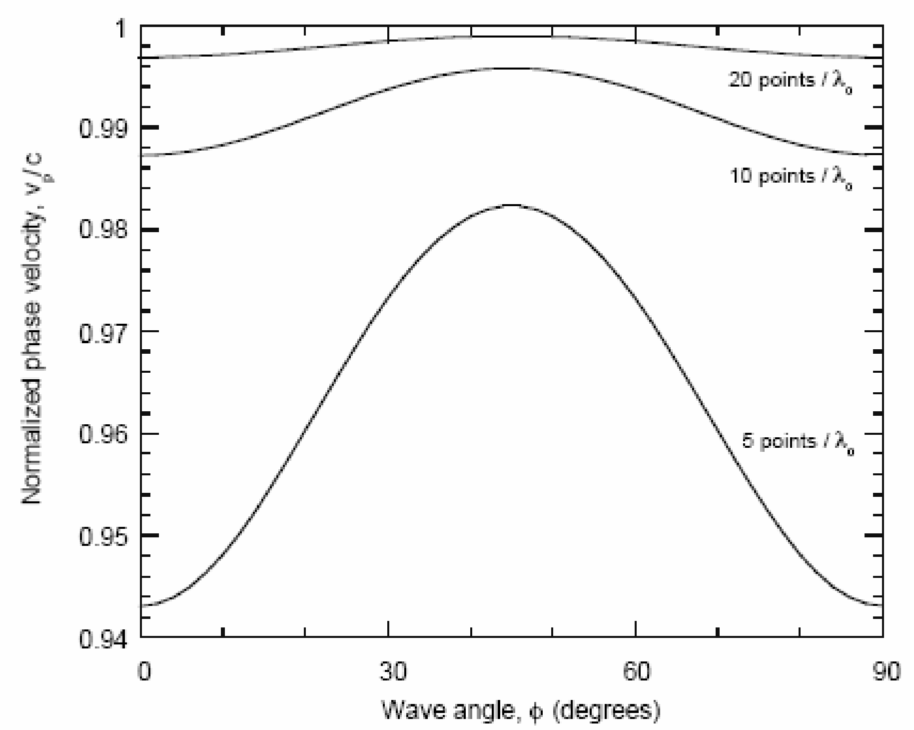

Figure 2.4: Variation of the numerical phase velocity with wave propagation angle in two-dimensional FDTD grid for three dimensions [3, 5].

2.4 Incident Wave Source Conditions

In this section, the issue of introducing the electromagnetic wave excitations into the FDTD lattice for modelling scattering problem will be elucidated. This can be easily done by using relatively *E* and *H* components to realize the wave source compared to the total number of field components in the space lattice, in order to accurately realize the physics of an electromagnetic wave source in as compact a manner as possible. In this way, the required computation time and resources to simulate the source is relatively small compared to the required ordinary time-stepping of the fields. Hence, the maximum algorithm efficiency is achieved. This section will only review two general classes of compact electromagnetic wave sources, i.e., the hard source and the total/field/scattered-field formulation for plane-wave excitation in one and three dimensional lattices.

2.4.1 The Hard Source

The hard source is set up simply by assigning a desired time function to specific electric or magnetic field components in FDTD space lattice. This can be explained more easily in a one dimensional TM (Transverse Magnetic) grid example. In TM grid, the hard source on E_z could be established at the grid source point i_s to generate a continuous sinusoidal wave of frequency f_o which is switched on at n=0. Therefore, the first type of hard source can be formulated in following expression [3, 5]:

$$E_z \big|_{i_s}^{n} = E_o \sin\left(2\pi f_o n\Delta t\right) \tag{2.27}$$

A second common hard source provides a wideband Gaussian pulse with finite dc content. The pulse is centred at time step n_o and has a 1/e characteristic decay of n_{decay} time steps:

$$E_z\Big|_{i_s}^{n} = E_o e^{-\left[(n-n_o)/n_{decay}\right]^2} \tag{2.28}$$

It should be noted that equation (2.28) has a nonzero value at n = 0. Therefore, if a smooth transition from zero into the Gaussian pulse is required, n_o should be taken a value at least $3\,n_{decay}$.

A third common hard source provides a zero-dc content, bandpass Gaussian pulse with Fourier spectrum symmetrical about f_o. The pulse is again centred at time step n_o and has a 1/e characteristic decay of n_{decay} time steps:

$$E_z\Big|_{i_s}^{n} = E_o e^{-\left[(n-n_o)/n_{decay}\right]^2} \sin\left[2\pi f_0 (n-n_o)\Delta t\right] \tag{2.29}$$

2.4.2 Incident Plane-Wave Source Excitations

Basically, an arbitrary incident plane wave is used for excitation purposes. The plane wave excitation model was firstly considered by Yee’s original paper in 1966 [6]. The modelling process of the incident plane wave was approximated within the FDTD grid. This includes a complete interaction between the scatterer under consideration and the excitation plane wave.

In this section, two techniques, i.e., Initial Condition and Total/Scattered Field Formulation Method, to realise incident waves on the space lattice will be demonstrated. Special attention will be given to Total/Scattered formulations which will be adapted later to be used in the proposed Quasi-static FDTD technique.

Initial Condition Method [6] was used by Yee in his early implementation of the FDTD method to represent an incident plane wave: this has especial applications in radar cross section simulations. In this method, all of the values of electric and magnetic field components at the zero time step of the incident wave throughout the problem space are preset in sign and magnitude, to give the desired polarisation of the incident plane wave. This method encounters two profound problems, for instance it is a non-compact wave source, it has implementation difficulties for oblique angles and it requires a large number of additional free space cells (that enlarge the problem space size) to contain initial conditions of long duration pulses or continuous sinusoids. As a result, this method current finds only limited and specialized usage.

Total/Scattered Field Formulation Method [7, 8] is the most popular method used in many FDTD software and codes due to it successes in all respects, permitting FDTD modelling of long-duration pulsed or sinusoidal illuminations for arbitrary plane-wave propagation directions. Figure 2.5 illustrates the zoning of the numerical space grid into two distinct regions, total field region and scattered field region, separated by a non-physical virtual surface implemented numerically with a special treatment to include the incident wave excitations and to split the problem space into total and scattered field regions at the same time. This leads to a very important feature which is that the scattered field vector values may be computed in the scattered field region (region 2) with no incident field included in that region. The second key feature of this formulation is the efficient modelling of arbitrary incident plane waves with different oblique incidence angles using an incident-field array (IFA) excitation scheme proposed by Taflove [3, 5]. The IFA is an FDTD-based look-up table from which incident-field values are and overlaid on the FDTD grid in the direction of propagation.

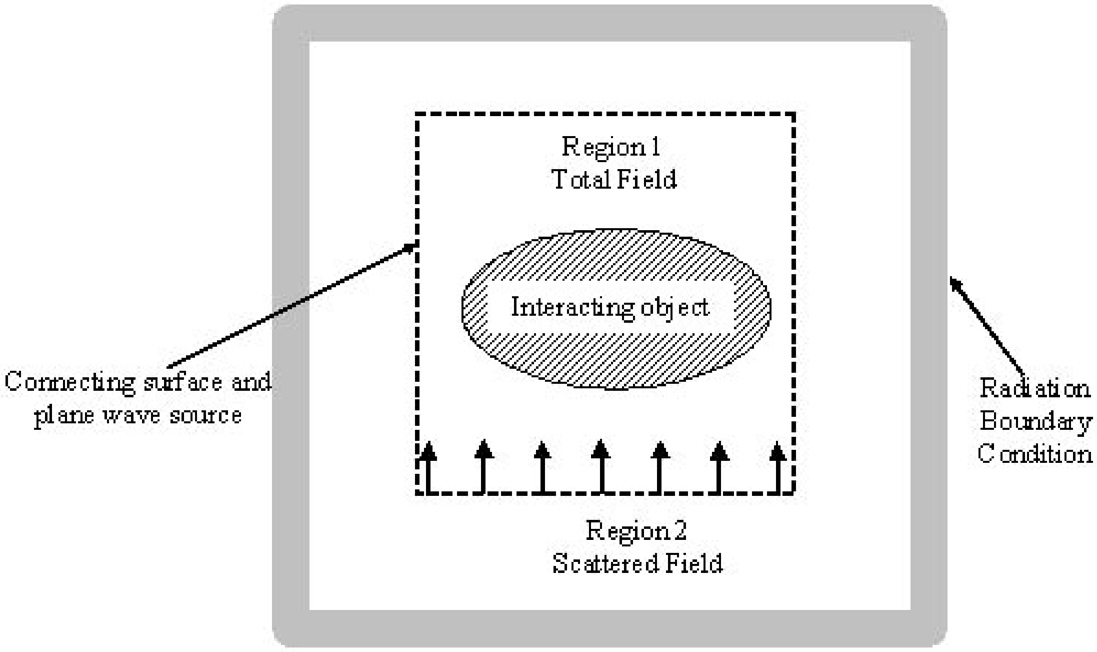

Figure 2.5: Overview of the total and scattered field zoning for a generic scattering problem.

2.4.2.1 Total/Scattered Field Formulation in One Dimension

The best example to explain the basic principle of the total/scattered formulation is to consider the simple one-dimensional transverse magnetic field (TM) case, as shown in Figure 2.6 (as in [3, 5]).

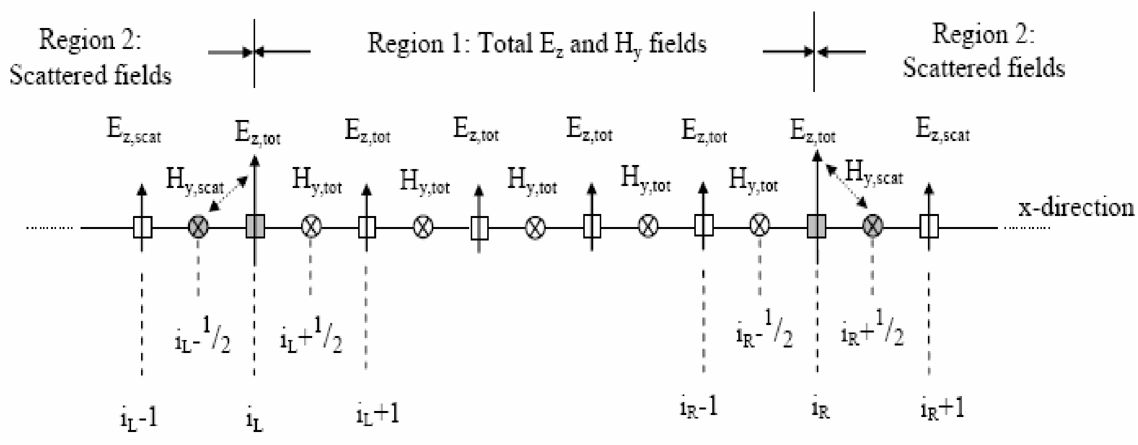

Figure 2.6: Total and Scattered Components for one dimensional FDTD grid

The set up of the total/scattered formulation divides the x-directed array of E_z and H_y components into two regions, region 1 (total fields) and region 2 (scattered fields) by a virtual surface. At this surface interface between the two regions there exists a special set of E and H components (the grey coloured components in the Figure 2.6). These four field components are E_z at i_L and i_R and H_y at (i_L-$^1/_2$) and (i_R +$^1/_2$). According to the Yee algorithm these have different types, total or scattered, respectively. The incident fields, E_{inc} and H_{inc} are known and may be calculated at outer interface points. They are added to the regular updating equations. For example, E_z at i_L, the left interface surface, is considered to be a total field component and by applying the basic FDTD algorithm it will be updated as shown in equation (2.30). (Note: The equations are reviewed here using symbols as close as possible to those used in [3, 5])

$$E_{z\,tot,i_L}^{n+1} = E_{z\,tot,i_L}^{n} + \frac{\Delta t}{\varepsilon_o\,\Delta}\left(H_{y\,tot,i_L+1/2}^{n+1/2} - H_{y\,scat,i_L-1/2}^{n+1/2} \right) \tag{2.30}$$

where the subscripts *tot, scat* and *inc* stand for total, scattered and incident fields respectively. It is clear that the above equation (2.30) is inconsistent, so $H_{y,tot}$ at (i_L-$^1/_2$) must be subtracted from $H_{y,tot}$ at (i_L+$^1/_2$) to advance the value of $E_{z,tot}$ at i_L. To correct this updating equation, the vector function $H_{y,inc}$ at (i_L-$^1/_2$) is added as an excitation wave source of the FDTD scheme. The boundary E_z updating equation will then be:

$$E_{z\,tot,i_L}^{n+1} = E_{z\,tot,i_L}^{n} + \frac{\Delta t}{\varepsilon_o\,\Delta}\left(H_{y\,tot,i_L+1/2}^{n+1/2} - H_{y\,scat,i_L-1/2}^{n+1/2} \right) - \frac{\Delta t}{\varepsilon_o\,\Delta} H_{y\,inc,i_L-1/2}^{n+1/2} \tag{2.31}$$

It should be noted that the added term is assumed to be a known function, for example a sinusoidal or Gaussian pulse for plane wave representation, while the rest of the terms of the right hand side are assumed stored in computer memory from the previous updating time step.

By following the proper modifications of equation (2.31), the updating equations for the other three special magnetic and electric boundary field components will be as follows:

$$H_{y\,scat,i_L-1/2}^{n+1/2} = H_{y\,scat,i_L-1/2}^{n-1/2} + \frac{\Delta t}{\mu_o\,\Delta}\left(E_{z\,tot,i_L}^{n} - E_{z\,scat,i_L-1}^{n} \right) - \frac{\Delta t}{\mu_o\,\Delta} E_{z\,inc,i_L}^{n} \tag{2.32}$$

$$E_{z\,tot,i_R}^{\,n+1} = E_{z\,tot,i_R}^{\,n} + \frac{\Delta t}{\varepsilon_o\,\Delta}\left(H_{y\,scat,i_R+1/2}^{\,n+1/2} - H_{y\,tot,i_R-1/2}^{\,n+1/2}\right) + \frac{\Delta t}{\varepsilon_o\,\Delta} H_{y\,inc,i_R+1/2}^{\,n+1/2} \qquad (2.33)$$

$$H_{y\,scat,i_R+1/2}^{\,n+1/2} = H_{y\,scat,i_R+1/2}^{\,n-1/2} + \frac{\Delta t}{\mu_o\,\Delta}\left(E_{z\,scat,i_R+1}^{\,n} - E_{z\,tot,i_R}^{\,n}\right) + \frac{\Delta t}{\mu_o\,\Delta} E_{z\,inc,i_R}^{\,n} \qquad (2.34)$$

Equations (2.31)-(2.34) are the one-dimensional total/scattered field FDTD formulations to generate the equivalent effects of the plane wave at one surface interface. The same principle can be extended to 2D and 3D scattering problems.

2.4.2.2 Total/Scattered Field Formulation in Three Dimension

The Equivalence principle surface implementation in a FDTD computer code is complicated by the fact that *H* and *E* nodes are located at different points, i.e. a half-cell apart from each other. We can visualise two rectangular equivalent closed surfaces. The locations of the Huygens electric current sources (tangential magnetic field) and the magnetic current sources (tangential electric field) are considered on the inner and outer of the closed surfaces respectively. These are computed with a special treatment (different from that previously defined in Section 2.3) and then applied to updating equations as follows.

To simplify the large number of equations required, the abbreviated notation used by Taflove in [3, 5] will be adopted. The basic updating equations are given in equations (2.15) to (2.20); the results of these are used here in the form $[9]_{(2.xx)}$ and modified forms for the field component *A* are then given below by adding appropriate additional terms. Referring to Figure 2.7(a), the E_y components at cells referenced ($i=i_o$, $j=j_o+{}^1/_2,\ldots, j_1-{}^1/_2$; $k=k_o,\ldots,k_1$) are given by:

$$E_{y_{i_o,j,k}}^{n+1} = \{E_{y_{i_o,j,k}}^{n+1}\}_{(2.19)} + C_{b,Ey}\Big|_{i_o,j,k} .H_{z,inc_{i_o-1/2,j,k}}^{n+1/2} \tag{2.35}$$

E_z components at cells referenced ($i=i_o$; $j=j_o,\ldots j_1$; $k=k_o+{}^1/_2,\ldots ,k_1-{}^1/_2$):

$$E_{z_{i_o,j,k}}^{n+1} = \{E_{z_{i_o,j,k}}^{n+1}\}_{(2.20)} - C_{b,E_z}\Big|_{i_o,j,k} H_{y,inc_{i_o-1/2,j,k}}^{n+1/2} \tag{2.36}$$

H_y components at cells referenced ($i=i_o-{}^1/_2$; $j=j_o,\ldots j_1$; $k=k_o+{}^1/_2,\ldots,k_1-{}^1/_2$):

$$H_{y_{i_o-1/2,j,k}}^{n+1/2} = \{H_{y_{i_o-1/2,j,k}}^{n+1/2}\}_{(2.16)} - D_{b,H_y}\Big|_{i_o-1/2,j,k} E_{z,inc_{i_o,j,k}}^{n} \tag{2.37}$$

H_z components at cells referenced ($i=i_o-{}^1/_2$; $j=j_o-{}^1/_2,\ldots, j_1+{}^1/_2$; $k=k_o,\ldots,k_1$):

$$H_{z_{i_o-1/2,j,k}}^{n+1/2} = \{H_{z_{i_o-1/2,j,k}}^{n+1/2}\}_{(2.17)} + D_{b,H_z}\Big|_{i_o-1/2,j,k} E_{y,inc_{i_o,j,k}}^{n} \tag{2.38}$$

E_y components at cells referenced ($i=i_1$, $j=j_o+{}^1/_2,\ldots, j_1-{}^1/_2$; $k=k_o,\ldots,k_1$):

$$E_{y_{i_1,j,k}}^{n+1} = \{E_{y_{i_1,j,k}}^{n+1}\}_{(2.19)} - C_{b,Ey}\Big|_{i_1,j,k} .H_{z,inc_{i_1+1/2,j,k}}^{n+1/2} \tag{2.39}$$

E_z components at cells referenced ($i=i_1$; $j=j_o,\ldots j_1$; $k=k_o+{}^1/_2,\ldots ,k_1-{}^1/_2$):

$$E_{z i_1,j,k}^{n+1} = \{E_{z i_1,j,k}^{n+1}\}_{(2.20)} + C_{b,E_z}\Big|_{i_1,j,k} H_{y,\mathrm{inc}\, i_1+1/2,j,k}^{n+1/2} \tag{2.40}$$

H_y components at cells referenced (*i*=i_1 +$^1/_2$; *j*=j_o,… j_1; *k*=k_o+$^1/_2$,… ,k_1-$^1/_2$):

$$H_{y i_1+1/2,j,k}^{n+1/2} = \{H_{y i_1+1/2,j,k}^{n+1/2}\}_{(2.16)} + D_{b,H_y}\Big|_{i_1+1/2,j,k} E_{z,\mathrm{inc}\, i_1,j,k}^{n} \tag{2.41}$$

H_z components at cells referenced (*i*=i_1 +$^1/_2$, *j*=j_o+$^1/_2$,…, j_1-$^1/_2$; *k*=k_o,…,k_1):

$$H_{z i_1+1/2,j,k}^{n+1/2} = \{H_{z i_1+1/2,j,k}^{n+1/2}\}_{(2.17)} - D_{b,H_z}\Big|_{i_1+1/2,j,k} E_{y,\mathrm{inc}\, i_1,j,k}^{n} \tag{2.42}$$

Referring now to Figure 2.7(b), the E_x components at cells referenced (*i*=i_o+$^1/_2$,……, i_1-$^1/_2$; *j*=j_o; *k*=k_o,…,k_1) are given by:

$$E_{x i,j_o,k}^{n+1} = \{E_{x i,j_o,k}^{n+1}\}_{(2.18)} - C_{b,Ex}\Big|_{i,j_o,k} .H_{z,\mathrm{inc}\, i,j_o-1/2,k}^{n+1/2} \tag{2.43}$$

E_z components at cells referenced (*i*=i_o,…,i_1;*j*=j_o; *k*=k_o+$^1/_2$,…,k_1-$^1/_2$):

$$E_{z i,j_o,k}^{n+1} = \{E_{z i,j_o,k}^{n+1}\}_{(2.20)} + C_{b,E_z}\Big|_{i,jo,k} H_{x,\mathrm{inc}\, i,j_o-1/2,k}^{n+1/2} \tag{2.44}$$

H_x components at cells referenced (*i*=i_o,…,i_1;*j*=j_o-$^1/_2$; *k*=k_o+$^1/_2$,…,k_1-$^1/_2$):

$$\mathrm{H}_{\mathrm{x}\,\mathrm{i},\mathrm{j}_\mathrm{o}-1/2,\mathrm{k}}^{\mathrm{n}+1/2} = \{\mathrm{H}_{\mathrm{x}\,\mathrm{i},\mathrm{j}_\mathrm{o}-1/2,\mathrm{k}}^{\mathrm{n}+1/2}\}_{(2.15)} + \mathrm{D}_{\mathrm{b},\mathrm{H}_\mathrm{x}}\Big|_{\mathrm{i},\mathrm{j}_\mathrm{o}-1/2,\mathrm{k}} \mathrm{E}_{\mathrm{z,inc}\,\mathrm{i},\mathrm{j}_\mathrm{o},\mathrm{k}}^{\mathrm{n}} \tag{2.45}$$

H_z components at cells referenced ($i=i_o+{}^1/_2,\ldots,i_1-{}^1/_2; j=j_o-{}^1/_2; k=k_o,\ldots,k_1$):

$$\mathrm{H}_{\mathrm{z}\,\mathrm{i},\mathrm{j}_\mathrm{o}-1/2,\mathrm{k}}^{\mathrm{n}+1/2} = \{\mathrm{H}_{\mathrm{z}\,\mathrm{i},\mathrm{j}_\mathrm{o}-1/2,\mathrm{k}}^{\mathrm{n}+1/2}\}_{(2.17)} - \mathrm{D}_{\mathrm{b},\mathrm{H}_\mathrm{z}}\Big|_{\mathrm{i},\mathrm{j}_\mathrm{o}-1/2,\mathrm{k}} \mathrm{E}_{\mathrm{x,inc}\,\mathrm{i},\mathrm{j}_\mathrm{o},\mathrm{k}}^{\mathrm{n}} \tag{2.46}$$

E_x components at cells referenced ($i=i_o+{}^1/_2,\ldots,i_1-{}^1/_2; j=j_1; k=k_o,\ldots,k_1$):

$$\mathrm{E}_{\mathrm{x}\,\mathrm{i},\mathrm{j}_1,\mathrm{k}}^{\mathrm{n}+1} = \{\mathrm{E}_{\mathrm{x}\,\mathrm{i},\mathrm{j}_1,\mathrm{k}}^{\mathrm{n}+1}\}_{(2.18)} + \mathrm{C}_{\mathrm{b},\mathrm{Ex}}\Big|_{\mathrm{i},\mathrm{j}_1,\mathrm{k}} .\mathrm{H}_{\mathrm{z,inc}\,\mathrm{i},\mathrm{j}_1+1/2,\mathrm{k}}^{\mathrm{n}+1/2} \tag{2.47}$$

E_z components at cells referenced ($i=i_o,\ldots,i_1; j=j_1; k=k_o+{}^1/_2,\ldots,k_1-{}^1/_2$):

$$\mathrm{E}_{\mathrm{z}\,\mathrm{i},\mathrm{j}_1,\mathrm{k}}^{\mathrm{n}+1} = \{\mathrm{E}_{\mathrm{z}\,\mathrm{i},\mathrm{j}_1,\mathrm{k}}^{\mathrm{n}+1}\}_{(2.20)} - \mathrm{C}_{\mathrm{b},\mathrm{E}_\mathrm{z}}\Big|_{\mathrm{i},\mathrm{j}_1,\mathrm{k}} \mathrm{H}_{\mathrm{x,inc}\,\mathrm{i},\mathrm{j}_1+1/2,\mathrm{k}}^{\mathrm{n}+1/2} \tag{2.48}$$

H_x components at cells referenced ($i=i_o,\ldots,i_1; j=j_1+{}^1/_2; k=k_o+{}^1/_2,\ldots,k_1-{}^1/_2$):

$$\mathrm{H}_{\mathrm{x}\,\mathrm{i},\mathrm{j}_1+1/2,\mathrm{k}}^{\mathrm{n}+1/2} = \{\mathrm{H}_{\mathrm{x}\,\mathrm{i},\mathrm{j}_1+1/2,\mathrm{k}}^{\mathrm{n}+1/2}\}_{(2.15)} - \mathrm{D}_{\mathrm{b},\mathrm{H}_\mathrm{x}}\Big|_{\mathrm{i},\mathrm{j}_1+1/2,\mathrm{k}} \mathrm{E}_{\mathrm{z,inc}\,\mathrm{i},\mathrm{j}_1,\mathrm{k}}^{\mathrm{n}} \tag{2.49}$$

H_z components at cells referenced ($i=i_o+{}^1/_2,\ldots,i_1-{}^1/_2; j=j_1+{}^1/_2; k=k_o,\ldots,k_1$):

$$H_{z\,i,j_1+1/2,k}^{n+1/2} = \{H_{z\,i,j_1+1/2,k}^{n+1/2}\}_{(2.17)} + D_{b,H_z}\Big|_{i,j_1+1/2,k} E_{x,inc\,i,j_1,k}^{n} \tag{2.50}$$

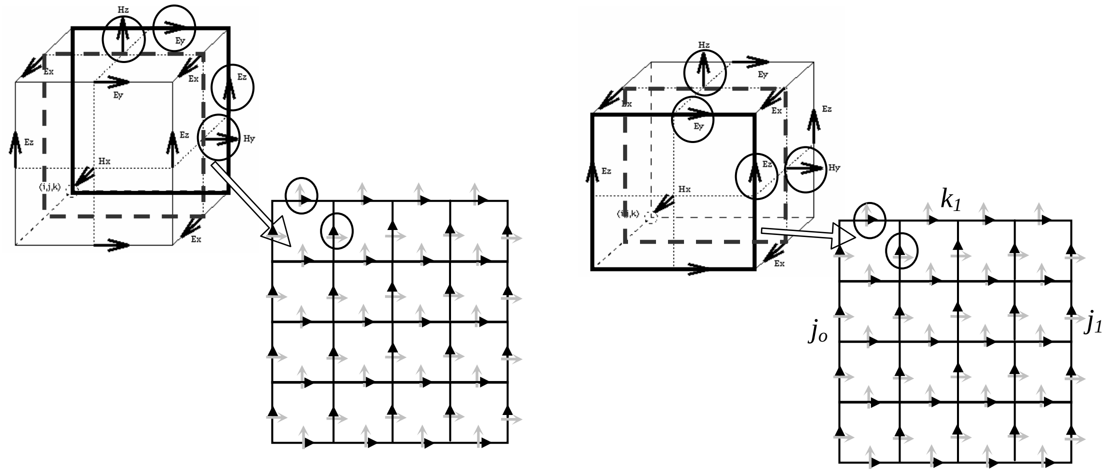

Figure 2.7(a):Location of E_y (→) and E_z(↑) components in planes $i=i_o$ and $i=i_1$ Location of H_z (↑) and H_y(→) components in planes $i=i_o-1/2$ and $i=i_1+1/2$

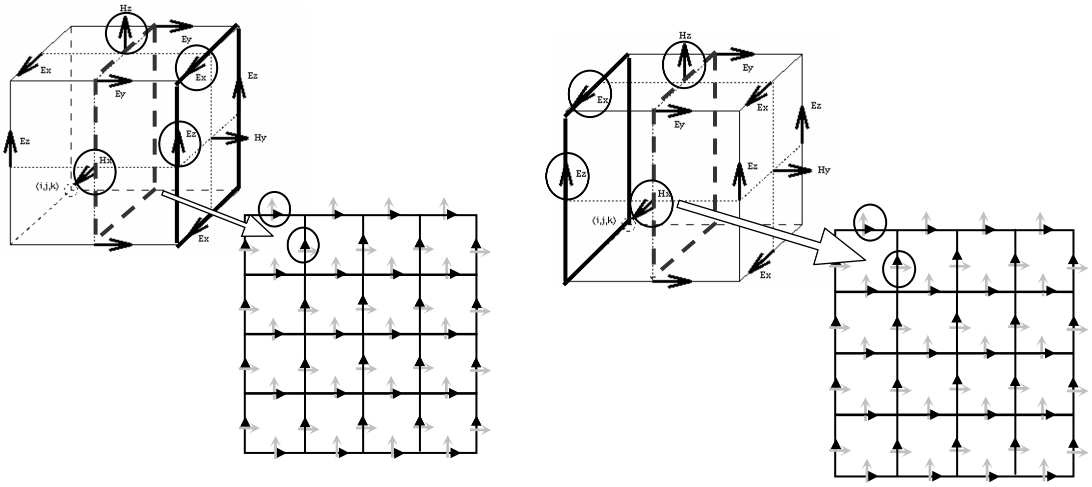

Figure 2.7(b):Location of E_x(→) and E_z (↑) components in planes $j=j_o$ and $j=j_1$ Location of H_z (↑) and H_x (→) components in planes $j=j_o-1/2$ and $j=j_1+1/2$

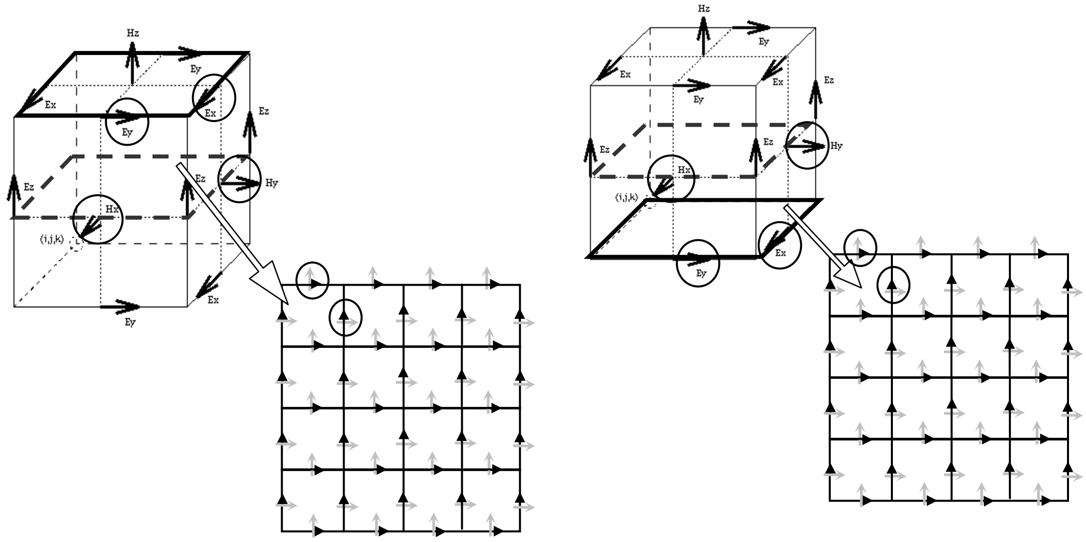

Figure 2.7(c) Location of E_x(→) and E_y (↑) components in planes $k=k_o$ and $k=k_1$ Location of H_x (↑) and H_y (→) components in planes $k=k_o$-1/2 and $k=k_1$+1/2

Considering Figure 2.7(c), the E_x components at cells referenced

($i=i_o+{}^1/_2,\ldots, i_1-{}^1/_2; j=j_o,\ldots,j_1; k=k_o$) are given by:

$$E_{x\,i,j,k_o}^{n+1} = \{E_{x\,i,j,k_o}^{n+1}\}_{(2.18)} + C_{b,Ex}\Big|_{i,j,k_o} . H_{y,inc\,i,j,k_o-1/2}^{n+1/2} \tag{2.51}$$

E_y components at cells referenced ($i=i_o,\ldots,i_1; j=j_o+{}^1/_2,\ldots,j_1-{}^1/_2; k=k_o$):

$$E_{y\,i,j,k_o}^{n+1} = \{E_{y\,i,j,k_o}^{n+1}\}_{(2.19)} - C_{b,Ey}\Big|_{i,j,k_o} . H_{x,inc\,i,j,k_o-1/2}^{n+1/2} \tag{2.52}$$

H_x components at cells referenced ($i=i_o,\ldots,i_1; j=j_o+{}^1/_2,\ldots,j_1-{}^1/_2; k=k_o-{}^1/_2$):

$$H_{x_{i,j,k_o-1/2}}^{n+1/2} = \{H_{x_{i,j,k_o-1/2}}^{n+1/2}\}_{(2.15)} - D_{b,H_x}\Big|_{i,j,k_o-1/2} E_{y,inc_{i,j,k_o}}^{n} \tag{2.53}$$

H_y components at cells referenced ($i=i_o+{}^1/_2,\ldots,i_1-{}^1/_2; j=j_o,\ldots,j_1;\ k=k_o-{}^1/_2$):

$$H_{y_{i,j,k_o-1/2}}^{n+1/2} = \{H_{y_{i,j,k_o-1/2}}^{n+1/2}\}_{(2.16)} + D_{b,H_y}\Big|_{i,j,k_o-1/2} E_{x,inc_{i,j,k_o}}^{n} \tag{2.54}$$

E_x components at cells referenced ($i=i_o+{}^1/_2,\ldots,i_1-{}^1/_2; j=j_o,\ldots,j_1;\ k=k_1$):

$$E_{x_{i,j,k_1}}^{n+1} = \{E_{x_{i,j,k_1}}^{n+1}\}_{(2.18)} - C_{b,Ex}\Big|_{i,j,k_1} .H_{y,inc_{i,j,k_1+1/2}}^{n+1/2} \tag{2.55}$$

E_y components at cells referenced ($i=i_o,\ldots,i_1; j=j_o+{}^1/_2,\ldots,j_1-{}^1/_2;\ k=k_1$):

$$E_{y_{i,j,k_1}}^{n+1} = \{E_{y_{i,j,k_1}}^{n+1}\}_{(2.19)} + C_{b,Ey}\Big|_{i,j,k_1} .H_{x,inc_{i,j,k_1+1/2}}^{n+1/2} \tag{2.56}$$

H_x components at cells referenced ($i=i_o,\ldots,i_1; j=j_o+{}^1/_2,\ldots,j_1-{}^1/_2;\ k=k_1+{}^1/_2$):

$$H_{x_{i,j,k_1+1/2}}^{n+1/2} = \{H_{x_{i,j,k_1+1/2}}^{n+1/2}\}_{(2.15)} + D_{b,H_x}\Big|_{i,j,k_1+1/2} E_{y,inc_{i,j,k_1}}^{n} \tag{2.57}$$

H_y components at cells referenced ($i=i_o+{}^1/_2,\ldots,i_1-{}^1/_2; j=j_o,\ldots,j_1;\ k=k_1+{}^1/_2$):

$$H_{y_{i,j,k_1+1/2}}^{n+1/2} = \{H_{y_{i,j,k_1+1/2}}^{n+1/2}\}_{(2.16)} - D_{b,H_y}\Big|_{i,j,k_1+1/2} E_{x,inc_{i,j,k_1}}^{n} \tag{2.58}$$

Auxiliary one-dimensional FDTD routine simulating the arbitrary propagation of the incident wave (IFA) is used to simplify the implementation of the two or three-dimensional computational domain. The common boundary of the total/scattered region's surface interface is considered same as the origin for the one-dimensional wave vector. Linear interpolation using the closest two points in the source grid is used, given the delay distance and source grid values as shown in [3, 5].

2.5 Absorbing Boundary Conditions (ABC)

In order to use Finite-Difference Time Domain method (FDTD) method to solve the electromagnetic wave interaction problems in unbounded regions, an absorbing boundary condition (ABC) must be introduced at the outer lattice boundary of the problem to simulate the extension of the lattice to infinity. For an ideal ABC, it should be able to absorb waves travelling outwardly from an FDTD mesh with extremely low boundary reflection. It should also possess the ability to be implemented for a distance close enough to the scatterers and radiators, in turn to make the computation more efficiently and effectively. Therefore, absorbing-Boundary conditions (ABC’s) become one of the most critical elements of finite-different time-domain (FDTD) analyses.

The more commonly used analytical absorbing-boundary conditions are Mur [7] and Liao [10], which provide effective reflection between -35 to -40 dB for most FDTD simulations. Besides, these methods unfortunately have been shown in the past to be very sensitive to the frequency and propagation direction of the radiation incident upon them [11]. As a result, these boundaries have had to be placed at large distances from radiators and scatterers, such that they can be effective. However, the Perfectly Matched Layer (PML), introduced by Berenger [12] in 1994, allowed the boundary reflections below -80dB to be realized. PML is based on surrounding the FDTD problem space with a highly lossy and matched non-physical absorber. This is analogous to be physical treatment of walls of an anechoic chamber. It has been found to be the most accurate technique of the ABCs available and has become a standard in most current FDTD simulations [13, 14]. Hence, PML is employed and implemented is this thesis and will be briefly discussed in the next sub-sections.

2.5.1 Berenger's Field-Splitting Formulation for 2D PML

In this section, the equations of a PML medium for two-dimensional TE (Transverse electric) problem will be first discussed. In Cartesian coordinates, the electromagnetic field involves only three components, i.e. E_x, E_y and H_z , and the Maxwell equations reduce to the three equations. In the most general case, which is a medium with an electric conductivity σ and a magnetic conductivity σ^*, these equations can be written as follows:

$$\varepsilon_o \frac{\partial E_x}{\partial t} + \sigma E_x = \frac{\partial H_z}{\partial y} \tag{2.59}$$

$$\varepsilon_o \frac{\partial E_y}{\partial t} + \sigma E_y = -\frac{\partial H_z}{\partial x} \tag{2.60}$$

$$\mu_o \frac{\partial H_z}{\partial t} + \sigma^* H_z = \frac{\partial E_x}{\partial y} - \frac{\partial E_y}{\partial x} \tag{2.61}$$

Moreover, it is known that a plane wave incident on a planar boundary of a dispersionless medium from free space is perfectly transmitted without reflection (matched across a planar boundary) for all normally incident waves if the following matching condition is satisfied for that medium.

$$\frac{\sigma}{\varepsilon_0} = \frac{\sigma^*}{\mu_0} \tag{2.62}$$

On the other hand, obliquely incident waves partially reflect back to the free space, thus affecting the numerical results. The PML technique solves this problem by matching the incident wave to the absorbing boundary medium for all polarisations, all frequencies and all angles of incidence.

The PML medium in the TE case is defined now. The basis of this definition is to splitting the magnetic component Hz into two subcomponents, i.e. H_{zx} and H_{zy}.. This makes the existence of four components E_x, E_y, H_{zx} and H_{zy} in the PML medium. Thus, the resultant four field components are coupled by the following equations [12]:

$$\varepsilon_o \frac{\partial E_x}{\partial t} + \sigma_y E_x = \frac{\partial (H_{zx} + H_{zy})}{\partial y} \tag{2.63}$$

$$\varepsilon_o \frac{\partial E_y}{\partial t} + \sigma_x E_y = -\frac{\partial(H_{zx} + H_{zy})}{\partial x} \tag{2.64}$$

$$\mu_o \frac{\partial H_{zx}}{\partial t} + \sigma_x^* H_{zx} = -\frac{\partial E_y}{\partial x} \tag{2.65}$$

$$\mu_o \frac{\partial H_{zy}}{\partial t} + \sigma_y^* H_{zy} = \frac{\partial E_x}{\partial y} \tag{2.66}$$

As can be observed from equations (2.63) to (2.66), if $\sigma_x^* = \sigma_y^*$, then the last two equations can be combined and the PML medium holds the particular cases through the usual media. If $\sigma_x = \sigma_y = \sigma_x^* = \sigma_y^*$, equation above reduce to the Maxwell equations of vacuum, if $\sigma_x = \sigma_y$ and $\sigma_x^* = \sigma_y^* = 0$, it reduces to the equations of conductive medium. Finally, if $\sigma_x = \sigma_y$ and $\sigma_x^* = \sigma_y^*$, it reduces to the equations of the absorbing medium.

In the other point of view, If $\sigma_y = \sigma_y^* = 0$, the PML medium can only absorb a plane wave (E_y, H_{zx}) propagating along x, but it does not absorb a wave (E_x, H_{zy}) propagating along y, this can be noticed from equations (2.64) and (2.65).Inversely, if $\sigma_x = \sigma_x^* = 0$, outgoing waves of ($E_y$, H_{zx}) propagating along x were not absorbed and waves of (E_x, H_{zy}) were absorbed propagating along y by the PML.

The general configuration of the PML technique is illustrated in Figure 2.8. Considering Figure 2.8, a source of outgoing waves is located in the centre of FDTD computational domain which is surrounded by a PML ABC of several cells thickness and terminated by Perfectly Electric Conducting (PEC) walls on the four sides.

On the both left and right sides of the PML layers, only existence of σ_x and σ_x^* and indicated as PML $(\sigma_x, \sigma_x^*, 0, 0)$, while on the top and bottom side of PML layers, only σ_y and σ_y^* are present and expressed as PML $(0, 0, \sigma_y, \sigma_y^*)$. Therefore, the matched PML $(\sigma_x, \sigma_x^*, 0, 0)$ on the left and right sides permit the outgoing waves propagate without reflection through interface vacuum-layer AB and CD which is normal to x axis. Likewise, the outgoing wave can propagate without reflection through the BC and DA interfaces normal to y with the presence of the matched PML $(0, 0, \sigma_y, \sigma_y^*)$ on the top and bottom sides of the computational domain [12].

At the corners where horizontal and vertical PML intersect, all four losses occur and give PML $(\sigma_x, \sigma_x^*, \sigma_y, \sigma_y^*)$ that contains the conductivities equal to those of the adjacent $(\sigma_x, \sigma_x^*, 0, 0)$ and $(0, 0, \sigma_y, \sigma_y^*)$. Again, this will allow the outgoing wave to propagate without reflection through the BB_1 and BB_2 interface [12].

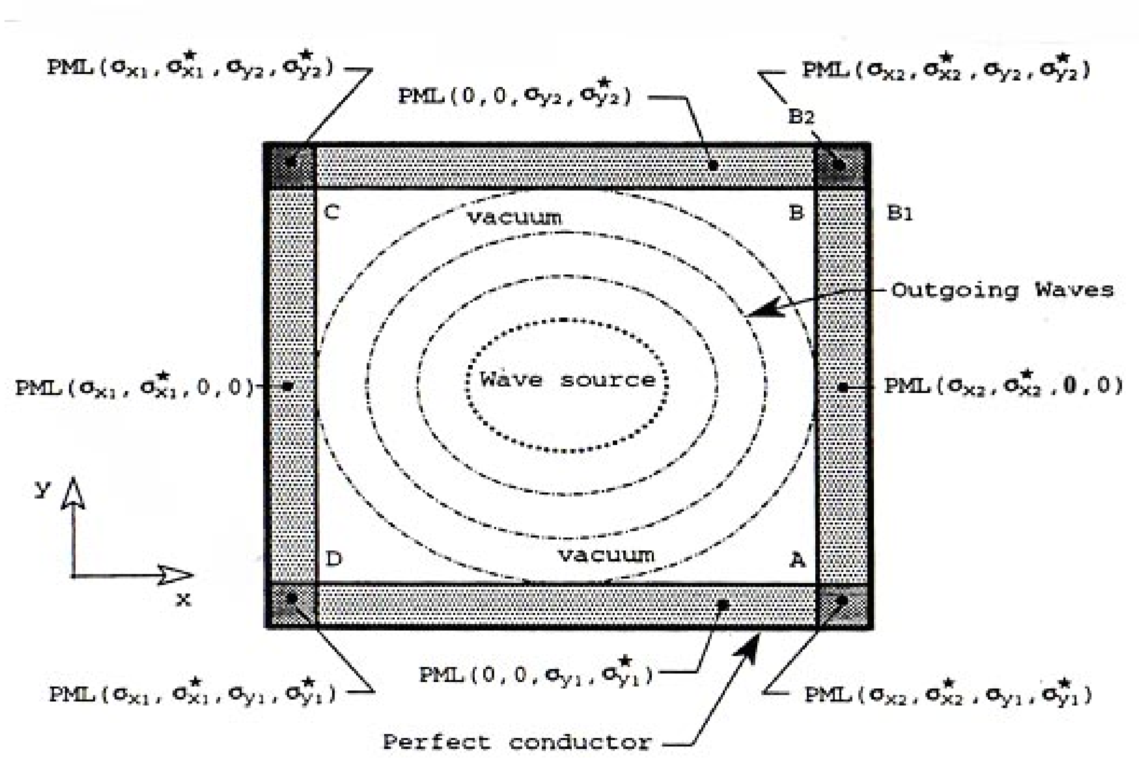

Figure 2.8: Implementation of Berenger's PML ABC on a 2-D FDTD grid [12].

In the other hand, Berenger also proposes that the electric and magnetic losses should increase gradually with a certain profile as a function of the depth of the PML layer. Therefore, power-law profile gives the electric and magnetic loss as a function of the depth as in equations (2.67) and (2.68) respectively [12].

$$\sigma(\rho_e) = \sigma_{\max}\left(\frac{\rho_e}{\delta}\right)^n \tag{2.67}$$

$$\sigma^*(\rho_m) = \sigma^*_{max}\left(\frac{\rho_m}{\delta}\right)^n \tag{2.68}$$

where thickness of the PML layer is δ, electric conductivity σ represent either σ_x or

σ_y , magnetic conductivity σ^* represent either $\sigma_x{}^*$ or $\sigma_y{}^*$, n is the integer number either 1 or 2 (n=1 for linear profile, n=2 for parabolic profile) and finally ρ_m and ρ_e is the depth into the PML (See Figure 2.9). With increasing depth, both losses should increase to the values of $\sigma_{\max}$ and $\sigma_{\max}{}^*$ next to the PEC walls. The net amount of reflection from the PEC wall at arbitrary angle of incidence θ is given as [12]:

$$R(\theta) = [R(0)]^{cos\,\theta} \tag{2.69}$$

with

$$\mathrm{R}(0) = \mathrm{e}^{-(2/\varepsilon_o c)\int_0^\delta \sigma(\rho)d\rho} \tag{2.70}$$

where c is the speed of light and ε_0 is the permittivity of free space. By inserting equations (2.67) and (2.68) into (2.70), this yields the normal incidence of PML reflection factor of

$$R(0) = e^{-2\sigma_{max}\delta/(n+1)\varepsilon_o c} \tag{2.71}$$

For the case of the PML layers with conductivities increasing geometrically, the profiles will be shown as follows [15]:

$$\sigma(\rho) = \sigma_0\left(g^{1/\Delta x}\right)^{\rho} \tag{2.72}$$

where the Δx is the spatial increment of the FDTD mesh and σ_0 is the conductivity in the vacuum-layer interface. The conductivity increases by grading factor g from one layer to the next. By substituting equation (2.72) into (2.70), for a N-cell layer the normal reflection is then shown as follows:

$$R(0) = e^{-(2/\varepsilon_o c)((g^N - 1)/\ln g)\sigma_o \Delta x} \tag{2.73}$$

From the equation (2.73), the conductivity σ_0 in term of N, g and R(0) can be obtained as follows:

$$\sigma_o = -\frac{\varepsilon_o c}{2\Delta x} \frac{ln\, g}{g^N - 1} ln\, R(0) \tag{2.74}$$

Figure 2.9 shows only right side of the FDTD computational domain surrounded by a PML layer. As can be seen, the conductivities at the mesh points were implemented as the average value in the cell around the index location. Hence, the conductivity that is considered at index L is given as follows:

$$\sigma_n(L) = \frac{1}{\Delta x} \int_{\rho(L) - \Delta x/2}^{\rho(L) + \Delta x/2} \sigma(u) du \tag{2.75}$$

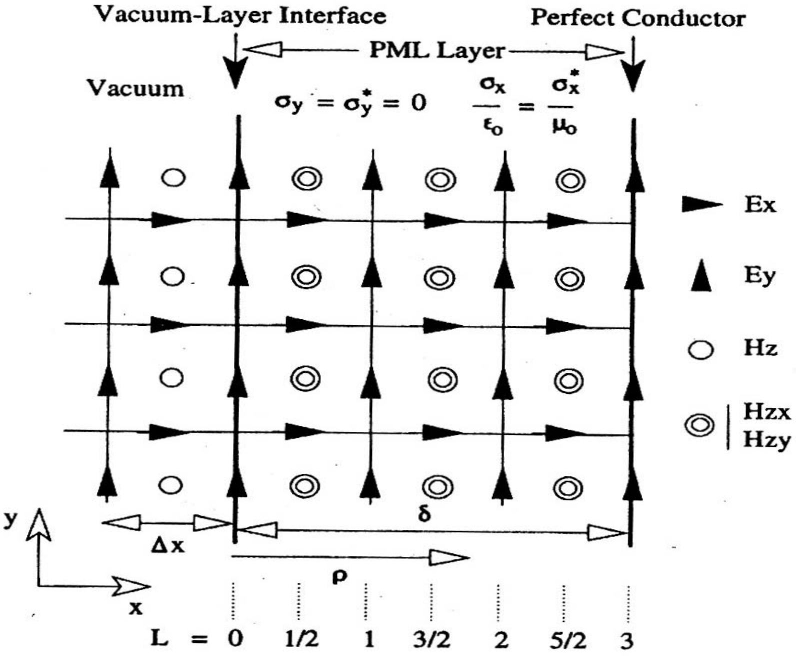

Figure 2.9: Right side of a domain surrounded by PML layer [12, 16].

For linear or parabolic profiles, the conductivities at index L=0,1/2,1,3/2,…….., can be obtained by inserting equation (2.67) into (2.75) and taking account of (2.71). The expression is shown in equations (2.76) and (2.77).

$$\sigma_n(0) = \frac{\sigma_m}{(n+1)2^{n+1}N^n} = -\frac{\varepsilon_0 c\, ln\, R(0)}{2^{n+2}\Delta x N^{n+1}} \tag{2.76}$$

$$\sigma_n(L>0) = \sigma(0)\left[(2L+1)^{n+1} - (2L-1)^{n+1}\right] \tag{2.77}$$

By implementing the similar progress, the conductivities in geometric progression profiles are [15]

$$\sigma_n(0) = \sigma_0 \frac{\sqrt{g}-1}{ln\, g} = -\frac{\varepsilon_0 c\left(1-\sqrt{g}\right) ln\, R(0)}{2\Delta x\left(g^N-1\right)} \tag{2.78}$$

$$\sigma_n(L>0) = \sigma_0 \frac{g-1}{\sqrt{g}\, ln\, g} g^L = \frac{\varepsilon_0 c(1-g) ln\, R(0)}{2\Delta x\sqrt{g}\left(g^N-1\right)} g^L \tag{2.79}$$

2.5.2 Berenger's PML in Three-Dimensions

For 3D structures, six Cartesian field vector components (equations (2.3) to (2.8)) are used to define the field components in which the following twelve modified version of Maxwell equations can be stated:

$$\mu_o \frac{\partial H_{xy}}{\partial t} + \sigma_y^* H_{xy} = -\frac{\partial(E_{zx}+E_{zy})}{\partial y} \tag{2.80}$$

$$\mu_o \frac{\partial H_{xz}}{\partial t} + \sigma_z^* H_{xz} = \frac{\partial(E_{yx}+E_{yz})}{\partial z} \tag{2.81}$$

$$\mu_o \frac{\partial H_{yz}}{\partial t} + \sigma_z^* H_{yz} = \frac{\partial(E_{xy}+E_{xz})}{\partial z} \tag{2.82}$$

$$\mu_o \frac{\partial H_{yx}}{\partial t} + \sigma_x^* H_{yx} = -\frac{\partial (E_{zx} + E_{zy})}{\partial x} \tag{2.83}$$

$$\mu_o \frac{\partial H_{zx}}{\partial t} + \sigma_x^* H_{zx} = -\frac{\partial (E_{yx} + E_{yz})}{\partial x} \tag{2.84}$$

$$\mu_o \frac{\partial H_{zy}}{\partial t} + \sigma_y^* H_{zy} = \frac{\partial (E_{xy} + E_{xz})}{\partial y} \tag{2.85}$$

$$\varepsilon_o \frac{\partial E_{xy}}{\partial t} + \sigma_y E_{xy} = \frac{\partial (H_{zx} + H_{zy})}{\partial y} \tag{2.86}$$

$$\varepsilon_o \frac{\partial E_{xz}}{\partial t} + \sigma_z E_{xz} = \frac{\partial (H_{yx} + H_{yz})}{\partial z} \tag{2.87}$$

$$\varepsilon_o \frac{\partial E_{yz}}{\partial t} + \sigma_z E_{yz} = \frac{\partial (H_{xy} + H_{xz})}{\partial z} \tag{2.88}$$

$$\varepsilon_o \frac{\partial E_{yx}}{\partial t} + \sigma_x E_{yx} = \frac{\partial (H_{zx} + H_{zy})}{\partial x} \tag{2.89}$$

$$\varepsilon_o \frac{\partial E_{zx}}{\partial t} + \sigma_x E_{zx} = \frac{\partial (H_{yx} + H_{yz})}{\partial x} \tag{2.90}$$

$$\varepsilon_o \frac{\partial E_{zy}}{\partial t} + \sigma_y E_{zy} = \frac{\partial (H_{yx} + H_{xz})}{\partial y} \tag{2.91}$$

PML matching conditions and grid structures are similar to those TM case are utilised, for three-dimensional PML layers in x, y and z directions.

2.5.3 Numerical Implementation of the PML in 3-D case

Due to the fact that the attenuation to outgoing waves afforded by PML medium is so rapidly that standard Yee time-stepping cannot be applied blindly, therefore, a suitable explicit exponential time step algorithm is proposed to be used in PML medium [12, 17]. For example, the updated equations for H_{zy} and E_{xy} in the PML region (applying equations (2.85) and (2.86)) are shown as follows:

$$H_{zy_{i,j,k}}^{n+1/2} = e^{\frac{-\sigma^*_{y_{i,j,k}}\Delta t}{\mu_{i,j,k}}} H_{z_{i,j,k}}^{n-1/2} + \frac{1-e^{\frac{-\sigma^*_{y_{i,j,k}}\Delta t}{\mu_{i,j,k}}}}{\sigma^*_{y_{i,j,k}}.\Delta}\begin{pmatrix} E_{xy_{i,j+1/2,k}}^{n} - E_{xy_{i,j-1/2,k}}^{n} \\ + E_{xz_{i,j+1/2,k}}^{n} - E_{xz_{i,j-1/2,k}}^{n} \end{pmatrix} \qquad (2.92)$$

$$E_{xy_{i,j,k}}^{n+1} = e^{\frac{-\sigma_{y_{i,j,k}}\Delta t}{\varepsilon_{i,j,k}}} E_{xy_{i,j,k}}^{n} + \frac{1-e^{\frac{-\sigma_{y_{i,j,k}}\Delta t}{\varepsilon_{i,j,k}}}}{\sigma_{y_{i,j,k}}.\Delta}\begin{pmatrix} H_{zx_{i,j+1/2,k}}^{n+1/2} - H_{zx_{i,j-1/2,k}}^{n+1/2} \\ + H_{zy_{i,j+1/2,k}}^{n+1/2} - H_{zy_{i,j-1/2,k}}^{n+1/2} \end{pmatrix} \qquad (2.93)$$

The updating equations for the rest of the ten components can be derived in a similar way as shown above.

It should be noted that the above updated equations are valid throughout the PML regions except at the interfaces. For example, at the y_L interface (equivalent to $j = j_L$)

in the discrete space, where j is the y direction cell reference as shown in equation (2.9), then the resultant equation at the interface for the E_{xy} component is

$$E_{xy\,i,j,k}^{\,n+1} = E_{xy\,i,j,k}^{\,n} + \frac{\Delta t}{\varepsilon_{i,j_L,k}.\Delta}\left(H_{z\,i,j+1/2,k}^{\,n+1/2} - H_{zx\,i,j-1/2,k}^{\,n+1/2} - H_{zy\,i,j-1/2,k}^{\,n+1/2}\right) \tag{2.94}$$

where it is assumed that σ_y is zero at the interface.

2.6 Conclusions

The fundamental principles of the FDTD method are reviewed implicitly and explicitly throughout this chapter. These cover the solution of Maxwell's curl equations using finite differences, derivation of FDTD updating equations for electric and magnetic field components in a 3D computational domain. It also includes the demonstration of the accuracy and stability factor that govern the FDTD technique. Moreover, introducing the hard source and incident plane wave excitation into the FDTD computational domain were also briefly discussed. In addition, the concepts on how the two- and three-dimensional Berenger’s perfectly matched layer (PML) absorbing boundary conditions were imposed to truncate the FDTD computational domain, were clearly elucidated. With the knowledge which was explained in this chapter, a three-dimensional FDTD Fortran 95 source code was written and ready to be used for bioelectromagnetic applications. These applications will eventually be shown in chapter four and five with different aspects of bioelectromagnetic problems.

2.7 References

[1] *International FDTD database: URL:* http://www.fdtd.org.

[2] K.S.Kunz and R.J.Luebbers, "The Finite Difference Time Domain for Electromagnetics," *Baco Raton,FL:CRC Press*, 1993.

[3] A.Taflove, *Computational Electrodynamics*: Norwood, MA: Artech House, 1995.

[4] A.Taflove, *Advances in Computational Electrodynamics: The Finite Difference Time Domain Method*: Dedham,MA:Artech House, 1998.

[5] A.Taflove and S.C.Hagness, *Computational Electrodynamics: the finite-difference time-domain method*, 2nd ed: Artech House,Inc, 2000.

[6] K.S.Yee, "Numerical solution of initial boundary value problems involving Maxwell's equation in isotropic media," *IEEE Trans. on Antennas Propagation*, vol. AP-14, pp. 302-307, 1966.

[7] G.Mur, "Absorbing boundary conditions for the Finite-Difference Approximation of the time-domain Electromagnetic-field equations," *IEEE Trans. On Electromagnetic compatibility*, vol. EMC-23, pp. 377-382, 1981.

[8] A.Taflove and K.R.Umashankar, "A novel method to analyze electromagnetic

scattering of complex objects," *IEEE Transactions on Electromagnetic Compatibility*, vol. 24, pp. 397-405, 1982.

[9] A.Taflove, "Advances in Computational Electrodynamics: The Finite-Difference Time-Domain Method," Artech House, 1998, pp. 627-632.

[10] Z.P.Liao, H.L.Wong, B.P.Yang, and Y.F.Yuan, "A Transmitting boundary for transient wave analysis," *Scientia Sinica (Series A)*, pp. 1063-1076, 1984.

[11] J.Fang, "Absorbing boundary conditions applied to model wave propagation in microwave integrated-circuits," *IEEE Trans. on Microwave Theory and Techniques*, vol. 42, pp. 1506-1513, 1994.

[12] J.Berenger, "A perfectly matched layer for Absorption of Electromagnetic waves," *Journal of computational physics*, vol. 114, pp. 185-200, 1994.

[13] D.T.Prescott and N.V.Shuley, "Reflection Analysis of FDTD Boundary Conditions -Part II: Berenger's PML Absorbing Layers," *IEEE Trans on MTT*, vol. 45, pp. 1171-1178, 1997.

[14] D.T.Prescott and N.V.Shuley, "Reflection Analysis of FDTD Boundary Conditions - Part I: Time-Space Absorbing Boundaries," *IEEE Transactions on Microwave Theory and Techniques*, vol. 45, pp. 1162-1170, 1997.

[15] J.Berenger, "Perfectly Matched layer for the FDTD Solution of wave-structure interaction problems," *IEEE Trans. on Ant. and Propag.*, vol. 44, pp. 110-117,

1996.

[16] J.Berenger, "Improved PML for the FDTD solution of wave-structure Interaction problem," *IEEE Trans. on Antennas and Propagation*, vol. 45, pp. 466-473, 1997.

[17] R.Holland, "Finite-difference Time-domain (FDTD) analysis of magnetic diffusion," *IEEE Trans on Electromagnetic Compatibility*, vol. 36, pp. 32-39, 1994.

Chapter 3

The Lumped-Element Finite Difference Time Domain Technique (LE-FDTD) for Hybrid Electromagnetic Systems with lumped-element Modelling

3.1 Introduction

The current capacity and bandwidth of the existing wireless communication systems are insufficient to meet the needs of future mobile requirements. In anticipation of this, new wireless systems, such as HSDPA (High-Speed Downlink Packet Access), 4G, WiMAX (Worldwide Interoperability for Microwave Access), IEEE 802.11n and UWB (Ultra Wideband), are currently being developed. This will increasingly make use of tremendous higher frequencies and high density microwave integrated circuit, such as monolithic microwave integrated circuits (MMIC), to develop and produce the new communication systems and electronic device for such application in order to keep abreast in time with the new technology.

This is an area which is evolving rapidly as technology seeks to utilise higher frequencies in the interest of ever greater bandwidth. To continue moves upward in frequency, the most existing computer-aided circuit design tools, (primarily SPICE [1, 2], which are limited at digital clock speeds not exceeding 300MHz and also ignores the approximated electromagnetic effects,) are not suitable to be used to model and predict the overall performance of the circuits. Several problems on dealing with electromagnetic effect of radiation and the coupling effect between circuit elements can be encountered, if the software is blindly used. Due to these reasons, the electromagnetic simulators which can include the effect of this phenomenon by solving Maxwell's equations and taking into account the interaction between electronic circuit and electromagnetic waves comprehensively, are indispensable for accurate characteristic.

Finite Different Time Domain (FDTD) technique, since it is first proposed by Yee in 1966 [3], has attracted several researchers, particularly for its simple implementation that can be directly applied the solutions of the Maxwell's equations in time domain. In recent years, a significant effort has been made to bridging the gap between electromagnetic-field and circuit-based simulators by using this technique and it is called Lumped-element FDTD (LE-FDTD) technique [4-8]. By spatial descretizing the simulated structure into a three-dimensional grid and include the desired active and passive lumped elements between adjacent grid nodes, LE-FDTD allows the complex microwave circuits to be analysed effectively and efficiently.

This chapter reviews the conventional FDTD method and then it is followed by a derivation of the relationships between the E and H fields. This also includes the voltages and currents that are used to extend the general equations to include the lumped elements inside the grid. Subsequently, the updated equations for passive lumped elements such as resistor and capacitor will be briefly derived and discussed. Finally, a conclusion of this work will be stated. It should be noted that several test cases are analysed by this method and the results are compared with analytical solutions to verify the validity of this technique. However, it will be elucidated extensively and intensively in chapter 5.

3.2 Basic Circuit Parameters

In order to relate the electric field and magnetic field stated in FDTD analysis to the usual circuit quantities in terms of voltage and current, the following fundamental expressions can be used [9, 10]:

$$V(t, x_i) = \int_{C_v} \vec{E}(t, x_i) \cdot d\bar{l} \tag{3.1a}$$

$$I(t, x_i) = \int_{C_I} \vec{H}(t, x_i) \cdot d\bar{l} \tag{3.1b}$$

where C_v is a contour extending from a defined voltage reference point (usually a ground plane) to the circuit at location, x_i . In most of the cases, x_i is a point on a metallic strip transmission line (a microstrip) that propagates the dominant TEM mode. In this situation, $V(t, x_i)$ is independent of the choice of C_v if this path is confined to the transverse plane, and C_v can be conveniently chosen to extend in a perpendicular manner from the ground plane to the adjacent surface of the microstrip. Likewise, the selection of the contour C_I to wrap completely around the strip conductor at its surface in the transverse plane provides the local current. However, for the case of non-TEM modes, the above assumption cannot be applied blindly [9, 10].

3.3 Basic FDTD Algorithm and Extension

3.3.1 Basic FD-TD Formulation

The basic FDTD update equations used to solve the Maxwell's equations, have been clearly derived in the previous chapter and literatures [9-11]. Therefore, it will not be repeated again here. Consider Maxwell's curl $\vec{H}$ equation (in which it is suitable for time-stepping the electric field [12]):

$$\nabla \times \vec{H} = \vec{J}_c + \frac{\partial \vec{D}}{\partial t} \tag{3.2}$$

where $\vec{J}_c$ and $\vec{D}$ are the conduction current and the electric displacement respectively. It should be noted that $\vec{J}_c = \sigma \vec{E}$ and $\vec{D} = \varepsilon \vec{E}$. By applying the central differencing into equation (3.2), the following expression is obtained:

$$E_z\Big|_{i,j,k}^{n+1} = \left(\frac{1-\dfrac{\sigma_{i,j,k}\Delta t}{2\varepsilon_{i,j,k}}}{1+\dfrac{\sigma_{i,j,k}\Delta t}{2\varepsilon_{i,j,k}}} \right) E_z\Big|_{i,j,k}^{n} + \left(\frac{\dfrac{\Delta t}{\varepsilon_{i,j,k}}}{1+\dfrac{\sigma_{i,j,k}\Delta t}{2\varepsilon_{i,j,k}}} \right) \left(\begin{array}{c} \dfrac{H_y\Big|_{i+1/2,j,k}^{n+1/2} - H_y\Big|_{i-1/2,j,k}^{n+1/2}}{\Delta x} + \\ \dfrac{H_x\Big|_{i,j-1/2,k}^{n+1/2} - H_x\Big|_{i,j+1/2,k}^{n+1/2}}{\Delta y} \end{array} \right) \tag{3.3}$$

As can be seen, all the H quantities on the right hand sides of equation (3.3) are taken at time step n+1/2, centred in time relative to the stored electric field, $E_z\Big|_{i,j,k}^{n}$, and the advance updated electric field, $E_z\Big|_{i,j,k}^{n+1}$. In addition, assuming that J_c is also evaluated at time step n+1/2. Hence, the semi-implicit formulation for the conduction current can be expressed as follows:

$$J_c\Big|_{i,j,k}^{n+1/2} = \sigma_{i,j,k} E_z\Big|_{i,j,k}^{n+1/2} = \frac{\sigma_{i,j,k}}{2}\left(E_z\Big|_{i,j,k}^{n} + E_z\Big|_{i,j,k}^{n+1} \right) \tag{3.4}$$

Another assumption is made by denoting the Yee finite-difference analogy to the curl of $\vec{H}$ observed at $E_z\Big|_{i,j,k}$ as:

$$\nabla \times H_{i,j,k}^{n+1/2} = \frac{H_y\Big|_{i+1/2,j,k}^{n+1/2} - H_y\Big|_{i-1/2,j,k}^{n+1/2}}{\Delta x} + \frac{H_x\Big|_{i,j-1/2,k}^{n+1/2} - H_x\Big|_{i,j+1/2,k}^{n+1/2}}{\Delta y} \tag{3.5}$$

For the sake of convenience, all the circuit components are located in a free space region $\left(\varepsilon = \varepsilon_0, \sigma = 0, \vec{J}_c = 0\right)$ are assumed. Then equation (3.3) can be rewritten in the following simplified form:

$$E_z\Big|_{i,j,k}^{n+1} = E_z\Big|_{i,j,k}^{n} + \frac{\Delta t}{\varepsilon_0}\nabla \times H_{i,j,k}^{n+1/2} \tag{3.6}$$

3.3.2 Extended FD-TD Formulation

According to [13] , the modification of the three-dimensional electric field time stepping algorithms of equation (3.6) permit the addition of lumped linear and nonlinear circuit elements. However, the basis of this formulation is originally reported by Sui et al. [5] for two-dimensional problems. Subsequently, Tsuei et al. [14] and Piket-May et al. [12] have successfully extended the same principles to model full wave propagation in 3-D circuits containing both active and passive lumped elements. The fundamental concept is that circuit elements can be accounted for in Maxwell's equations by adding a lumped electric current density term J_L to the conduction and displacement currents on the right-hand sides of equation (3.6), hence, the equation now becomes

$$\nabla \times \vec{H} = \vec{J}_c + \frac{\partial \vec{D}}{\partial t} + \vec{J}_L \tag{3.7}$$

Assuming that the lumped element is located in free space at the electric field point (i,j,k), and it is also oriented in z direction of the grid. Then, the local current density that is related to the total element current I_L can be given as follows:

$$J_L = \frac{I_L}{\Delta x \Delta y} \tag{3.8}$$

Here, I_L can possibly consider as a time-derivative, time-integral, scalar multiple, or nonlinear function of the electric potential, $V = E_z\big|_{i,j,k}\Delta z$, that is developed across the element. It should be mentioned that the positive direction of the I_L is +z. Thus, the modified version of equation (3.6) that describes the presence of the lumped element can be expressed as follows:

$$E_z\Big|_{i,j,k}^{n+1} = E_z\Big|_{i,j,k}^{n} + \frac{\Delta t}{\varepsilon_0}\nabla\times H_{i,j,k}^{n+1/2} - \frac{\Delta t}{\varepsilon_0 \Delta x \Delta y} I_L^{n+1/2} \tag{3.9}$$

At the observing point of view, the lumped current in equation (3.9) is computed at time n+1/2, in which it is the same time stated to the conduction current J_c in equation (3.4). Since the lumped element current is a function of the E-field at the circuit element, hence it requires averaging $E_z\big|_{i,j,k}^{n+1}$ and $E_z\big|_{i,j,k}^{n}$ in order to produce a stable semi-implicit time-stepping algorithm. As for x- and y- orientations of a lumped element, the equation can be simply derived by permuting the coordinate subscripts of the fields.

3.4 Linear Lumped Components

3.4.1 The Resistor

Assuming a z-directed resistor R located in free space at the field component $\mathrm{E}_z\big|_{\mathrm{i,j,k}}$ and $V = E_z\big|_{i,j,k}\Delta z$ is known. According to Ohm's law (I= V/R), the resistor value (R) is directly proportional to the voltage (V) and inversely proportional to the current (I). For the operation of the FDTD field solver, the formula to include the resistor inside the FDTD computational domain can be expressed in the following form [12]:

$$\mathrm{I_z}\Big|_{\mathrm{i,j,k}}^{\mathrm{n+1/2}} = \frac{\Delta \mathrm{z}}{2\mathrm{R}}\left(\mathrm{E_z}\Big|_{\mathrm{i,j,k}}^{\mathrm{n+1}} + \mathrm{E_z}\Big|_{\mathrm{i,j,k}}^{\mathrm{n}}\right) \tag{3.10a}$$

$$J_L = \frac{I_z\Big|_{i,j,k}^{n+1/2}}{\Delta x \Delta y} \tag{3.10b}$$

By substituting equation (3.10a) into equation (3.9), the corresponding time-stepping relation can be obtained as follows

$$E_z\Big|_{i,j,k}^{n+1} = \left(\frac{1-\dfrac{\Delta t \Delta z}{2R\varepsilon_{i,j,k}\Delta x \Delta y}}{1+\dfrac{\Delta t \Delta z}{2R\varepsilon_{i,j,k}\Delta x \Delta y}}\right) E_z\Big|_{i,j,k}^{n} + \left(\frac{\dfrac{\Delta t}{\varepsilon_{i,j,k}}}{1+\dfrac{\Delta t \Delta z}{2R\varepsilon_{i,j,k}\Delta x \Delta y}}\right)\nabla \times H_{i,j,k}^{n+1/2} \tag{3.11}$$

Piket-May et al. [12] are using one or the other to terminate a 50 Ω transmission line excited by a 90-ps Gaussian pulse (spectral width of 20GHz), in order to prove the validity of equation (3.11) for FDTD modelling. The research outcomes from [12] is depicted in Figure 3.1. Figure 3.1 illustrates a comparison of the impedance matching that is provided by the numerical resistor of equation (3.11) and the physical resistor model that is composed of a one-cell-thick resistive slab in the FDTD lattice [12]. As can be found, both resistor models provide reflection coefficients of less than 1% up to 1GHz. For operating frequencies above 1GHz, the two resistor models continue to provide very close agreement in terms of reflection coefficients, although, as expected, the match to the line degrades because of presence of parasitic capacitance and inductance in each model [10].

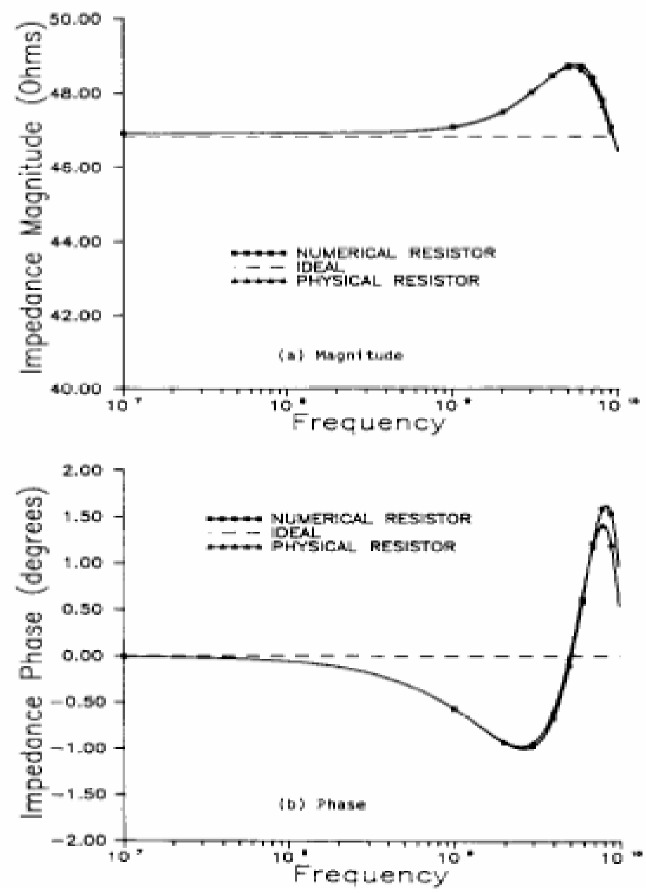

Figure 3.1: Agreement of FD-TD computed effective load impedance (low frequency to 10GHz) for the numerical resistor and the physical resistor: (a) Magnitude (b) phase [12] .

3.4.2 The Resistive Voltage Source

To model a nonreflecting (matched) source as a resistive voltage source in FDTD grid, and also assumes a z-directed lumped element, the voltage-current characteristic that describes the behaviour of a resistive voltage source in a semi-implicit manner is [12]:

$$I_z\Big|_{i,j,k}^{n+1/2} = \frac{\Delta z}{2R_s}\left(E_z\Big|_{i,j,k}^{n+1} + E_z\Big|_{i,j,k}^{n}\right) + \frac{V_s^{n+1/2}}{R_s} \tag{3.12a}$$

$$J_L = \frac{I_z\Big|_{i,j,k}^{n+1/2}}{\Delta x \Delta y} \tag{3.12b}$$

where $V_S^{n+1/2}$ is the source voltage and R_s is the internal source resistance. By substituting equation (3.12a) into equation (3.9), the corresponding time-stepping relation is derived as shown in equation (3.13).

$$\begin{aligned} E_z\Big|_{i,j,k}^{n+1} = {} & \left(\frac{1-\dfrac{\Delta t\Delta z}{2R\varepsilon_{i,j,k}\Delta x\Delta y}}{1+\dfrac{\Delta t\Delta z}{2R\varepsilon_{i,j,k}\Delta x\Delta y}}\right) E_z\Big|_{i,j,k}^{n} + \left(\frac{\dfrac{\Delta t}{\varepsilon_{i,j,k}}}{1+\dfrac{\Delta t\Delta z}{2R\varepsilon_{i,j,k}\Delta x\Delta y}}\right)\nabla\times H_{i,j,k}^{n+1/2} \\ & + \left(\frac{\dfrac{\Delta t}{R_s\varepsilon_{i,j,k}\Delta x\Delta y}}{1+\dfrac{\Delta t\Delta z}{2R_s\varepsilon_{i,j,k}\Delta x\Delta y}}\right) V_s^{n+1/2} \end{aligned} \tag{3.13}$$

3.4.3 The Capacitor

3.4.3.1 Intrinsic Capacitance

A charge can be stored into the adjacent cells in FDTD grid, therefore, it is imperative to define an intrinsic capacitance between cells of the grid. This intrinsic capacitance (grid capacitance) of adjacent cell in free space in FDTD grid can be derived in the following manner. The standard definition of capacitance is [15]:

$$C = \frac{Q}{V} \tag{3.14}$$

where Q is the stored charge and V is the voltage between the charges. The charge can be expressed in terms of the flux integral and yields an electric field term in the numerator of equation (3.14), thus, the electric field that subsequently appears in the denominator can be cancelled. Consider a cubical cell of Gaussian surface that encloses a charge Q. The relationship between the charge and field on the faces of the cell surrounding the charge is [15]:

$$Q = \varepsilon_o (\Delta)^2 \sum_{\text{six faces}} \left(E_{\text{face}}\right) = 6\varepsilon_o (\Delta)^2 E_{\text{enclosed}} \tag{3.15}$$

where $\vec{E}_{\text{face}} = \vec{E}_{\text{enclosed}} + \vec{E}_{\text{dis tan ce}}$, $\vec{E}_{\text{enclosed}}$ and $\vec{E}_{\text{dis tan ce}}$ are the electric field from the enclosed charge and external source respectively , Δ is the length of one side of the cubical cell and ε_o is the permittivity of the free space. Without the existence of the external source, $\vec{E}_{\text{enclosed}}$ is not contributing to the integral. Then, the difference in potential between the two adjacent cells containing charges of equal magnitude and opposite sign is given as follows:

$$V = -\int_{-Q_{\text{position}}}^{+Q_{\text{position}}} \vec{E} \bullet d\vec{l} = 2(\Delta)E_{\text{enclosed}} \tag{3.16}$$

By substituting equations (3.15) and (3.16) into equation (3.14), the intrinsic/grid capacitance between adjacent nodes in the FDTD grid can be found as follows:

$$C_{\text{lattice}} = 3\varepsilon_0 \Delta \tag{3.17}$$

In order to verify the presence of grid capacitance in FDTD computational domain, a simple example from [15] was presented and is confirmed here by the above equation. According to the example in [15], authors justify the grid capacitance between adjacent nodes in FDTD grid for 1-m cubical cell is 26.6pF. This can be done by discharging the deposited charge through a conductance in which can be introduced into the grid. The rate of discharge can easily be measured and can be used to obtain the associated time constant. From this time constant and the known resistance, the capacitance value can be obtained. Charge deposited into the grid will discharge through conductance with a time constant

$$\tau = R_{\text{load}} C_{\text{lattice}} \tag{3.18}$$

where R_{load} is the resistance associated with the conductivity at the grid location. Assuming the conductivity is $\sigma = 2\times10^{-4}$ S/m that is equivalent to 5 kΩ in which a single-element current source driven by a Gaussian pulse is used to excite the structure. By implementing equations (3.18) and (3.17), the expected time constant is 133 ns.

Figure 3.2 shows the measured time constant which characterizes the decay is precisely equal to 133ns and this also verifies the capacitance value that is predicted by equation (3.18).

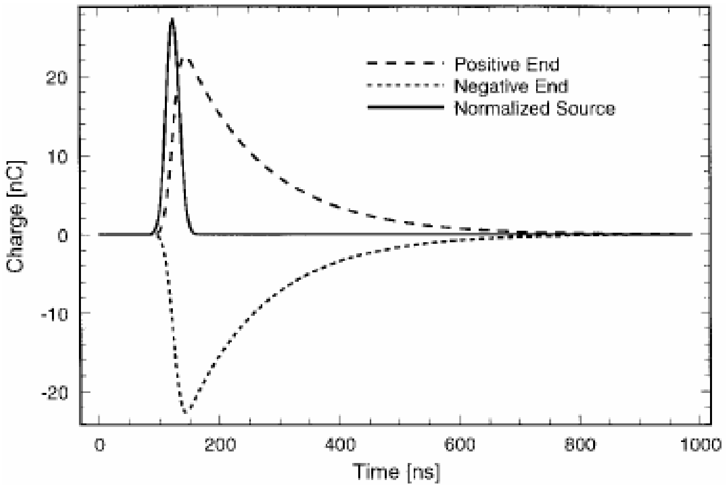

Figure 3.2: Charge versus time when the conductivity is present [15] .

3.4.3.2 Extrinsic Capacitance

In this section, insertion of capacitor C into the FDTD space lattice is discussed. Again assuming a z-directed lumped element is located in free space at $E_z\big|_{i,j,k}$, the voltage-current characteristic that depicts the capacitor's behaviour in a semi-implicit manner is [12]:

$$I_z\Big|_{i,j,k}^{n+1/2} = \frac{C\Delta z}{\Delta t}\left(E_z\Big|_{i,j,k}^{n+1} - E_z\Big|_{i,j,k}^{n}\right) \tag{3.19a}$$

$$J_L = \frac{I_z\big|_{i,j,k}^{n+1/2}}{\Delta x \Delta y} \tag{3.19b}$$

For the sake of consistency with the time stepping used for inclusion of the numerical resistor described above, equation (3.19a) is dissimilar to [16] in which the E-field samples are separated here by one time-step rather than two. The corresponding time-stepping relation is [12]:

$$E_z\big|_{i,j,k}^{n+1} = \left(\frac{1 - \dfrac{C\Delta z}{\varepsilon_{i,j,k}\Delta x \Delta y}}{1 + \dfrac{C\Delta z}{\varepsilon_{i,j,k}\Delta x \Delta y}} \right) E_z\big|_{i,j,k}^{n} + \left(\frac{\dfrac{\Delta t}{\varepsilon_{i,j,k}}}{1 + \dfrac{C\Delta z}{\varepsilon_{i,j,k}\Delta x \Delta y}} \right) \nabla \times H_{i,j,k}^{n+1/2} \tag{3.20}$$

It should be noted that the C capacitor value being modelled includes the additive contribution of the intrinsic lattice capacitance defined in section 3.4.3.1.

For the case of Parallel combination of Capacitor C and Resistor R located at $E_z\big|_{i,j,k}$, the equations (3.10) ,(3.11), (3.19) and (3.20) are combined to yield the following time-stepping relation [12]:

$$E_z\big|_{i,j,k}^{n+1} = \left(\frac{1 - \dfrac{\Delta t \Delta z}{2R\varepsilon_{i,j,k}\Delta x \Delta y} + \dfrac{C\Delta z}{\varepsilon_{i,j,k}\Delta x \Delta y}}{1 + \dfrac{\Delta t \Delta z}{2R\varepsilon_{i,j,k}\Delta x \Delta y} + \dfrac{C\Delta z}{\varepsilon_{i,j,k}\Delta x \Delta y}} \right) E_z\big|_{i,j,k}^{n}$$

$$+ \left(\frac{\dfrac{\Delta t}{\varepsilon_{i,j,k}}}{1 + \dfrac{\Delta t \Delta z}{2R\varepsilon_{i,j,k}\Delta x \Delta y} + \dfrac{C\Delta z}{\varepsilon_{i,j,k}\Delta x \Delta y}} \right) \nabla \times H_{i,j,k}^{n+1/2} \tag{3.21}$$

The tests of this FDTD approach, in a variety of numerical capacitive loads were modelled at the end of a long $50\,\Omega$ microstrip line (≈ 1-mil scale in the transverse plane). This is subjected to a rectangular step-pulse excitation of 1000 time-steps long, in which it is reported in reference [12] . Figure 3.3 shows the FDTD-computed voltage response versus time for each capacitor, and then the results are compared to the exact theoretical response. Results are in an excellent agreement for microstrips terminated with 4-nF and 20-nF capacitors.

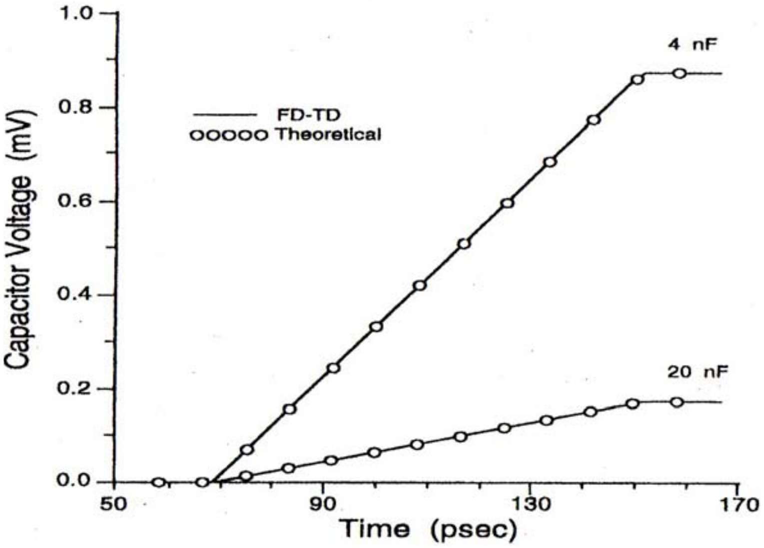

Figure 3.3: Comparison of FDTD and SPICE calculation of voltage across capacitor [12].

3.5 Conclusions

In this chapter, the standard three-dimensional FDTD equations are extended to analyse various electrical components such as resistor and capacitor elements. This yields a set of equations in which the method is called LE-FDTD. These equations were derived by specifying the appropriate voltage-current characteristics of sources and lumped elements. The characteristics of linear lumped elements including resistor and capacitor within FDTD grid were demonstrated and an example was given to prove the validity of the derived LE-FDTD formulas for all lumped elements respectively. Furthermore, the inherent grid capacitor which is a function of grid spacing was also discussed in the context. The knowledge acquired from this chapter will be broadly extended to include the analysis of the interaction between electromagnetic and biological tissue modelling that will be discussed in chapter five. In addition, the derived equations for linear components such as resistor and capacitor will be validated and the LE-FDTD will be implemented on the surface of the tissue as an equivalent circuit for cell membrane.

3.6 References

[1] L.W.Nagel, "SPICE-2: A computer program to simulate semiconductor circuits," *ERL-M520, Electronics Research Laboratory,Univ. of California, Berkeley*, 1975.

[2] G.Massobrio and P.Antognetti, "Semiconductor Device Modelling with SPICE," *2nd edition,McGraw-Hill*, 1993.

[3] K.S.Yee, "Numerical solution of initial boundary value problems involving Maxwell's equation in isotropic media," *IEEE Trans. on Antennas Propagation*, vol. AP-14, pp. 302-307, 1966.

[4] P.Ciampolini, P.Mezzanotte, L.Roselli, and R.Sorrentino, "Accurate and Efficient Circuit Simulation with Lumped-element FDTD technique," *IEEE Trans on MTT*, vol. 44, pp. 2207-2214, 1996.

[5] W.Sui, D.A.Christensen, and C.H.Durne, "Extending the two-dimensional FDTD method to hybrid electromagnetic systems with active and passive lumped elements," *IEEE Trans. MTT*, vol. MTT-40, pp. 724-730, 1992.

[6] P.Ciampolini, P.Mezzanotte, L.Roselli, D.Sereni, P.Torti, and R.Sorrentino, "Simulation of HF circuits with FDTD technique including nonideal lumped elements," *in IEEE MTT-S Int.Microwave Symp. Dig. Orlando,FL*, pp. 361-364, 1995.

[7] J.A.Pereda, F.Alimenti, P.Mezzanotte, L.Roselli, and R.Sorrentino, "A New Algorithm for the Incorporation of Arbitrary Linear Lumped Networks into FDTD Simulators," *IEEE Transactions on Microwave Theory and Techniques*, vol. 47, pp. 943-949, 1999.

[8] G.Emili, F.Alimenti, P.Mezzanotte, L.Roselli, and R.Sorrentino, "Rigorous Modelling of Packaged Schottky Diodes by the Nonlinear Lumped Network - FDTD Approach," *IEEE Transactions on Microwave Theory and Techniques*, vol. 48, pp. 2277-2282, 2000.

[9] A.Taflove, *Computational Electrodynamics*: Norwood, MA: Artech House, 1995.

[10] A.Taflove and S.C.Hagness, *Computational Electrodynamics: The Finite-Difference Time-Domain*, 2nd ed: Artech House:Boston, 2000.

[11] A.Taflove, *Advances in Computational Electrodynamics: The Finite Difference Time Domain*: Artech House, 1998.

[12] M.Piket-May, A.Taflove, and J.Baron, "FDTD modeling of Digital Signal Propagation in 3D circuits with Passive and Active Loads," *IEEE Trans. MTT*, vol. MTT-42, pp. 1514-1523, 1994.

[13] D.M.Sheen, S.M.Ali, M.D.Abouzahra, and J.A.Kong, "Application of the three-dimensional finite-difference time-domain method to the analysis of planar microstrip circuits," *IEEE Transactions on Microwave Theory and Techniques*, vol. 38, pp. 849-857, 1990.

[14] Y.-S. Tsuei, A.C.Cangellaris, and J.L.Prince, "Rigorous electromagnetic modeling of chip-to-package (first level) interconnections," *IEEE Transactions on Components, Hybrids, and Manufacturing Technology*, vol. 16, pp. 876-883, 1993.

[15] C.L.Wagner and J.B.Schneider, "Divergent Fields,Charge, and Capacitance in FDTD Simulations," *IEEE Transactions on Microwave Theory and Techniques*, vol. 46, pp. 2131-2136, 1998.

[16] V.A.Thomas, M.E.Jones, M.J.Piket-May, A.Taflove, and E.Harrigan, "The use of

SPICE lumped circuits as sub-grid models for FDTD high-speed electronic circuit design," *IEEE Microwave and Guided Wave Letters*, vol. 4, pp. 141-143, 1994.

[17] T.L.Floyd, *Electronic devices*, 7th ed: Pearson Prentice Hall, 2005.

[18] S.M.Sze, *Physics of Semiconductor Devices*: New York: Wiley, 1981.

Chapter 4

Quasi-Static FDTD Scheme for Electrically-Small Regions in Free Space, Lossless and Lossy Penetrable Media

4.1 Introduction

The problem of modelling electromagnetic field interaction with structures whose dimensions are a few wavelengths has been the subject of many studies and numerical simulations for bioelectromagnetic applications. The methods used for such numerical simulations generally fall into one of three categories, method of moment (MOM) [1-4], finite element (FE) [5-8] and finite difference time domain (FDTD) [9-11].

Method of moment (MOM) does an excellent job of analyzing unbounded radiation problems and they excel at analyzing perfect electric conductor and homogeneous dielectrics. However, it is not very effective when applied to arbitrary configurations with complex geometries or inhomogeneous dielectrics. As for finite element method (FEM), it is a very versatile technique because it allows the analysis of complex inhomogeneous structures. However, it requires unaffordable computation resources to solve extremely large problem, due to discretising the entire problem space and lack of adequate free-space boundary conditions that can be placed close to the objects modelled.

In contrast, the finite difference time domain (FDTD), since its first introduction by Yee [12], has been used extensively over the last decade for bioelectromagnetic dosimetry - numerical assessment of electromagnetic fields coupled to complex heterogeneous biological entities at powerline frequency and radio frequency. The use of FDTD is very attractive for this application, due mainly to its algorithmic simplicity, capable to solve complicated heterogeneous geometries and ease of modularization and parallelisation of the algorithm on massively parallel computers. Moreover, it is also capable to model electromagnetic wave interaction problems requiring the solution of considerably more than 10^8 field vector unknowns. At this level of complexity, it is possible to develop detailed, three-dimensional models of complete engineering systems.

The classical form of Finite-difference Time-domain (FDTD) method requires extremely small time-step sizes when modelling electrically-small regions (much smaller than a wavelength). Thus, it can become impractical due to the unaffordable computation times required. This problem can be solved by implementing a quasi-static approximate version of FDTD. This approach is based on transferring the working frequency to a higher frequency, to reduce the number of time steps required. Then, the generated internal field at the higher frequency can be scaled back to the frequency of interest [10, 13-16]. It should be noted that this approach is only valid if the size of the interacting structure in the problem space is 10 times or more smaller than the wavelength and $|\sigma + j\omega\varepsilon| >> \omega\varepsilon_o$ [10, 13], where σ and ε are the conductivity and permittivity of the tissues respectively, ω is the radian frequency, and ε_o is the permittivity of free space. In order to prove the validity of the quasi-static approach, this chapter will develop a three-dimensional FDTD program to directly model a single homogeneous or multi-layered sphere inside a lossless or lossy problem space. The sphere was excited by a plane wave, which is replaced by an equivalent surface. The edge of the problem space was truncated by a properly modified Berenger's perfectly matched layer (PML) absorbing boundary condition (ABC), with matching impedance condition ($\sigma/\varepsilon = \sigma^*/\mu$ for lossless or lossy media, whereas $\sigma/\varepsilon_o = \sigma^*/\mu_o$ for free space) [17-20]. An optimum value of the g factor is properly chosen to provide efficient low reflection termination of the computational space for different penetrable media problem at the interface layer.

The remainder of this chapter is organized as follows. In section 5.2, the formulation for plane wave solution in free space, lossless and lossy medium will be derived and discussed in order to be used in the numerical analysis. The analytical solution for the field scattered by a sphere is demonstrated thoroughly in section 5.3 as well. Then, the methodologies of studying the problem of modelling electromagnetic field interaction with structures whose dimensions are a few wavelengths, using Quasi-static FDTD and modified Berenger's Perfectly matched layer are elucidated in detail in section 5.4. Numerical results are presented in section 5.4, where the perfect agreement with analytical solution confirms the validity of our technique. Finally, the entire work of this chapter is summarized in section 5.5.

4.2 Basic Plane Wave Solutions

The major goal of this section is to solve Maxwell's equations and derive Electromagnetic wave motion in free space, lossless and lossy penetrable media [21, 22].

4.2.1 Plane Waves in Lossy Medium

In a source-free, linear, isotropic, homogeneous, lossy dielectric medium, Maxwell's equations in phasor form are:

$$\nabla \times E = -j\omega\mu H \tag{4.1}$$

$$\nabla \times H = (\sigma + j\omega\varepsilon)E \tag{4.2}$$

$$\nabla \cdot E = 0 \tag{4.3}$$

$$\nabla \cdot H = 0 \tag{4.4}$$

Taking the curl of both side of equation (4.1) gives

$$\nabla \times \nabla \times E = -j\omega\mu\nabla \times H \tag{4.5}$$

Applying the vector identity

$$\nabla \times \nabla \times \mathrm{A} = \nabla(\nabla \cdot \mathrm{A}) - \nabla^2 \mathrm{A} \tag{4.6}$$

to the left-hand side of equation (4.5) and invoking equations (4.2) and (4.3), the following expression is obtained

$$\nabla^2 \mathrm{E} - \gamma^2 \mathrm{E} = 0 \tag{4.7}$$

where

$$\gamma^2 = j\omega\mu(\sigma + j\omega\varepsilon) \tag{4.8}$$

where γ is called the propagation constant(in per meter) of the medium.

An identical equation for H can be derived in the same manner:

$$\nabla^2 \mathrm{H} - \gamma^2 \mathrm{H} = 0 \tag{4.9}$$

Equations (4.7) and (4.9) are known as homogeneous vector Helmholtz's equations or simple vector wave equations.

Since γ shown in equations (4.7) to (4.9), is a complex quantity, given by:

$$\gamma = \alpha + \mathrm{j}\beta = \mathrm{j}\omega\sqrt{\mu\varepsilon}\sqrt{1 - \mathrm{j}\frac{\sigma}{\omega\varepsilon}} \tag{4.10}$$

$$\alpha = \omega\sqrt{\frac{\mu\varepsilon}{2}\left[\sqrt{1+\left[\frac{\sigma}{\omega\varepsilon}\right]^2}-1\right]} \tag{4.11}$$

$$\beta = \omega\sqrt{\frac{\mu\varepsilon}{2}\left[\sqrt{1+\left[\frac{\sigma}{\omega\varepsilon}\right]^2}+1\right]} \tag{4.12}$$

where α is known as the attenuation constant or attenuation factor of the medium and is measured in nepers per meter (Np/m) or in decibels per meter (dB/m). The quantity β is a measure of the phase shift per length and is called the phase constant or wave number. σ, μ and ε are respectively the conductivity, permeability and permittivity of the media. $\omega = 2\pi f$ is the radian frequency. It should be noted that in term of β, the wave velocity u and wavelength λ can be expressed in the following form:

$$u = \frac{\omega}{\beta}, \quad \lambda = \frac{2\pi}{\beta} \tag{4.13}$$

A basic plane wave solution to the above wave equations can be found by considering the wave is propagating in z direction and polarised in x direction. Therefore, the helmholtz equation of (4.7) reduces to

$$\frac{d^2E_x}{dz^2} - \gamma^2 E_x = 0 \tag{4.14}$$

which has solutions

$$E_x(z) = E^+ e^{-\gamma z} + E^- e^{\gamma z} \tag{4.15}$$

where E^+ and E^- are arbitrary amplitude constants.

The positive travelling wave then has a propagation factor of the form

$$e^{-\gamma z} = e^{-\alpha z} e^{-j\beta z} \tag{4.16}$$

which in time domain can be given as follows:

$$e^{-\gamma z} = e^{-\alpha z} \cos(\omega t - \beta z) \tag{4.17}$$

As can be seen, this represents a wave travelling in the +z direction with a phase velocity $v_p = \omega/\beta$, a wavelength $\lambda = 2\pi/\beta$, and an exponential damping factor. The rate of decay with distance is given by the attenuation constant α. The negative travelling wave term of (4.15) is similarly damped along the –z axis. Hence, the solution for positive electric travelling wave is obtained in equation (4.18).

$$\begin{gathered} E(z,t) = Re(E_0 e^{-\alpha z} e^{j(\omega t - \beta z)} a_x) \\ \text{or} \\ E(z,t) = E_0 e^{-\alpha z} \cos(\omega t - \beta z) a_x \end{gathered} \tag{4.18}$$

As for the solution for the positive magnetic travelling wave, the H(z,t) can be gained by taking the similar steps to solve equation(4.9).

$$H(z,t) = Re(H_0 e^{-\alpha z} e^{j(\omega t - \beta z)} a_y)$$

or (4.19)

$$H(z,t) = H_0 e^{-\alpha z} \cos(\omega t - \beta z) a_y$$

Now, by using equation (4.18) with equations (4.1) and (4.2), the relationship between E_o and H_o can be solved in the following way.

From Faraday's law, equation (4.1) can be expressed in the following forms:

$$\nabla \times E = -\mu \frac{\partial H}{\partial t}$$

$$H = -\frac{1}{\mu} \int (\nabla \times E) dt \tag{4.20}$$

Since

$$\nabla \times E = \begin{vmatrix} i & j & k \\ \frac{\partial}{\partial x} & \frac{\partial}{\partial y} & \frac{\partial}{\partial z} \\ E_x & 0 & 0 \end{vmatrix} = \frac{\partial}{\partial z} E_x = -E_0 e^{-\alpha z} (\alpha + j\beta) e^{j(\omega t - \beta z)} a_y \tag{4.21}$$

Hence,

$$H = \frac{1}{j\mu\omega} E_0(\alpha + j\beta) e^{-\alpha z} e^{j(\omega t - \beta z)} a_y \tag{4.22}$$

From Ampere's law, equation (4.2) can be expressed in the following form.

$$\nabla \times H = \sigma E + \varepsilon \frac{\partial E}{\partial t} \tag{4.23}$$

Since

$$\nabla \times H = \begin{vmatrix} i & j & k \\ \frac{\partial}{\partial x} & \frac{\partial}{\partial y} & \frac{\partial}{\partial z} \\ 0 & H_y & 0 \end{vmatrix} = -\frac{\partial}{\partial z} H_y = \frac{E_0(\alpha + j\beta)^2}{j\omega\mu} e^{-\alpha z} e^{j(\omega t - \beta z)} a_x \tag{4.24}$$

Then,

$$\nabla \times H = (\sigma + j\omega\varepsilon) E_0 e^{-\alpha z} e^{j(\omega t - \beta z)} \tag{4.25}$$

Comparing equations (4.24) and (4.25), equation (4.26) is obtained.

$$(\alpha + j\beta) = \sqrt{(\sigma + j\omega\varepsilon)(j\omega\mu)} \tag{4.26}$$

Substitute equation (4.26) into equation (4.22), eventually equation (4.27) is gained.

$$H_0 = \frac{E_0}{\eta} \tag{4.27}$$

where η is a complex quantity known as the intrinsic impedance (scalar element stated by ohm values) of the medium.

$$\eta = \sqrt{\frac{j\omega\mu}{\sigma + j\omega\varepsilon}} = |\eta|\angle\theta_\eta = |\eta|e^{j\theta_\eta} \tag{4.28}$$

$$|\eta| = \frac{\sqrt{\frac{\mu}{\varepsilon}}}{\left[1+\left(\frac{\sigma}{\omega\varepsilon}\right)^2\right]^{1/4}} \quad \text{and} \quad tan\,2\theta_\eta = \frac{\sigma}{\omega\varepsilon} \tag{4.29}$$

where $0 \leqslant \theta_\eta \leqslant 45^{o}$. Substituting equations (4.27) and (4.28) into equation (4.19) gives

$$H(z,t) = Re(\frac{E_0}{|\eta|e^{j\theta_\eta}} e^{-\alpha z} e^{j(\omega t - \beta z)} a_y\ )$$

or

$$H(z,t) = \frac{E_0}{|\eta|e^{j\theta_\eta}} e^{-\alpha z}\, cos(\omega t - \beta z - \theta_\eta) a_y \tag{4.30}$$

4.2.2 Plane Waves in Lossless Medium

In a lossless dielectric, $\sigma << \omega\varepsilon$, in which is a special case of that given in previous section except that

$$\sigma \cong 0, \qquad \varepsilon = \varepsilon_0 \varepsilon_r, \qquad \mu = \mu_0 \mu_r \tag{4.31}$$

where μ_r and ε_r are the relative permeability and permittivity of the media respectively. μ_o and ε_o are the free space permeability and permittivity.

Substituting these into equations (4.11) and (4.12) gives

$$\alpha = 0, \qquad \beta = \omega\sqrt{\mu\varepsilon}, \tag{4.32}$$

$$u = \frac{\omega}{\beta} = \frac{1}{\sqrt{u\varepsilon}}, \qquad \lambda = \frac{2\pi}{\beta}, \tag{4.33}$$

Also

$$\eta = \sqrt{\frac{\mu}{\varepsilon}} \angle 0^{\circ} \tag{4.34}$$

And thus E and H are shown to be in time phase with each other.

4.2.3 Plane Waves in Free Space

In a free space, the following equations can be stated:

$$\sigma = 0, \qquad \varepsilon = \varepsilon_0, \qquad \mu = \mu_0 \tag{4.35}$$

$$\alpha = 0, \qquad \beta = \omega\sqrt{\mu_0 \varepsilon_0} = \frac{\omega}{c}, \tag{4.36}$$

$$u = \frac{\omega}{\beta} = \frac{1}{\sqrt{u_0 \varepsilon_0}} = c, \qquad \lambda = \frac{2\pi}{\beta}, \tag{4.37}$$

$$\eta_0 = \sqrt{\frac{\mu_0}{\varepsilon_0}} = 120\pi \approx 377\Omega \tag{4.38}$$

where c ≈ 3 ×108 m/s, the speed of light in a vacuum.

4.3 Analytical Solution

The exact solution for describing the characteristics of electromagnetic radiation scattered by a homogenous sphere when it is excited by a plane wave, was first solved by Mie [23] in 1908 and has been concisely formulated by Stratton [24] in 1941. A solution of scattering problem of a sphere with one concentric shell has been given by Aden and Kerker [25] and the scattering from an inhomogeneous spherically symmetric object has been calculated by Wyatt [26]. Since Mie series solution is simple and easy to be modified for any composition of sphere, therefore it was adapted by various authors for comparisons to investigate bioelectromagnetic problems, either to be used as an analytical solution to the problems [27-37] or as a solution to proposed numerical methods [13, 38-42] for comparisons. This section gives the solutions in a form readily amenable to machine computation for both the scattered and the interior fields. The spherical core is surrounded by arbitrary number of concentric shells. It should be noted that this exact solution will be implemented as a tool for comparison against our proposed quasi-static FDTD method throughout this chapter.

4.3.1 Sphere with arbitrary Concentric Layers

Figure 4.1 depicts the orientation of the plane wave with respect to a rectangular and spherical coordinate system having its origin at the centre of the sphere. The plane wave is assumed to propagate in the positive z-direction and the electric field is linearly polarised in the x-direction. A stratified sphere with arbitrary thickness and electrical characteristics is shown in Figure 4.2. The basic idea of the analysis is performed by expanding the incident and secondary fields in vector spherical harmonics appropriate to each region and matching the tangential components of the fields at each boundary to determine the expansion coefficients.

The expansion of the incident plane wave is given in Stratton [24] and the same identical notation will be implemented in this work. This incident wave will induce fields in all of the regions and the general solution of the vector wave equation for the transverse fields in any shell layer can be written as a linear combination of the spherical vector wave functions, $\vec{\mathrm{m}}$ and $\vec{n}$, that was used by Stratton [24]. In general, the radial field dependence is an arbitrary solution to any linear combination of the spherical Bessel and Hankel function of first and second kinds.

Each type of Bessel and Hankel function with its associated properties will be discussed as follows:

1. The spherical Bessel function of the first kind, $\mathrm{B}_{\mathrm{n}(1)} = \mathrm{J}_{\mathrm{n}}(\mathrm{r})$, indicates a standing wave.
2. The spherical Bessel function of the second kind, $B_{n(2)} = Y_n(r)$, indicates a standing wave as well and is also called the spherical Neumann function or Weber function.
3. The spherical Bessel function of the third kind, $\mathrm{B}_{\mathrm{n}(3)} = \mathrm{J}_{\mathrm{n}}(\mathrm{r}) + \mathrm{iY}_{\mathrm{n}}(\mathrm{r})$, indicates an inward traveling wave and is also called the Hankel function of the first kind, $\mathrm{H}_{\mathrm{n}(1)}(\mathrm{r})$.
4. The spherical Bessel function of the fourth kind, $\mathrm{B}_{\mathrm{n}(4)} = \mathrm{J}_{\mathrm{n}}(\mathrm{r}) - \mathrm{iY}_{\mathrm{n}}(\mathrm{r})$, indicates an outward traveling wave and is also called the spherical Hankel function of second kind, $\mathrm{H}_{\mathrm{n}(2)}(\mathrm{r})$.

For the innermost layer of the sphere the spherical Bessel function of first kind, J_{n}, is the only admissible solution, while for the surrounding medium the fields will consist of incident waves and scattered waves in order to satisfy the radiation condition at infinity.

Hence, the general solution of the electric and magnetic field vectors in p$^{\text{th}}$ region of concentric sphere can be formulated as follows:

$$\vec{E}_p = E_o e^{i\omega t}\sum_{n=1}^{\infty} i^n \frac{2n+1}{n(n+1)}\left[a_n^p \vec{m}_{o1n}^{(1)} - i b_n^p \vec{n}_{e1n}^{(1)} + \alpha_n^p \vec{m}_{o1n}^{(3)} - i\beta_n^p \vec{n}_{e1n}^{(3)}\right] \tag{4.39}$$

$$\vec{H}_p = -\frac{k_p E_o e^{i\omega t}}{\mu_p \omega}\sum_{n=1}^{\infty} i^n \frac{2n+1}{n(n+1)}\left[b_n^p \vec{m}_{e1n}^{(1)} - i a_n^p \vec{n}_{o1n}^{(1)} + \beta_n^p \vec{m}_{e1n}^{(3)} - i\alpha_n^p \vec{n}_{o1n}^{(3)}\right] \tag{4.40}$$

where a, b, α, β are the expansion coefficients (see Section 4.3.2) and

$\vec{\mathrm{m}}, \vec{\mathrm{n}}$ are the spherical vector wave functions as given by Stratton [24].

$$\begin{aligned} \vec{m}_{\substack{o\\e}1n}^{(z)} &= \pm\frac{1}{\sin\theta} B_n^z(k_p r) P_n^1(\cos\theta)\begin{bmatrix}\cos\phi\\ \sin\phi\end{bmatrix}\hat{\theta} \\ &- B_n^z(k_p r)\frac{\partial}{\partial\theta} P_n^1(\cos\theta)\begin{bmatrix}\sin\phi\\ \cos\phi\end{bmatrix}\hat{\phi} \end{aligned} \tag{4.41}$$

$$\begin{aligned} \vec{n}_{\substack{o\\e}1n}^{(z)} &= \frac{n(n+1)}{k_p r} B_n^z(k_p r) P_n^1(\cos\theta)\begin{bmatrix}\sin\phi\\ \cos\phi\end{bmatrix}\hat{r} \\ &+ \frac{1}{k_p r}\frac{\partial}{\partial(k_p r)}\left[k_p r B_n^z(k_p r)\right]\frac{\partial}{\partial\theta} P_n^1(\cos\theta)\begin{bmatrix}\sin\phi\\ \cos\phi\end{bmatrix}\hat{\theta} \\ &\pm \frac{1}{k_p r\sin\theta}\frac{\partial}{\partial(k_p r)}\left[k_p r B_n^z(k_p r)\right] P_n^1(\cos\theta)\begin{bmatrix}\cos\phi\\ \sin\phi\end{bmatrix}\hat{\phi} \end{aligned} \tag{4.42}$$

where:

1. k_p is the complex propagation constant for the p^{th} region:

$$\begin{matrix}Re\\Im\end{matrix}\left(k_p\right)=\frac{\omega}{c}\left[\frac{\varepsilon_r^p}{2}\left(\sqrt{1+\left(\frac{\sigma_p}{\varepsilon_o\varepsilon_r^p\omega}\right)^2}\pm 1\right)\right]^{\frac{1}{2}} \tag{4.43}$$

ε_o is the free space permittivity, ε_r^p and σ_p are the relative permittivity and electrical conductivity of the p^{th} layer, and the positive value of the square root is used.

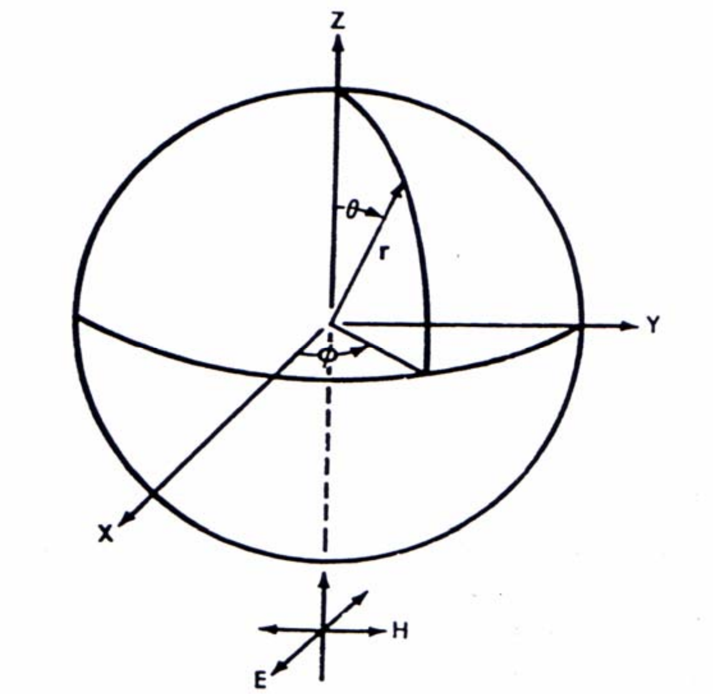

Figure 4.1: Spherical co-ordinates and incident plane wave configurations.

2. The nth term of $P_n^1(cos\theta)$ is the associated first order Legendre Polynomials,

properties for which can be found in literature [43] or might be computed using the follow recursive relations:

Let: $Q_n(\theta) = \frac{P_n^1(cos\,\theta)}{sin\,\theta}$ and $R_n(\theta) = \frac{\partial}{\partial\theta} P_n^1(cos\,\theta)$ then:

$$Q_n(\theta) = \frac{(2n-1)cos\,\theta Q_{n-1}(\theta) - nQ_{n-2}(\theta)}{n-1}$$

and

$$R_n(\theta) = n\,cos\,\theta Q_n(\theta) - (n+1)Q_{n-1}(\theta)$$

which can be solved using initial value of $Q_0(\theta) = 0.0, Q_1(\theta) = 1.0, R_1(\theta) = cos\,\theta$

3. The subscript "*e*" and "*o*" correspond to the even or odd character of the vector wave functions $\vec{m}$ and $\vec{n}$.

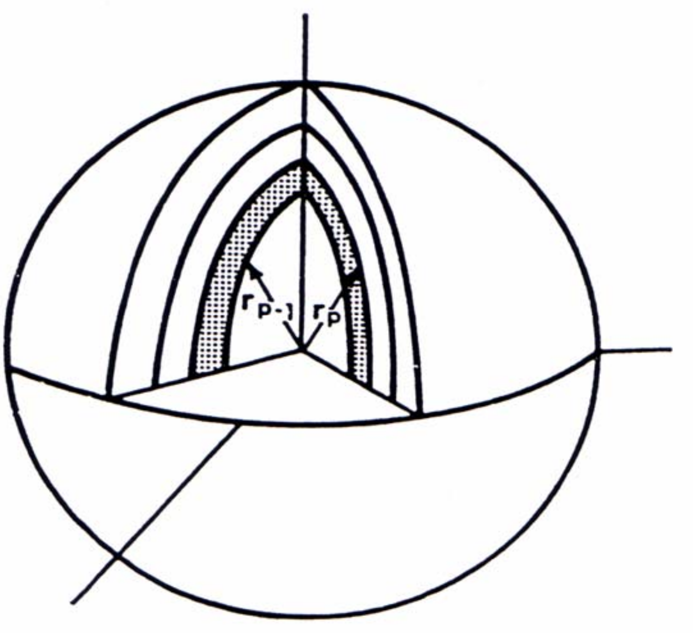

Figure 4.2: M-Layered Concentric Spherical System. Shaded region represents Pth layer of the system with the radius of r_p and electrical parameters of ε_p, μ_p, and σ_p.

4.3.2 Solution for Expansion Coefficients

The electric and magnetic fields can be determined using equations (4.39) and (4.40) with four expansion coefficients a, b, α, β determined by the requirement that the tangential components $\vec{\mathrm{E}}$ and $\vec{\mathrm{H}}$ be continuous at the interfaces between all regions. This requirement yields the following four relationships at the interface to each layer:

$$\begin{aligned} \left(E_p\right)_\theta &= \left(E_{p+1}\right)_\theta \\ \left(E_p\right)_\phi &= \left(E_{p+1}\right)_\phi \\ \left(H_p\right)_\theta &= \left(H_{p+1}\right)_\theta \end{aligned} \qquad (4.44)$$

$$\left(H_p\right)_\phi = \left(H_{p+1}\right)_\phi$$

Substituting the $\vec{m}$ and $\vec{\mathrm{n}}$ functions into equations (4.39) and (4.40) and applying the four relationships in equation (4.44), the expansion coefficients may be written as follows [28, 44]:

$$a_n^p = \frac{1}{\Delta_n^p}\left[\left(\zeta_n^p j_n^p - \tau^p h_n^p \eta_n^{p+1}\right)a_n^{p+1} + \left(\zeta_n^p h_n^{p+1} - \tau^p h_n^p \zeta_n^{p+1}\right)\alpha_n^{p+1}\right] \tag{4.45a}$$

$$\alpha_n^p = \frac{1}{\Delta_n^p}\left[\left(\tau^p j_n^p \eta_n^{p+1} - \eta_n^p j_n^{p+1}\right)a_n^{p+1} + \left(\tau^p j_n^p \zeta_n^{p+1} - \eta_n^p h_n^{p+1}\right)\alpha_n^{p+1}\right] \tag{4.45b}$$

$$b_n^p = \frac{1}{\Delta_n^p}\left[\left(\tau_n^p \zeta_n^p j_n^{p+1} - h_n^p \eta_n^{p+1}\right)b_n^{p+1} + \left(\tau_n^p \zeta_n^p h_n^{p+1} - h_n^p \zeta_n^{p+1}\right)\beta_n^{p+1}\right] \tag{4.45c}$$

$$\beta_n^p = \frac{1}{\Delta_n^p}\left[\left(j_n^p \eta_n^{p+1} - \tau^p \eta_n^p j_n^{p+1}\right)b_n^{p+1} + \left(j_n^p \zeta_n^{p+1} - \tau^p \eta_n^p h_n^{p+1}\right)\beta_n^{p+1}\right] \tag{4.45d}$$

where:

$$j_n^p = j_n^p\left(k_p r_p\right)$$

$$h_n^p = h_n^p\left(k_p r_p\right)$$

$$\Delta_n^p = j_n^p \zeta_n^p - h_n^p \eta_n^p$$

$$\tau^p = \frac{k_{p+1}}{k_p}\frac{\mu_p}{\mu_{p+1}}$$

$$\eta_n^p = \frac{1}{(k_p r_p)} \frac{\partial}{\partial (k_p r_p)} \left(k_p r_p j_n^p\right) = \frac{1}{2n+1}\left[(n+1) j_{n-1}^p - n j_{n+1}^p\right]$$

$$\zeta_n^p = \frac{1}{(k_p r_p)} \frac{\partial}{\partial (k_p r_p)} \left(k_p r_p h_n^p\right) = \frac{1}{2n+1}\left[(n+1) h_{n-1}^p - n h_{n+1}^p\right]$$

All of the Bessel functions are now understood to be evaluated at the values of p and p+1 corresponding to the interface between the two regions.

For the solution of coefficients a_n^p, α_n^p, b_n^p and β_n^p, equations (4.45a), (4.45b) and equations (4.45c), (4.45d) can be represented in matrix form as follows:

$$\begin{bmatrix} a_n^p \\ \alpha_n^p \end{bmatrix} = \begin{bmatrix} Q_{11}^p & Q_{12}^p \\ Q_{21}^p & Q_{22}^p \end{bmatrix} \begin{bmatrix} a_n^{p+1} \\ \alpha_n^{p+1} \end{bmatrix} \tag{4.46}$$

$$\begin{bmatrix} b_n^p \\ \beta_n^p \end{bmatrix} = \begin{bmatrix} U_{11}^p & U_{12}^p \\ U_{21}^p & U_{22}^p \end{bmatrix} \begin{bmatrix} b_n^{p+1} \\ \beta_n^{p+1} \end{bmatrix} \tag{4.47}$$

From [28], for a M-layered sphere, the above equations can be stated as follows:

$$\begin{bmatrix} a_n^1 \\ \alpha_n^1 \end{bmatrix} = \begin{bmatrix} T_{11} & T_{12} \\ T_{21} & T_{22} \end{bmatrix} \begin{bmatrix} a_n^M \\ \alpha_n^M \end{bmatrix} \tag{4.48}$$

$$\begin{bmatrix} b_n^1 \\ \beta_n^1 \end{bmatrix} = \begin{bmatrix} V_{11} & V_{12} \\ V_{21} & V_{22} \end{bmatrix} \begin{bmatrix} b_n^M \\ \beta_n^M \end{bmatrix} \tag{4.49}$$

where $T_{ij} = \prod_{p=1}^{M-1} Q_{ij}^p$ and $V_{ij} = \prod_{p=1}^{M-1} U_{ij}^p$ (4.50)

Using the fact that $\alpha_n^1 = \beta_n^1 = 0$ (i.e., the Hankel function, in which its divergent at the origin at the innermost sphere, must be absent for this region), and $a_1^M = b_1^M = 1$. Equations (4.46) and (4.47) yield

$$\begin{bmatrix} a_n^1 \\ 0 \end{bmatrix} = \begin{bmatrix} T_{11} & T_{12} \\ T_{21} & T_{22} \end{bmatrix} \begin{bmatrix} 1 \\ \alpha_n^M \end{bmatrix} \tag{4.51}$$

$$\begin{bmatrix} b_n^1 \\ 0 \end{bmatrix} = \begin{bmatrix} V_{11} & V_{12} \\ V_{21} & V_{22} \end{bmatrix} \begin{bmatrix} 1 \\ \beta_n^M \end{bmatrix} \tag{4.52}$$

Equations (4.51) and (4.52) represent a simple simultaneous equation form which a_n^1, α_n^M and b_n^1, β_n^M can be computed. Using the modified version of equations (4.46) and (4.47), all remaining expansion coefficients can be found as follows:

$$\begin{bmatrix} a_n^{p-1} \\ \alpha_n^{p-1} \end{bmatrix} = \begin{bmatrix} Q_{11}^{p-1} & Q_{12}^{p-1} \\ Q_{21}^{p-1} & Q_{22}^{p-1} \end{bmatrix} \begin{bmatrix} a_n^{p} \\ \alpha_n^{p} \end{bmatrix} \tag{4.53}$$

$$\begin{bmatrix} b_n^{p-1} \\ \beta_n^{p-1} \end{bmatrix} = \begin{bmatrix} U_{11}^{p-1} & U_{12}^{p-1} \\ U_{21}^{p-1} & U_{22}^{p-1} \end{bmatrix} \begin{bmatrix} b_n^{p} \\ \beta_n^{p} \end{bmatrix} \tag{4.54}$$

4.4 Numerical Method

4.4.1 Quasi-Static FDTD Scheme

The interaction between animals or humans exposed to extremely low frequency electric fields were investigated by Kaune and Gillis [45] and Guy et al. [46] in 1981 and 1982 respectively. Their research outcomes furnish valuable analytical and experimental verification of the idea of quasi-static nature of coupling at power-line frequency. Later, the works presented in [13, 14, 41] showed the same principles using finite difference time domain (FDTD) in which the numerical dosimetry of anatomically based models were discussed. Recently, the same idea has been further extended to model the interaction between electromagnetic (EM) fields and biological tissue at mobile communication frequencies, i.e. GSM900 and GSM1800 [16].

By using the similar methodologies of authors [45, 46], and in order to implement the Quasi static approximation to analyse any scattering problems, following two conditions have to be satisfied:

1. The size of the structure under consideration is a factor of 10th or more smaller than the wavelength.

2. $|\sigma + j\omega\varepsilon| >> \omega\varepsilon_o$

where σ and ε are the conductivity and permittivity of the analysed structure respectively, ω is the radian frequency, and ε_o is the permittivity of free space.

Under these conditions, electric fields outside the analysed object are not dependent on the internal analysed object properties, but also on the shape of the body. The components of the electric field tangent to the surface of the model and the internal fields are approximately zero compared to the applied field. For these conditions the external field E can be considered to be perpendicular to the body of the analysed structure.

From the Maxwell equation div D = ρ, the boundary condition for the normal component of electric field at the surface of the region of interest is :

$$j\omega\varepsilon_{\circ}\hat{n} \bullet \vec{E}_{air} = (\sigma_{tissue} + j\omega\varepsilon_{tissue})\hat{n} \bullet \vec{E}_{tissue} \tag{4.55}$$

where subscripts refer to the regions of interests and "•" refers to vector dot product.

From equation (4.55), and under the two conditions given above in which the problem space 10 times or more smaller than the wavelength and $|\sigma + j\omega\varepsilon| >> \omega\varepsilon_o$, the scaling relationship can be derived as follows [13, 46]:

$$\begin{aligned}\vec{E}_{tissue}(f) &= \left(\frac{\omega}{\omega'}\right)\left[\frac{\sigma'(f')+j\omega'\varepsilon(f')}{\sigma(f)+j\omega\varepsilon(f)}\right]\vec{E}'_{tissue}(f') \\ &\cong \left[\frac{f\sigma'(f')}{f'\sigma(f)}\right]\vec{E}'_{tissue}(f')\end{aligned} \tag{4.56}$$

Assuming that $\omega\varepsilon(f) << \sigma(f)$ and $\omega'\varepsilon'(f') << \sigma'(f')$, then according to equation (4.56), a higher working frequency (f') which falls within the quasi-static regime, can be chosen to excite the model, to reduce the computation time. Thus, the resultant internal fields, E', evaluated at higher frequency can be transferred back to the desired low frequency.

4.4.2 Modified Berenger's Perfectly Matched Layer (PML)

The primary difficulty of FDTD method when modelling open-region electromagnetic wave scattering problems, is that an artificial boundary or absorbing boundary condition (ABC) is required to be imposed at the outer grid boundaries of the computational domain, in order to truncate the size volume. Therefore, Absorbing boundary conditions (ABC's) are one of the most critical elements of finite-difference time domain analysis, that must be applied to absorb the required wave of this bounded problem.

Several analytical ABC's , such as Mur [47] and Liao [48], have been invented in order to overcome this problem. The proposed ABCs provide effective reflection coefficients in order of -35 to -45dB for most FDTD simulations. Recently, The capabilities of the ABC have been significantly enhanced with the introduction of Berenger's perfectly matched layer (PML) [17, 19, 20]. This is based on surrounding the FDTD problem space with highly lossy and matched non-physical absorber. It also allowed for boundary reflections below -80dB to be realized. The PML, therefore, became the boundary of choice for the simulation problems of this chapter.

It is known that a plane wave incident on a planar boundary of a dispersionless medium from free space is perfectly transmitted without reflection (matched across a planar boundary) for all normally incident waves if the matching condition in equation (4.57) is satisfied for that medium [17].

$$\frac{\sigma}{\varepsilon_o} = \frac{\sigma^*}{\mu_o} \tag{4.57}$$

The idea of matching condition in free space for the PML will be extended to lossless and lossy media with the following modified matching condition.

$$\frac{\sigma}{\varepsilon_r \varepsilon_o} = \frac{\sigma^*}{\mu_r \mu_o} \tag{4.58}$$

where σ and σ^* are the electric conductivity and magnetic conductivity of the medium respectively. ε_o and μ_o are the free space permittivity and permeability and the relative permittivity and permeability are ε_r and μ_r .

In order to reduce the reflection on the interface layer, an optimum value of the geometric grading factor (g) has been selected, by using an empirical expression as in [19]:

$$\sigma = -\frac{\varepsilon c}{2\Delta x}\frac{\ln g}{g^N - 1}\ln R(0) \tag{4.59}$$

where Δx is the spatial increment of FDTD mesh, R(0) is the normal reflection coefficient, N is the number of the cells in the PML thickness, c is the velocity of EM waves in free space or lossy medium.

4.5 Results and Method Verification

In order to verify the validity of quasi-static approximation (using a higher frequency f' to obtain induced E fields) in finite difference time domain (FDTD) method, four examples will be illustrated and discussed in this section. Due to the existence of the analytical solution for a spheres exposed to plane wave, therefore, all examples demonstrated here will be discussed subject to a homogeneous and layered sphere involving for free space, lossless and lossy penetrable media to confirm the accuracy of the solution obtained from numerical results with analytical solution.

This section is classified into two sub-sections, i.e. verification at powerline frequency and verification at mobile communication frequency, in which three examples will be given at powerline frequency and one example will be shown at mobile communication frequency. It should be noted that Examples 4.1 and 4.2 are drawn from paper [13] for proving the proposed FDTD method and compared with Mie-series solution codes that is working at powerline frequency for free space case. Then, the media of the Examples 4.1 and 4.2 are replaced with lossless case and the results are compared as shown in Example 4.3. This example gives stable results and shows the feasibility of using the quasi-static approach to biological application at mobile communication. Finally, the quasi-static concept is extended to model a biological equivalent spherical cell in lossy penetrable media at mobile communication frequency and it is clearly depicted in Example 4.4.

In FDTD computational domain, Examples 4.1 to 4.3 are modelled in a domain of 63 × 63 ×63 cm space size, with a grid resolution of 1cm in each direction and δt of 16.67ps. The Example 4.4 uses 100× 100 ×100 μm space size, with grid cell of 1μm in each direction and δt of 1.3 fs. The model is excited by a plane wave of 1V/m, which is propagating in z-direction and polarised in x-direction. Moreover, the domain was terminated by a PML (6, Gx, 40dB) (six layers, with geometric progression profile and geometric grading factor of Gx of the media used, for which 40-dB attenuation for normal incidence is considered) on all sides. Moreover, the simulation time of order of four oscillation periods of the source field is found necessary to calculate the steady state conditions.

For the convenience of illustration of the problem, consider Figures 4.3 and 4.4, which show the 2- and 3-dimensional view of geometry stated in FDTD computation domain. This shows the equivalent surface (Huygens surface) that replaces the plane wave. It also shows the Berenger's perfectly matched layer (PML) that implements the absorbing boundary condition (ABC). This layer has been applied surrounding the edge of the problem space, with matching impedance condition ($\sigma/\varepsilon = \sigma^*/\mu$ for lossless or lossy media, whereas $\sigma/\varepsilon_o = \sigma^*/\mu o$ for free space). In addition, in order to explain the results systematically, all 1-dimensional and 2-dimensional plot of the induced electric and magnetic fields components are standardised for ease of comparison for all test cases. For one dimensional plots, it should be noted that only dominated Ex component versus y and z, it also includes Ez component versus x. Moreover, the dominated Hy vesus x and z for the central axes of the sphere are shown for discussion. For 2-dimensional plots, they display logarithmic value of 2-dimensional field strengths are demonstrated when eight grid cells are considered between the PML and the structure.

4.5.1 Verification at Low Frequency (Powerline Frequency)

This section demonstrates the feasibility of frequency scaled FDTD method to solve scattering problem at powerline frequency of 60Hz. All the test cases in this section will initially transfer the working frequency to 20MHz, in order to make the simulation time reasonable to be computed. Then, the obtained induced fields are scaled back to 60Hz by using equation (4.56). As can be observed, if the same problem is solved directly at frequency of 60H and four oscillation-period criterion is used, then the number of the time step requires is 4×(1/(δt*60)). This is equivalent to about 4 billions of time steps at desired operating frequency of 60Hz. By scaling the operating frequency to 20MHz, the number of time steps can be reduced, i.e., from few billions to few thousands. In the other hand, due to $\sigma >> \omega\varepsilon$ at both 20MHz and 60Hz, the selection of the ε_r of the scatterer properties can be considered relatively insignificant for the calculations. Hence, $\varepsilon_r = 1$ is used for the scatterer.

4.5.1.1 Free Space Penetrable Media

For sake of checking the correct implementation of equivalent surface (Huygens surface) that replaces the plane wave and the Berenger's PML absorbing boundary condition in FDTD computation domain, thus, the simulation is initially performed without the presence of the analysed object. Figure 4.5 shows the Huyghens surface in free space of the FDTD computational domain. As can be seen, the fields inside the problem space is about 0dB, while the numerical reflection is about -40dB between the Huygens surface and PML region. This proves that the FDTD code is working perfectly with the Huygens surface and berenger's PML absorbing boundary conditions.

Example 4.1: A single layer sphere of radius 16.5cm with conductivity $\sigma = 0.35$ S/m and dielectric constant $\varepsilon_r = 1.0$. Properties of free space ($\sigma = 0$, $\varepsilon_r = 1.0$) are assumed here in the perfectly matched layers (PML) and the problem space, where the PML (6, G5.4, 40dB) (six layers, with geometric progression profile and geometric grading factor of 5.4, with 40-dB attenuation for normal incidence) is used on all sides. Figure

4.6 shows the intensity of Ex component in coordinate plane of the structure at 20MHz, while Figure 4.7 depicts the electric field distribution along various central axes for a single-layer sphere in free space media at 60Hz. The induced magnetic field inside the structure are also shown in Figure 4.8 and Figure 4.9 respectively. It can be observed from Figure. 4.9 that the magnitude of magnetic field Ey component is about 1/377 A/m (which is equivalent to the incident magnetic field) constantly along x and z axis of the structure at both 20MHz and 60Hz, where 377 Ω is the characteristic impedance for free space medium. This result confirms that under quasi-static condition, the magnetic and electric field are decoupled. As can seen, the results of the proposed method agree well with the Mie series solution.

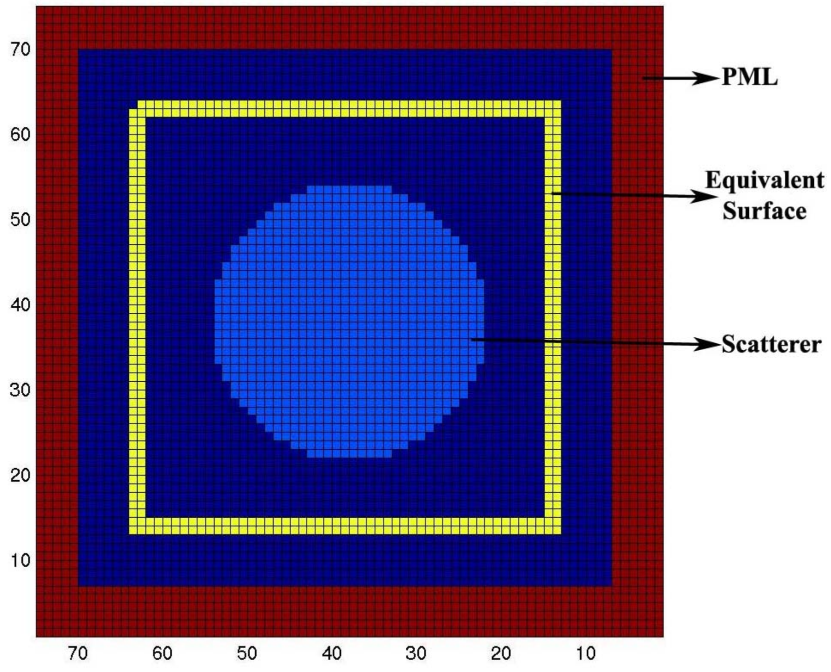

Figure 4.3: Basic structure of the problem for FDTD computational domain.

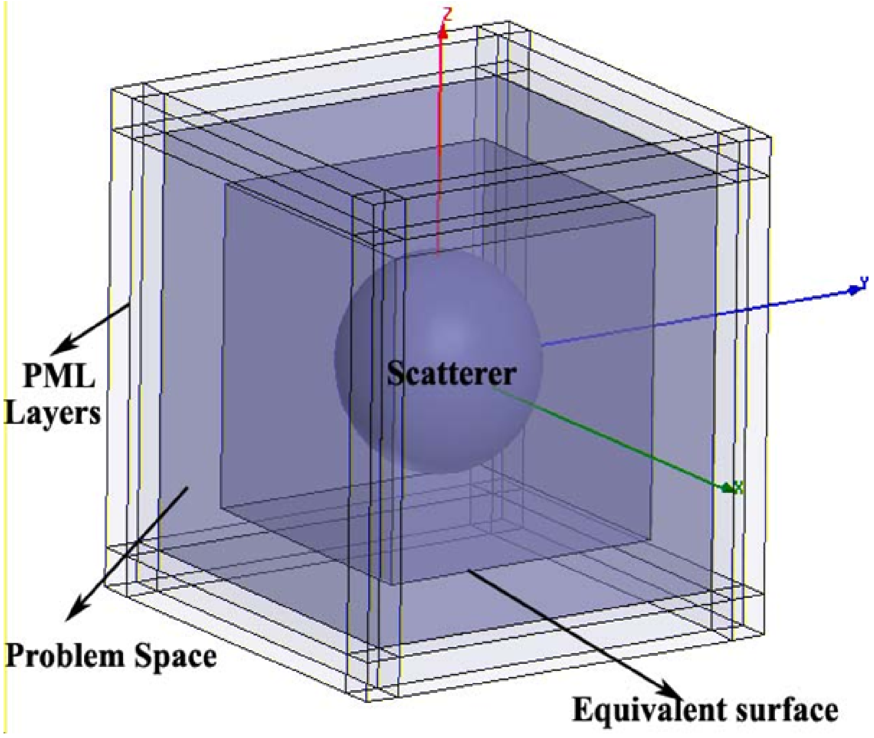

Figure 4.4: 3-D view of the problem for FDTD computational domain.

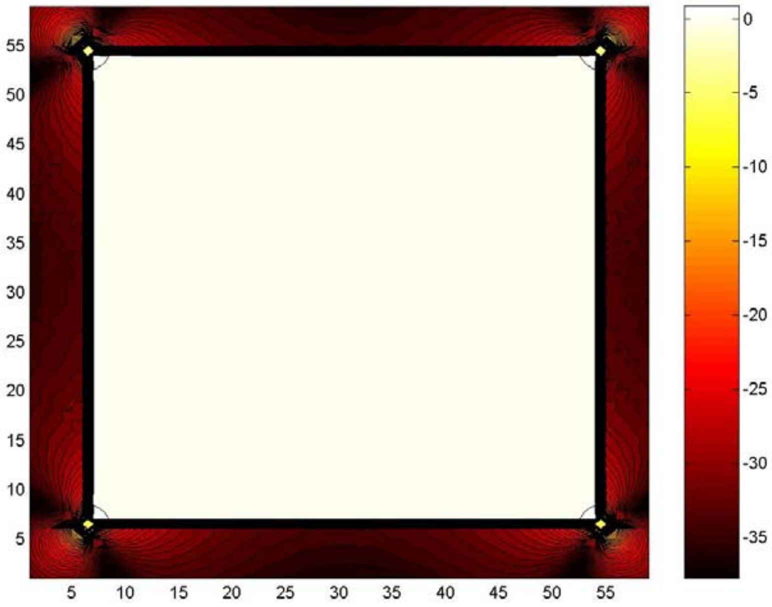

Figure 4.5: Huyghens surface in free space FDTD computational domain (logarithmic scale).

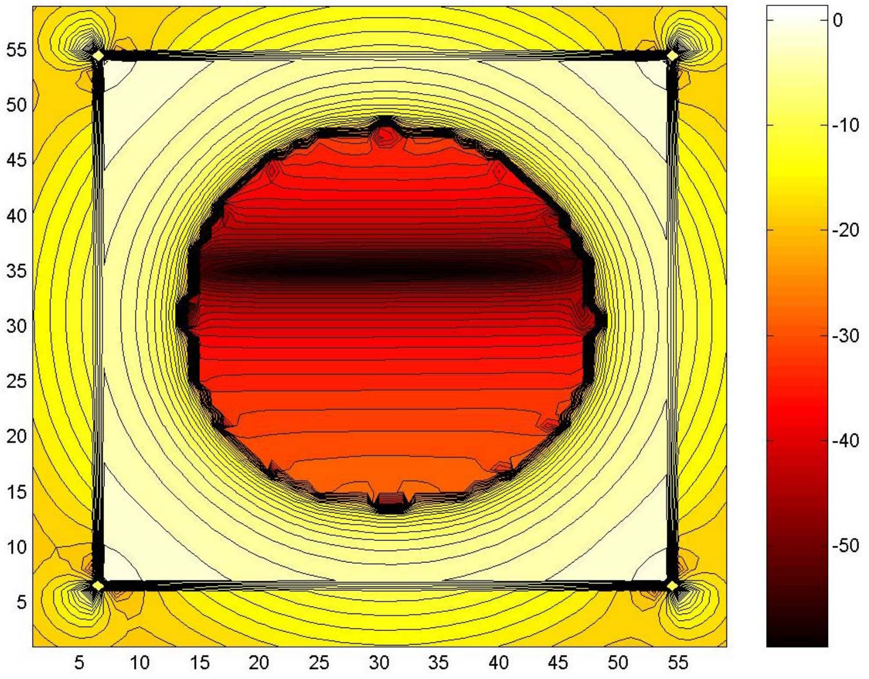

Figure 4.6: Ex component at yzplane for single-layer sphere excited by plane wave of 1V/m at 20MHz (logarithmic scale).

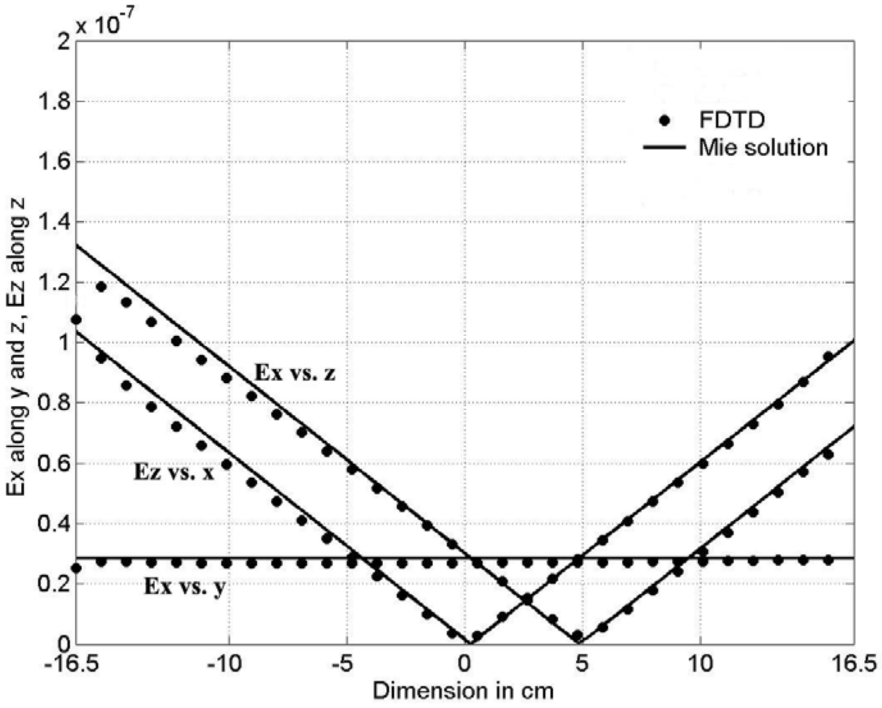

Figure 4.7: Electric Fields distribution along various central axes for single-layer sphere excited by plane wave of 1V/m at 60Hz in free space.

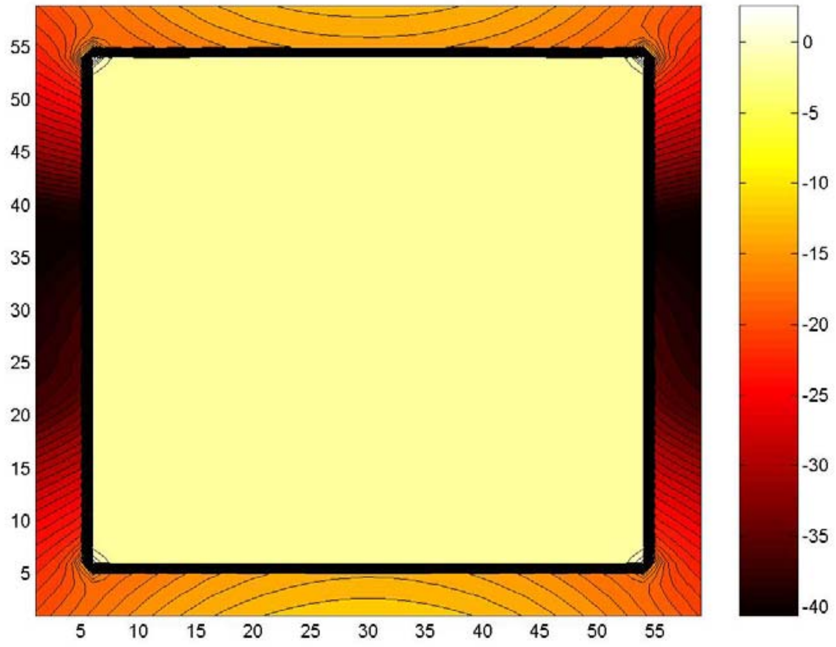

Figure 4.8: Hy component at xzplane for single-layer sphere excited by plane wave of 1V/m at 20MHz and 60Hz (logarithmic scale)

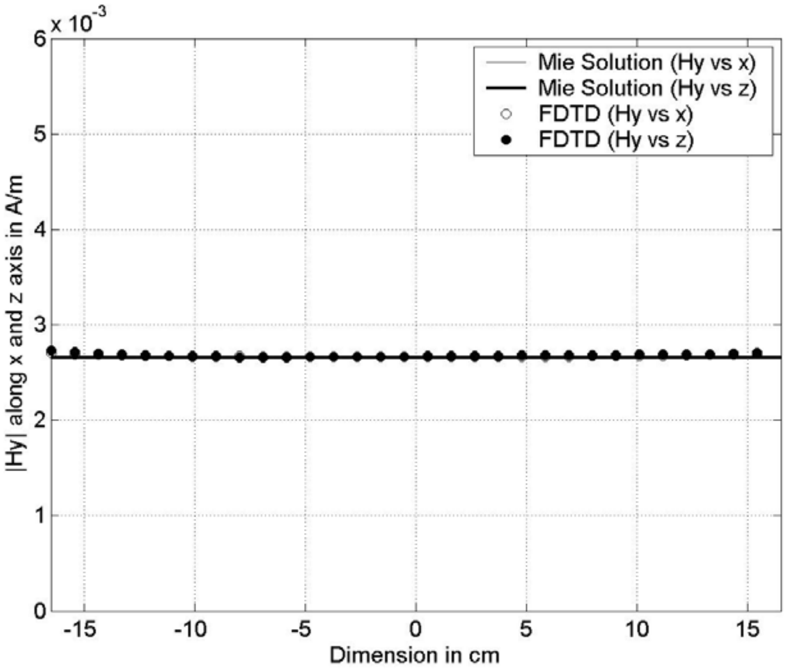

Figure 4.9: Magnetic Field Hy component distribution along various central axes for single-layer sphere excited by plane wave of 1V/m at 60Hz and 20MHz in free space.

Example 4.2: A three-layer concentric sphere is modelled in free space here. The assumed properties are listed as follows: $\sigma_1 = 0.52$ S/m (corresponding to properties of skeletal muscle) for innermost sphere $0 < r < 8$ cm, $\sigma_2 = 0.2$ S/m (corresponding to the properties of fat) for the intermediate sphere $8 < r < 12$ cm, and $\sigma_3 = 0.04$ S/m (corresponding to the properties of bone) for the outermost sphere $12 < r < 16.5$ cm. Since $\sigma >> \omega\varepsilon_o$ for each layers at 20MHz and 60Hz, thus, the choice of ε_r is insignificant in calculation results. Due to the reason above, $\varepsilon_r = 1$ is assumed in all layers of the sphere. Figure 4.10 shows the Ex component in yz coordinate plane for three-layers sphere excited by plane wave of 1V/m at 20MHz. The calculated results of 60Hz are well agreed with the analytical one as illustrated in Figure 4.11.

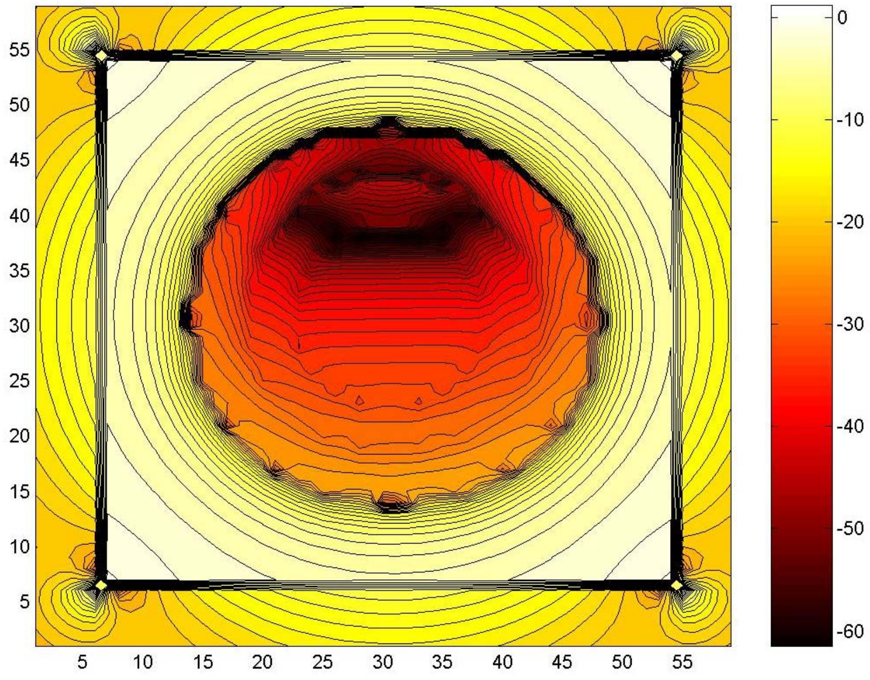

Figure 4.10: Ex component at yzplane for three-layers sphere excited by plane wave of 1V/m at 20MHz in free space (logarithmic scale).

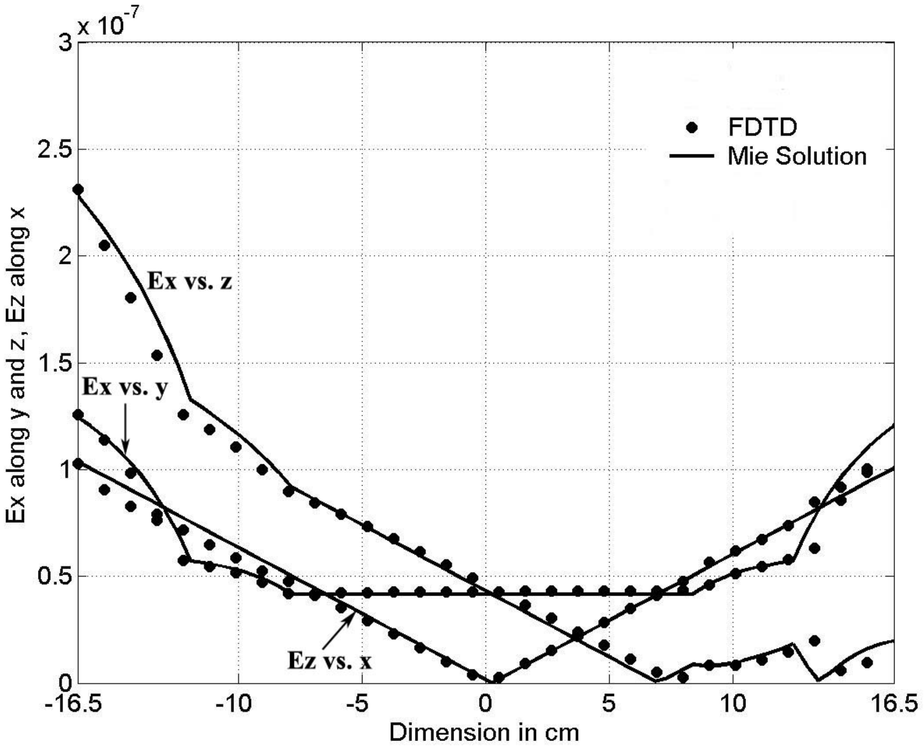

Figure 4.11: Electric Fields distribution along various central axes for three-layer sphere excited by plane wave of 1V/m at 60Hz in free space.

4.5.1.2 Lossless Penetrable Media

By using equations (4.58) and (4.59), the Berenger's PML absorbing boundary conditions in FDTD computational domain is modified to permit the modelling of lossless media. To validate the correctness of PML absorbing boundary conditions, the simulation is first running without the presence of the scatterer. Figure 4.12 shows Huyghens surface in lossless media of the FDTD computational domain. The results are well agreed with the predicted results, in which the fields inside the problem space is about 0dB and numerical reflection is found about -40dB between the Huygens surface and PML region.

Example 4.3: A homogenous single layer sphere with the same conductivity and permittivity of previous example, are being used in this example, except the properties of the surrounding media and perfectly matched layers (PML) are assumed to be (σ = 13e-9 $\approx$ 0 , ε_r= 50) in order to consider the sphere in a lossless media. It should be noted that the PML (6, G9.5, 40dB) (six layers, with geometric progression profile and geometric grading factor of 9.5, with 40-dB attenuation for normal incidence) is implemented on all sides, in order to reduce the reflection of the interface layer. Figure 4.13 describes the intensity of the Ex component in yzplane at 20MHz. Figure 4.14 depicts the electric field distribution along various central axes in lossless media. The magnetic field distributions are also shown in Figure 4.15 and 4.16 respectively. It proves that within quasi-static regime, the electric and magnetic field are decoupled, in the other words, the scattered magnetic field is insignificant compared to incident field since the induced magnetic field is equal to incident magnetic field which is about $1/\eta \cong$ 18.8 mA/m at both 20MHz and 60Hz, where η is the characteristic impedance of lossless media which is about $\sqrt{\frac{\mu_o}{\varepsilon_o \varepsilon_r}} \cong 53.27\Omega$. As can be observed, excellent agreement has been reached between the numerical and analytical result.

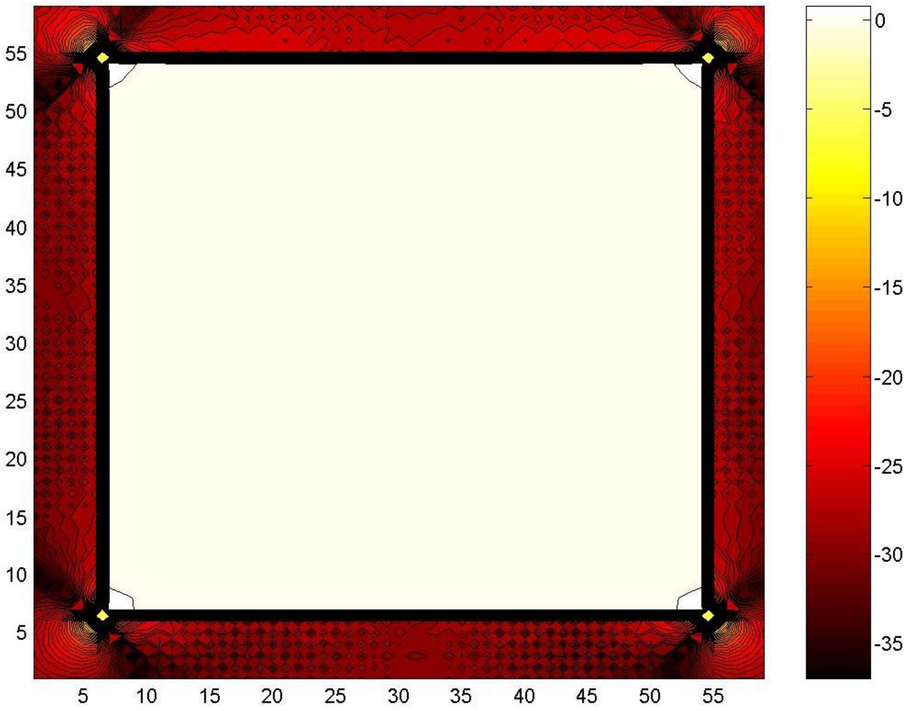

Figure 4.12: Huyghens surface in lossless media FDTD computational domain (logarithmic scale).

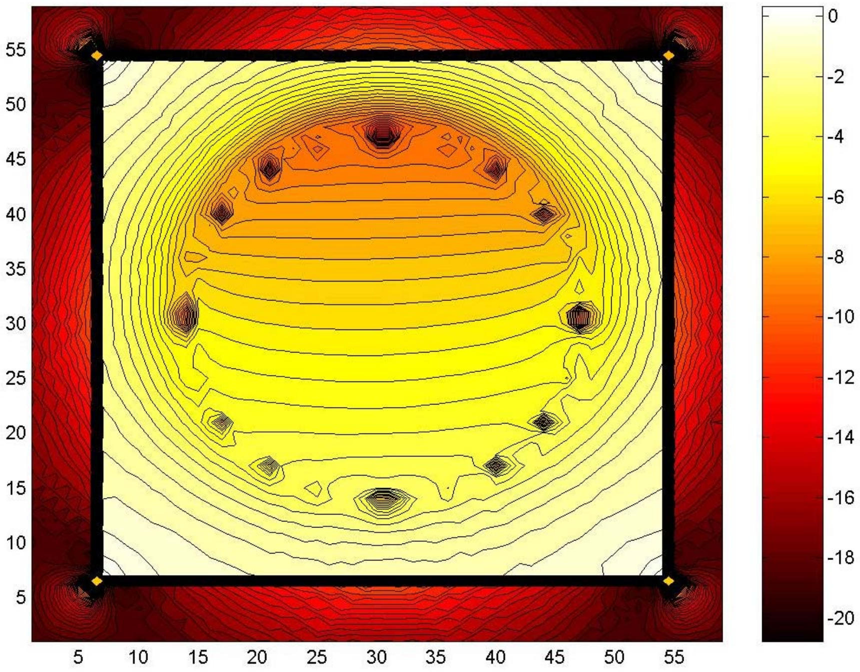

Figure 4.13: Ex component at yzplane for single-layer sphere excited by plane wave of 1V/m at 20MHz in lossless media (logarithmic scale).

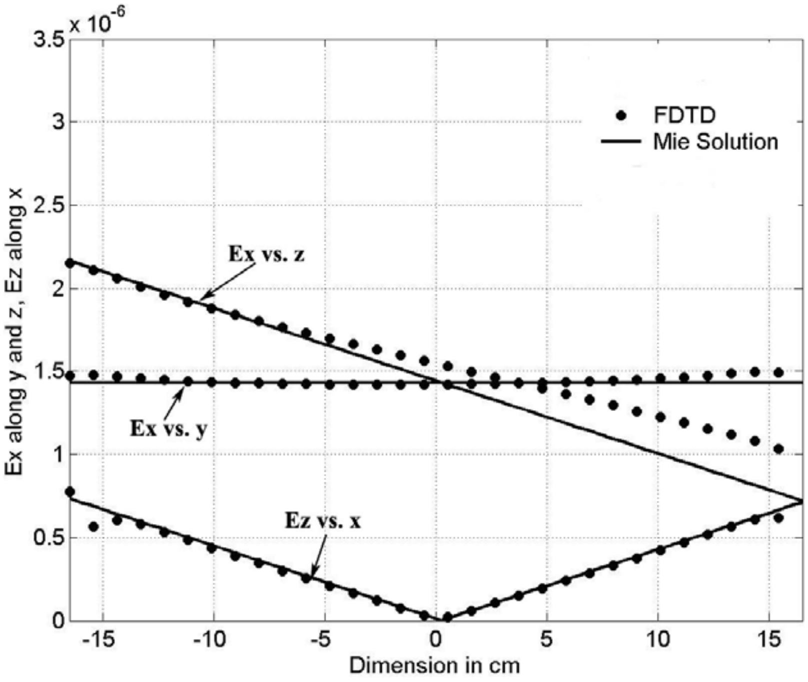

Figure 4.14: Electric Fields distribution along various central axes for single-layer sphere excited by plane wave of 1V/m at 60Hz in lossless medium (logarithmic scale).

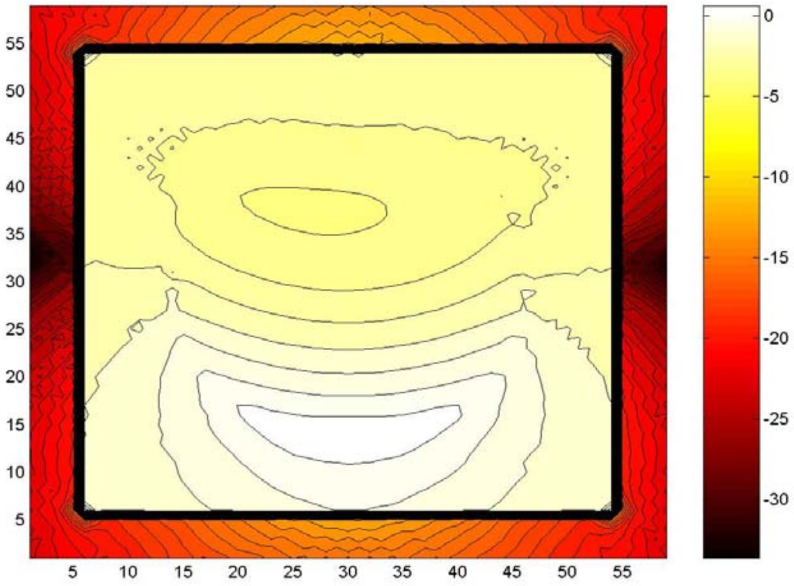

Figure 4.15: Hy component at xzplane for single-layer sphere excited by plane wave of 1V/m at 60Hz and 20MHz in lossless media (logarithmic scale).

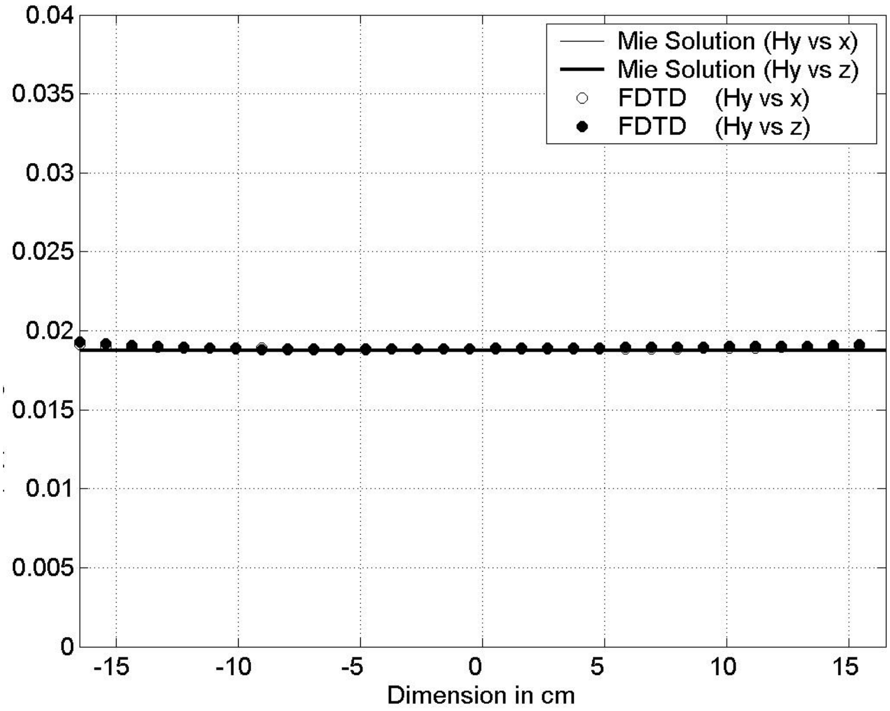

Figure 4.16: Magnetic Field distribution along various central axes for single-layer sphere excited by plane wave of 1V/m at 60Hz and 20MHz in lossless medium.

4.5.2 Verification at High Frequency (Mobile Communication Frequency)

The frequency scaled FDTD technique is applied to biological cell modelling at mobile communication frequency of 2450MHz. Since the cell size of this problem is considered about micrometer, therefore $\delta t \le \frac{\Delta s}{c\sqrt{3}} \cong 10^{-15}$ s where Δs is the cell size and c is the speed of light in lossy penetrable media. Since four oscillations period of the incident wave are required for the completion of the simulation to reach the steady state. This would involve some millions of iteration, hence, apply the operating frequency to

2450MHz to the problem will increase the number of iterations required. Consequently, frequency of 30GHz is selected as transferable working frequency at initial state, to support the simulation time at affordable level to be computed. Then, the obtained induced fields are scaled back to 2450MHz by using equation (4.56).

4.5.2.1 Lossy Penetrable Media

The stability and the correctness of the implementation of modified lossy Berenger's PML absorbing boundary conditions are initially performed, by running the simulation without the presence of the analysed scatterer. Figure 4.17 shows Huyghens surface in lossy FDTD computational. According to Figure 4.17, the electric field inside the problem space is 0dB, while numerical reflection between the Huygens surface and PML region is nearly -40dB. As can be seen, the results are well agreed with the predicted one.

Example 4.4: A two-layer sphere simulating a biological cell inside a lossy medium, for which the assumed properties are as follows: cytoplasm (internal) $\varepsilon_r = 48.699$, $\sigma = 1.412$; membrane $\varepsilon_r = 11.3$, $\sigma = 0.0$; and lossy medium (external) $\varepsilon_r = 70.87$, $\sigma = 2.781$. The internal radius (internal region) is 25μm and the membrane thickness is set to 2μm. The operating frequency is 2.45 GHz whereas the interim transformed frequency used in this example is 30 GHz. From equation (4.59), the optimum grading factor g is calculated as 6.07 for which the FDTD cell size is 1μm. The Electric field distributions inside the simulated biological equivalent spherical cell are shown in Figure 4.18-4.20, while magnetic field distributions are depicted in Figures 4.21 and 4.22 at the operating frequency of 2450MHz. From the inspection of Figure 4.22, the induced magnetic field is constant over the sphere at both 2.45GHz and 30GHz. The value of these fields, is about $1/\eta_{lossy}$ A/m, in which the η_{lossy} is the characteristic impedance of the lossy media which can be calculated using equation (4.28). From equation (4.28), the value of η_{lossy} is computed and is approximately found 44.77 Ω. In the light of all the obtained simulated results, as can be noticed that the numerical and analytical results are indistinguishable.

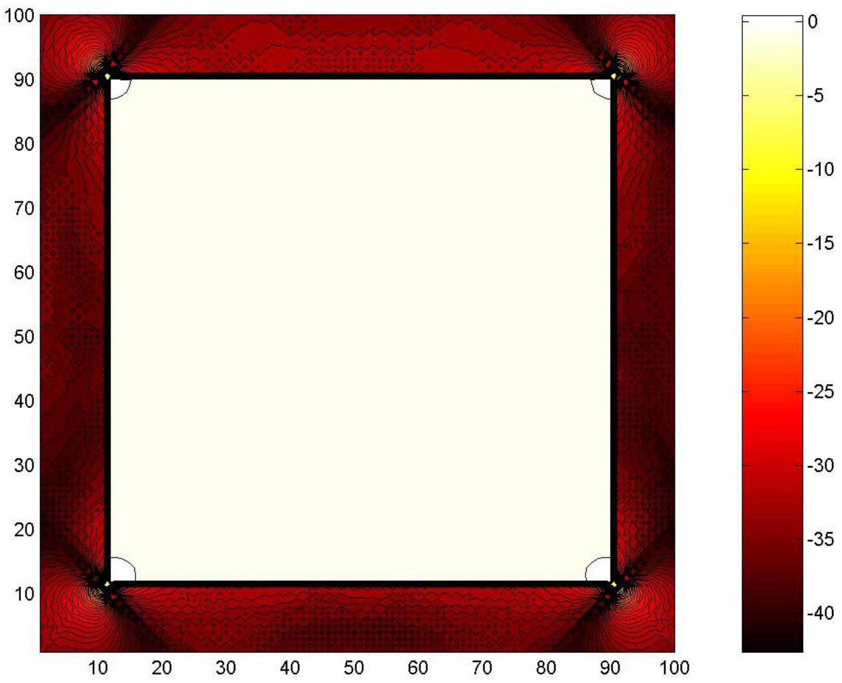

Figure 4.17: Huyghens surface in lossy medium FDTD computational domain (logarithmic scale).

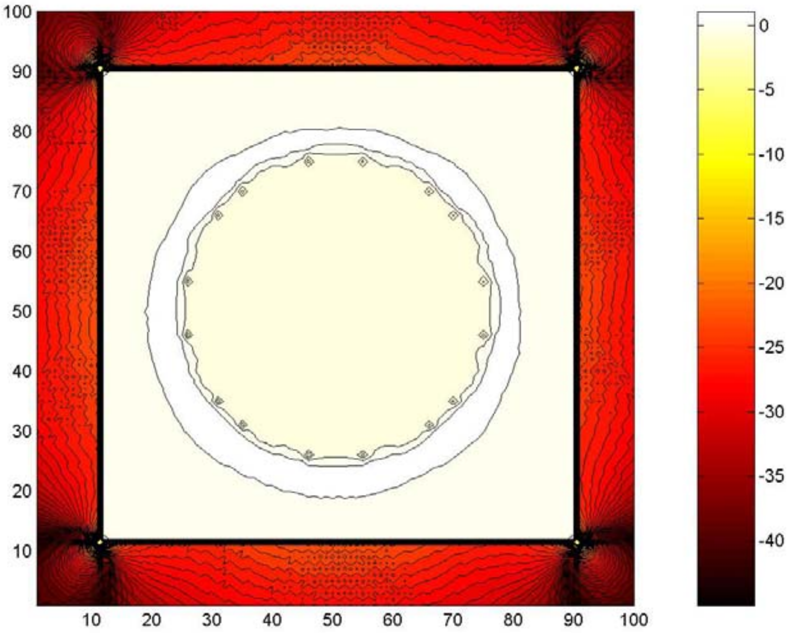

Figure 4.18: Ex component at yzplane for double-layers sphere excited by plane wave of 1V/m at 30GHz in lossy medium (logarithmic scale).

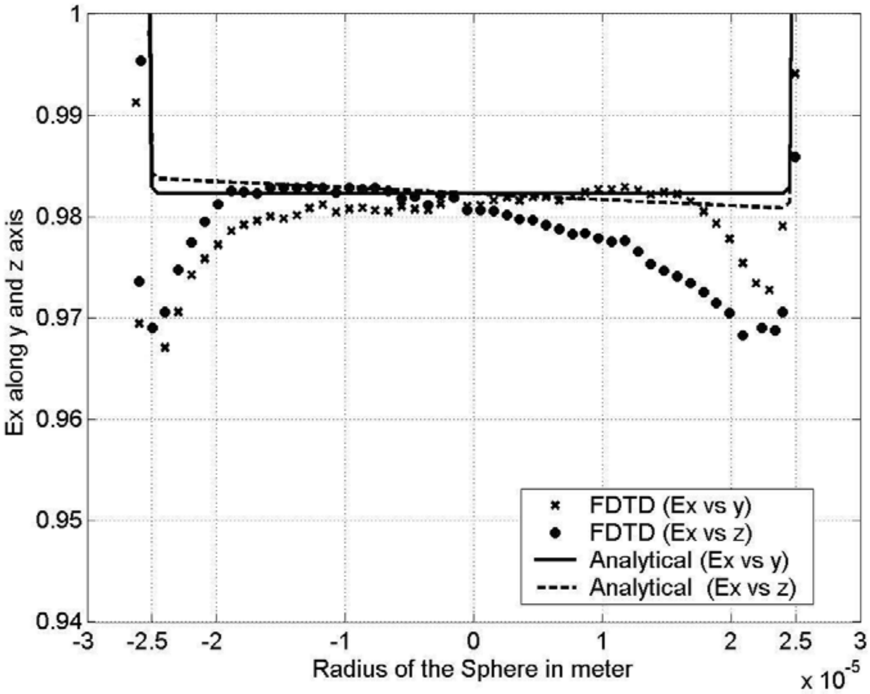

Figure 4.19: Electric Field (Ex) distribution along various central axes for double-layers sphere excited by plane wave of 1V/m at 2450MHz in lossy medium.

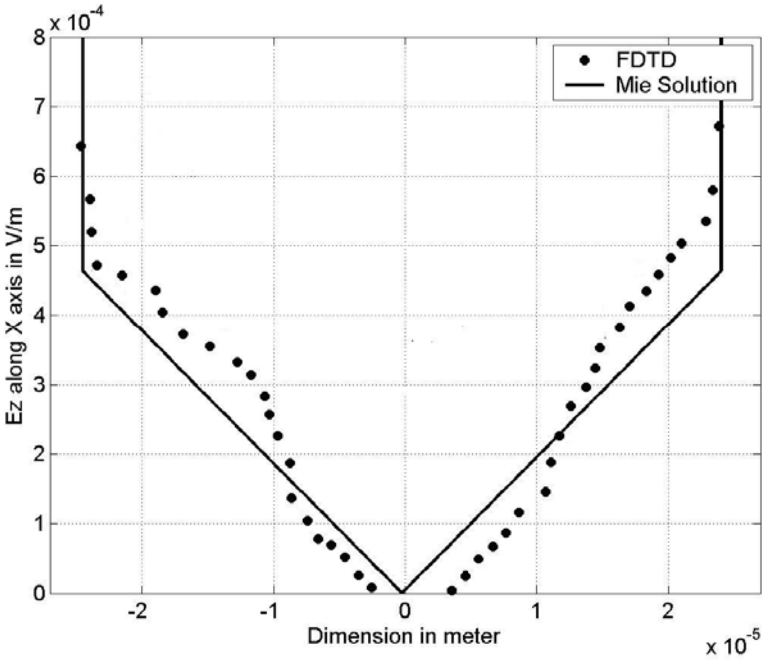

Figure 4.20: Electric Field (Ez) distribution along x-axes for double-layer sphere excited by plane wave of 1V/m at 2450MHz in lossy medium.

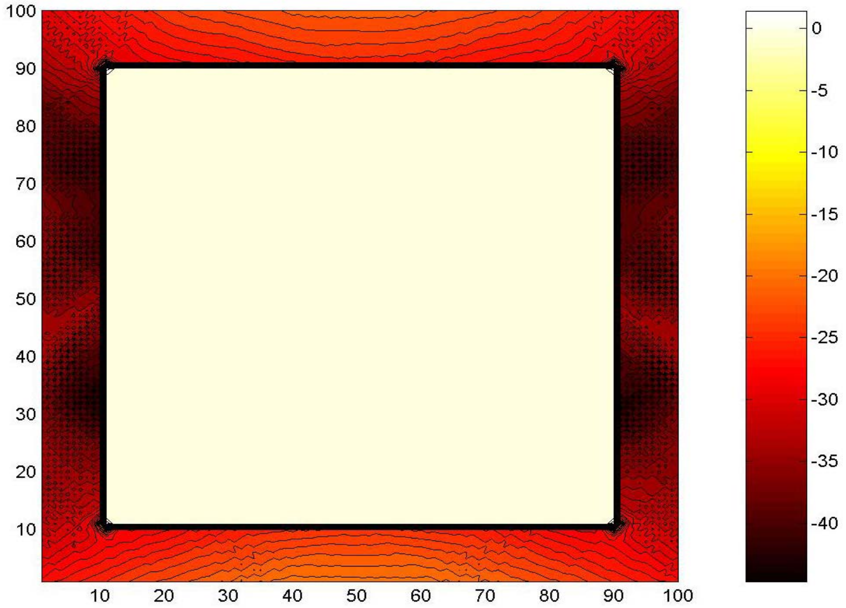

Figure 4.21: Hy component at xzplane for double-layers sphere excited by plane wave of 1V/m at 2450MHz and 30GHz in lossy medium (logarithmic scale).

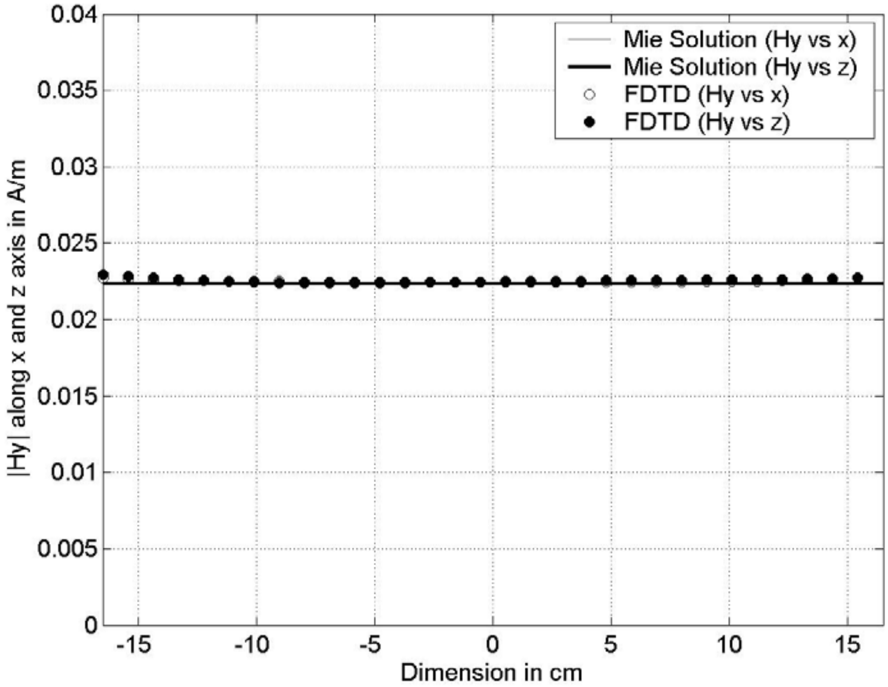

Figure 4.22: Magnetic Field distribution along various central axes for double-layer sphere excited by plane wave of 1V/m at 2450MHz and 30GHz in lossy medium.

4.6 Conclusions

By implementing the frequency scaling approach, the number of FDTD time steps can be reduced. The reflection on the interface layers inside the FDTD computation domain, has also been successfully reduced in lossless and lossy penetrate media. The accuracy of the FDTD scaling approach with the models of homogenous and layered spheres in free space, lossless and lossy media, was verified. The numerical results were in good agreement with the analytical ones. This lending its support to the validity of using the scaled-frequency FDTD method to obtain induced E fields at power-line and mobile communication frequencies, as long as the quasi-static conditions are valid.

4.7 References

[1] Y.U.Vorobev, *Method of Moments in Applied Mathematics (translated from Russian by Seckler)*: New York: Gordon & Breach, 1965.

[2] R.F.Harrington, *Field Computation by Moment Methods*: The Macmillan Co., New York, 1968.

[3] B.J.Strait, "Applications of the Method of Moments to Electromagnetics," *St.Cloud,FL:SCEEE Pres*, 1980.

[4] M.M.Ney, "Method of Moments as applied to electromagnetic problems," *IEEE Transactions on Microwave Theory and Techniques*, vol. 33, pp. 972-980, 1985.

[5] J.P.Webb, "Developments in a Finite Element Method for Three-Dimensional Electromagnetic Problems," *PHD Dissertation, University of Cambridge*, 1981.

[6] G.L.Maile, "Three-Dimensional Analysis of Electromagnetic Problems by Finite Element Methods," *PHD Dissertation, University of Cambridge*, 1979.

[7] J. Jin, *The Finite Element Method in Electromagnetics*, 2nd ed. New York: John Wiley & Sons,Inc,, 2002.

[8] M.N.O.Sadiku, "A simple introduction to finite element analysis of electromagnetic problems," *IEEE Transactions on Education*, vol. 32, pp. 85-93, 1989.

[9] K.S.Kunz and K.M.Lee, "A three-dimensional finite-difference solution of the external response of an aircraft to a complex transient EM environment I: The method and its implementation," *IEEE Trans. On Electromagnetic compatibility*, vol. 20, pp. 328-333, 1978.

[10] A.Taflove, "Advances in Computational Electrodynamics: The Finite-Difference Time-Domain Method," Artech House, 1998, pp. 627-632.

[11] A.Taflove and S.C.Hagness, *Computational Electromagnetics: the finite-different time-domain method*, 2nd ed: Artech House,INC., 2000.

[12] K.S.Yee, "Numerical solution of initial boundary value problems involving Maxwell's equations," *IEEE Transactions on Antennas and Propagation*, vol. 3, pp. 302-307, 1966.

[13] O.P.Gandhi and J.Chen, "Numerical dosimetry at powerline frequencies using anatomically based models," *Bioelectromagnetic*, vol. 1, pp. 43-60, 1992.

[14] J.D.Moerloose, T.W.Dawson, and M.A.Stuchly, "Application of the finite difference time domain algorithm to quasi-static field analysis," *Radio Science*, vol. 32, pp. 329-341, 1997.

[15] M.E.Potter, M.Okoniewski, and M.A.Stuchly, "Low Frequency Finite Difference Time Domain (FDTD) for Modelling of Induced Fields in Humans Close to Line Sources," *Journal of computational physics*, vol. 162, pp. 82-103, 2000.

[16] G.Emili, A.Schiavoni, F.L.Roselli, and R.Sorrentino, "Computation of electromagnetic field inside a tissue at mobile communications frequencies," *IEEE Trans on MTT*, vol. 51, pp. 178-186, 2003.

[17] J.Berenger, "A perfectly matched layer for Absorption of Electromagnetic waves," *Journal of computational physics*, vol. 114, pp. 185-200, 1994.

[18] D.S.Katz, E.T.Thiele, and A.Taflove, "Validation and Extension to Three Dimensions of the Berenger PML Absorbing Boundary Condition for FD-TD Meshes," *IEEE Trans. on Microwave and Guided Wave Letters*, vol. 4, pp. 268-270, 1994.

[19] J.Berenger, "Perfectly Matched layer for the FDTD Solution of wave-structure interaction problems," *IEEE Trans. on Ant. and Propag.*, vol. 44, pp. 110-117, 1996.

[20] J.Berenger, "Improved PML for the FDTD solution of wave-structure Interaction problem," *IEEE Trans. on Antennas and Propagation*, vol. 45, pp. 466-473, 1997.

[21] M.N.O.Sadiku, "Elements of Electromagnetics," 3rd ed. New York: Oxford University Press, Inc., 2001, pp. 417-435.

[22] D.M.Pozar, "Microwave Engineering," 3rd ed: John Wiley & Sons, Inc., 2005, pp. 14-44.

[23] G.Mie, "Contributions to the optics of diffusing media," *Ann. Physik*, vol. 25, pp.

377, 1908.

[24] J.Stratton, *Electromagnetic Theory*: New York: McGraw-Hill, pp.563-573, 1941.

[25] A.L.Aden and M.Kerker, "Scattering of electromagnetic waves from two concentric spheres," *J. Appl. Phys.*, vol. 22, pp. 1242-1246, 1951.

[26] P.Wyatt, "Scattering of electromagnetic plane waves from inhomogenous spherically symmetric objects," *Phys. Rev.*, vol. 5, pp. 1837-1842, 1962.

[27] A.Anne, M.Satio, O.M.Salati, and H.P.Schwan, "Relative microwave absorption cross section of biological significance," *biological effect of Microwave Radiation*, vol. 1, pp. 153-176, 1960.

[28] A.R.Shapiro, R.F.Lutomirski, and H.T.Yura, "Induced fields and heating within a cranial structure irradiated by an electromagnetic plane wave," *IEEE Transactions on Microwave Theory and Techniques*, vol. 19, pp. 187-196, 1971.

[29] H.N.Kritikos and H.P.Schwan, "Hot spots generated in conducting spheres by electromagnetic waves and biological implications," *IEEE Transactions on Biomedical Engineering*, vol. 19, pp. 53-58, 1972.

[30] W.T.Joines and R.J.Spiegel, "Resonance absorption of microwaves by the human skull," *IEEE Transactions on Biomedical Engineering*, vol. 21, pp. 46-48, 1974.

[31] C.M.Weil, "Absorption characteristics of multi-layered sphere models exposed to

UHF/microwave radiation," *IEEE Transactions on Biomedical Engineering*, vol. 22, pp. 468-476, 1975.

[32] H.N.Kritikos and H.P.Schwan, "Formation of hot spots in multi-layer spheres," *IEEE Transactions on Biomedical Engineering*, vol. 23, pp. 168-172, 1976.

[33] A.Hizal and Y.K.Baykal, "Heat potential distribution in an inhomogeneous spherical model of a cranial structure exposed to microwaves due to loop or dipole antennas," *IEEE Transactions on Microwave Theory and Techniques*, vol. 26, pp. 607-612, 1978.

[34] J.Li and W.Lin, "Inverse scattering for dielectric spheres," *Antennas and Propagation Society International Symposium,1990. AP-S. 'Merging Technologies for the 90's'. Digest.*, vol. 2, pp. 1048-1051, 1990.

[35] L.M.Liu and S.F.Cleary, "Absorbed Energy Distribution from radiofrequency electromagnetic radiation in a mammalian cell model: effect of membrane-bound water," *Bioelectromagnetic*, vol. 16, pp. 160-171, 1995.

[36] D.D.Smith and K. A. K.AFuller, "Mie scattering by concentric multilayers," *Quantum Electronics and Laser Science Conference*, pp. 119-120, 2002.

[37] F.Apollonio, M.Liberti, G.D.Inzeo, and L.Tarricone, "Integrated Models for Analysis of Biological Effects of EM fields used for mobile Communications," *IEEE Transactions on Microwave Theory and Techniques*, vol. 48, pp. 2082-2093, 2000.

[38] D.M.Sullivan, D.T.Borup, and O.P.Gandhi, "Use of the Finite-Difference Time-Domain Method in Calculating EM Absorption in Human Tissue," *IEEE Transactions on Biomedical Engineering*, vol. 34, pp. 148-157, 1987.

[39] X.Yuan, "Three-dimensional electromagnetic scattering from inhomogeneous objects by the hybrid moment and finite element method," *IEEE Transactions on Microwave Theory and Techniques*, vol. 38, pp. 1053 - 1058, 1990.

[40] I.El-Babli, A.Sebak, and N.Simons, "Application of the TLM method to the interaction of EM fields with dispersive dielectric bodies," *Microwaves, Antennas and Propagation, IEE Proceedings*, vol. 147, pp. 211-217, 2000.

[41] M.E.Potter, M.Okaniewski, and M.A.Stuchly, "Low Frequency Finite Difference Time Domain(FDTD) for Modeling of Induced Fields in Humans Close to Line Sources," *Journal of Computational Physics*, vol. 162, pp. 82-103, 2000.

[42] R.S.Schechter, M.Kragalott, M.S.Kluskens, and W.P.Pala, "Splitting of Material Cells and Averaging Properties to Improve Accurary of the FDTD Method at Interfaces," *ACES Journal*, vol. 17, pp. 198-208, 2002.

[43] M.Abramowitz and I.A.Stegun, "Handbook of Mathematical Functions," NBS Math Series, Dover Publications, New York., 1970.

[44] G.T.Ruck, D.E.Barrick, W.D.Stuart, and C.K.Krichbaum, *Radar Cross Section Handbook*, vol. 1. New York: Plenum Press, 1970.

[45] W.T.Kaune and M.F.Gillis, "General Properties of the Interaction Between Animals and ELF Electric Fields," *Bioelectromagnetics*, vol. 2, pp. 1-11, 1981.

[46] A.W.Guy, S.Davidow, G-Y.Yang, and C-K.Chou, "Determination of Electric Current Distributions in Animals and Humans Exposed to a Uniform 60-Hz High-Intensity Electric Field," *Bioelectromagnetics*, vol. 3, pp. 47-71, 1982.

[47] G. Mur, "Absorbing boundary conditions for the Finite-Difference Approximation of the time-domain Electromagnetic-field equations," *IEEE Trans. On Electromagnetic compatibility*, vol. EMC-23, pp. 377-382, 1981.

[48] Z.P.Liao, H.L.Wong, B.P.Yang, and Y.F.Yuan, "A transmitting boundary for transient wave analysis," *Scientia Sinica (series A)*, pp. 1063-1076, 1984.

Chapter 5

Computation of Electromagnetic Field inside a Tissue Using Quasi-Static and Lumped-Element FDTD Scheme

5.1 Introduction

Research into possible mechanisms of interaction of electromagnetic (EM) fields with biological tissues and cells in culture has motivated a growing need for accurate models describing the EM behaviour of cells exposed to these fields. Therefore, several numerical models have been set up in order to study the interaction between electromagnetic (EM) fields and biological entities, at tissue level, cell level and ionic level. In this area, the most frequently used technique for computing the EM field is the finite-difference time-domain (FDTD) method [1, 2], due to its independence from the material parameters.

The standard Finite-Difference Time-Domain (FDTD) method [1, 2] requires extremely small time-step when modelling electrically-small regions (much smaller than a wavelength): this is especially the case when modelling biological cells, since they have maximum dimensions of a few tens of micrometers. Thus, it can become impractical due to the unaffordable computation times required. This problem can be solved by implementing a quasi-static approximate version of FDTD. This approach is based on transferring the working frequency to a higher frequency, to reduce the number of time steps required. Then, the generated internal field at the higher frequency can be scaled back to the frequency of interest [3-6].

Cells are surrounded by thin membranes, typically about a few nanometres thick [7]. They are the major barrier in the cell, separating the inside of the cell from the exterior medium. This structure will allow cells to selectively interact with their environment. Therefore, the cell membrane has been identified as the primary target of the action of the EM field on biological structures. Since the thickness of the membrane is about 1000 times smaller than the biological cell, and if the standard FDTD procedure were to be blindly applied to model detail in the membrane within a complete cell model, then this will take some millions of iterations to complete one cycle of simulation. This again will cause excessive computation time. To overcome this problem in standard FDTD, the lumped element finite different time domain (LE-FDTD) method [8-12] was implemented in such a way to model the behaviour of the membrane, based on the Hodgkin-Huxley (HH) model [13-17] on the surface of the biological cell.

This chapter presents a new approach to model and analyse of the HH (Hodgkin and Huxley) membrane model [13-17]. The HH model is represented as an electrical circuit on the surface of the biological equivalent spherical cells. For the sake of simplicity, the analysed structure has been represented with spherical cells and then Floquet periodic boundary conditions [18-21] have been applied to the border of the analysed structure in order to mimic the presence of the surrounding cells. Despite the cellular tissues are not perfectly periodic and the living cells are not precisely spheres, this approximation allows the modelling of biological tissue with only a small part of the structure and alleviates the problem of huge requirement of computer resources for the simulation of a complete tissue. Since the external medium of the biological tissue is lossy fluid, the modified Berenger's perfectly matched layer (PML) absorbing boundary condition (ABC) is used to truncate the computation grid [22-25], in order to reduce the reflections on the interface layers. It should be noted that Berenger's PML ABC is more accurate than the Mur ABC [26], used in other recent work [6].

A further difficulty is the limited extent of studies on the dielectric properties of cell tissues [27]; thus, the complex permittivity of each cell tissue is not clearly established for radio frequencies. However, in this study, an analytical method for estimating the electrical properties of cell tissues in the RF band [28] will be adopted throughout the analysis. Earlier work only considered two media (water and membrane) [6], but the procedure adopted here enables the tissue model to consist of three media (lossy medium, membrane and cytoplasm). In addition, a mass of connected biological tissue is simulated by creating an equivalent stack of compact cell structures (such as spherical and cylindrical with interstices, and cubical). The total electric fields along the central axes of rows of these spherical, cubical and cylindrical cell structures will be investigated.

5.2 Summary of the Method

5.2.1 Modified Berenger's Perfectly Match Layer (PML)

Consider Figure 5.1, it describes the geometry of the FDTD computation domain. It shows the equivalence-principle surface (Huygens surface) that replaces the plane wave. It also depicts the Berenger perfectly matched layer (PML) that implements the absorbing boundary condition (ABC). This layer has been applied to surround the edge of the problem space, by using appropriate matching impedance that satisfies to certain condition (such as $\sigma/\varepsilon = \sigma^*/\mu$ for lossless or lossy media, whereas $\sigma/\varepsilon_o = \sigma^*/\mu_o$ for free space). In order to reduce the reflection on the interface layer, an optimum value of the geometric grading factor (g) has been selected, by using an empirical expression as in [22, 24, 25]:

$$\sigma = -\frac{\varepsilon c}{2\Delta x}\frac{\ln g}{g^{N}-1}\ln R(0) \tag{5.1}$$

where Δx is the spatial increment of FDTD mesh, $R(0)$ is the normal reflection coefficient, N is the number of the cells in the PML thickness, c is the velocity of EM waves in free space or lossy medium.

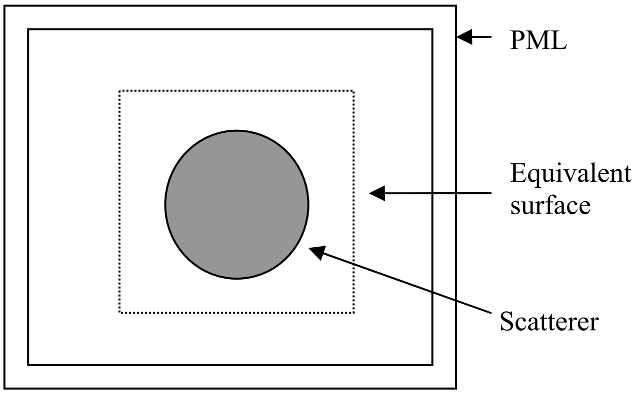

Figure 5.1: Basic structure of the problem of FDTD computational domain

5.2.2 Floquet Periodic Boundary Condition (PBC)

Many structures of electromagnetic interest are extremely large and periodic in one or more dimensions. In order to perform the EM analysis of these types of structure with reasonable computational time, the structures are assumed to be an infinite grid and subsequently reducing the problem into a unit-cell analysis by using floquet boundary condition. This will enable the numerical solution to simulate the effect of the periodic replication. In this area, Photonic Bandgap (PBG) structure, Frequency Selective Surface (FSS) and antenna array are the typical candidates for EM analysis that use the same boundary condition. These structures may contain complex arbitrary shape of scatterers comprised of dielectrics and conductors, thus, numerical methods that can easily handle complex and inhomogeneous geometries are indispensable in this scope of research.

For the purpose of numerical modelling, the finite-difference time-domain (FDTD) technique appears to be an attractive choice for this problem due to its simplicity and comprehensibility. In fact, the floquet theorem has been successfully implemented inside the FDTD to analyse the case of normal [18, 29] and oblique incidence [30, 31] for two- and three-dimensional problems. The techniques used to perform FDTD with the floquet periodic boundary condition can be classified into two categories, i.e., direct field methods and field transformation methods. Direct field methods comprise of Normal incidence, Sine-Cosine, Multiple Unit Cell and Angled Update Method, whereas the field transformation methods consist of Multi-Spatial Grid and Split-Field method [2]. In order to understand basic theory and implementation of floquet periodic boundary into FDTD, the case of normal incidence method for 2-D and 3-D problems is demonstrated in the following context.

5.2.2.1 Two-dimensional Transverse Magnetic (TM) case

Consider a 2-D Transverse Magnetic (TM) case of analysis, Figure 5.2 depicts a simple geometry of a 2-dimensional infinite periodic scatterer illuminated by a normal incidence plane wave which is propagating in y direction. As can be seen, part of the scatterer is repeated along x direction, while magnetic walls will be formed at the unit cell boundaries at x=0 and x=d. The upper and lower boundaries along y axis are truncated with the absorbing boundary condition [22, 26] can be observed. Due to the scatterer structure is periodic in y direction, therefore, this problem can be simplified and analysed on a basis of a finite size unit cell in the FDTD computation domain, as shown in Figure 5.2.

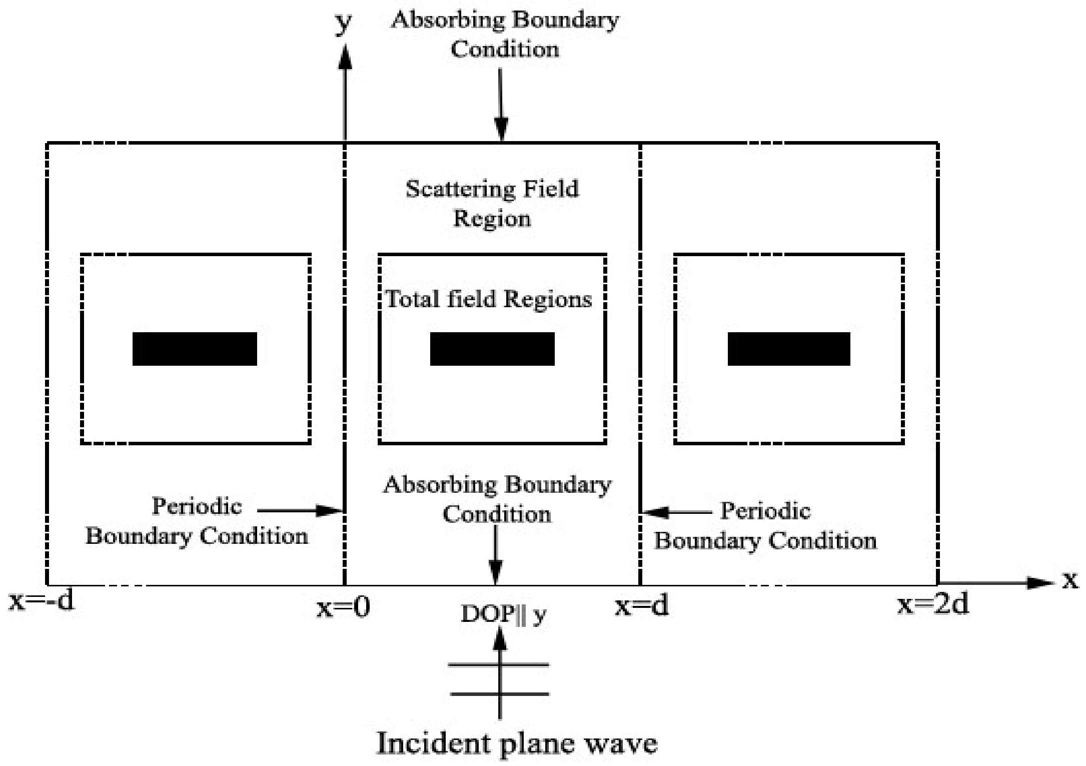

Figure 5.2: Basic configuration of 2-D infinite periodic structure illuminated by a plane wave at broadside incidence in FDTD computational domain.

In TM case of analysis, only the sets of (E_z, H_x, H_y) components are included. Assume a lossless medium problem space (σ=0, $\varepsilon = \varepsilon_0\varepsilon_r$ and $\mu = \mu_0$) is considered, in which σ, ε and μ are the conductivity, permittivity and permeability of the lossless medium respectively. Therefore, the 3-dimensional FDTD updating equations of (2.15), (2.16) and (2.20) can be reduced to the proper algorithms for 2-dimensional TM case periodic problem analysis. Thus, the equations can be written in the following simplified form:

$$E_z^{n+1}(i,j) = E_z^n(i,j) + \frac{\Delta t}{\varepsilon\Delta}\begin{bmatrix} H_y^{n+\frac{1}{2}}(i+1/2,j) - H_y^{n+\frac{1}{2}}(i-1/2,j) \\ + H_x^{n+\frac{1}{2}}(i,j-1/2) - H_x^{n+\frac{1}{2}}(i,j+1/2) \end{bmatrix} \tag{5.2}$$

$$H_x^{n+\frac{1}{2}}(i,j) = H_x^{n-\frac{1}{2}}(i,j) + \frac{\Delta t}{\mu\Delta}\left[E_z^n(i,j-1/2) - E_z^n(i,j+1/2)\right] \tag{5.3}$$

$$H_y^{n+\frac{1}{2}}(i,j) = H_y^{n-\frac{1}{2}}(i,j) + \frac{\Delta t}{\mu\Delta}\left[E_z^n(i+1/2,j) - E_z^n(i-1/2,j)\right] \tag{5.4}$$

where Δ is the lattice increment and Δt is the time increment.

On the border at x=0 and x=d, the periodic boundary conditions have to be imposed in order to mimic the periodic structure of the problem. This can be done by modifying the updating equation (5.4) of the tangential component (H_y) along the border x=0 and x=d, in the following forms [18]:

$$\mathrm{H}_y^{n+\frac{1}{2}}(\mathrm{i},\mathrm{j}) = \mathrm{H}_y^{n-\frac{1}{2}}(\mathrm{i},\mathrm{j}) + \frac{\Delta \mathrm{t}}{\mu\Delta}\left[\mathrm{E}_z^n(\mathrm{i}+1/2,\mathrm{j}) - \mathrm{E}_z^n(\mathrm{M}-1/2,\mathrm{j})\right] \tag{5.5a}$$

$$H_y^{n+\frac{1}{2}}(M,j) = H_y^{n+\frac{1}{2}}(i,j) \tag{5.5b}$$

where M is the largest lattice grid number in the x direction. In general, equations (5.5a) and (5.5b) are well known as a periodic boundary condition. As for TE case of analysis, the magnetic walls are replaced with the electric walls at x=0, d, and a dual forms of the previous equations can be obtained.

5.2.2.2 Three-Dimensional case

Figure 5.3 shows a simple geometry for the elucidation of three-dimensional periodic boundary implementation. As can be observed, the periodic boundaries are imposed on the x- and y-sides of the structures, while ABCs are applied to truncate the space lattice along z-axis. The coordinate point (i_o,j_o,k_o) and (i_N, j_M, k_p) denote a space point in a uniform rectangular lattice, where i_o, j_o,k_o are the smallest lattice grid number in x, y, z direction respectively and i_N, j_M, k_p are the largest lattice gird number in x, y, z direction respectively.

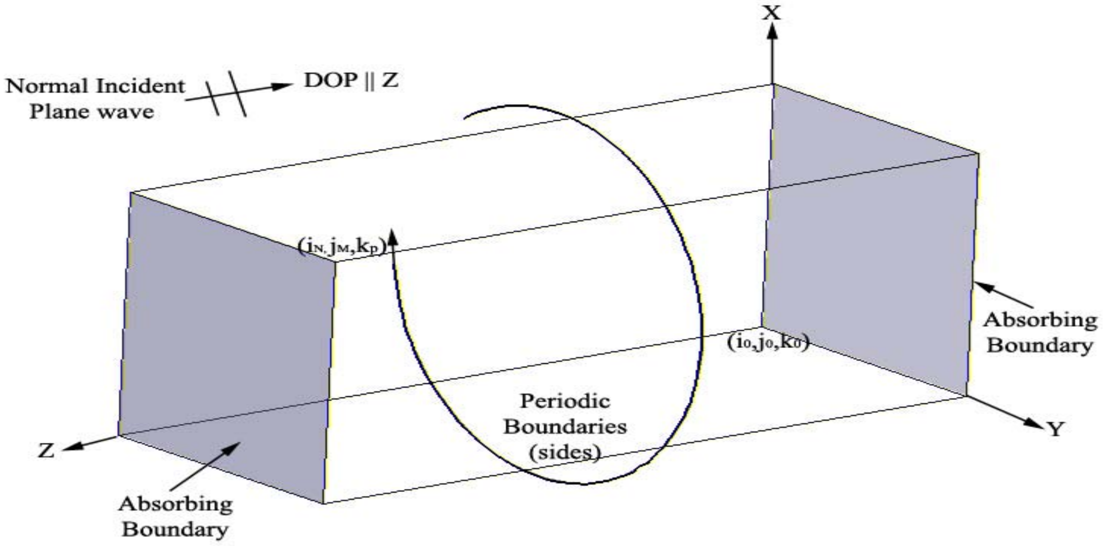

Figure 5.3: Geometry used in the analysis of 3-D infinite periodic structure illuminated by a normal incident plane wave.

Consider the problem space is filled with the lossless medium (σ =0, $\varepsilon = \varepsilon_0 \varepsilon_r$ and $\mu = \mu_0$) and the normal incident plane wave is propagating along z axis. The tangential electric fields distribution on plane i_0, i_N, j_0 and j_M are illustrated in Figure 5.4.

As can be seen, the red arrows are representing the tangential electric field components which are located on edge of the surface plane, while the black arrows are indicated as the least of the tangential electric field components which are located on the surface plane. It should be noted that the explanation of the implementation method of the periodic boundary condition into FDTD computation domain in the following context, are based on the normal incidence methods [2], therefore, it is only applicable when the normal incidence plane wave is used.

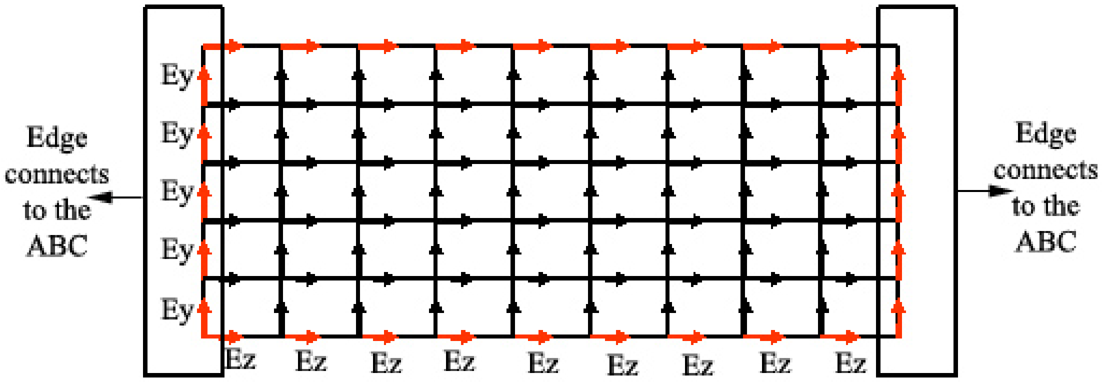

(a)

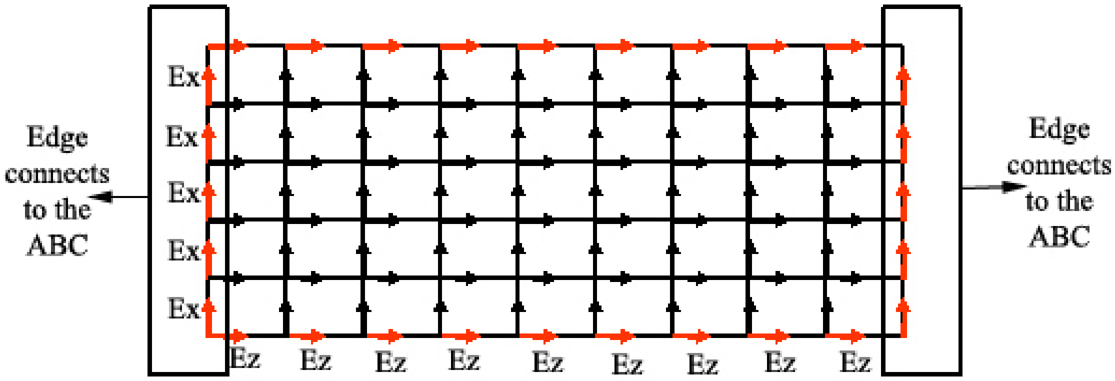

(b)

Figure 5.4:(a) Location of $E_z(\rightarrow)$ and E_y $(\uparrow)$ components in plane $i = i_0$ and i_N

(b) Location of $E_z(\rightarrow)$ and E_x $(\uparrow)$components in plane $j = j_0$ and j_M

For the sake of simplicity and consistency of explanation of updating equations for the periodic boundary condition on the surfaces of the geometry shown in Figure 5.3, the updating equations of the tangential electric components (E_x, E_z and E_y) which are not on the edge of the surface will be firstly to be discussed, and subsequently, the updating equations of the edged tangential electric component (E_z) are demonstrated.

Consider the four surfaces planes at $i=i_0$, i_N and $j=j_0$, j_M, in which the floquet periodic boundary condition should be applied as shown in Figure 5.3. From Figure 5.4(a), the 3D updating equations for the tangential electric components (E_y and E_z) which are not located on the edge of surface plane $i=i_0$ and i_N, can be modified from equations (2.19) and (2.20), and then the new following forms are stated:

$$E_y^{n+1}(i,j,k) = E_y^{n}(i,j,k) + \frac{\Delta t}{\varepsilon\Delta}\begin{pmatrix} H_x^{n+\frac{1}{2}}(i,j,k+1/2) - H_x^{n+\frac{1}{2}}(i,j,k_p-1/2) \\ + H_z^{n+\frac{1}{2}}(i-1/2,j,k) - H_z^{n+\frac{1}{2}}(i+1/2,j,k) \end{pmatrix} \tag{5.6a}$$

$$E_y^{n+1}(i_N,j,k) = E_y^{n+1}(i,j,k) \tag{5.6b}$$

$$E_z^{n+1}(i,j,k) = E_z^{n}(i,j,k) + \frac{\Delta t}{\varepsilon\Delta}\begin{pmatrix} H_y^{n+\frac{1}{2}}(i+1/2,j,k) - H_y^{n+1/2}(i_N-1/2,j,k) \\ + H_x^{n+\frac{1}{2}}(i,j-1/2,k) - H_x^{n+\frac{1}{2}}(i,j+1/2,k) \end{pmatrix} \tag{5.7a}$$

$$E_z^{n+1}(i_N,j,k) = E_z^{n+1}(i,j,k) \tag{5.7b}$$

where Δt is the time increment and Δ is the space lattice increment.

As for the 3-D updating equations for the tangential components (E_x and E_z) which are not located on the edge of the surface at plane $j=j_0$ and j_M as shown in Figure 5.4 (b), can be derived from equations (2.18) and (2.20), thus, the following expressions can be obtained:

$$E_x^{n+1}(i,j,k) = E_x^{n}(i,j,k) + \frac{\Delta t}{\varepsilon\Delta}\begin{pmatrix} H_z^{n+\frac{1}{2}}(i,j+1/2,k) - H_z^{n+\frac{1}{2}}(i,j_M-1/2,k) \\ +H_y^{n+\frac{1}{2}}(i,j,k-1/2) - H_y^{n+\frac{1}{2}}(i,j,k+1/2) \end{pmatrix} \tag{5.8a}$$

$$E_x^{n+1}(i,j_M,k) = E_x^{n+1}(i,j,k) \tag{5.8b}$$

$$E_z^{n+1}(i,j,k) = E_z^{n}(i,j,k) + \frac{\Delta t}{\varepsilon\Delta}\begin{pmatrix} H_y^{n+\frac{1}{2}}(i+1/2,j,k) - H_y^{n+1/2}(i-1/2,j,k) \\ +H_x^{n+\frac{1}{2}}(i,j_M-1/2,k) - H_x^{n+\frac{1}{2}}(i,j+1/2,k) \end{pmatrix} \tag{5.9a}$$

$$E_z^{n+1}(i,j_M,k) = E_z^{n+1}(i,j,k) \tag{5.9b}$$

As for the case of the edged tangential electric components (E_x, E_y, E_z) on plane $i=i_0$, i_N and $j=j_0$, j_M, and due to the E_x and E_y components are on the edge of the absorbing boundary conditions as seen in Figure 5.4 (a) and (b), therefore, they are assumed to be updated by the ABC updating equations. It should be noted that the only edged E_z tangential components will be considered here for the periodic boundary condition. According to Figure 5.5, due to the normal incidence plane wave, hence, four equations of E_z tangential components can be updated simultaneously. This can be simply done by modifying the equation (2.20) and then the following four formulas can be obtained:

$$E_z^{n+1}(i,j,k) = E_z^{n}(i,j,k) + \frac{\Delta t}{\varepsilon \Delta}\begin{pmatrix} H_y^{n+\frac{1}{2}}(i+1/2,j,k) - H_y^{n+1/2}(i_N - 1/2,j,k) \\ + H_x^{n+\frac{1}{2}}(i,j_M - 1/2,k) - H_x^{n+\frac{1}{2}}(i,j+1/2,k) \end{pmatrix} \tag{5.10a}$$

$$E_z^{n+1}(i_N, j_M, k) = E_z^{n+1}(i,j,k) \tag{5.10b}$$

$$E_z^{n+1}(i_N, j_0, k) = E_z^{n+1}(i,j,k) \tag{5.10c}$$

$$E_z^{n+1}(i_0, j_M, k) = E_z^{n+1}(i,j,k) \tag{5.10d}$$

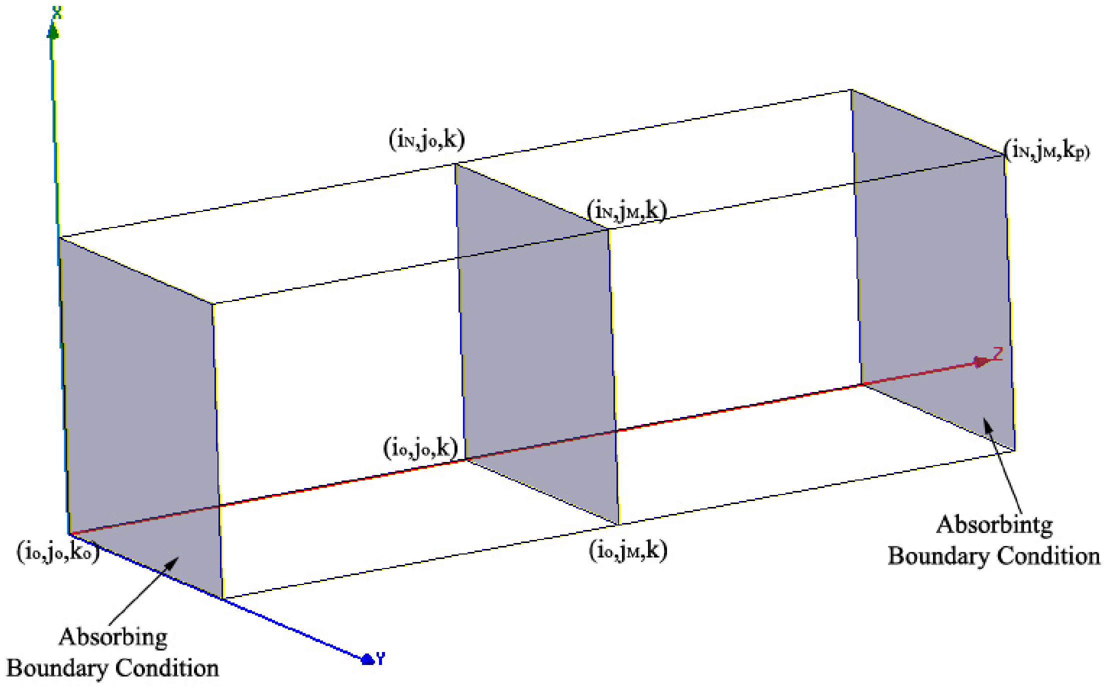

Figure 5.5: Location of the edged tangential component (Ez)

5.2.3 Hodgkin and Huxley (HH) Membrane Model

Cells are surrounded by thin membranes. It is the major barrier in the cell, separating cell contents from outside. Since the cell is separated from its environment, the membrane must be able to accommodate the required cell functions. Therefore, the membrane has to act as a selective barrier, allowing nutrients to pass in but keeping out many harmful substances to the cell, and as a dynamic barrier medium, constantly adapting to changing environmental conditions (different concentrations of ions).

The dimensions of a biological cell are around a few tens of micrometres while the thickness of the membranes is in the scale of a few nanometres, strongly depending on the type of the tissue. Depending on the type of the cell, voltages in the range of 20-200mV can be obtained across the membrane. When the cell is in a resting state, the current across the membrane averages zero, but more generally it depends on the variation on the membrane voltage [13, 14].

Hodgkin and Huxley (H&H) gave a general description of the time course of the current which flows through the membrane of a squid giant axon when the potential difference across the membrane is suddenly changed from its steady state [13, 14]. The results in [13], suggest that the behaviour of a membrane may be represented by the electrical circuit shown in Figure 5.6. Current can be carried through the membrane either by charging the membrane capacitance or by movement of ions through the nonlinear conductance in parallel with the membrane capacitance. The equations that describe the HH model are [13]:

$$\begin{aligned} I = C_m \frac{dV_m}{dt} &+ g_k n^4 [V,t](V_m - E_k) \\ &+ g_{Na} m^3 [V,t] h[V,t](V_m - E_{Na}) \\ &+ g_l (V_m - E_L) \end{aligned} \tag{5.11}$$

$$\frac{dn[V,t]}{dt} = a_n(V)(1 - n[V,t]) - b_n(V) n[V,t] \tag{5.12}$$

$$\frac{dm[V,t]}{dt} = a_m(V)(1 - m[V,t]) - b_m(V) m[V,t] \tag{5.13}$$

$$\frac{dh[V,t]}{dt} = a_h(V)(1 - h[V,t]) - b_h(V) h[V,t] \tag{5.14}$$

where

$$V = V_m - V_r \tag{5.15}$$

The element definitions of the HH model of the above equations are given as follows:

- g_l is the leakage conductance of chloride or other ionic channels.
- m, n, h are the probability parameters determining the percentage of open channels (where an ion passes through the membrane). All variables change between 0 and 1 as functions of time and voltage.
- C_m is the membrane capacity per unit area.
- V_m is the voltage across the membrane.
- E_k , E_{na} , and E_l are the resting potentials of the various ionic channels. They contribute to the steady-state voltage on the membrane for each ionic channel.
- g_k and g_{na} are the nonlinear conductances of potassium and sodium channels.
- V_r is the resting potential of the membrane.
- V is the potential difference between the resting potential and the potential of the membrane, expressed in millivolts.
- I is the total ionic current across the membrane due to flux of ions. It is equal to zero if the membrane voltage equals the resting potential.

TABLE 5.1

CONSTANT VALUES OF THE PARAMETERS IN EQUATION (5.11)

C_m	E_k	g_k	E_{Na}	g_{Na}	E_L	g_L
0.01F/m^2	72mV	360 S/m^2	-55mV	1200 S/m^2	50mV	3 S/m^2

Table I quotes the constant value of all the components in HH model, as stated in [13]. According to [13], the percentage of the open Potassium channels is n^4 and the percentage of the open sodium channels is m^{3}h. It also needs to be highlighted that the quantities appearing in equations (5.12) to (5.14) are defined as [13]:

$$a_n(V) = \frac{0.01(V+10)}{e^{((V+10)/10)} - 1} \tag{5.16}$$

$$a_m(V) = \frac{0.1(V+25)}{e^{((V+25)/10)} - 1} \tag{5.17}$$

$$a_h(V) = 0.07e^{(V/20)} \tag{5.18}$$

$$b_n(V) = 0.125e^{(V/80)} \tag{5.19}$$

$$b_m(V) = 4e^{(V/18)} \tag{5.20}$$

$$b_h(V) = \frac{1}{e^{((V+30)/10)}+1} \tag{5.21}$$

Equations from (5.16) to (5.21) can be redefined and rearranged in more general form as follows:

$$\frac{d\psi}{dt} = -(a_\psi + b_\psi)\psi + \alpha_\psi \tag{5.22}$$

where:

$$\Psi \in \{n, m, h\}$$

After solving the first order partial differential equation of (5.22), the expression for ψ can be obtained:

$$\psi(t) = \frac{a_\psi}{a_\psi + b_\psi}\left(1 - \frac{e^{-(a_\psi + b_\psi)t}}{K}\right) \tag{5.23}$$

where K is the constant that defines the initial condition. As can be observed, if the time (t) is much greater than the time constant $\tau = 1/\,(a_\psi + b_\psi)$, the parameter ψ can be considered and replaced to the following constant:

$$\psi(t)_{t>>\tau} \cong \frac{a_\psi}{a_\psi + b_\psi} \tag{5.24}$$

Consider a biological cell excited by a plane wave of 1V/m. Since the dimension of the membrane is just a few nanometres, the potential difference on the membrane can be estimated as a few nanovolts. This leads to the conclusion that the variables m, n, h in equations (5.16)-(5.21) can be assumed as constant values at steady state, and the HH model can be treated as a linear model. Figure 5.7 shows the percentage variations of a_ψ and b_ψ versus V in the range of ± 1μV. Table II quotes the constant values of n, m and h at steady state.

TABLE 5.2

STEADY-STATE VALUES FOR THE PARAMETERS n,m AND h.

n	m	h
0.3177	0.0529	0.5961

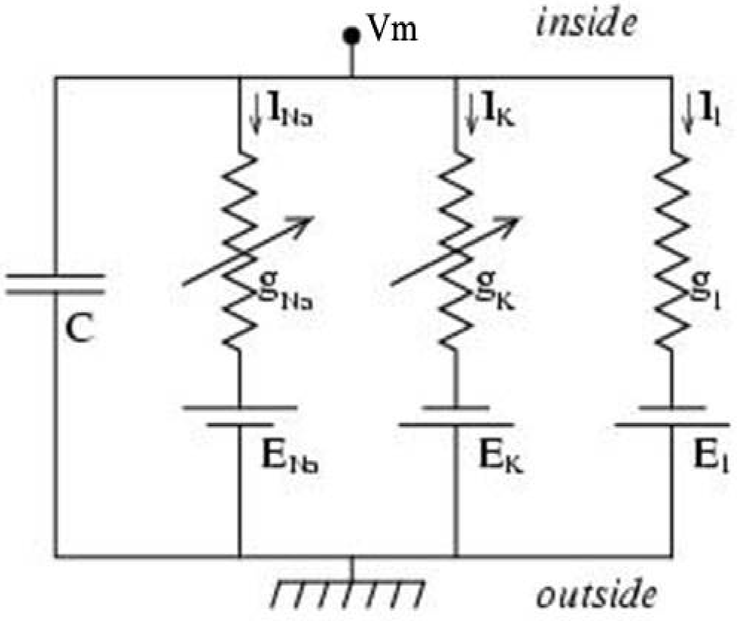

Figure 5.6: Equivalent electrical circuit for the cell’s membrane

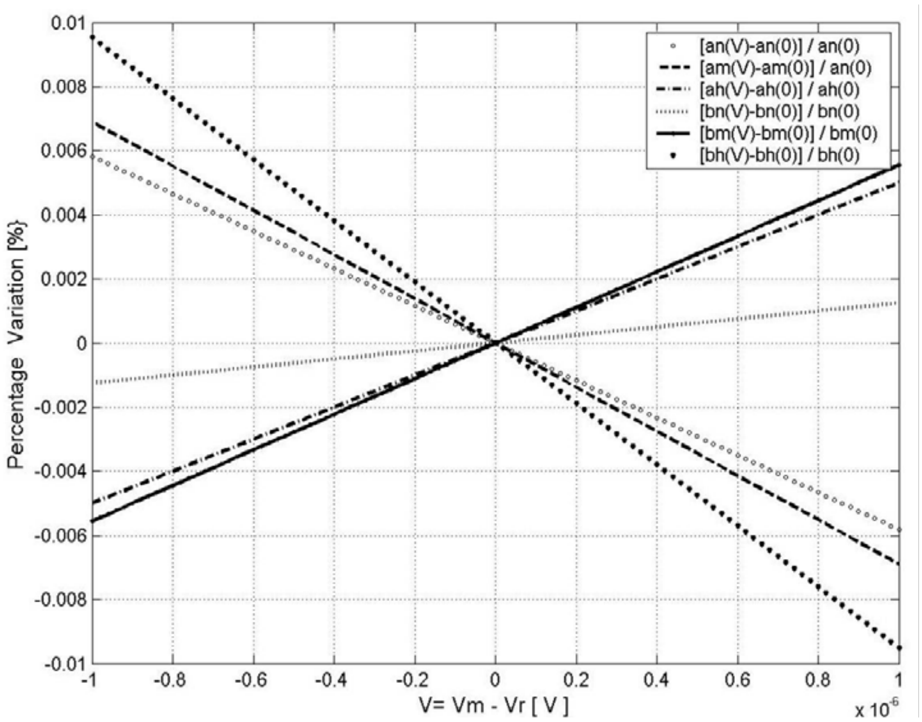

Figure 5.7: Percentage variation of a_ψ and b_ψ (ψ = n,m,h) versus voltage.

5.3 Implementation and Validation

5.3.1 Implementation of Floquet Boundary Condition

This section demonstrates the implementation of Floquet boundary conditions, quasi-static FDTD and the present modified PML for a lossy medium excited by a 100 V/m plane wave at an operating frequency of 900 MHz. The lossy medium properties were $\varepsilon_r = 1.0$, $\sigma = 25$ S/m. The problem space and cell sizes were 21×21×121 and 10μm respectively. The Floquet boundary conditions were imposed on four sides of the lossy medium. The remaining two sides were each terminated by a PML of 6 cells. The analyses were performed at 10, 15 and 20GHz and then transferred back to the desired operating frequency of 900MHz. As can be observed in Figure 5.8, the analytical and computed results are in good agreement.

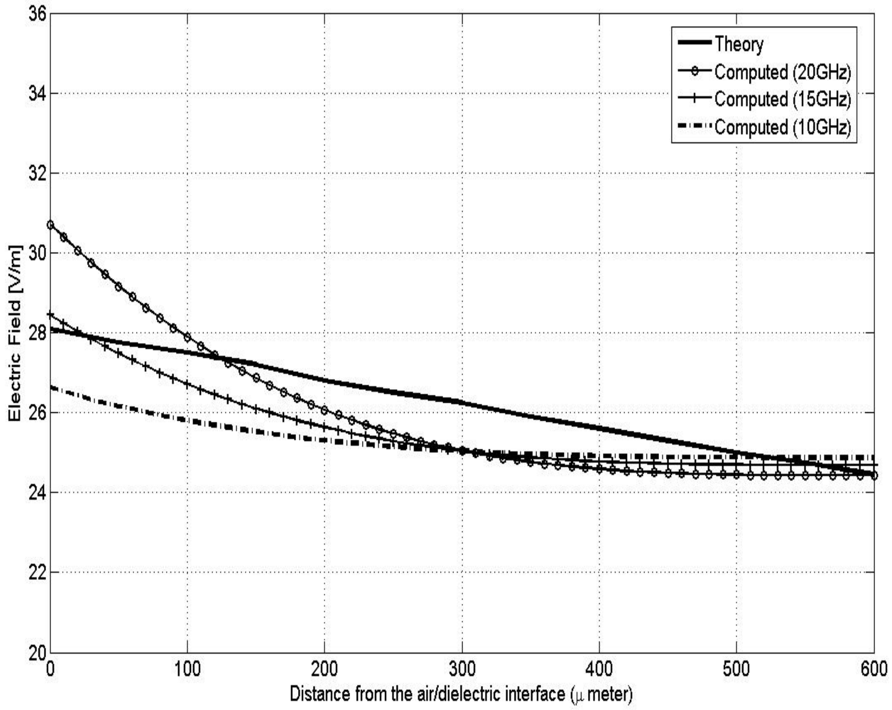

Figure 5.8: Electric Field along the centre of the lossy medium.

5.3.2 HH Model Implementation

To verify the correctness of the implementation of the HH model within the FDTD framework, the results of the analytically computed solution have been used for comparison.

In the first test case, the HH model will be included in one FDTD grid cell which is aligned with the grid. In order to observe the transient phenomena and the steady-state with a reasonable period of computation time, the cell size of the FDTD framework is assumed to be 10cm. Since the entire system is linear, these assumptions do not affect the validity of this test case. No external excitation will be given in this test case until the steady-state is reached. It should be noted that the direction of the cell's membrane is normal to the x-axis. Therefore, the following equations are exploited for this analysis in FDTD computational domain.

$$E_x\Big|_{i,j+1/2,k+1/2}^{n+1/2} = C_{a,E_x|i,j+1/2,k+1/2} E_x\Big|_{i,j+1/2,k+1/2}^{n-1/2} + C_{b,E_x|i,j+1/2,k+1/2} \cdot \begin{pmatrix} H_z\Big|_{i,j+1,k+1/2}^{n} - H_z\Big|_{i,j,k+1/2}^{n} \\ + H_y\Big|_{i,j+1/2,k}^{n} - H_y\Big|_{i,j+1/2,k+1}^{n} \end{pmatrix}$$
$$+ C_{c,E_x|i,j+1/2,k+1/2} \cdot \left(g_k n^4 V_k\Big|^n + g_{Na} m^3 h V_{Na}\Big|^n + g_l V_l\Big|^n \right) \qquad (5.25)$$

$$C_{a_{m,n,p}}\Big|_{i,j,k} = \frac{\left(1 - \frac{\sigma_{i,j,k}\Delta t}{2\varepsilon_{i,j,k}} + \frac{C\Delta_m}{\Delta_n \Delta_p \varepsilon_{i,j,k}} - \frac{g_k n^4 \Delta_m \Delta t}{2\Delta_n \Delta_p \varepsilon_{i,j,k}} - \frac{g_{Na} m^3 h \Delta_m \Delta t}{2\Delta_n \Delta_p \varepsilon_{i,j,k}} - \frac{g_l \Delta_m \Delta t}{2\Delta_n \Delta_p \varepsilon_{i,j,k}}\right)}{\left(1 + \frac{\sigma_{i,j,k}\Delta t}{2\varepsilon_{i,j,k}} + \frac{C\Delta_m}{\Delta_n \Delta_p \varepsilon_{i,j,k}} + \frac{g_k n^4 \Delta_m \Delta t}{2\Delta_n \Delta_p \varepsilon_{i,j,k}} + \frac{g_{Na} m^3 h \Delta_m \Delta t}{2\Delta_n \Delta_p \varepsilon_{i,j,k}} + \frac{g_l \Delta_m \Delta t}{2\Delta_n \Delta_p \varepsilon_{i,j,k}}\right)}$$

(5.26)

$$C_{b_{m,n,p}}\Big|_{i,j,k} = \frac{\left(\dfrac{\Delta t}{\varepsilon_{i,j,k}\Delta_m}\right)}{\left(1+\dfrac{\sigma_{i,j,k}\Delta t}{2\varepsilon_{i,j,k}}+\dfrac{C\Delta_m}{\Delta_n\Delta_p\varepsilon_{i,j,k}}+\dfrac{g_k n^4\Delta_m\Delta t}{2\Delta_n\Delta_p\varepsilon_{i,j,k}}+\dfrac{g_{Na}m^3h\Delta_m\Delta t}{2\Delta_n\Delta_p\varepsilon_{i,j,k}}+\dfrac{g_l\Delta_m\Delta t}{2\Delta_n\Delta_p\varepsilon_{i,j,k}}\right)} \tag{5.27}$$

$$C_{c_{m,n,p}}\Big|_{i,j,k} = \frac{\left(\dfrac{1}{\Delta_n\Delta_p}\right)}{\left(1+\dfrac{\sigma_{i,j,k}\Delta t}{2\varepsilon_{i,j,k}}+\dfrac{C\Delta_m}{\Delta_n\Delta_p\varepsilon_{i,j,k}}+\dfrac{g_k n^4\Delta_m\Delta t}{2\Delta_n\Delta_p\varepsilon_{i,j,k}}+\dfrac{g_{Na}m^3h\Delta_m\Delta t}{2\Delta_n\Delta_p\varepsilon_{i,j,k}}+\dfrac{g_l\Delta_m\Delta t}{2\Delta_n\Delta_p\varepsilon_{i,j,k}}\right)} \tag{5.28}$$

where V_k=72mV, V_{Na}=-55mV, V_L=50mV

$g_k = 360\Delta_n\Delta_p, g_{Na} = 1200\Delta_n\Delta_p, g_k = 3\Delta_n\Delta_p, C = 0.01\Delta_n\Delta_p$

Now, by setting current I = 0 in Equation (5.11), the steady state condition for the cell can be attained, which means the average rate of the ions crossing the membrane is zero. Under this steady state conditions, the resting voltage is equal to the membrane's voltage ($V_r = V_m$), then voltage (V_r) can be computed as follows:

$$V_r = \frac{G_K n^4 E_k + G_{Na} m^3 h E_{Na} + G_L E_L}{G_K n^4 + G_{Na} m^3 h + G_L} = 60.27\text{mV}$$

Figure 5.9 shows the comparison between the FDTD model and the analytical computed membrane voltage versus time. As can be seen, the analytical and FDTD results are indistinguishable in the steady state.

Since the HH model contains a large capacitor, it causes the transient of the HH circuit to require hundreds of thousands of time-steps to reach the steady state when simulation considers the dimensions of a realistic biological cell. To speed up the computation time, the actual FDTD simulation is performed in two steps. In the first step (known as d.c. simulation), simulation is performed with the capacitor in the circuit and then removed and its effects on the system is energized by the step voltage (d.c) sources. Once the steady state is reached, the electric and magnetic fields on each FDTD discretisation cell are used as the initial values for the second step. During the transient simulation, the capacitor and the sinusoidal source are activated. In short, to speed up the computation time, the value obtained in the steady state without excitation can be used as the initial value of the membrane voltage. This procedure is similar to the approach used by the SPICE computer program [14] for the transient and AC analysis of electronic circuits.

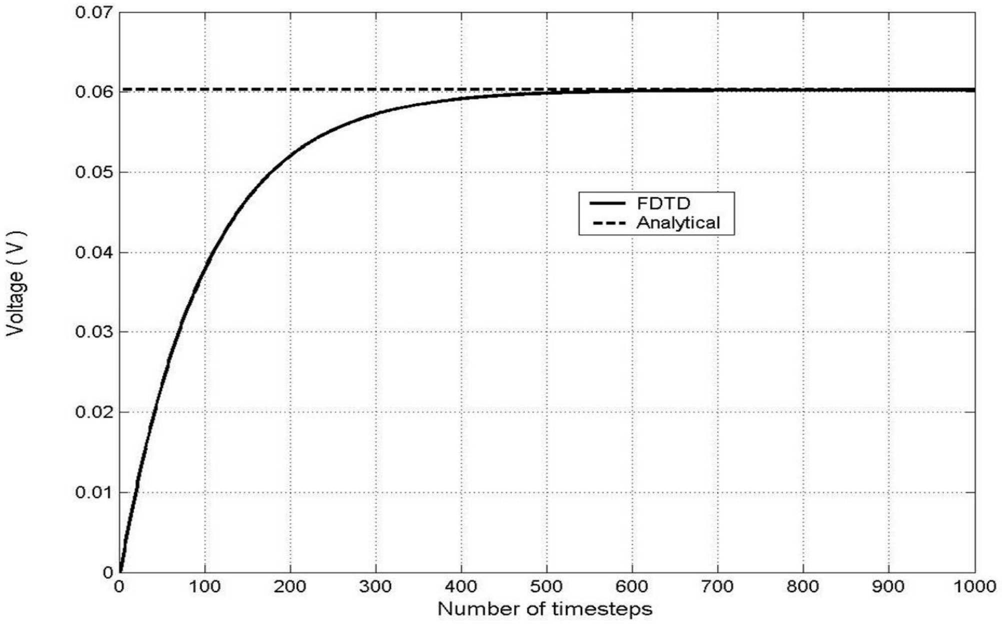

Figure 5.9: Steady state membrane’s voltage verse number of time steps (The normal is directed along X.)

In the second test case, it was shown that the method above gives the same results as when complete transient simulation is performed. The HH model was again inserted in one of the FDTD grid cells, with dimension of 10cm. Then, it was excited by a plane wave at a frequency of 10MHz. Two initial conditions were assumed in the simulation; firstly the membrane voltage was set at zero, and then at 60.27 mV. Figure 5.10 depicts the comparison of the two initial conditions, leading to the conclusion that the computation time can be speeded up by assigning the resting voltage on the cell's membrane at the initial state of the simulation.

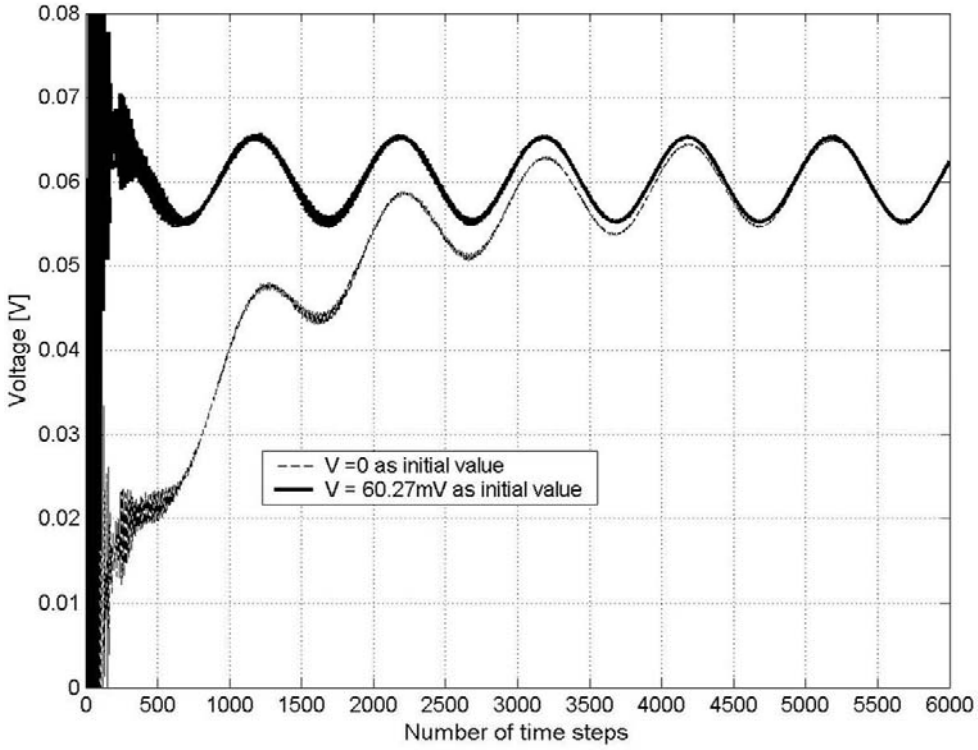

Figure 5.10: Comparison between membrane voltage with different initial conditions

In a third test case, all the parameters in equation (5.11) were set to zero, except for n = 1 and $g_k = 2000000$ S/m^2, so the HH model behaves like a resistor whose value is

$$R = \frac{1}{g_k \Delta s^2} = 50\Omega$$

In this case, the grid cell's size is 0.1 mm, and a plane wave excitation was used propagating in the z-direction and polarised in the x-direction at 40GHz. Figure 5.11 shows the distribution of voltage and current on the membrane. The ratio between the peak values of voltage and current on the membrane was 50.0 Ω.

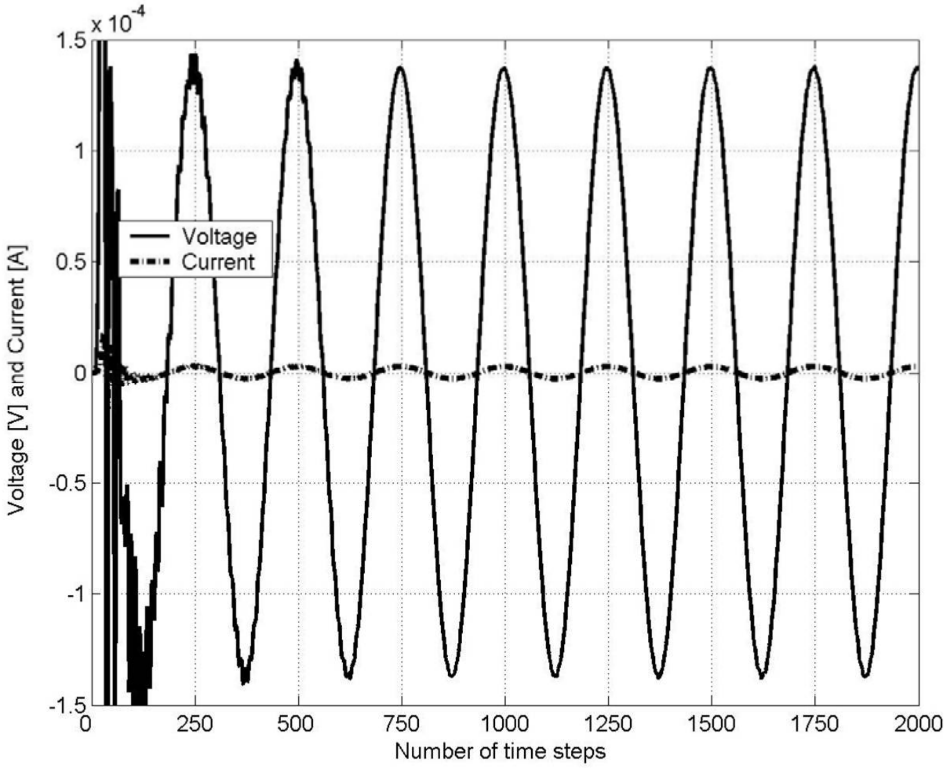

Figure 5.11: Voltage and current on the membrane

5.3.3 Single Cell Simulation

In this section, the HH model was modelled on a spherical structure with diameter 50μm and discretised with 1μm steps, in order to check the polarization voltage of 60.27 mV on the membrane. The HH model is included on the surface of the cell. The inner and external mediums of the cell geometry, have been considered as cytoplasm ($\varepsilon_r = 48.699$, $\sigma = 1.412$ S/m) and lossy medium ($\varepsilon_r = 70.87$, $\sigma = 2.781$ S/m) respectively. It should be noted that the LE-FDTD method has been successfully modified in order to accommodate the case when the position of the lumped element inside the membrane's cell is not aligned with the FDTD grid (see Figure 5.12), so that it can be excited by the electric field component normal to its surface. The rotation was done subject to the fields in spherical co-ordinates and then transferred to the actual grid of the FDTD at each time step. A matrix transformation was implemented on each FDTD cell surface.

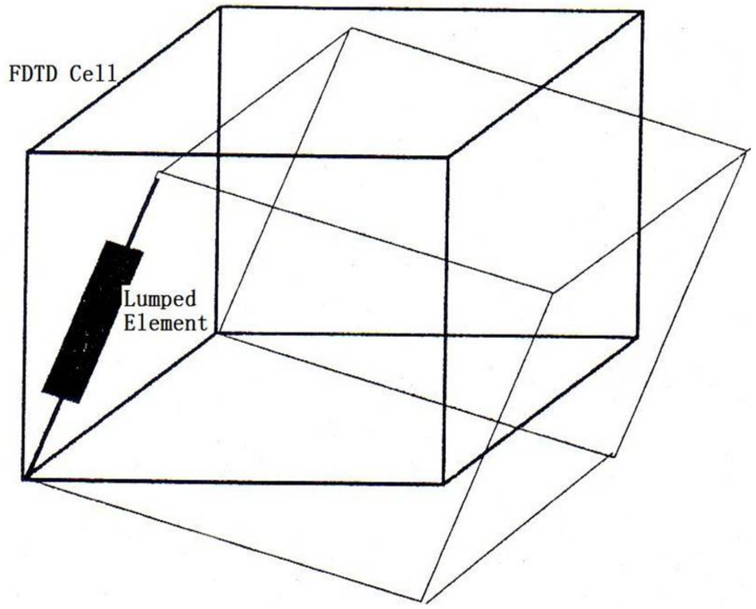

Figure 5.12: Modified LE-FDTD cell on normal FDTD cell grid

Figure 5.13 depicts the polarization voltage value of 60.27mV on the membrane of the spherical structure without any external excitation. From Figure 5.14, it can be observed that the field in the centre of the spherical structure is not zero. This effect can be described to a type of numerical noise which is created by the geometry of the structure. In order to verify whether the noise is random or deterministic, two simple simulations have been carried out. In one, the structure was irradiated with a plane wave of 100kV/m at 100GHz and in the other there was no excitation. It should be noted that the plane wave in the first case is propagating along the z-axis and electric field is parallel to the x-axis. Figure 5.15 shows the numerical noise in the centre of the structure without excitation. Figure 5.16 shows that the dominant component (E_x) is corrupted by the numerical noise along the z-axis of the structure, whereas Figure 5.17 shows that the noise is deterministic and the harmonic excitation can be retrieved. This can be done by subtracting the numerical noise in Figure 5.15 from the excitation field in Figure 5.16.

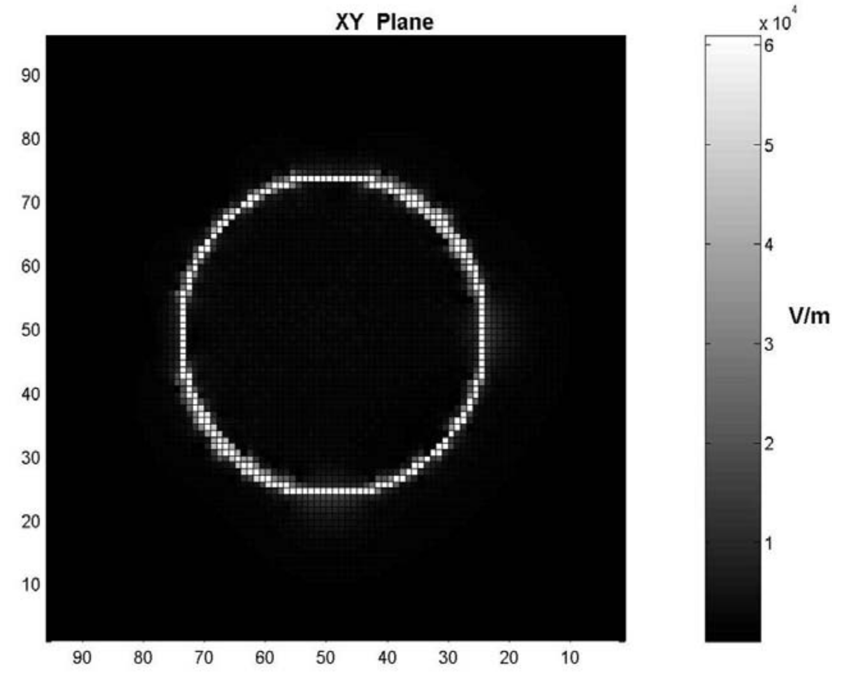

Figure 5.13: Field distribution on coordinate plane

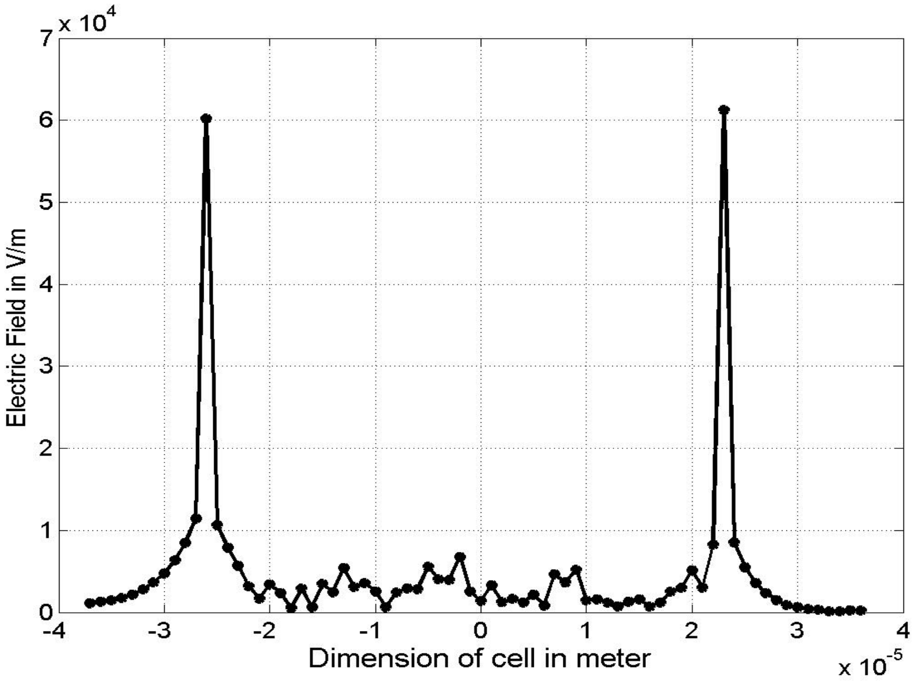

Figure 5.14: Total electric field along central axis of the structure

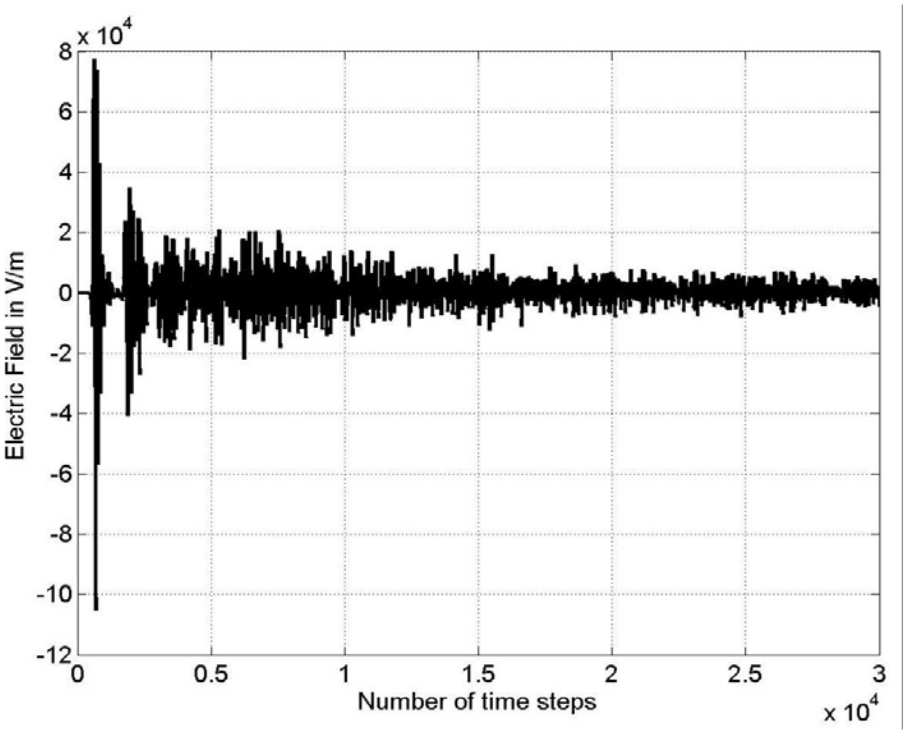

Figure 5.15: The field versus time in the central FDTD cell of the structure in lossy medium without excitation

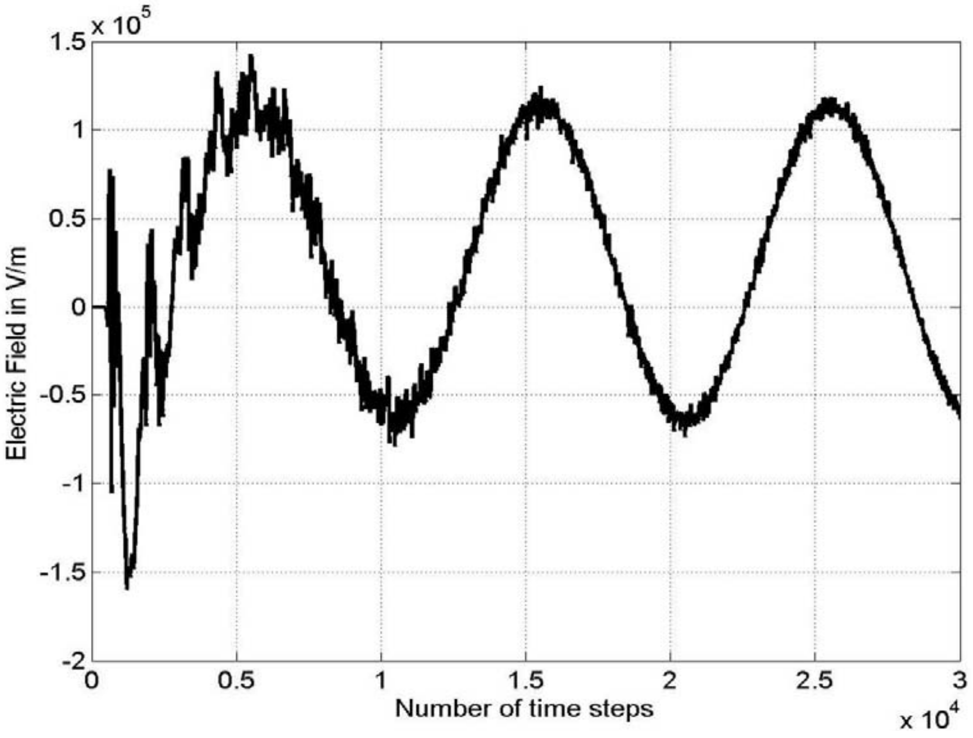

Figure 5.16: The corrupted excitation field in the centre of the FDTD cell of the structure.

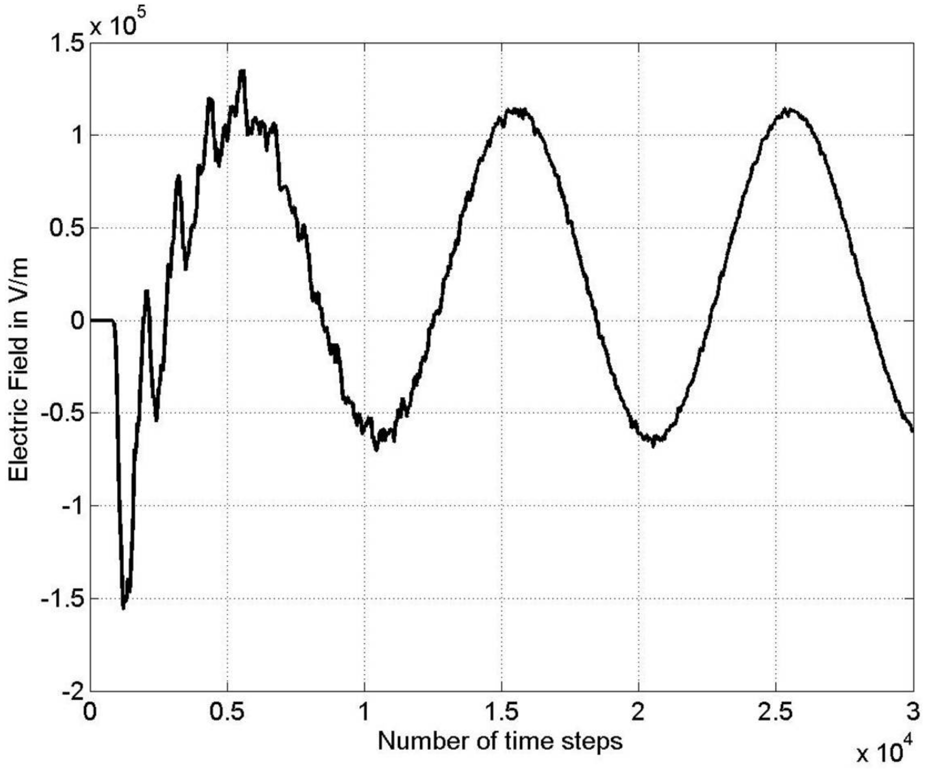

Figure 5.17: Excitation field removed from the numerical noise

5.4 Simulation and Results

By incorporating the aforementioned and validated theories, i.e., Floquet Periodic Boundary Conditions (FPBCs), modified PML, Quasi-Static and Lumped-Element FDTD approach, this section will model biological tissue with different structures that consider a cluster of spherical, cubical and cylindrical cells and examine the electromagnetic field behaviour inside the tissue when it is exposed by a plane wave.

In general, the radius of the each biological cell in a tissue was 10 μm. The biological cell consists of three layers, which are cytoplasm, membrane and extracellular medium and the dielectric properties of these were obtained from [28]. In paper [28], the equations of the effective conductivity $\sigma(\omega)$ and effective dielectric permittivity $\varepsilon(\omega)$ of the material of biological cells are given in the following two forms:

$$\sigma(\omega) = \sigma(0) + \omega \sum_{k=1}^{n} \frac{\Delta\varepsilon_k \omega \tau_k}{1 + \omega^2 \tau_k^2} \tag{5.29}$$

$$\varepsilon(\omega) = \varepsilon(0) - \sum_{k=1}^{n} \frac{\Delta\varepsilon_k \omega^2 \tau_k^2}{1 + \omega^2 \tau_k^2} \tag{5.30}$$

where $\omega = 2\pi f$, f is the frequency of the field, n is the number of steps of dielectric relaxation of the material, $\Delta\varepsilon_k$ and τ_k are the magnitude of the k-th relaxation step and the time constant of the k-th step respectively, while $\sigma(0)$ and $\varepsilon(0)$ are the conductivity and dielectric permittivity of the material and it is measured at $\omega << 1/\tau_1$. It should be noted that all the fixed parameters that govern the equations are well defined in Tables

5.3 and 5.4. Once all the parameters are known, the material of the biological cell, as function of field frequency, can be established easily as shown in Figures 5.18 and 5.19 which are the ones in [28]. From the inspection of Figures 5.18 and 5.19, the electrical properties of cytoplasm, membrane and extracellular medium are found and all the desired parameters of this analysis at various frequency of interest, i.e. 900MHz, 1800MHz, 2000MHz, 2450MHz and 10GHz, are tabulated in Table 5.5 respectively.

TABLE 5.3

THE ELECTRICAL PROPERTIES OF THE BIOLOGICAL CELL MODEL

Parameter	Symbol	Value
Permittivity of Cytoplasm	$\varepsilon_i(0)$	$6.4\times10^{-10}\ As/Vm$
Conductivity of Cytoplasm	$\sigma_i(0)$	$0.3\ S/m$
Permittivity of Membrane	$\varepsilon_m(0)$	$6.4\times10^{-10}\ As/Vm$
Conductivity of Membrane	$\sigma_m(0)$	$3\times10^{-7}\ S/m$
Permittivity of Extracellular Medium	$\varepsilon_e(0)$	$4.4\times10^{-11}\ As/Vm$
Conductivity of Extracellular Medium	$\sigma_e(0)$	$1.2\ S/m$

TABLE 5.4

PARAMETERS OF DIELECTRIC RELAXATION OF CYTOPLASM, MEMBRANE AND EXTRACELLULAR MEDIUM

Parameter	Symbol	Value
Dielectric relaxation of cytoplasm and extracellular medium		
First relaxation time	τ_{re} / τ_{ri}	$6.2 \times 10^{-12}\ s$
First relaxation step	$\Delta\varepsilon_e / \Delta\varepsilon_i$	$5.9 \times 10^{-10}\ As/Vm$
Dielectric relaxation of membrane		
First relaxation time	τ_{rm1}	$3.0 \times 10^{-9}\ s$
First relaxation step	$\Delta\varepsilon_{rm1}$	$2.3 \times 10^{-11}\ As/Vm$
Second relaxation time	τ_{rm2}	$4.6 \times 10^{-10}\ s$
Second relaxation step	$\Delta\varepsilon_{rm2}$	$7.4 \times 10^{-12}\ As/Vm$

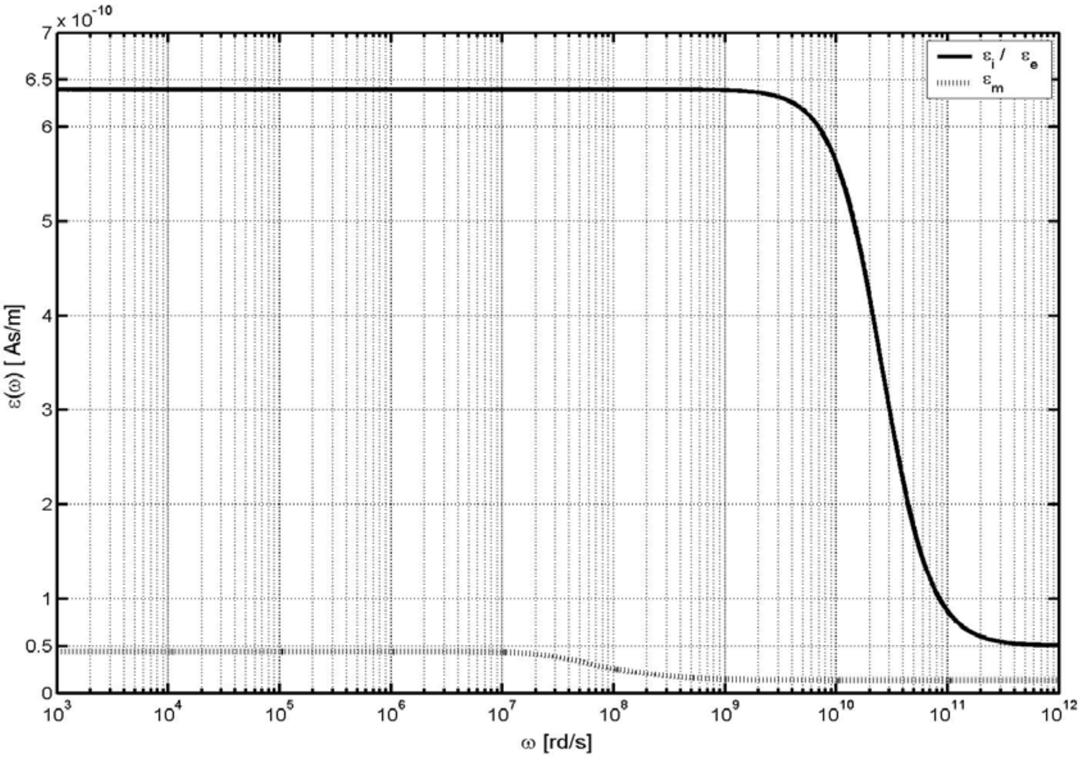

Figure 5.18: Effective permittivity of cytoplasm, membrane and extracellular medium of the biological cells as a function of frequency

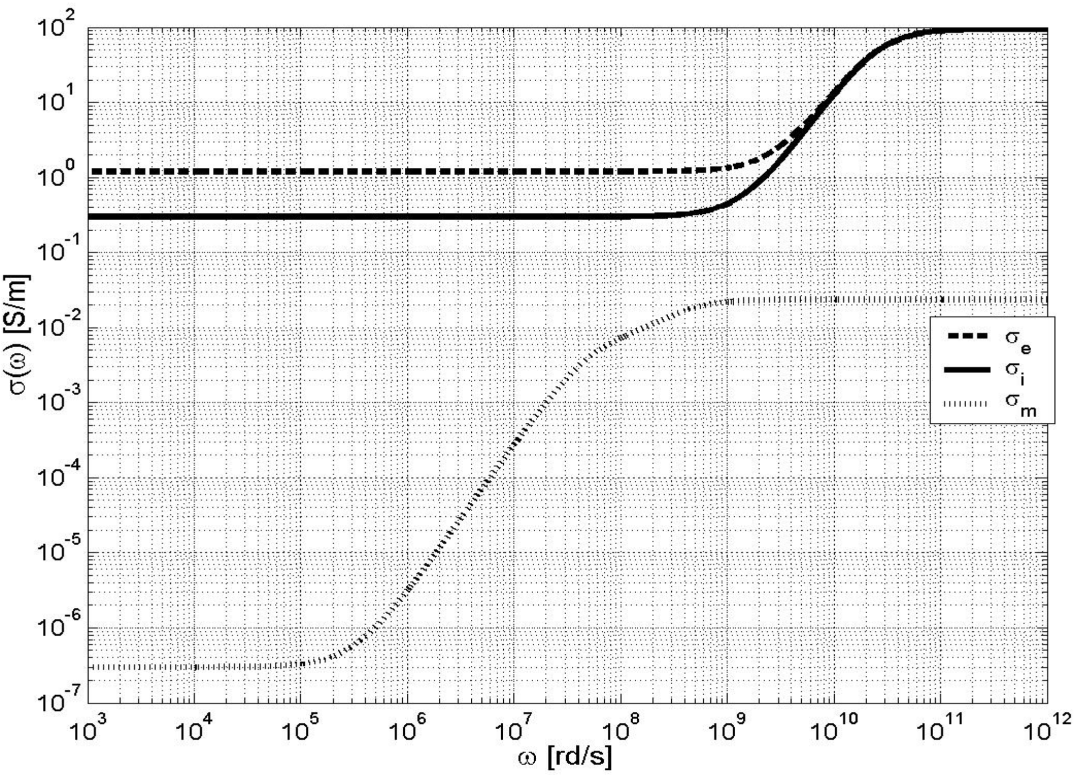

Figure 5.19: Effective conductivities of cytoplasm, membrane and extracellular medium of the biological cells as a function of frequency.

TABLE 5.5

ELECTRICAL PROPERTY OF THE SIMULATED STRUCTURE AT MOBILE COMMUNICATION FREQUENCIES

900 MHz	1800MHz	2000MHz	2450MHz	10GHz
$\varepsilon_i = 72.2003$	$\varepsilon_i = 71.956$	$\varepsilon_i = 71.88$	$\varepsilon_i = 71.6806$	$\varepsilon_i = 63.5023$
$\sigma_i = 0.4168$	$\sigma_i = 0.7656$	$\sigma_i = 0.8742$	$\sigma_i = 1.1590$	$\sigma_i = 12.8384$
$\varepsilon_m = 1.6526$	$\varepsilon_m = 1.5680$	$\varepsilon_m = 1.5621$	$\varepsilon_m = 1.5536$	$\varepsilon_m = 1.5371$
$\sigma_m = 0.0217$	$\sigma_m = 0.0232$	$\sigma_m = 0.0233$	$\sigma_m = 0.0234$	$\sigma_m = 0.0237$
$\varepsilon_e = 72.2003$	$\varepsilon_e = 71.956$	$\varepsilon_e = 71.88$	$\varepsilon_e = 71.6806$	$\varepsilon_e = 63.5023$
$\sigma_e = 1.3168$	$\sigma_e = 1.6656$	$\sigma_e = 1.7742$	$\sigma_e = 2.0590$	$\sigma_e = 13.7384$

5.4.1 Connected Tissue Model Using Spherical cells

A stack of ten spherical cells was investigated, as shown in Figs. 5.20 and 5.21. The radius of the each cell was 10 μm. A plane wave of 100 V/m, propagating in the z-direction and polarized in the x-direction was used as the excitation. Note that the incident plane wave excitation was applied on a plane lying between the PML region and the outer limit of the FDTD grid. In addition, in order to reduce high-frequency transients [32, 33] and DC offsets [34, 35], associated with unramped sine wave excitations, the following ramped sinusoidal source in equation (5.31) was adopted [34]: .

$$f(t) = \begin{cases} 0 & t < 0 \\ 0.5[1 - \cos(\omega_r t)]\sin(\omega_r t) & 0 \le t \le \frac{T_r}{2} \\ \sin(\omega_r t) & t > \frac{T_r}{2} \end{cases} \tag{5.31}$$

Where T_r is the period of the ramped cosine which is about 3 source cycles.

The PML, shown in Figure 5.21, was 6 FDTD elements wide, the grading factor g was 10.1383 and the grid structure was effectively extended to infinity in the x- and y-directions, by imposing the Floquet boundary condition along the x and y axes. The Floquet periodic boundary condition plays an important role to mimic the presence of an extended 3-dimensional structure of biological cells, simulating connected tissue. This can be easily imagined in two dimensions, as shown in Figure 5.20. The FDTD problem space was 220×20×20 FDTD elements of size 1μm while a discretization time step δt of 1.3 femtoseconds was chosen to drive the FDTD computation, to meet the requirements of the Courant stability criterion.

Before implementing the Hodgkin-Huxley model into the simulated structure, the effect of moving the Floquet boundaries gradually away from the simulated structure was studied. Figures 5.22 and 5.23 depict the field distribution through the centre of the simulated structure at 10GHz with varying locations of the Floquet boundaries, where Ncell is the number of FDTD elements between the Floquet boundaries and the boundaries of the biological cells, in the x and y directions. Figure 5.24 shows the field distribution on the xz-plane of the simulated structure for the case of Ncell = 10. When the Floquet boundaries are exactly adjacent to the simulated structure (Ncell = 0), the strongest coupling effect between cells can be obtained: the highest induced field on the membrane and lowest induced field in the cytoplasm of the cell can be observed. Conversely, when the Floquet boundaries are far away from the simulated structure (Ncell = 10), the lowest induced field on the membrane and highest induced field in the cytoplasm of the cell are observed. It should be noted that all the following analysis will be based on Ncell = 0, which is assumed to be the most appropriate model for the real living biological tissues or cells in this micro-dosimetry study.

The simulations were performed at the transformed intermediate frequency of 10GHz and the overall model was then transformed to the intended lower frequencies. Table 5.6 reports the transformation factors at 900MHz, 1800MHz, 2000MHz and 2450MHz used in the analysis.

Figure 5.25 illustrates the 10GHz field distribution on the xz-plane of the simulated structure. The distributions of the electric field through the centre of the simulated structure, along the incident wave propagation direction, at 900MHz, 1800MHz, 2000MHz and 2450MHz are given in Figures 5.26 and 5.27, where Figure 5.27 is an enlarged version of Figure 5.26. The magnified version of Figure 5.27 is also plotted in Figure 5.28 and 5.29 as well. From inspection of Figures 5.27, 5.28 and 5.29, the field inside the cells is not constant and the induced field intensity is directly proportional to the frequency. In the other words, the higher the operating frequency that is used to excite the model, the higher the electric field intensity that will be induced within the analyzed structures.

To complete the simulation, the Hodgkin-Huxley models were embedded in the surface of the spherical cells, in a direction normal to the surface, to represent the membrane effect of the tissue model. Versions including this were studied at frequencies of 900MHz and 2450MHz. As can be seen in Figures 5.30 and 5.31, there is a difference of approximately 15% in the field strength due to the contribution of the membrane effect from the Hodgkin-Huxley model: these variations were in well agreement with expectations [6, 13, 28].

5.4.2 Connected Tissue Model Using Cubical cells

Since living cells, when compacted into connected tissue, are not perfectly spheres, a cluster of cubical cells was also chosen for study on the foundation of the previous spherical-cells analysis. Figure 5.32 depicts the proposed cluster of cubical cells in a three dimensional view of the FDTD computational domain. In order to compare the results obtained from the previous model with this analysis, an FDTD simulation was executed, keeping the same parameter values unchanged. The 2D view of the electric field inside the cubical-cell tissue is shown in Figure 5.33. The field distributions along the propagation direction of the incident wave, through the centre of the simulated structure at various frequencies, are illustrated in Figures 5.34 and 5.35, while the magnified version of Figure 5.35 are depicted in Figures 5.36 and 5.37.

The contribution of the Hodgkin-Huxley model to the cubical tissue model has also been investigated, as shown in Figures 5.38 and 5.39. The effects of adding the Hodgkin-Huxley model are about 15% difference in field magnitude, as can be easily observed in the figures.

The peak field values on the membrane of the cubical structure are observed to be about three times higher than in the cytoplasm, which agrees well with the results from the structure based on spherical cells. However, the absolute field strength is approximately doubled in the spherical-cell case, presumably because of the curvature at the points studied: it is to be expected that much higher fields would be observed at the corners of the cubical cells, but it might be argued that, as a localised matter, these points do not correspond well with biological reality.

5.4.3 Connected Tissue Model Using Cylindrical cells

The shape of the living cells can be so diverse. In order to have better understanding on the subject of EM field interaction with different geometry of biological tissue, a cluster of cylindrical cells model of the tissue is proposed, as depicted in Figure 5.40. This analysis is performed in which the material properties unchanged as in the case of spherical and cubical cell structures. Figure 5.41 describes the 2D view of electric filed distribution of the proposed cylindrical-cell tissue at 10GHz, while the electric field distribution along the centre of the analysed structure is shown in Figure 5.42 to 5.45, where the Figures 5.43-5.45 are the amplified version of the Figure 5.42.

The loading effect of the HH model into the cylindrical-cell tissue has also been studied. Figure 5.46 and 5.47 demonstrate the difference of 15% in field magnitude with and without the presence of HH model in the proposed simulated structure. The results show consistent difference with the previous spherical- and cubical-cells tissue simulated structures.

The comparison of the field distribution of spherical-, cubical- and cylindrical- cells tissue model, through the centre of the analysed structure, is elucidated in Figure 5.48. The peak field on the membrane of the cylindrical structure is found to be about 1.7 times higher than in the cytoplasm, which is distinct with the previous two models. As can be noticed, the peak field value of this cylindrical model is higher than the cubical model and lower than the spherical model, whereas the peak field value on the cytoplasm is the about the same as in the spherical model and double the value found in the cubical structure.

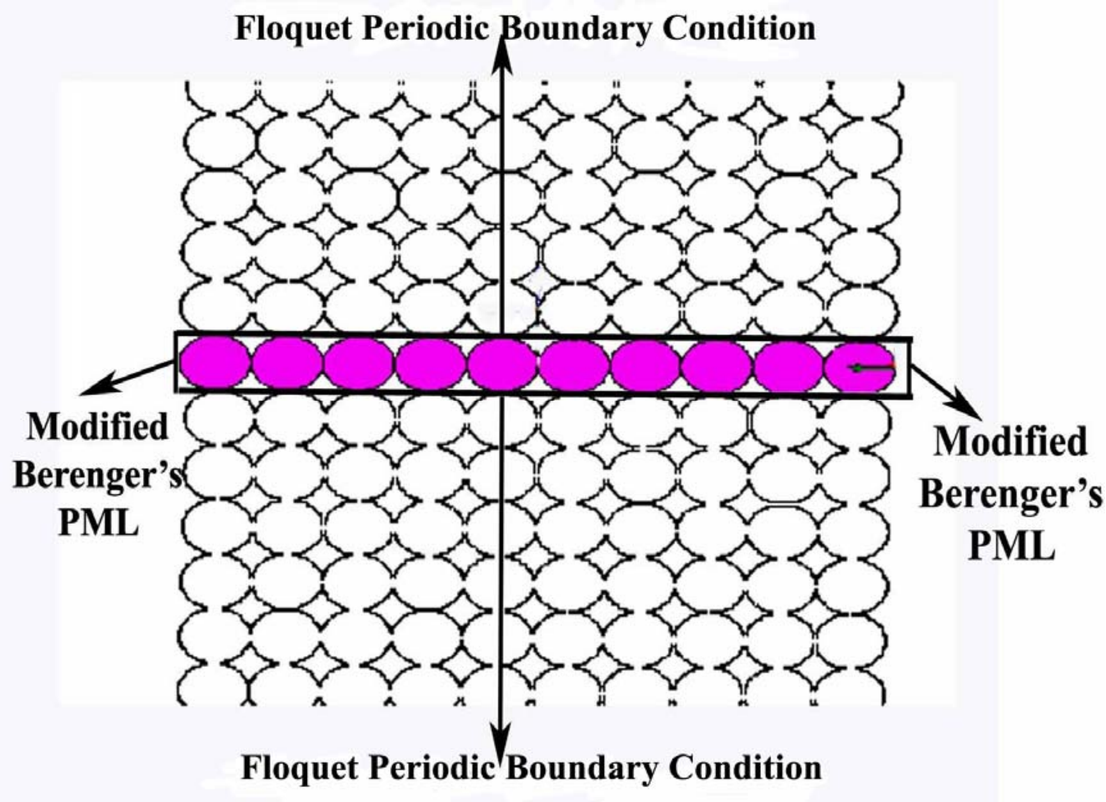

Figure 5.20: The two-dimensional view of the simulated structures in FDTD computational domain

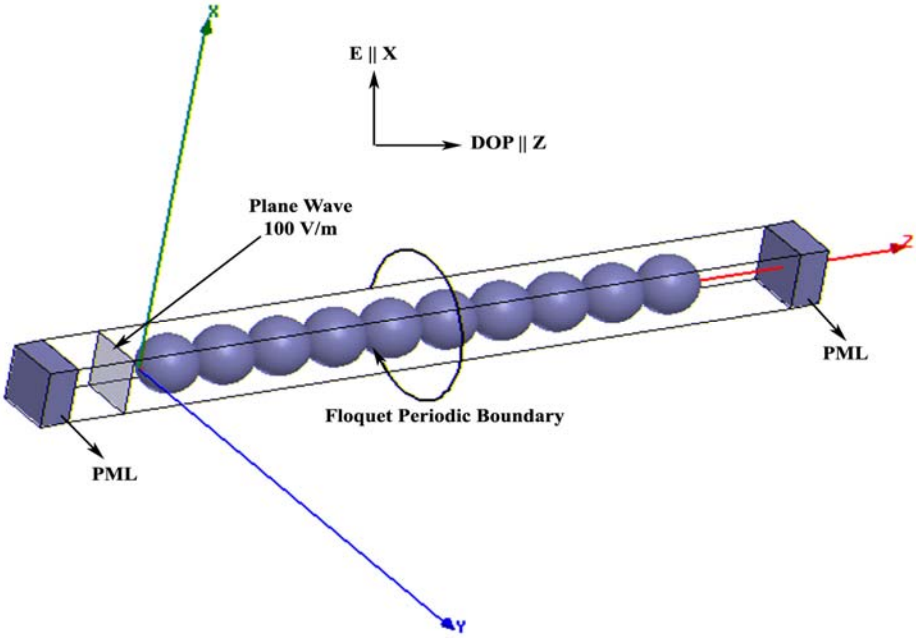

Figure 5.21: The three-dimensional view of the simulated spherical structures in FDTD computational domain.

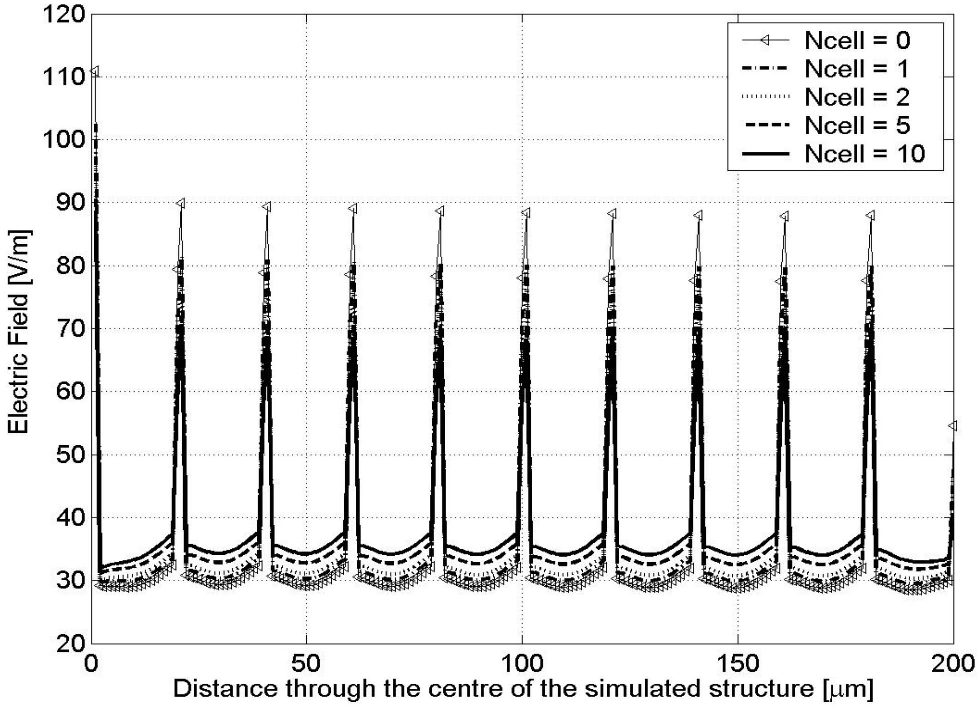

Figure 5.22: Penetration of Electric Field along z axis, through the centre of the simulated structure with different location of the floquet boundary condition.

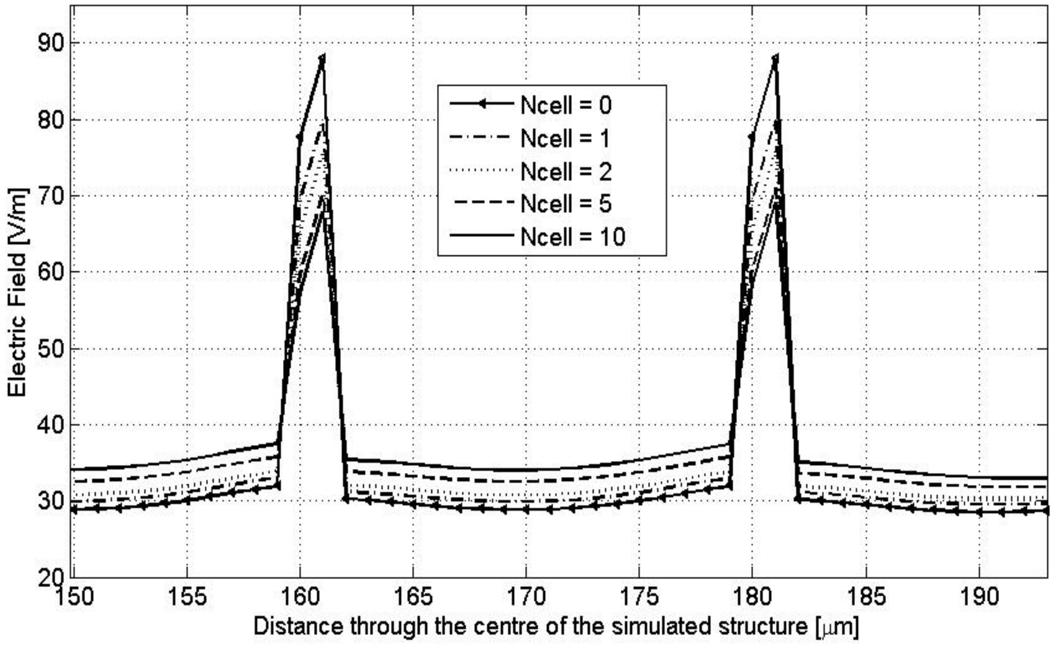

Figure 5.23: Penetration of Electric Field (Enlargement of Figure 5.22)

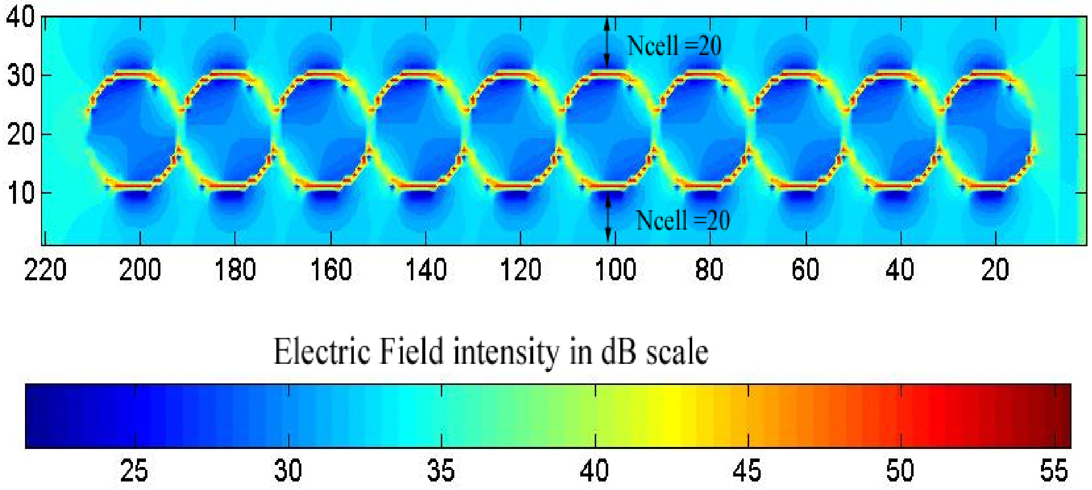

Figure 5.24: Ncell = 20, modulus of the electric field on xz-plane at intermediate frequency 10GHz (logarithmic scale).

TABLE 5.6

FREQUENCY SCALING TRANSFORMATION FACTOR FROM 10GHz TO FOLLOWING MOBILE COMMUNICATION FREQUENCIES

Parameter	900MHz	1800MHz	2000MHz	2450MHz
Cytoplasm	0.9296	0.9337	0.9344	0.9360
Membrane	0.9	0.97	0.9756	0.9838
Extracellular	0.8867	0.9226	0.9254	0.9301

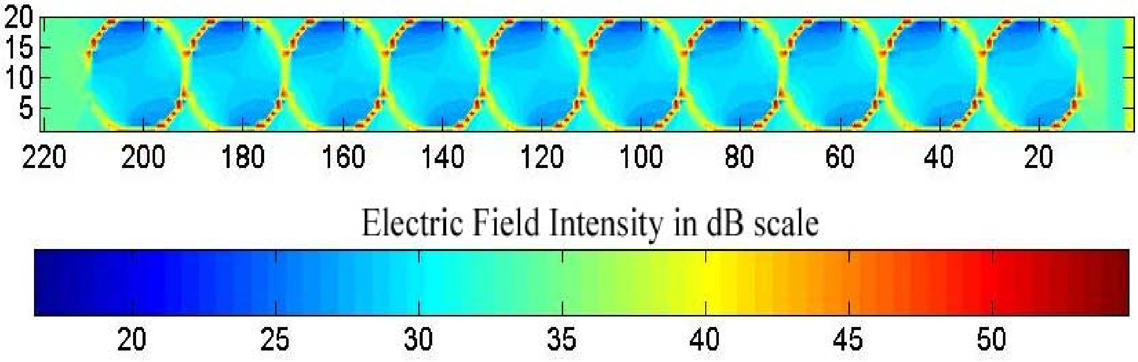

Figure 5.25: Modulus of the electric field on xz-plane at intermediate frequency 10GHz (logarithmic scale)

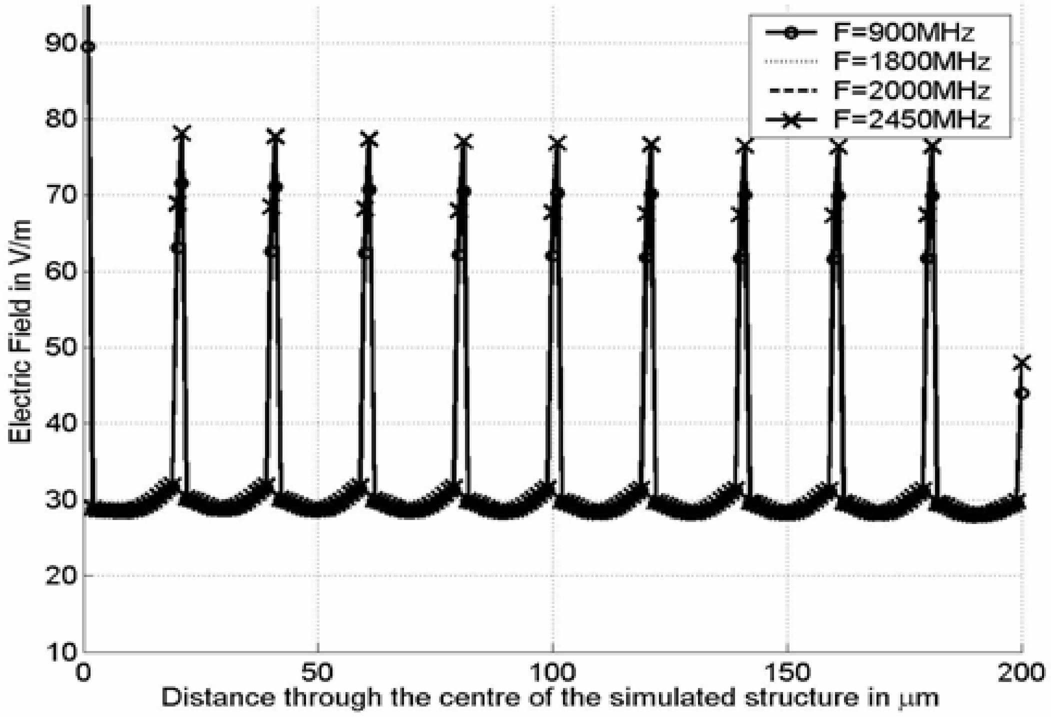

Figure 5.26: Penetration of Electric Field along z axis, through the centre of the simulated structure

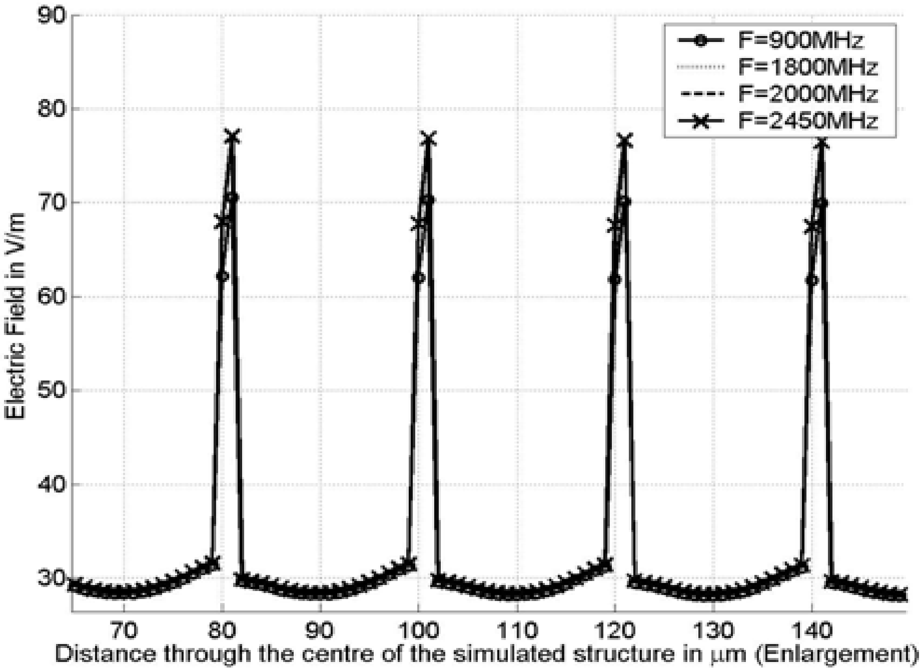

Figure 5.27: Penetration of electric field (Enlargement of Figure5.26)

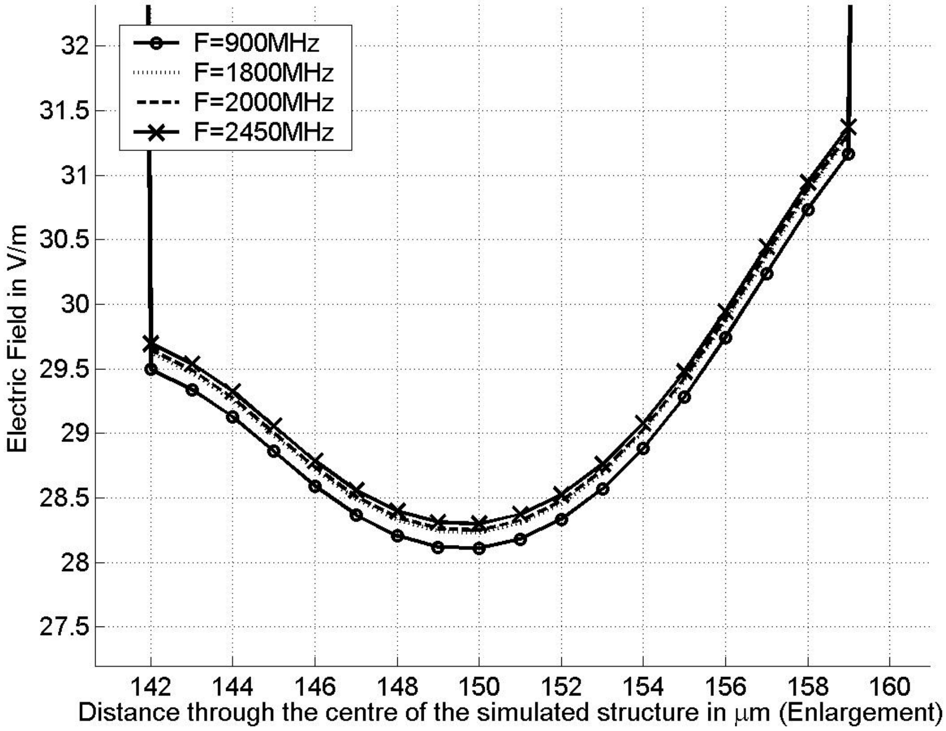

Figure 5.28: Penetration of electric field on the cytoplasm (Enlargement of Figure 5.27)

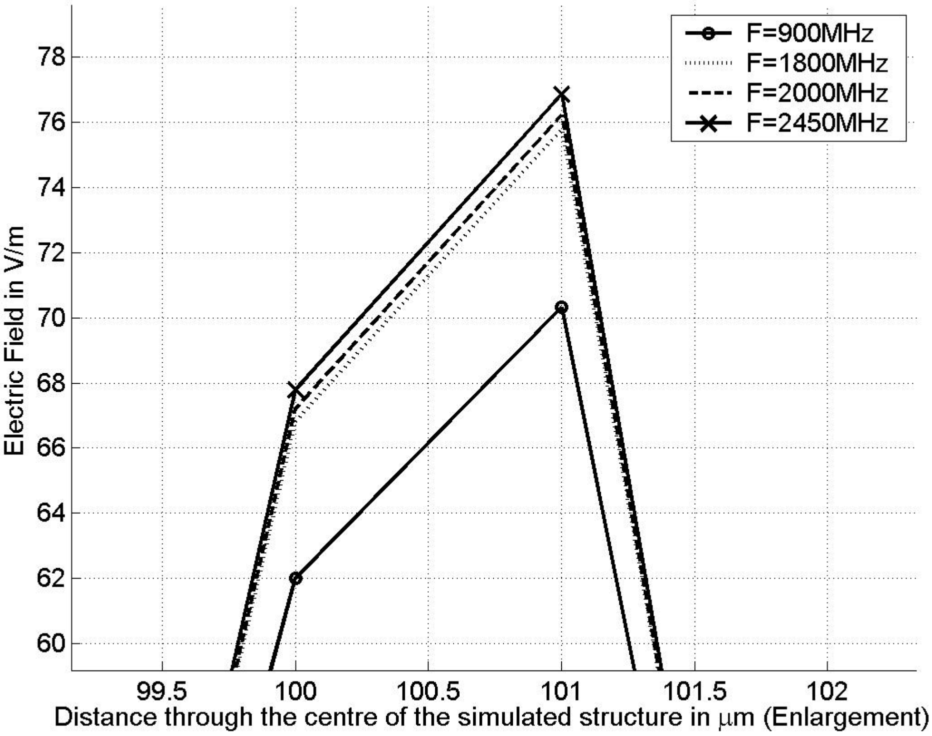

Figure 5.29: Penetration of electric field on the membrane (Enlargement of Figure.5.27)

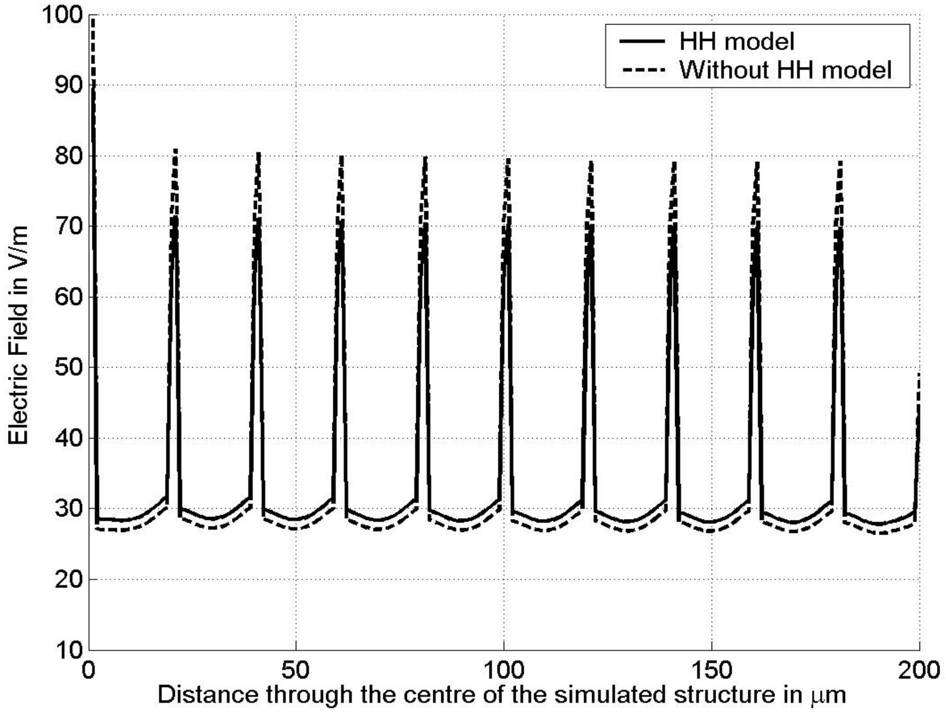

Figure 5.30: Electric field distribution along z-axis, through the centre of the simulated spherical structure in Figure 5.21, incorporating Hodgkin-Huxley model and driven at 900MHz.

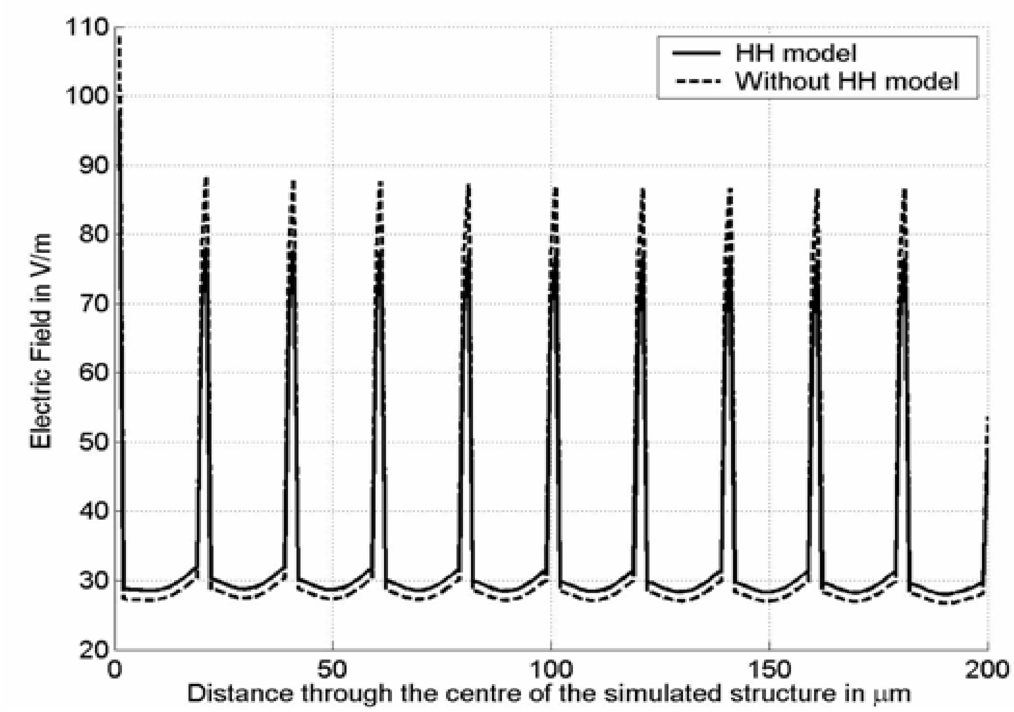

Figure 5.31: As Figure 5.30, driven at 2450MHz.

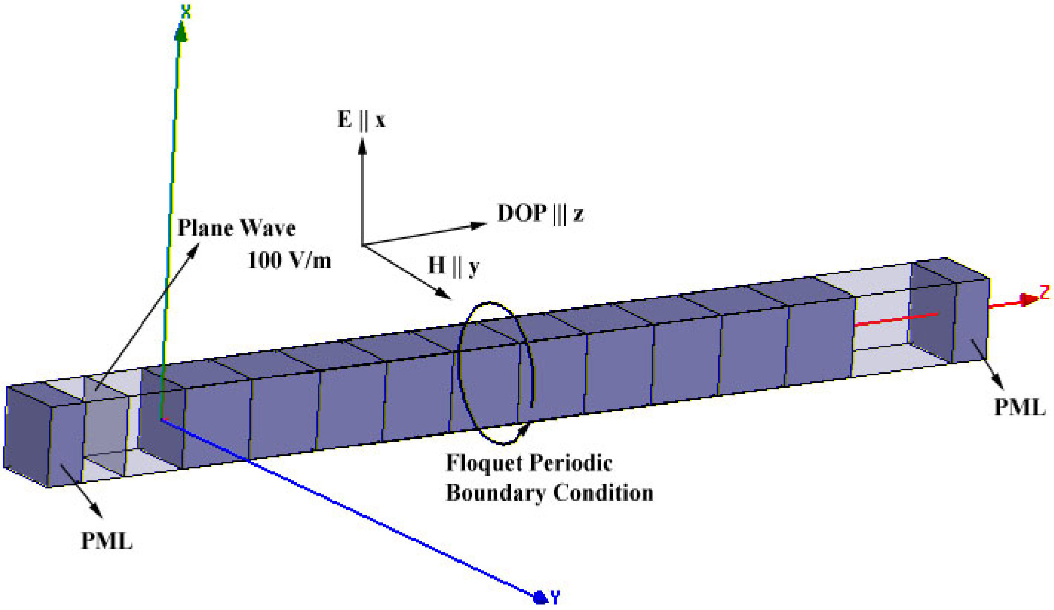

Figure 5.32: The three-dimensional view of the simulated cubical structures in FDTD computational domain.

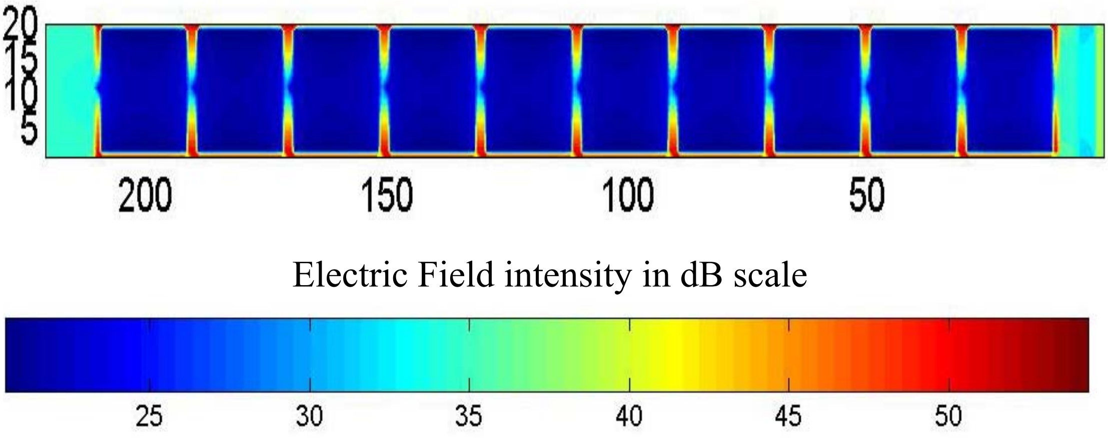

Figure 5.33: Modulus of the electric field on xz-plane at intermediate frequency 10GHz (logarithmic scale)

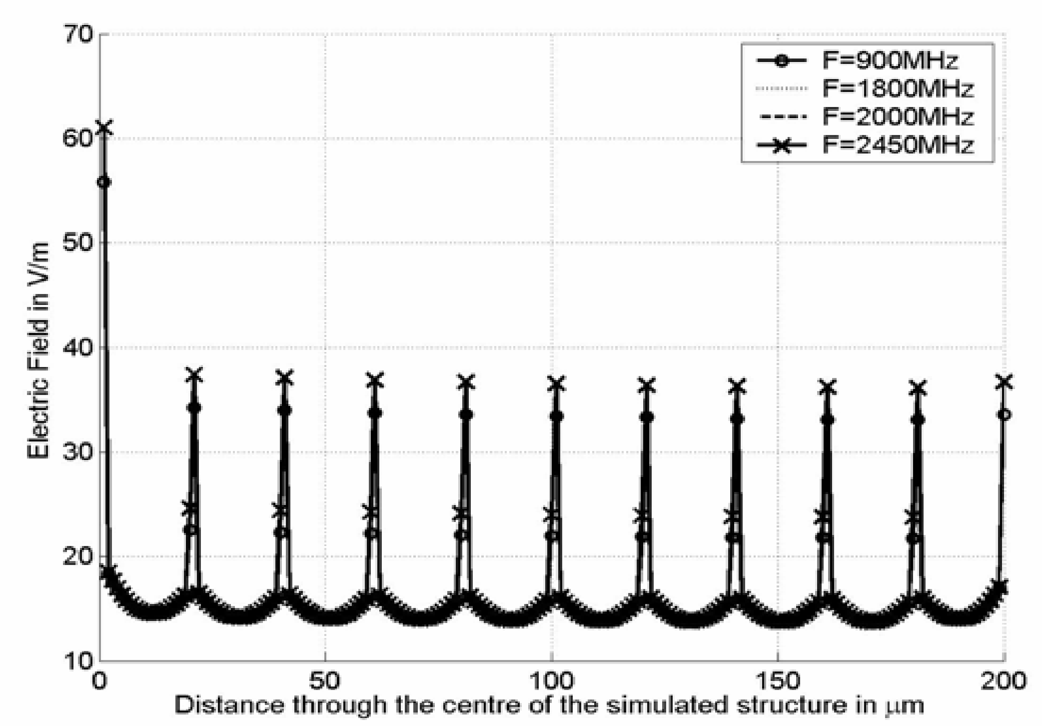

Figure 5.34: Penetration of Electric Field along z axis, through the centre of the simulated structure

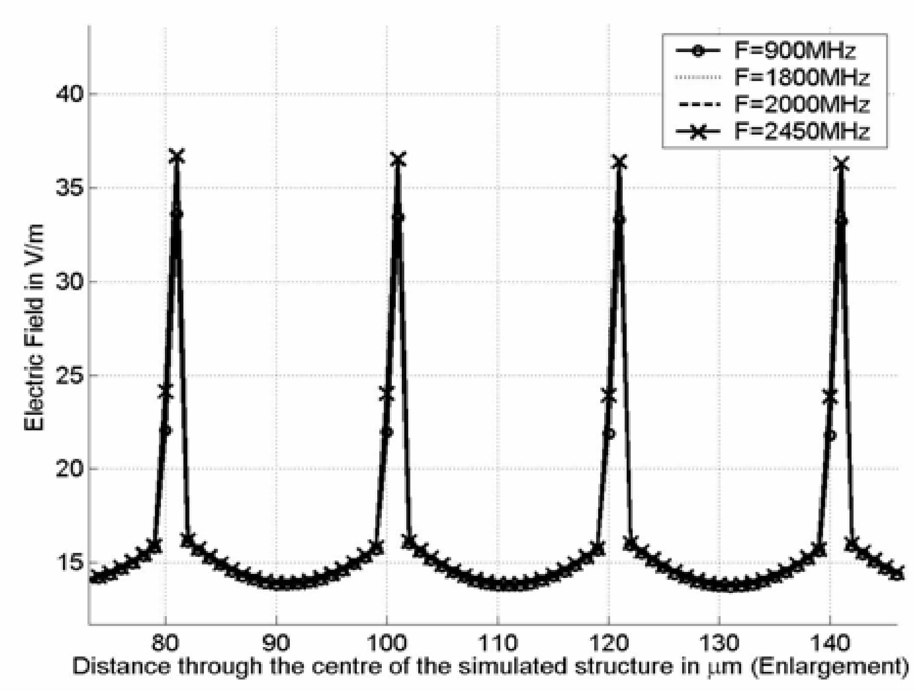

Figure 5.35: Penetration of Electric Field (Enlargement of Figure 5.34)

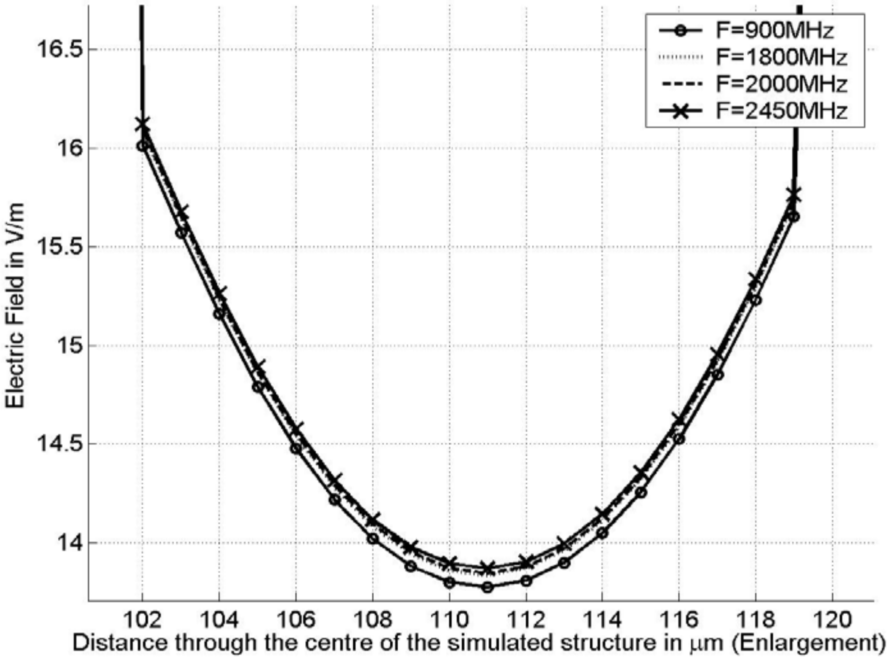

Figure 5.36: Penetration of electric field on the cytoplasm (Enlargement of Figure 5.35)

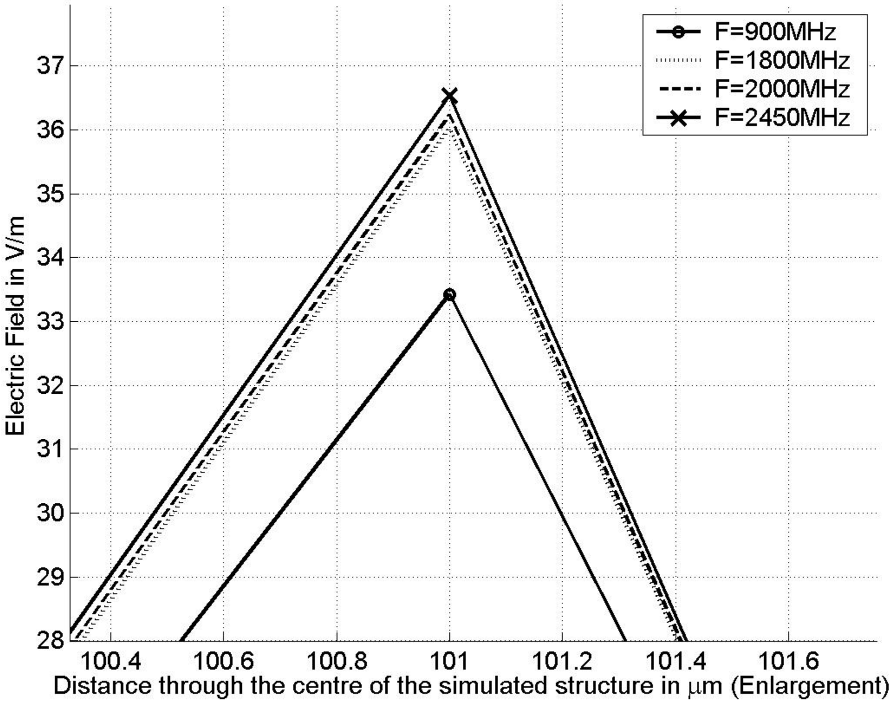

Figure 5.37: Penetration of electric field on the membrane(Enlargement of Figure 5.35).

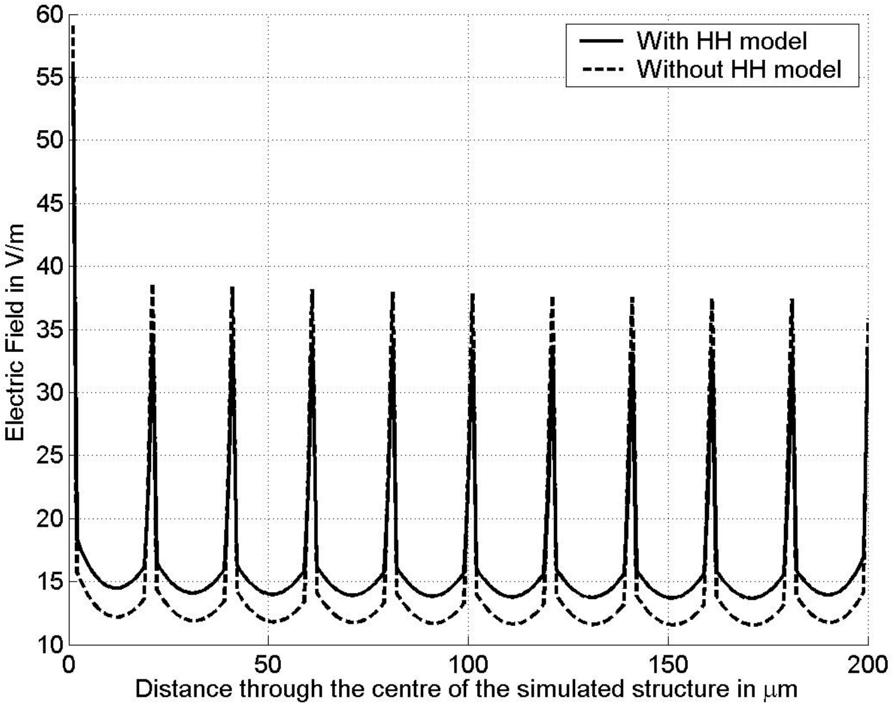

Figure 5.38: Electric field distribution along z-axis, through the centre of the simulated cubical-cell structure in Figure 5.32, incorporating Hodgkin-Huxley model and driven at 900MHz.

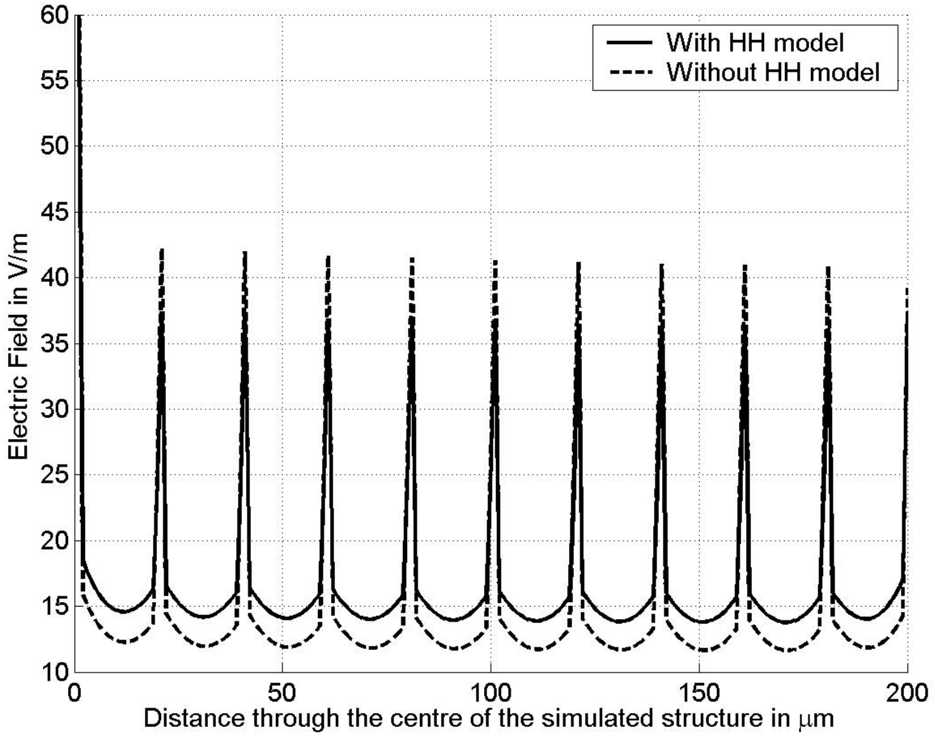

Figure 5.39: As Figure 5.38, driven at 2450MHz.

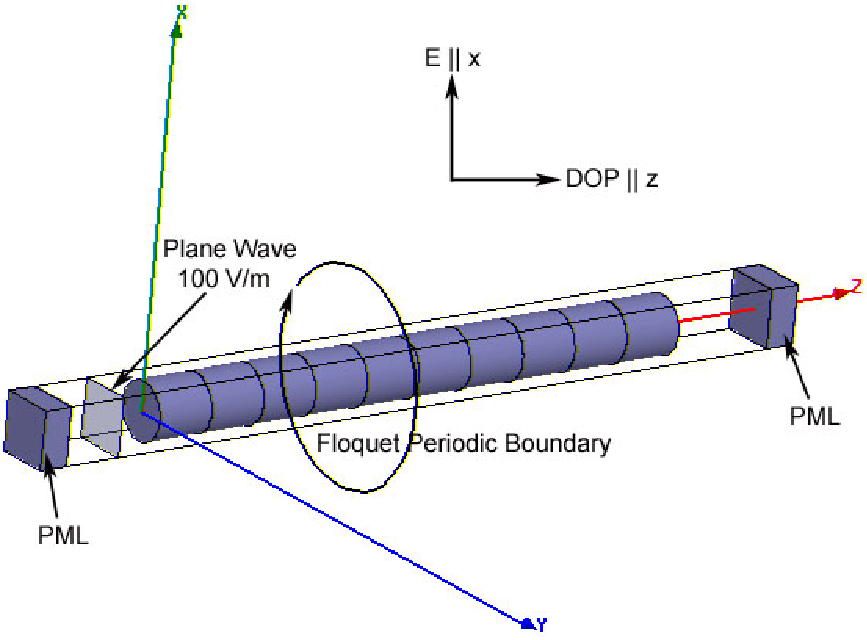

Figure 5.40: The three-dimensional view of the simulated cylindrical structures in FDTD computational domain.

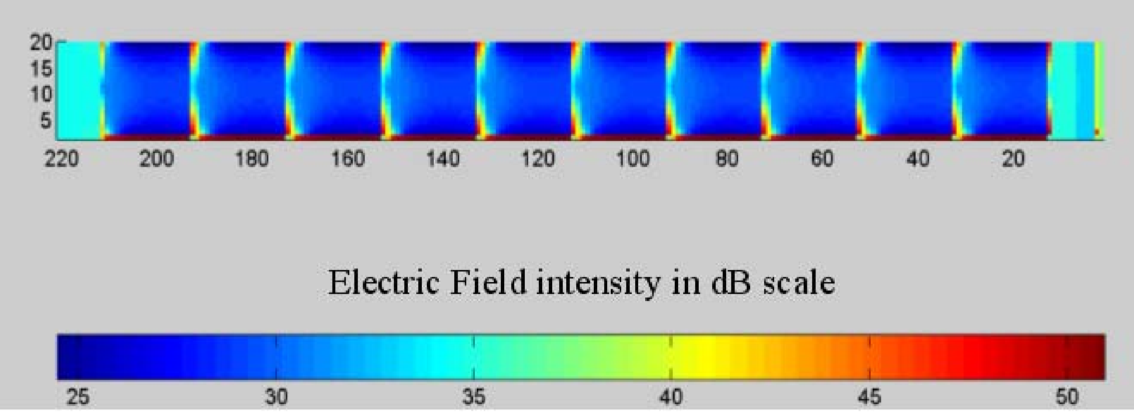

Figure 5.41: Modulus of the electric field on xz-plane at intermediate frequency 10GHz (logarithmic scale)

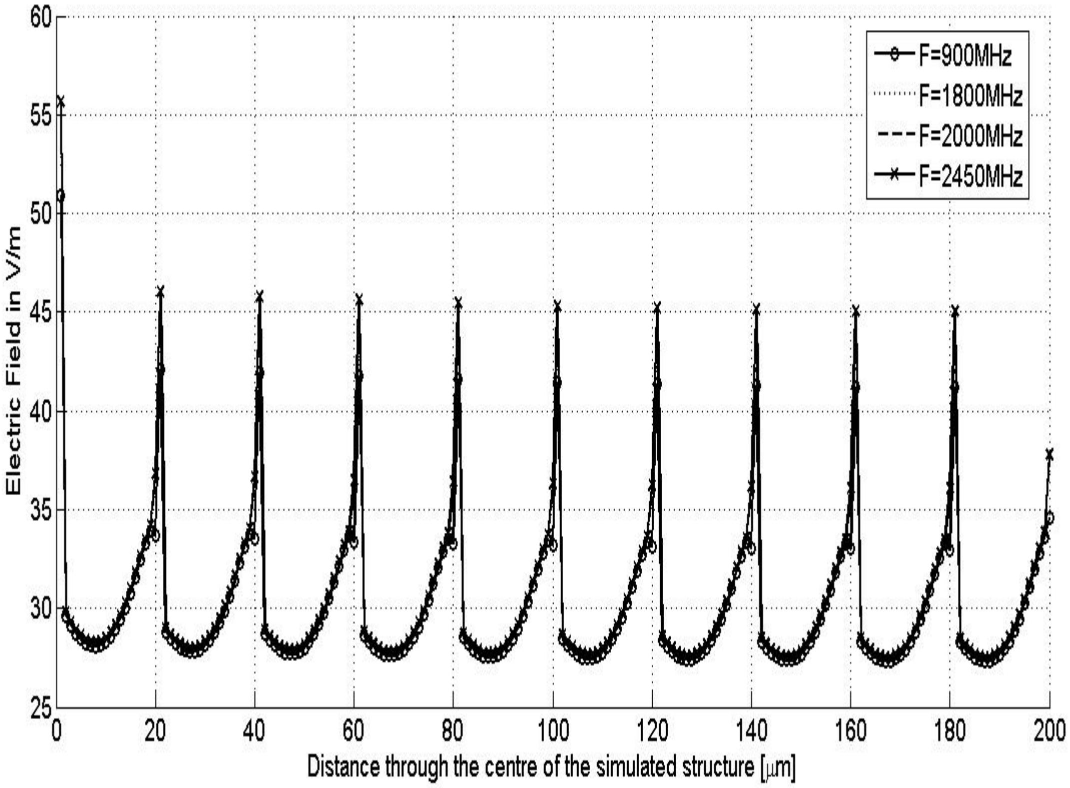

Figure 5.42: Penetration of Electric Field along z axis, through the centre of the simulated structure

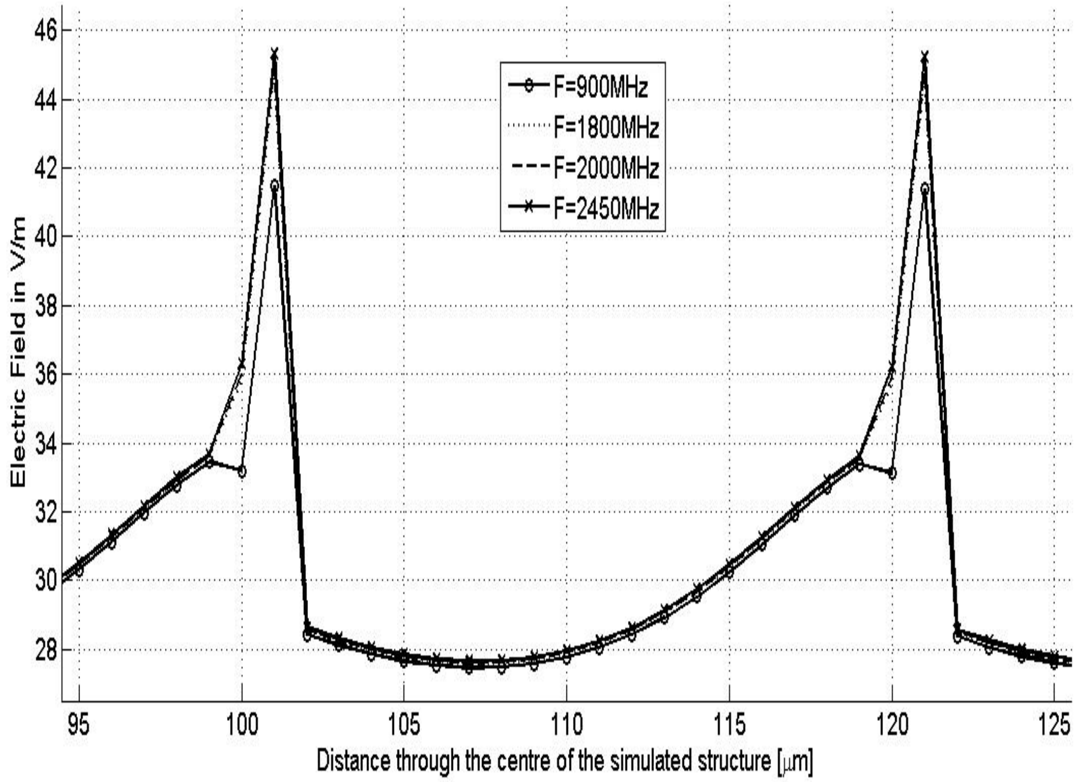

Figure 5.43: Penetration of electric field (Enlargement of Figure 5.42)

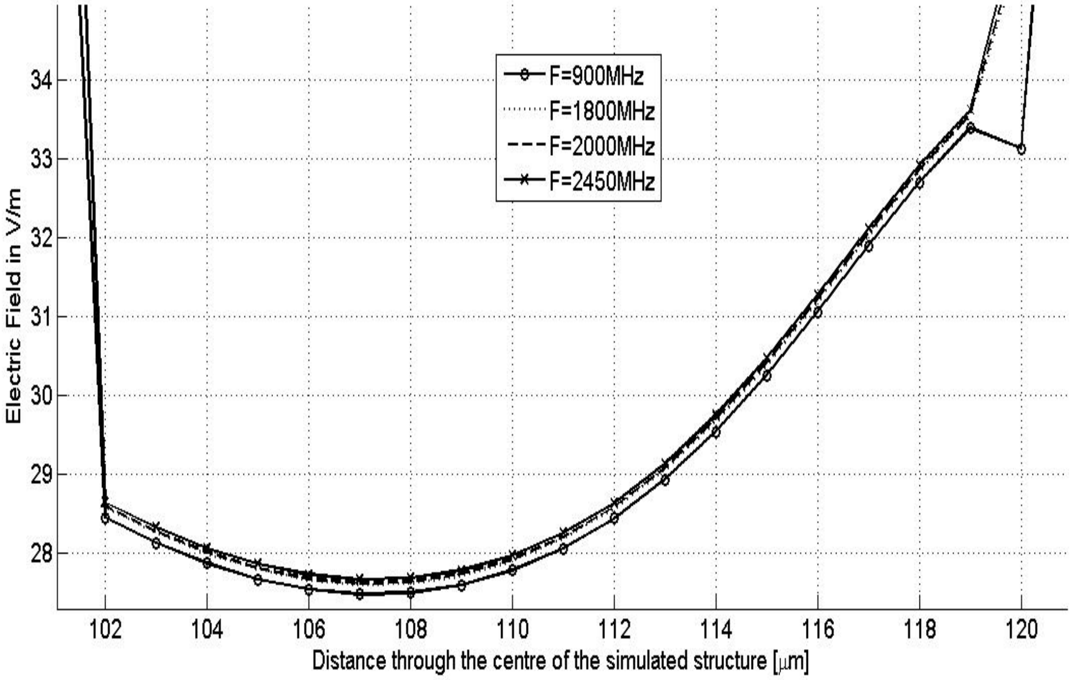

Figure 5.44: Penetration of electric field on the cytoplasm (Enlargement of Figure 5.43)

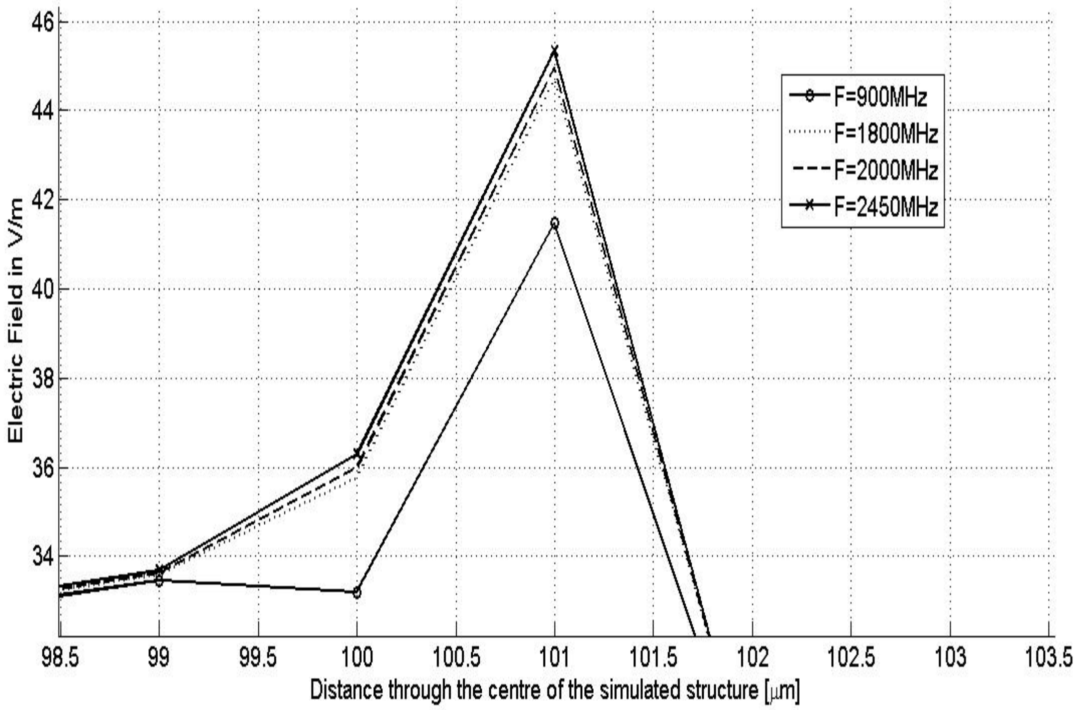

Figure 5.45: Penetration of electric field on the membrane (Enlargement of Figure 5.43)

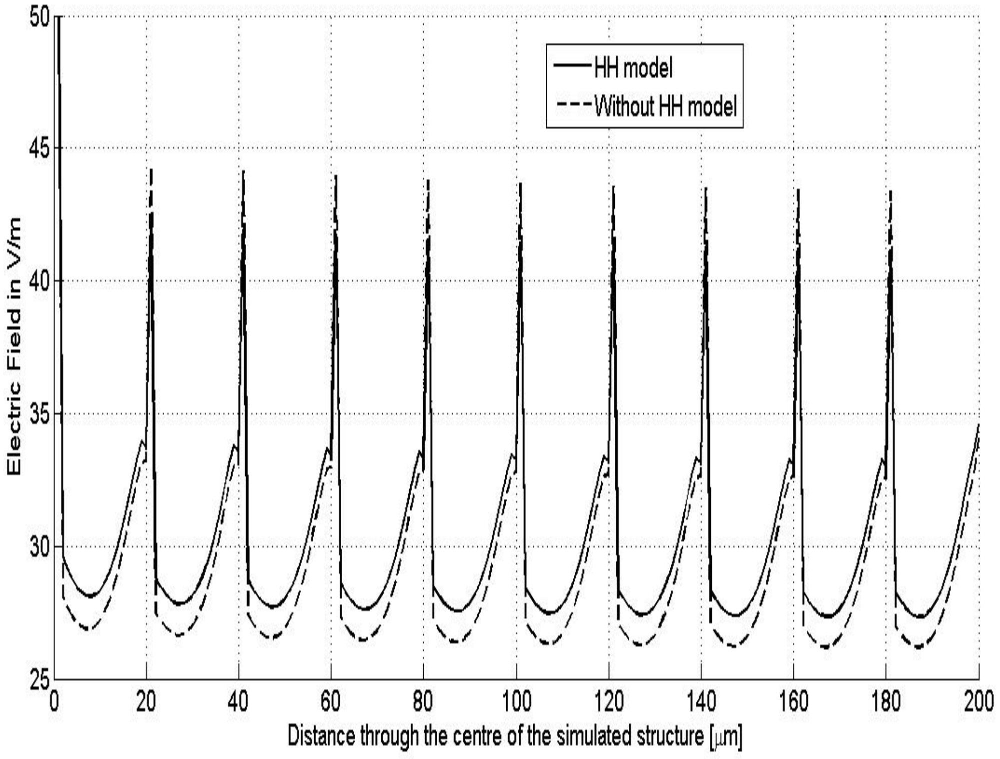

Figure 5.46: Electric field distribution along z-axis, through the centre of the simulated cubical-cell structure in Figure 5.40, incorporating Hodgkin-Huxley model and driven at 900MHz.

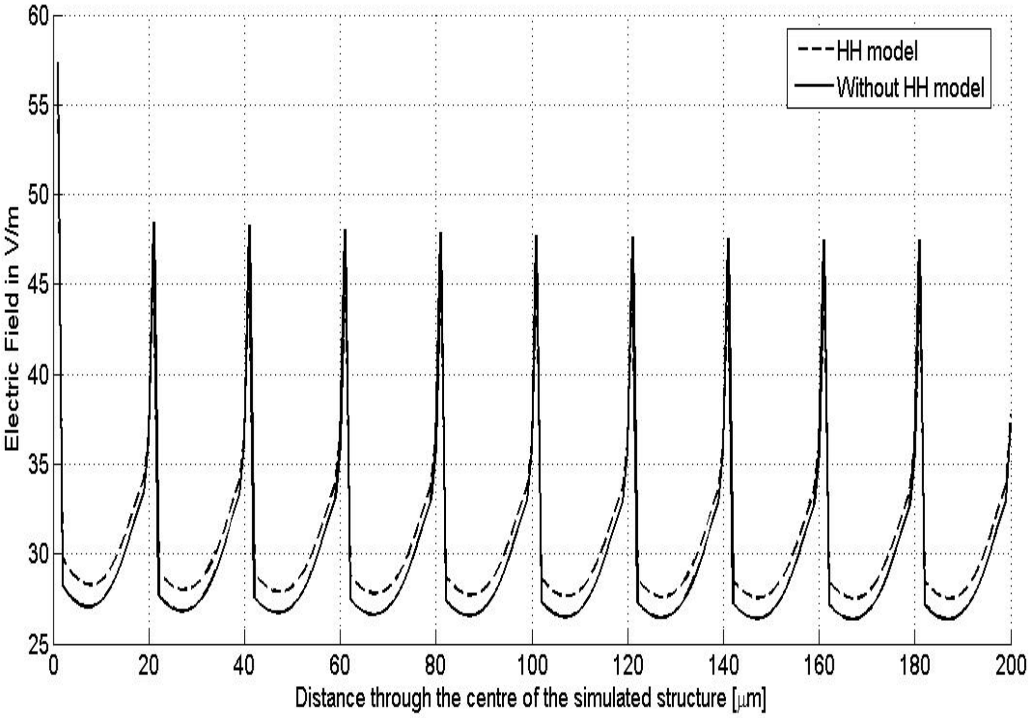

Figure 5.47: As Figure 5.46, driven at 2450MHz

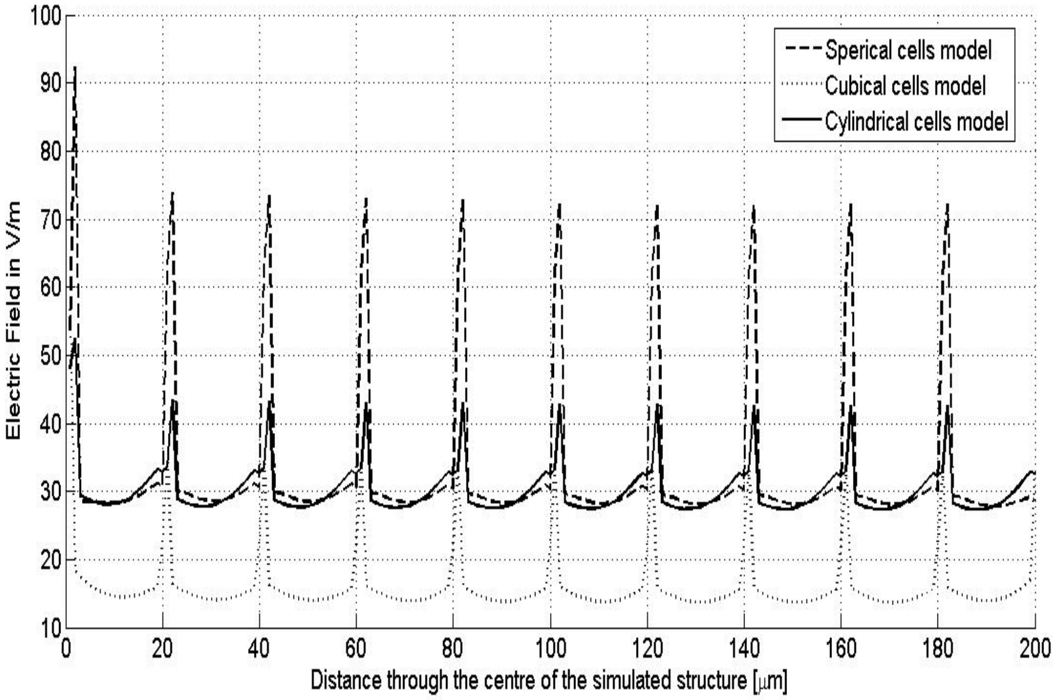

Figure 5.48: Comparison of three different simulated structures at 900MHz

5.4 Conclusions

An approach to microdosimetric modeling of bioelectromagnetic interactions at the cellular level has been presented. This uses the FDTD method, combined with an arbitrarily-oriented implementation of the Hodgkin-Huxley cell-membrane model and the Floquet periodic boundary condition. By implementing a frequency-scaling approach, the number of FDTD time steps for such an electrically-small structure can be reduced from several millions to a few tens of thousands. The reflection on the interface layers inside the FDTD computation domain has also been successfully reduced, even though it is within lossy penetrable media, by using a modified version of Berenger's absorbing boundary condition. The accuracy of the FDTD scaling approach was verified with idealized models of spherical cells in lossy media. The feasibility of the inclusion of the HH model inside the FDTD computation domain was demonstrated. This leads to the conclusion that the application of the HH model allows cells of arbitrary geometries to be handled and demonstrates the viability of embedding other types of lumped-element model for membrane behavior. It can be argued that the HH model is imperfect for microwave frequencies, but it is reasonable to use it as a working hypothesis (as have others [6]) to develop modeling techniques while operational versions of improved models are still in development.

Use of the Floquet boundary condition enables a non-trivial region of connected biological tissue to be simulated. Such a tool will facilitate deeper investigation of the phenomena in the interaction between EM fields and biological systems at various levels of spatial definition. The combination of quasi-static FDTD with an arbitrarily-oriented lumped element membrane model, the modified Berenger absorbing boundary condition and the Floquet periodic boundary condition represents a significant advance in verisimilitude of biological cell modeling.

5.5 References

[1] K.S.Yee, "Numerical solution of initial boundary value problems involving Maxwell's equation in isotropic media," *IEEE Trans. on Antennas Propagation*, vol. AP-14, pp. 302-307, 1966.

[2] A.Taflove and S.C.Hagness, *Computational Electrodynamics: The Finite-Difference Time-Domain*, 2nd ed: Artech House:Boston, 2000.

[3] O.P.Gandhi and J.Chen, "Numerical dosimetry at power-line frequencies using anatomically based models," *Bioelectromagnetics*, vol. 1, pp. 43-60, 1992.

[4] O.P.Gandhi, "FDTD in Bioelectromagnetics: Safety Assessment and Medical Applications," in *Advances in Computational Electrodynamics: The Finite-Difference Time-Domain Method*, A.Taflove, Ed., 1st ed: Artech House, 1998, pp. 627-632.

[5] M.E.Potter, M.Okoniewski, and M.A.Stuchly, "Low Frequency Finite Difference Time Domain (FDTD) for Modelling of Induced Fields in Humans Close to Line Sources," *Journal of computational physics*, vol. 162, pp. 82-103, 2000.

[6] G.Emili, A.Schiavoni, F.L.Roselli, and R.Sorrentino, "Computation of electromagnetic field inside a tissue at mobile communications frequencies," *IEEE Trans on MTT*, vol. 51, pp. 178-186, 2003.

[7] L.M.Liu and S.F.Cleary, "Absorbed Energy distribution from radio frequency electromagnetic radiation in a mammalian cell model: Effect of membrane-Bound

water," *Bioelectromagnetics*, vol. 16, pp. 160-171, 1995.

[8] W.Sui, D.A.Christensen, and C.H.Durne, "Extending the two-dimensional FDTD method to hybrid electromagnetic systems with active and passive lumped elements," *IEEE Trans. MTT*, vol. MTT-40, pp. 724-730, 1992.

[9] M.Piket-May, A.Taflove, and J.Baron, "FDTD modeling of Digital Signal Propagation in 3D circuits with Passive and Active Loads," *IEEE Trans. MTT*, vol. MTT-42, pp. 1514-1523, 1994.

[10] P.Ciampolini, P.Mezzanotte, L.Roselli, D.Sereni, P.Torti, and R.Sorrentino, "Simulation of HF circuits with FDTD technique including nonideal lumped elements," *in IEEE MTT-S Int.Microwave Symp. Dig. Orlando,FL*, pp. 361-364, 1995.

[11] P.Ciampolini, P.Mezzanotte, L.Roselli, and R.Sorrentino, "Accurate and Efficient Circuit Simulation with Lumped-element FDTD technique," *IEEE Trans on MTT*, vol. 44, pp. 2207-2214, 1996.

[12] C. N. Kuo, B. Houshmand, and T. Itoh, "Full-Wave Analysis of Packaged Microwave Circuits with Active and Nonlinear Devices: An FDTD Approach," *IEEE Transactions on Microwave Theory and Techniques*, vol. 45, pp. 819-826, 1997.

[13] A.L.Hodgkin and A.F.Huxley, "A quantitative description of membrane current and its application to conduction and excitation in nerve," *J.Physiol.*, vol. 117, pp. 500-544, 1952.

[14] A.L.Hodgkin and A.F.Huxley, "Current carried by sodium and potassium ions through the membrane of the giant axon of Loligo," *J.Physiol.*, vol. 116, pp. 449-472, 1952.

[15] A.L.Hodgkin, A.F.Huxley, and B.Katz, "Measurement of current-voltage relations in the membrane of the giant axon of Loligo," *J.Physiol.*, vol. 116, pp. 424-448, 1952.

[16] A.L.Hodgkin and A.F.Huxley, "The components of membrane conductance in the giant axon of Loligo," *J.Physiol.*, vol. 116, pp. 473-496, 1952.

[17] A.L.Hodgkin and A.F.Huxley, "The dual effect of membrane potential on sodium conductance in the giant axon of Loligo," *J.Physiol.*, vol. 116, pp. 497-506, 1952.

[18] W-J.Tsay and D.M.Pozar, "Application of the FDTD Technique to Periodic Problems in Scattering and Radiation," *IEEE Microwave and Guided Wave Letters*, vol. 3, pp. 250-252, 1993.

[19] J.Ren, O.P.Gandhi, L.R.Walker, J.Fraschilla, and C.R.Boerman, "Floquet-Based FDTD Analysis of Two-dimensional Phased Array Antennas," *IEEE Microwave and Guided Wave Letters*, vol. 4, pp. 109-111, 1994.

[20] A.Alexanian, N.J.Kolias, R.C.Compton, and R.A.York, "Three-dimensional FDTD analysis of quasi-optical arrays using Floquet boundary conditions and Berenger's PML," *IEEE Microwave and Guided Wave Letters*, vol. 6, pp. 138-140, 1996.

[21] J.G.Maloney and M.P.Kesler, "Analysis of Periodic Structures," in *Computational Electrodynamics: The Finite-Difference Time-Domain Method*, A.Taflove, Ed., 2nd ed. London: Artech House, 2000, pp. 569-625.

[22] J.Berenger, "A perfectly matched layer for Absorption of Electromagnetic waves," *Journal of computational physics*, vol. 114, pp. 185-200, 1994.

[23] D.S.Katz, E.T.Thiele, and A.Taflove, "Validation and Extension to Three Dimensions of the Berenger PML Absorbing Boundary Condition for FD-TD

Meshes," *IEEE Trans. on Microwave and Guided Wave Letters*, vol. 4, pp. 268-270, 1994.

[24] J.Berenger, "Perfectly Matched layer for the FDTD Solution of wave-structure interaction problems," *IEEE Trans. on Ant. and Propag.*, vol. 44, pp. 110-117, 1996.

[25] J.Berenger, "Improved PML for the FDTD solution of wave-structure Interaction problem," *IEEE Trans. on Antennas and Propagation*, vol. 45, pp. 466-473, 1997.

[26] G.Mur, "Absorbing boundary conditions for the Finite-Difference Approximation of the time-domain Electromagnetic-field equations," *IEEE Trans. On Electromagnetic compatibility*, vol. EMC-23, pp. 377-382, 1981.

[27] H.Ebara, K.Tani, T.Onishi, S.Uebayashi, and O.Hashimoto, "Method for estimating complex permittivity based on measuring effective permittivity of dielectric mixtures in radio frequency band," *IEICE Transactions on Communication*, vol. E88-B, pp. 3269-3274, 2005.

[28] T.Kotnik and D.Miklavcic, "Theorectical Evaluation of the Distributed Power Dissipation in Biological cells Exposed to Electric Fields," *Bioelectromagnetics*, vol. 21, pp. 385-394, 2000.

[29] E.A.Navarro, B.Gimeno, and J.L.Cruz, "Modelling of periodic structures using the finite-difference time-domain method combined with the floquet theorem," *Electronic Letters*, vol. 29, pp. 446-447, 1993.

[30] D.T.Prescott and N.V.Shuley, "Extensions to the FDTD Method for the Analysis of Infinitely Periodic Arrays," *IEEE Microwave and Guided Wave Letters*, vol. 4, pp. 352-354, 1994.

[31] M.E.Veysoglu, R.T.Shin, and J.A.Kong, "A finite-difference time-domain analysis

of wave scattering from periodic surfaces: Oblique incidence case," *J.Electron. Waves Appl.*, vol. 7, pp. 1595-1607, 1993.

[32] C.M.Furse, J.Y.Chen, and O.P.Gandhi, "The use of the frequency-dependent finite-difference time-domain method for induced current and SAR calculations for a heterogeneous model of the human body," *IEEE Transactions on Electromagnetic Compatibility*, vol. 36, pp. 128-133, 1994.

[33] D.H.Roper and J.M.Baird, "Analysis of Overmoded Waveguides Using the Finite-Difference Time Domain Method," *IEEE MTT-S International Microwave Symposium Digest*, pp. 401-404, 1992.

[34] C.M.Furse, S.P.Mathur, and O.P.Gandhi, "Improvements to the finite-difference time-domain method for calculating the radar cross section of a perfectly conducting target," *IEEE Transactions on Microwave Theory and Techniques*, vol. 38, pp. 919-927, 1990.

[35] C.M.Furse, D.H.Roper, D.N.Buechler, D.A.Christensen, and C.H.Durney, "The Problem of Treatment of DC offsets in FDTD Simulations," *IEEE Transactions on Antennas and Propagations*, vol. 48, pp. 1198-1201, 2000.

Chapter 6

Numerical and Experimental Analysis of Proposed Cylindrical Cavity For Detection of Nonlinear Response in Biological Cells Exposed to RF Energy

6.1 Introduction

With the explosive growth of mobile communications, large numbers of researchers around the world have studied the interaction mechanism between electro-magnetic fields and biological tissues. The result has been the development of research streams in different aspects of bioelectromagnetic problems at various levels of definition such as tissue level, cell level and ionic level, with intensive effort worldwide [1].

However, most of the previous analyses have been performed treating bulk tissue effects as a linear problem. Recently, the tendency of research in this area has moved towards seeking evidence for the existence of nonlinear tissue responses, involving more microscopic studies of cellular and molecular processes. Many experiments have been proposed in order to clarify the various nonlinearity hypotheses for biological tissue [2-

6]. Some interested research works in the same field have suggested that the detection of the presence of nonlinear interactions can be investigated by exposing living cells with low-amplitude unmodulated RF carriers and observing the possible generation of second harmonics [7-11]. Such harmonics would be inherent in any unsymmetrically-nonlinear medium: a property essential for demodulation of modulated waveforms. Demodulation has been postulated as a plausible mode for putative non-thermal effects of RF radiation on living organisms.

By implementing the doubly harmonic resonant cavity model proposed in [7-9, 12, 13], this chapter will firstly focus on the numerical modelling of the cylindrical doubly harmonic resonant cavity prior to the experiment works take place, then, a series of practical measurement is performed to validate the numerical results and verify the hypothesis of the nonlinearity response on the biological tissue.

On the numerical analysis, particular attention will be paid on designing the dimension of the cylindrical cavity, field distribution on the proposed cylindrical cavity, allocating the position of the bio-preparation support structure, transmit and receive antennas for second harmonic detection, verifying second harmonic generation from a known nonlinear device and suggesting the required level of input power to excite the bio-preparation.

6.2 Theory of Doubly Resonant Cavity

The doubly resonant cavity is first proposed by [7-9] to detect the nonlinearity of the biological tissue. Due to the amount of nonlinearity in biological cell is unknown, and might be very weak, the amount of energy conversion is minimal. Thus, by storing the converted energy in a cavity instead of radiating it in open space, the chance of detection of the nonlinearity behaviour of the bio-preparation will be higher. Therefore, the doubly resonant cavity is exploited in the analysis of this chapter.

In general, the doubly resonant cavity should able to store energy at both fundamental and second harmonic frequencies. By compromising between size of the cavity and the availability of the instrument at selected frequency used to carry out this experiment, a high quality factor doubly resonant cylindrical cavity with height of 272mm and diameter of 248mm is designed and tested for this analysis at 900MHz and 1800MHz.

6.3 Computation of Modes and Quality factor Q

This section is devoted to compute and understand the resonant frequencies for the TE_{nml} (Transverse Electric) and TM_{nml} (Transverse Magnetic) of the cylindrical cavity modes and quality factor (Q) of the TE_{nml} mode. By using the equations (6.1) to (6.2), the first 25 modes of the proposed cylindrical cavity is tabulated and reported in Table 6.1 [14]:

$$f_{n,m,l}=\frac{c}{2\pi\sqrt{\mu_r\varepsilon_r}}\sqrt{\left(\frac{p'_{nm}}{a}\right)^2+\left(\frac{l\pi}{d}\right)^2} \tag{6.1}$$

$$f_{n,m,l}=\frac{c}{2\pi\sqrt{\mu_r\varepsilon_r}}\sqrt{\left(\frac{p_{nm}}{a}\right)^2+\left(\frac{l\pi}{d}\right)^2} \tag{6.2}$$

$$Q_c=\frac{\omega_0 W}{P_c}=\frac{(ka)^3\eta ad}{4(p'_{nm})^2R_s}\frac{1-\left(\frac{n}{p'_{nm}}\right)^2}{\left\{\frac{ad}{2}\left[1+\left(\frac{\beta an}{(p'_{nm})^2}\right)^2\right]+\left(\frac{\beta a^2}{p'_{nm}}\right)^2\left(1-\frac{n^2}{(p'_{nm})^2}\right)\right\}} \tag{6.3}$$

Table 6.1: The characteristic of the proposed cylindrical cavity

Mode	**1 (TE) or 2 (TM)**	**n**	**m**	**l**	p_{nm} **or** p'_{nm}	**Freq**	**Q-factor (Gold)**
1	1	1	1	0	1.84E+00	7.09E+08	2.96E+04
2	1	1	1	1	1.84E+00	8.98E+08	3.41E+04
3	2	0	1	0	2.40E+00	9.26E+08	4.80E+04
4	2	0	1	1	2.40E+00	1.08E+09	5.30E+04
5	1	2	1	0	3.05E+00	1.18E+09	3.09E+04
6	1	2	1	1	3.05E+00	1.30E+09	3.28E+04
7	1	1	1	2	1.84E+00	1.31E+09	4.21E+04
8	2	0	1	2	2.40E+00	1.44E+09	6.31E+04
9	2	1	1	0	3.83E+00	1.48E+09	5.64E+04
10	1	0	1	0	3.83E+00	1.48E+09	6.06E+04
11	2	1	1	1	3.83E+00	1.58E+09	5.89E+04
12	1	0	1	1	3.83E+00	1.58E+09	6.33E+04
13	1	2	1	2	3.05E+00	1.61E+09	3.70E+04
14	1	3	1	0	4.20E+00	1.62E+09	3.11E+04
15	1	3	1	1	4.20E+00	1.71E+09	3.21E+04
16	1	1	1	3	1.84E+00	1.80E+09	4.98E+04
17	2	1	1	2	3.83E+00	1.84E+09	6.50E+04
18	1	0	1	2	3.83E+00	1.84E+09	6.99E+04
19	2	0	1	3	2.40E+00	1.90E+09	7.36E+04
20	1	3	1	2	4.20E+00	1.96E+09	3.47E+04
21	2	2	1	0	5.14E+00	1.98E+09	5.95E+04
22	1	2	1	3	3.05E+00	2.03E+09	4.20E+04
23	1	4	1	0	5.32E+00	2.05E+09	3.10E+04
24	1	1	2	0	5.33E+00	2.05E+09	6.89E+04
25	2	2	1	1	5.14E+00	2.05E+09	6.09E+04

6.4 Field Distribution inside the designated cylinder cavity

After several computations attempted, then, two modes were found and used for nonlinearity study. These modes are TE_{111} mode at 898MHz and TE_{113} mode at 1796 MHz. With the aids of the commercial 3D computational software package CST [15], the electric fields (E_x, E_y, E_z and E_{total}) and magnetic fields (H_x, H_y, H_z and H_{total}) distribution within the cavity will be investigated. The results give indication on the location required inside the cavity to provide the maximum electric or magnetic fields required for maximum coupling. Electric or magnetic field distribution components play a major role on contributing to the maximum field points. Figures 6.1 to 6.4 and 6.5 to 6.8 show the 2D view of the electric and magnetic fields distribution at TE_{111} and TE_{113} mode of the proposed cavity respectively.

From the observation point of view, at the fundamental TE_{111} mode, the cavity has a field maximum in the centre of the cavity, whereas the second harmonic of TE_{113} mode has maximum field points at h/6, h/2 and 5h/6, where h is the height of the cavity. In the light of this information, the locations of the bio-preparation, transmit and receive antenna can be identified.

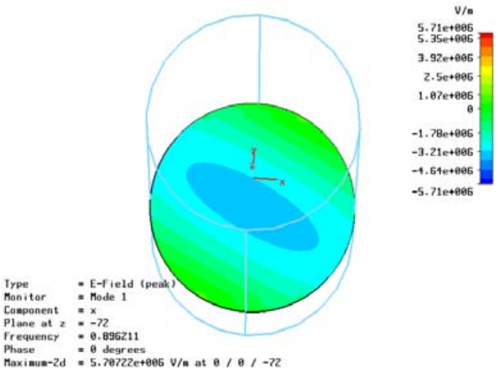

Type = E-Field (peak)
Monitor = Mode 1
Component = x
Plane at z = -72
Frequency = 0.896211
Phase = 0 degrees
Maximum-2d = 5.70722e+006 V/m at 0 / 0 / -72

(a) Ex

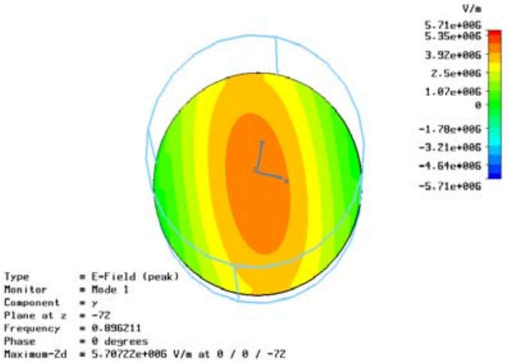

Type = E-Field (peak)
Monitor = Mode 1
Component = y
Plane at z = -72
Frequency = 0.896211
Phase = 0 degrees
Maximum-2d = 5.70722e+006 V/m at 0 / 0 / -72

(b) Ey

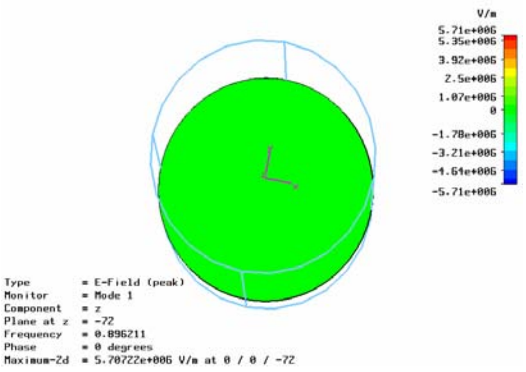

Type = E-Field (peak)
Monitor = Mode 1
Component = z
Plane at z = -72
Frequency = 0.896211
Phase = 0 degrees
Maximum-2d = 5.70722e+006 V/m at 0 / 0 / -72

(c) Ez

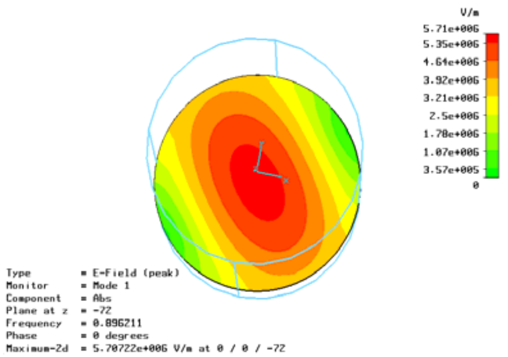

Type = E-Field (peak)
Monitor = Mode 1
Component = Abs
Plane at z = -72
Frequency = 0.896211
Phase = 0 degrees
Maximum-2d = 5.70722e+006 V/m at 0 / 0 / -72

(d) Total E-field

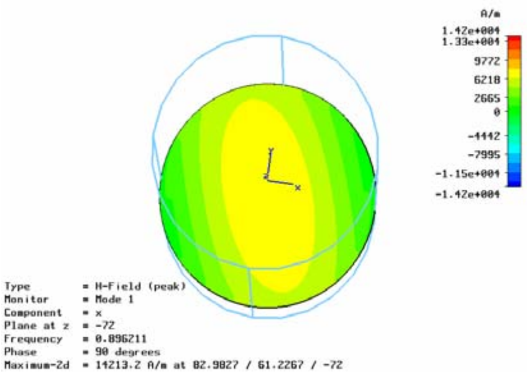

Type = H-Field (peak)
Monitor = Mode 1
Component = x
Plane at z = -72
Frequency = 0.896211
Phase = 90 degrees
Maximum-2d = 14213.2 A/m at 82.9827 / 61.2267 / -72

(e) Hx

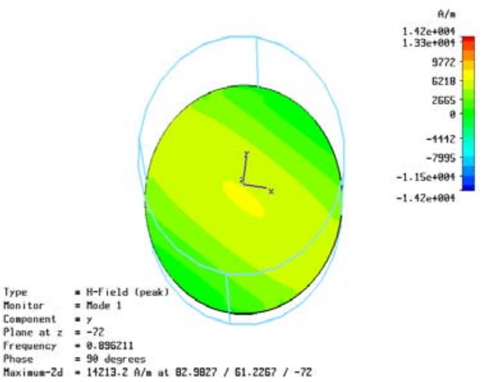

Type = H-Field (peak)
Monitor = Mode 1
Component = y
Plane at z = -72
Frequency = 0.896211
Phase = 90 degrees
Maximum-2d = 14213.2 A/m at 82.9827 / 61.2267 / -72

(f) Hy

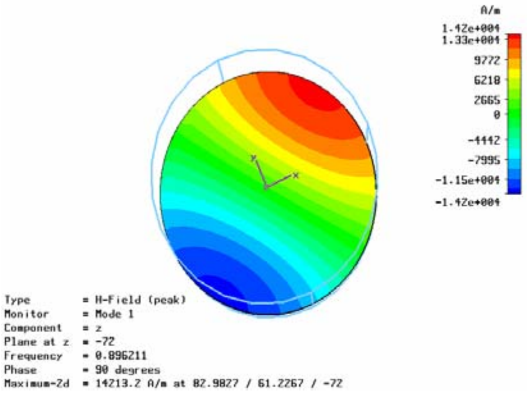

Type = H-Field (peak)
Monitor = Mode 1
Component = z
Plane at z = -72
Frequency = 0.896211
Phase = 90 degrees
Maximum-2d = 14213.2 A/m at 82.9827 / 61.2267 / -72

(g) Hz

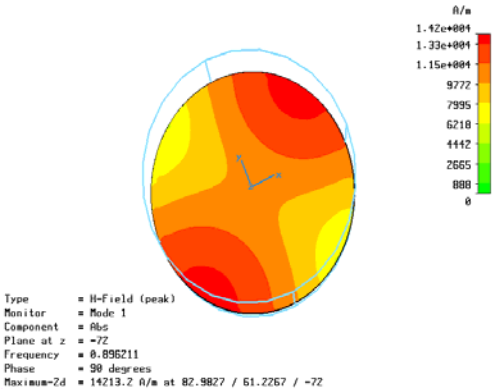

Type = H-Field (peak)
Monitor = Mode 1
Component = Abs
Plane at z = -72
Frequency = 0.896211
Phase = 90 degrees
Maximum-2d = 14213.2 A/m at 82.9827 / 61.2267 / -72

(h) Total H-field

Figure 6.1: TE_{111} mode of Cavity (height=272mm, diameter=248mm)
0.25h=0.25*272mm (xyplane)

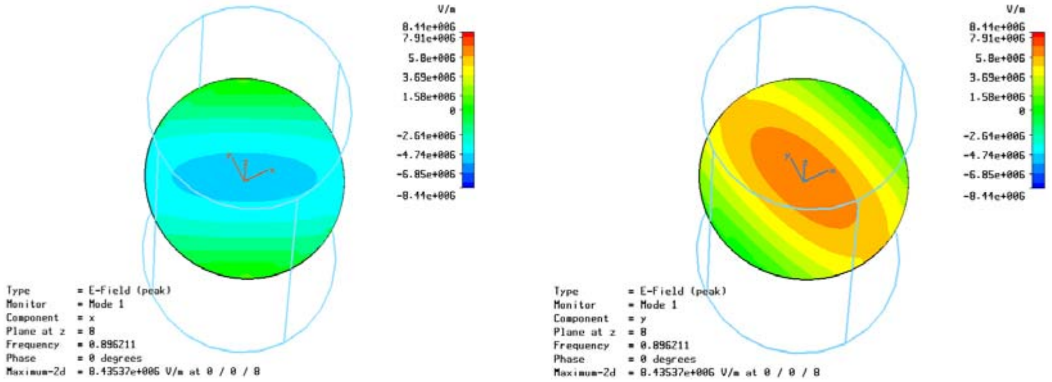

(a) Ex (b) Ey

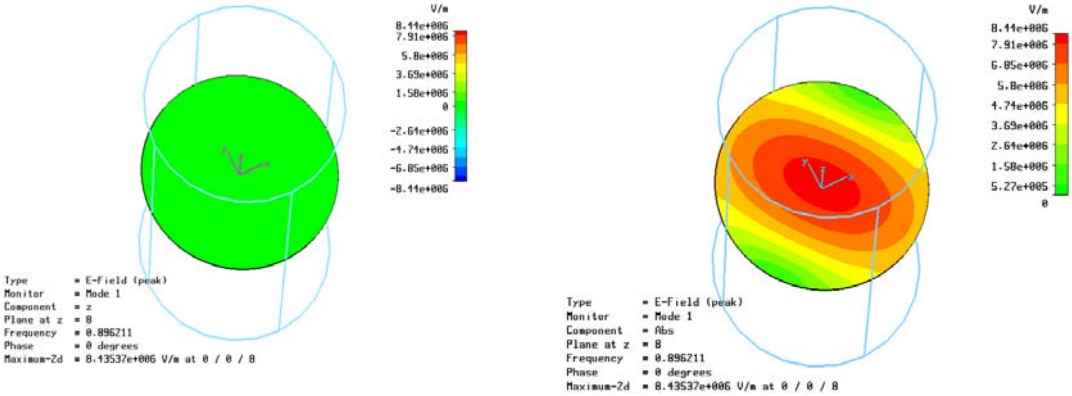

(c) Ez (d) Total E-field

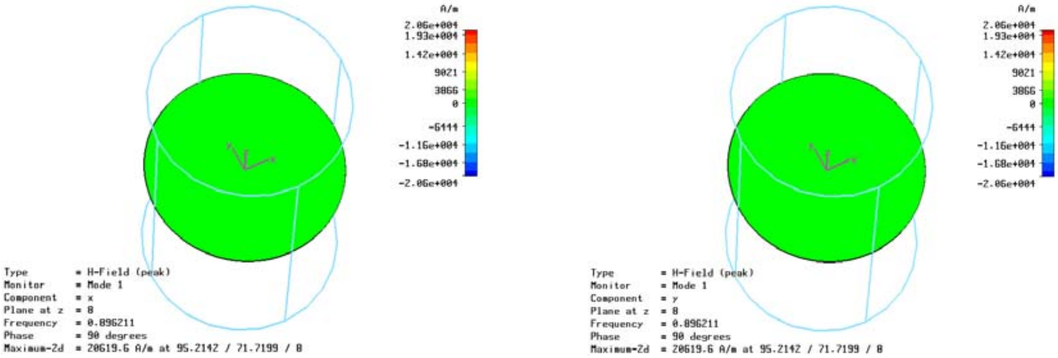

(e) Hx (f) Hy

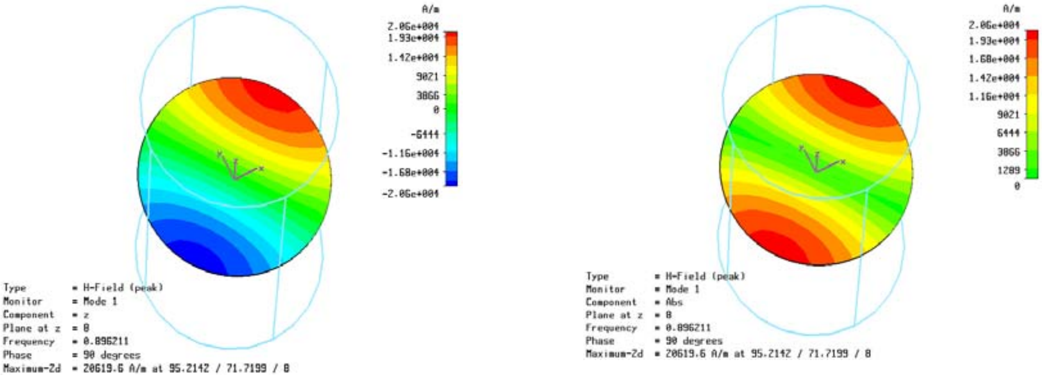

(g) Hz (h) Total H-field

Figure 6.2: TE_{111} mode of Cavity (height=272mm, diameter=248mm) 0.75h=0.75*272mm (xyplane)

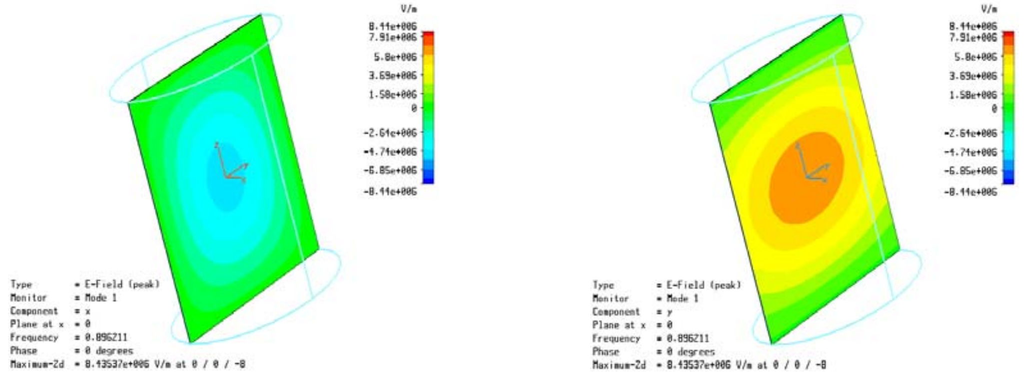

(a) Ex (b) Ey

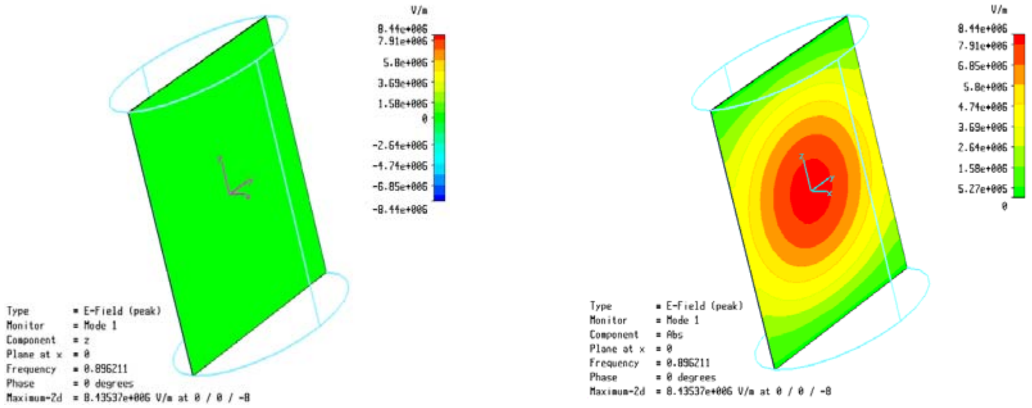

(c) Ez (d) Total E-field

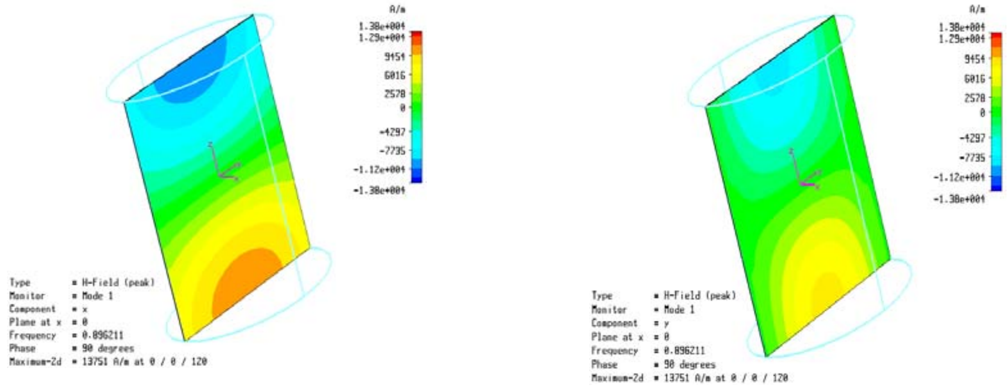

(e) Hx (f) Hy

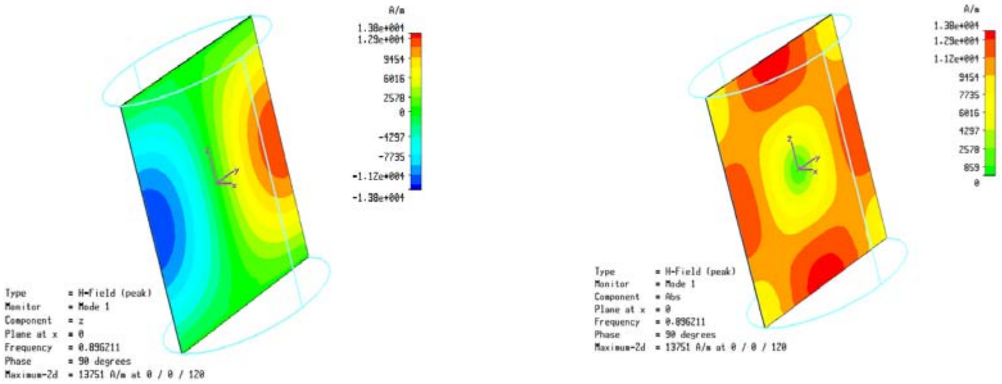

(g) Hz (h) Total H-field

Figure 6.3: TE_{111} mode, yzplane through the centre of the cavity.

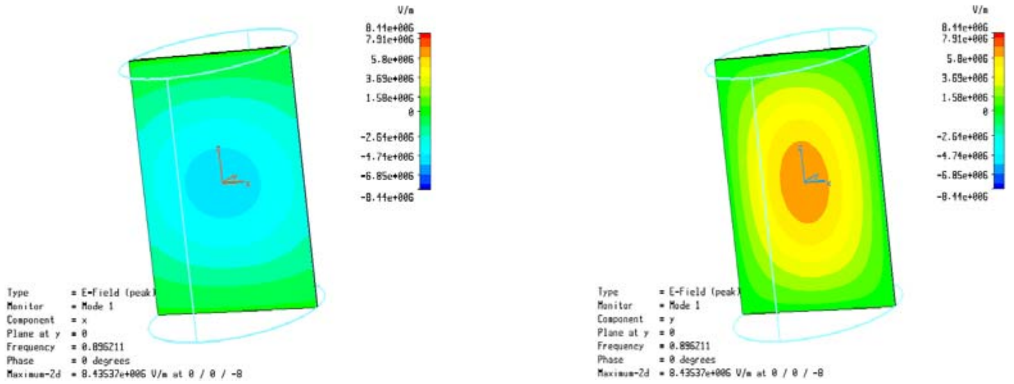

(a) Ex (b) Ey

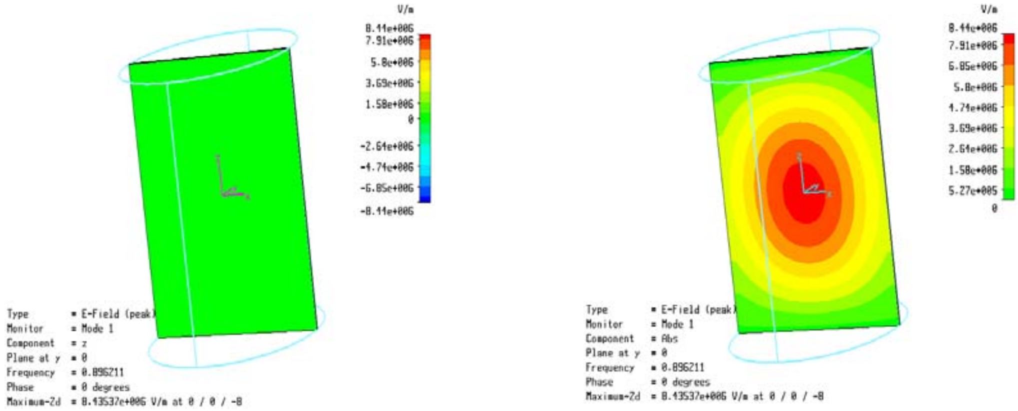

(c) Ez (d) Total E-field

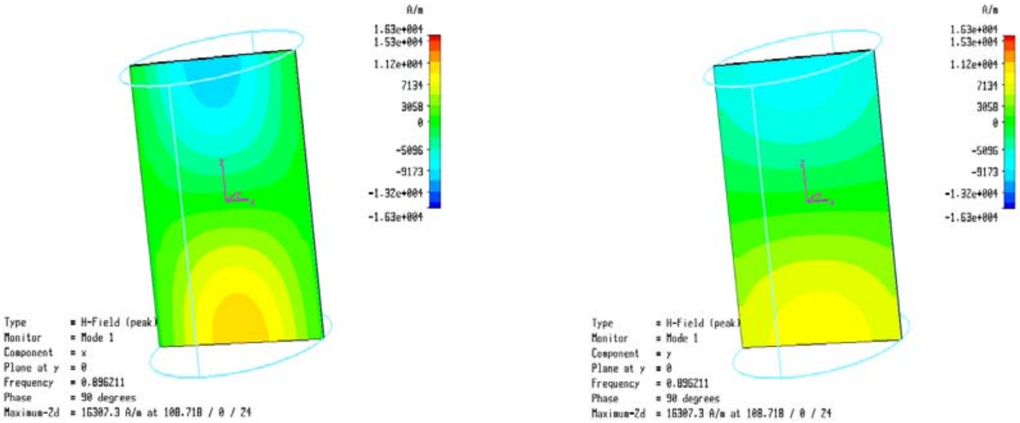

(e) Hx (f) Hy

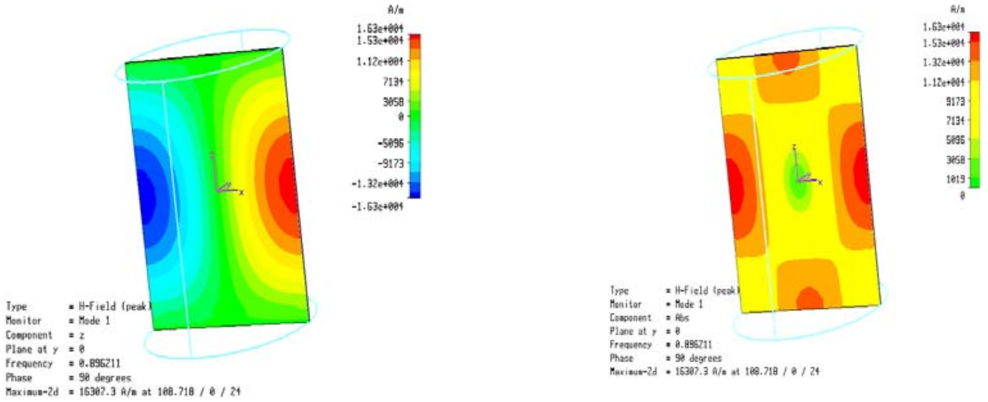

(g) Hz (h) Total H-field

Figure 6.4: TE_{111} mode, xzplane through the centre of the cavity.

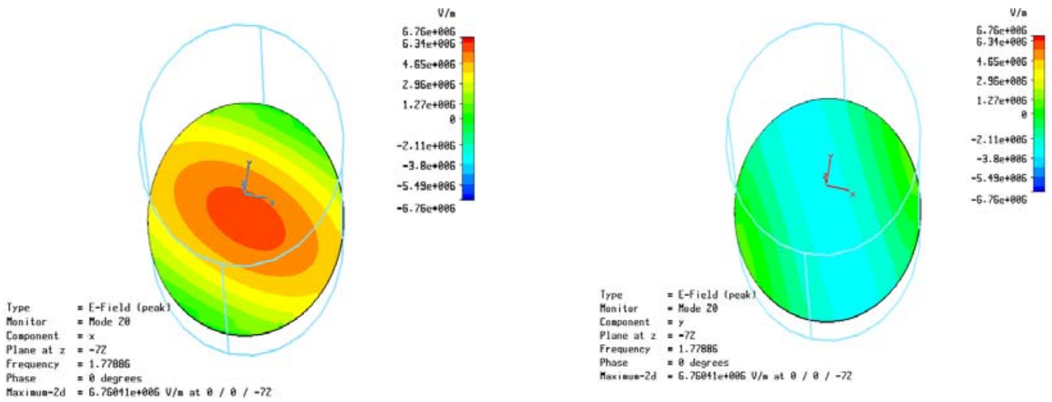

(a) Ex (b) Ey

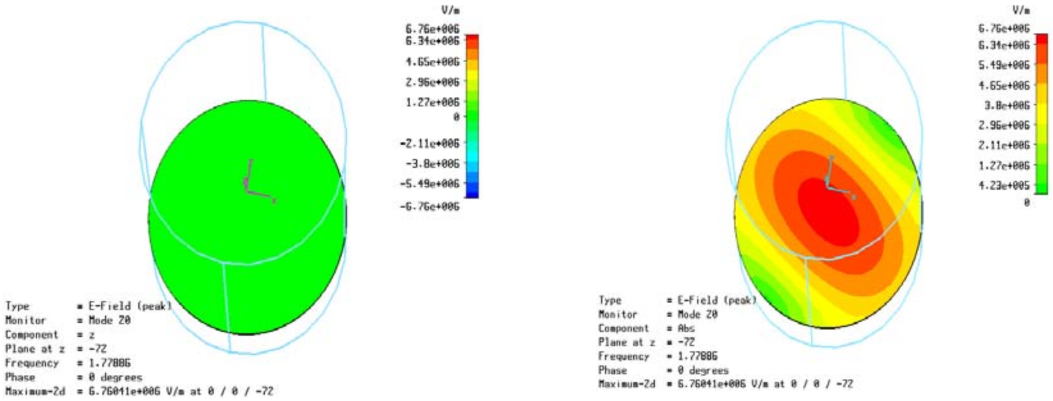

(c) Ez (d) Total E-field

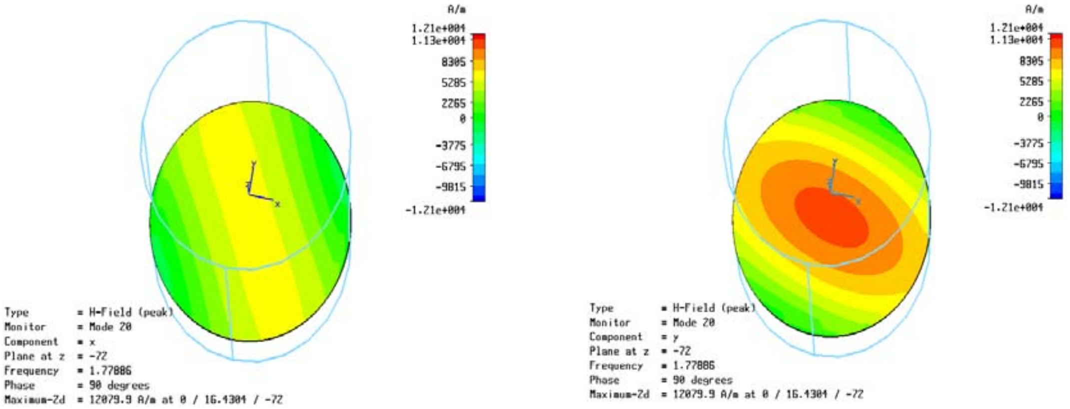

(e) Hx (f) Hy

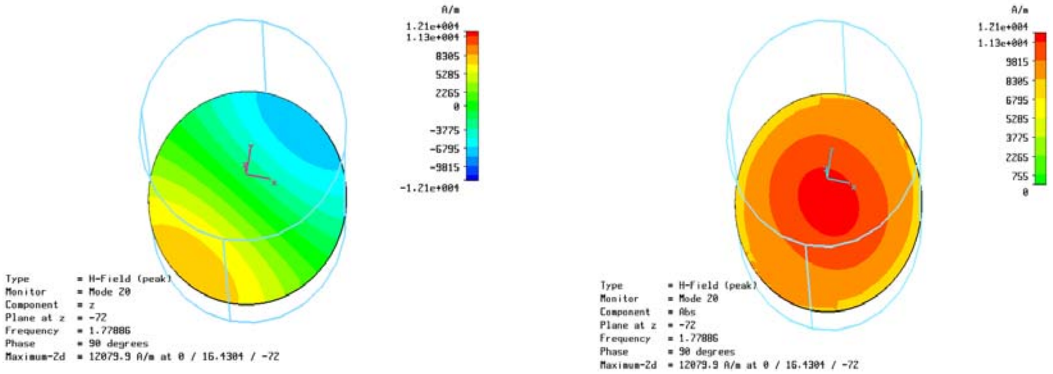

(g) Hz (h) Total H-field

Figure 6.5: TE_{113} mode of Cavity (height=272mm, diameter=248mm)
0.25h=0.25*272mm (xyplane)

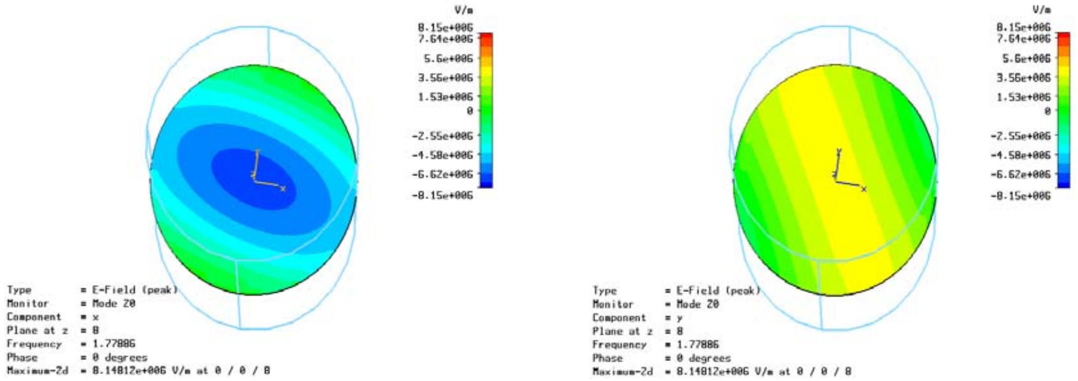

(a) Ex (b) Ey

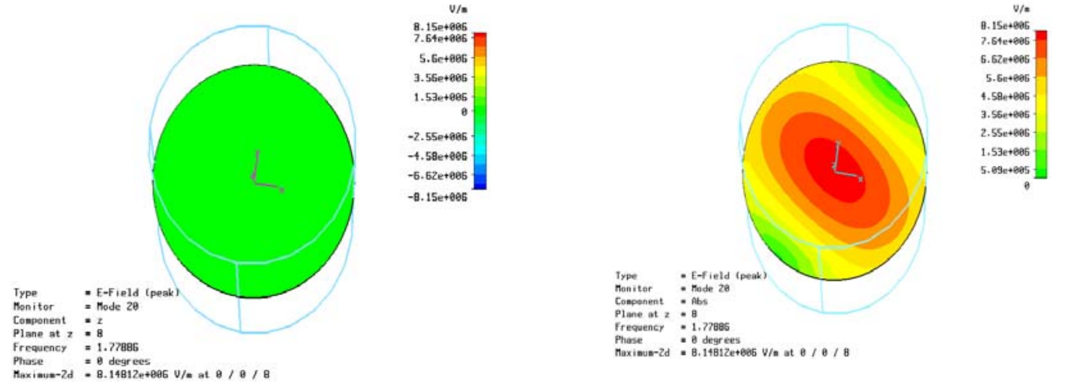

(c) Ez (d) Total E-field

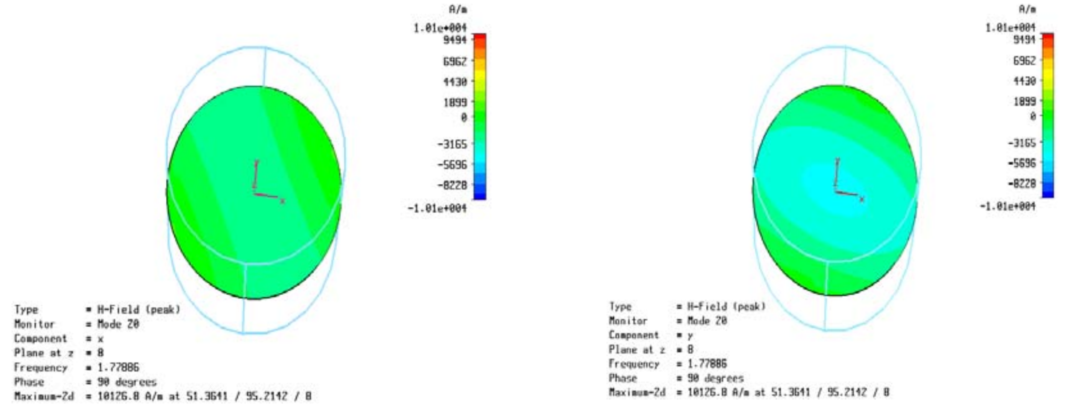

(e) Hx (f) Hy

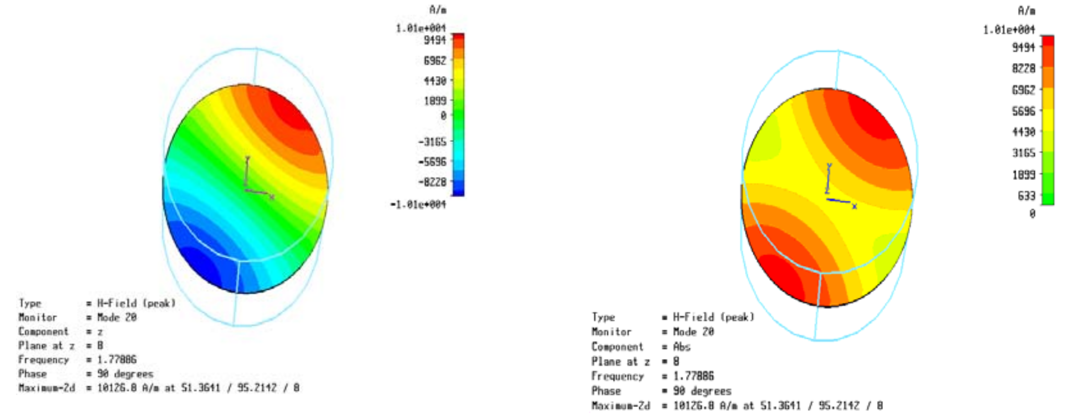

(g) Hz (h) Total H-field

Figure 6.6: TE_{113} mode of Cavity (height=272mm, diameter=248mm) 0.5h=0.5*272mm (xyplane)

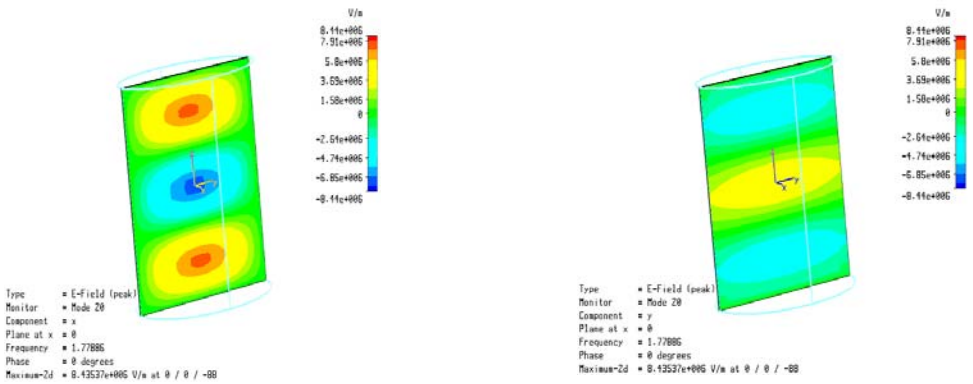

(a) Ex (b) Ey

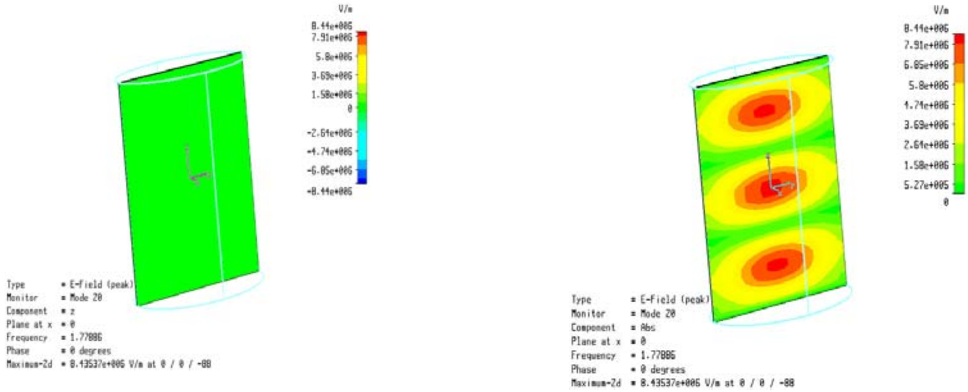

(c) Ez (d) Total E-field

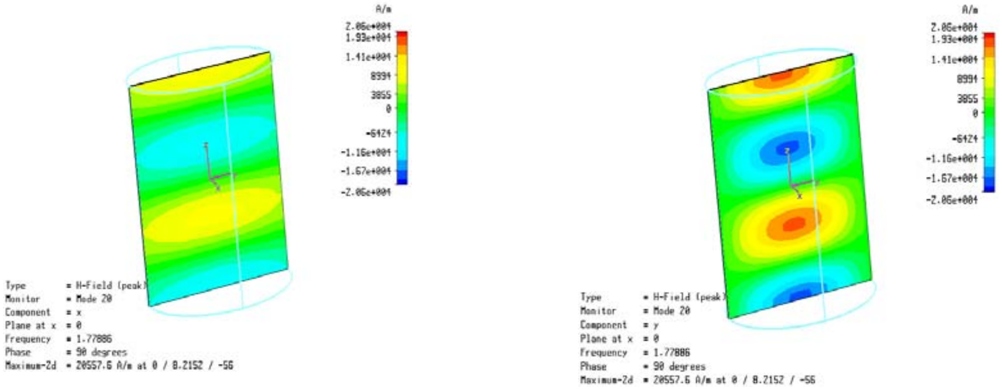

(e) Hx (f) Hy

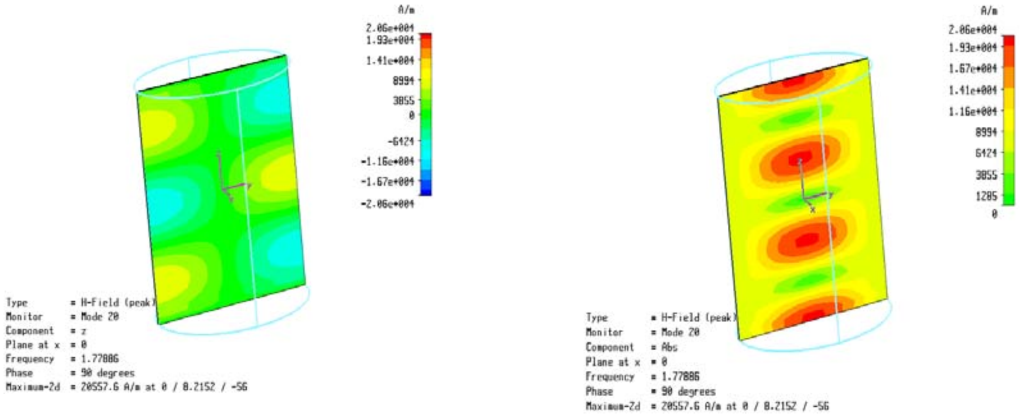

(g) Hz (h) Total H-field

Figure 6.7: TE_{113} mode, yzplane through the centre of the cavity.

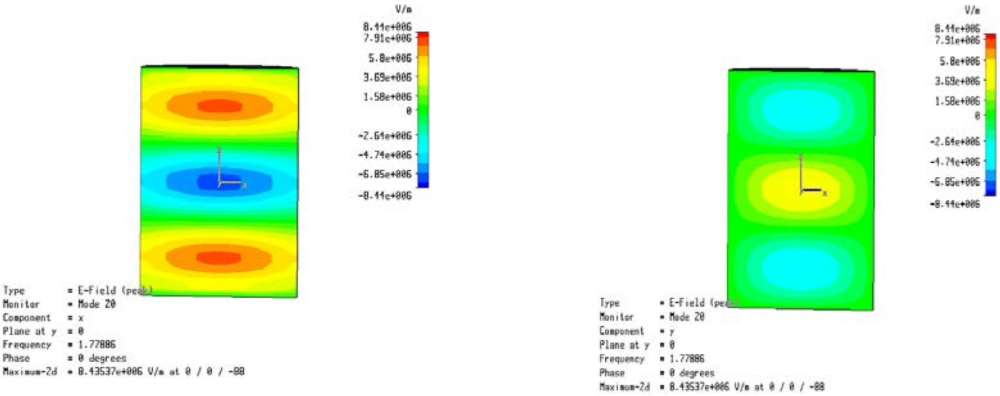

(a) Ex (b) Ey

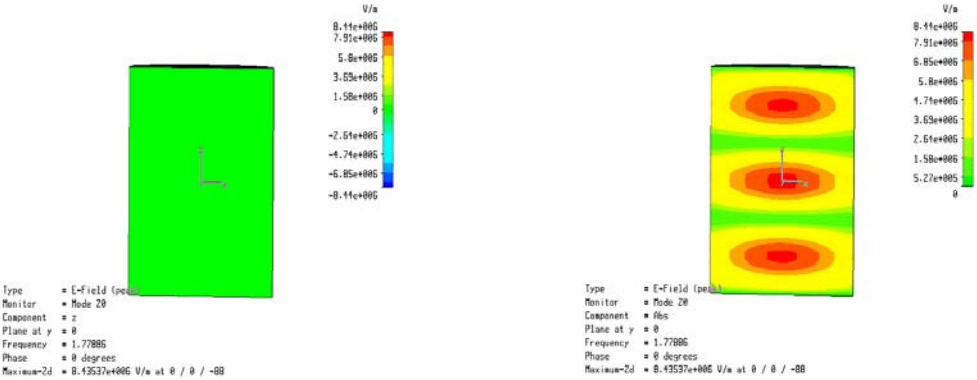

(c) Ez (d) Total E-field

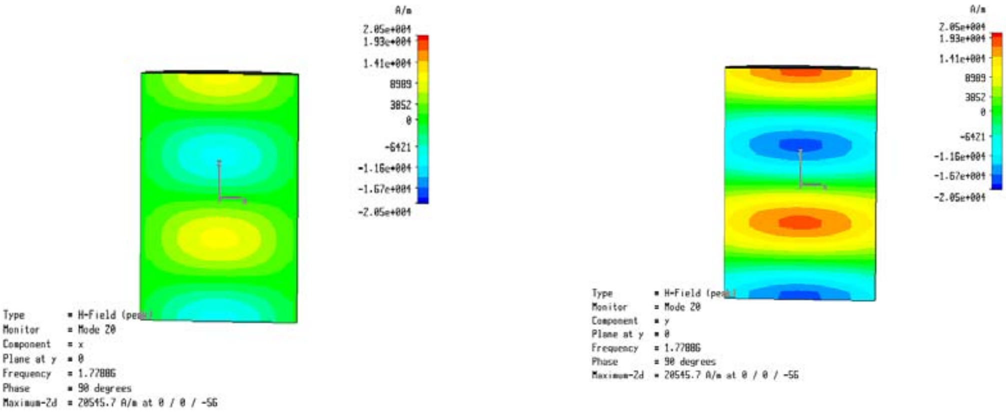

(e) Hx (f) Hy

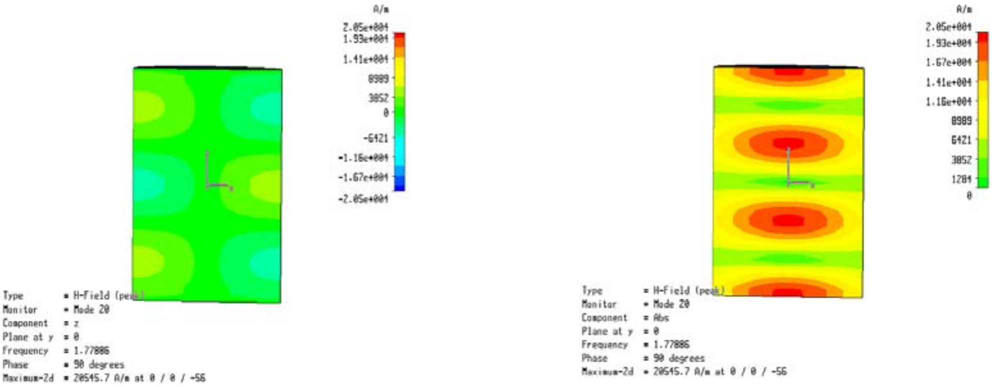

(g) Hz (h) Total H-field

Figure 6.8: TE$_{113}$ mode, xzplane through the centre of the cavity.

6.5 Antenna and bio-preparation support structure design

The proposed cylindrical cavity is built with two rectangular loop antennas and support structure for biopreparation (i.e. butterfly shaped Lexan lamina and Petri dish, as shown in Figure 6.9). As can be seen in Figure 6.9, the antenna with size of (14x105 mm) at the bottom of the cavity acts as a transmitter to excite the TE_{111} cavity mode in the 880-890 MHz band. The antenna with size of 12.5 x 56.5mm at the side wall of the cavity, is used to receive the energy of TE_{113} cavity mode that appears between 1760-1790MHz frequency band. Moreover, the electrical properties such as the relative permittivity of the Lexan sample that supports the structure and the Petri dish are 2.75 and 2.56 [16] respectively. It should be noted the length of the transmitter and receiver antennas have been tuned in order to achieve the resonant mode TE_{113} at double the frequency of the TE_{111}. In addition, the detailed dimension of the butterfly shaped Lexan sample structure is also shown in Figure 6.10.

The bands of the operation of the two antennas are shown in Figure 6.11. According to Figure 6.11, the dashed line represents the return loss of the bottom antenna at its frequency of operation with an empty 3cm Petri dish. The operating frequency has been multiplied by a factor of two to display the second harmonic performance in the same band of the receiver antenna of the mode TE_{113}. Solid line in Figure 6.11 illustrates the shift of operating frequency band when 15μl lossy water with properties of ε_r =78.24, σ=0.173 [17] is added to the Petri dish inside the cavity.

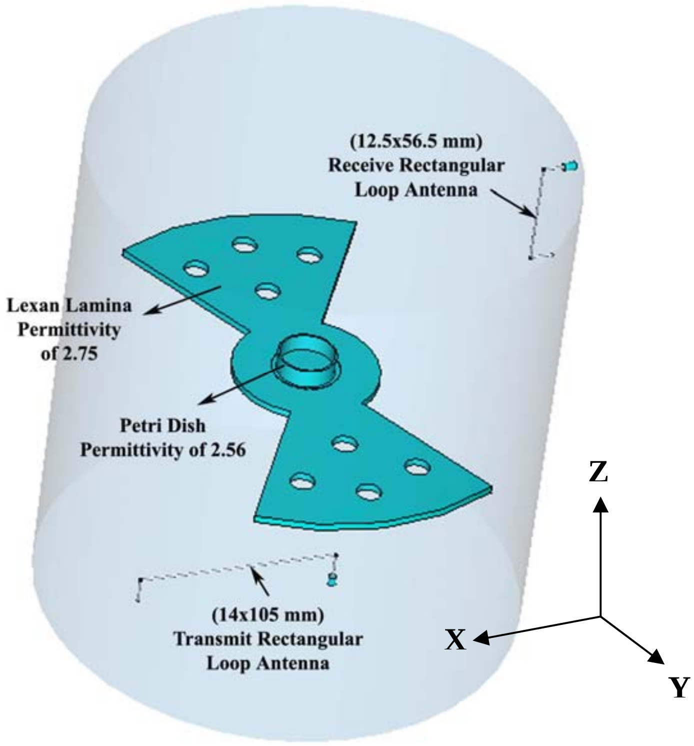

Figure 6.9: The dimension of the proposed cavity model with its Lexan sample support structure and two rectangular loop antennas

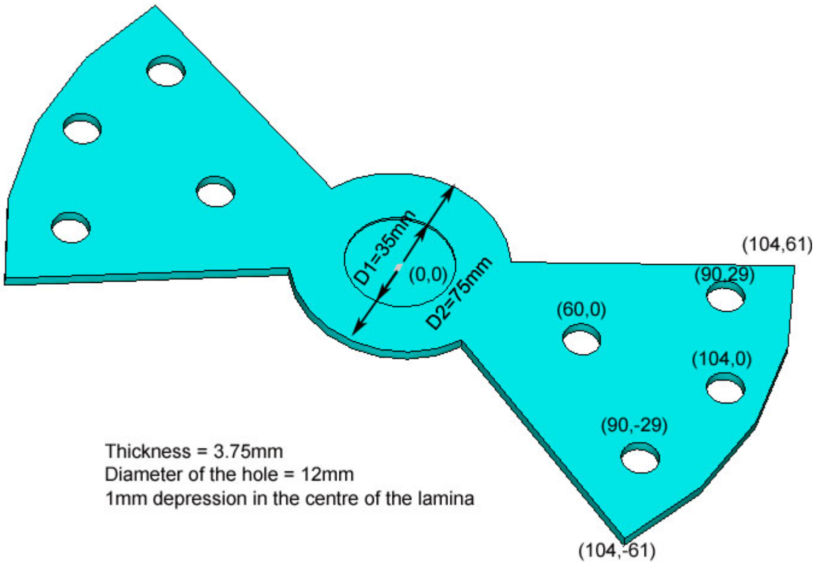

Figure 6.10: The detailed dimension of the butterfly shaped Lexan sample support structure.

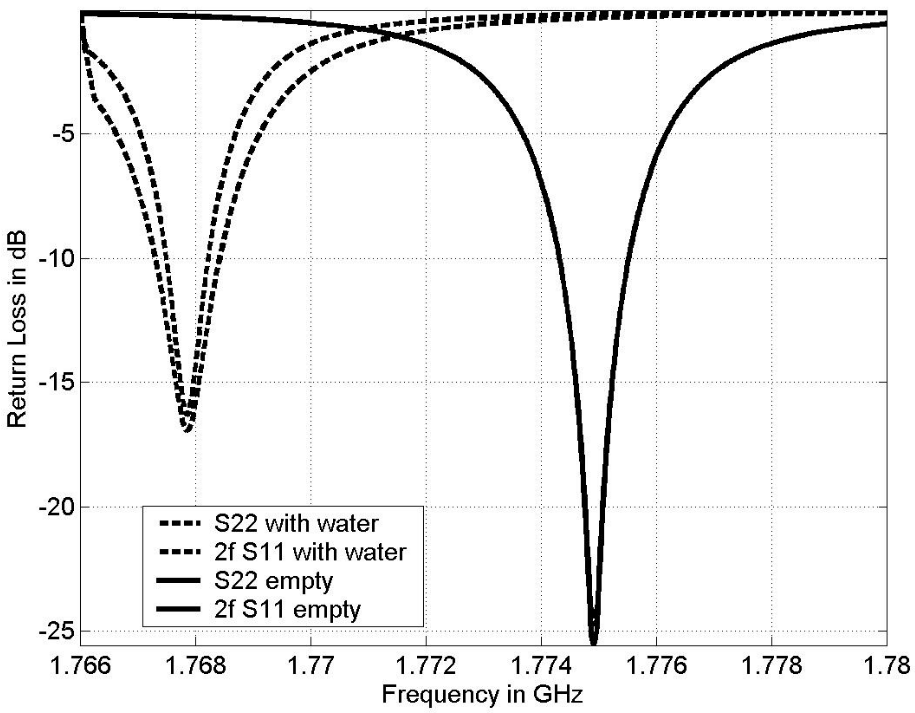

Figure 6.11: The fundamental and second harmonic responses of the cavity

6.6 Tests with a Schottky diode

This section predicts the level of detectable second harmonic signal from a nonlinear frequency conversion process in the cavity in the presence of a known nonlinear device such as Schottky diode. A nonlinear high tangential sensitivity diode [18] is used and placed on the bio-preparation support structure. Figures 6.12 and Fig.6.13 demonstrate the diode model in [18] and microwave studio software package [15] respectively, while Figure 6.14 describes the practical UHF diode used and the simulated diode model.

The time domain solver [15] is employed by using narrow input pulse to excite the antenna sensors. The simulation is carried out by placing a narrow band Gaussian pulse that covers the frequency band of 0.88 to 0.89 GHz to the antenna ports 1 and 2. After the simulation is completed, the FFT (Fast Fourier Transform) is used; in which the time domain output signals on port1 and port2 can be converted to frequency domain to find any sign of the presence of the second harmonic.

In order to confirm the proposed configuration for the second harmonic with pulse excitation signal, a simulation was conducted without the presence of the diode in the cavity. Figure 6.15 depicts the narrow band Gaussian pulse signal in time domain. After the process of FFT, this excitation signal is transformed to frequency domain and then Figure 6.16 can be presented. The input and output signals on both excitations at port1 and 2 are found with no presence of second harmonic, as shown in Figure 6.17.

6.6.1 Testing for the orientation of the diode in the cavity

Tests to force the generation of second harmonics have been undertaken by placing a small schottky diode in place of the biological test material inside the cavity. Simulations were performed with two different orientation of the diode: (i) parallel (x axis in Figure 6.9) and (ii) orthogonal (y axis in Figure 6.9), to the transmitter antenna. The results shown, as broadly expected, strong generation of second harmonics when the presumed current axis in the diode is oriented parallel to the electric field and zero generation when these directions are orthogonal. Figure 6.18 illustrates the presence of the second harmonic on the output port of receiver port 2 when the diode is oriented parallel to the transmitter at port 1. By analogy with the problem of searching for an antenna null with a portable radio, the orientation of the diode to achieve zero harmonic generation should be highly critical.

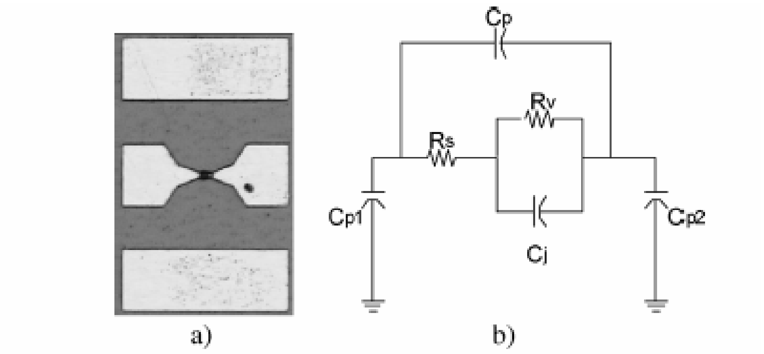

(a) Micrograph of the diode. (b) Small signal equivalent circuit

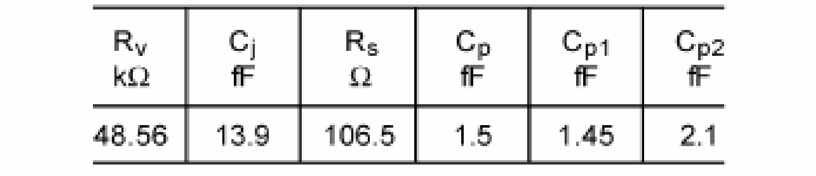

R_v kΩ	C_j fF	R_s Ω	C_p fF	C_{p1} fF	C_{p2} fF
48.56	13.9	106.5	1.5	1.45	2.1

Figure 6.12: Diode Model from ref. [18]

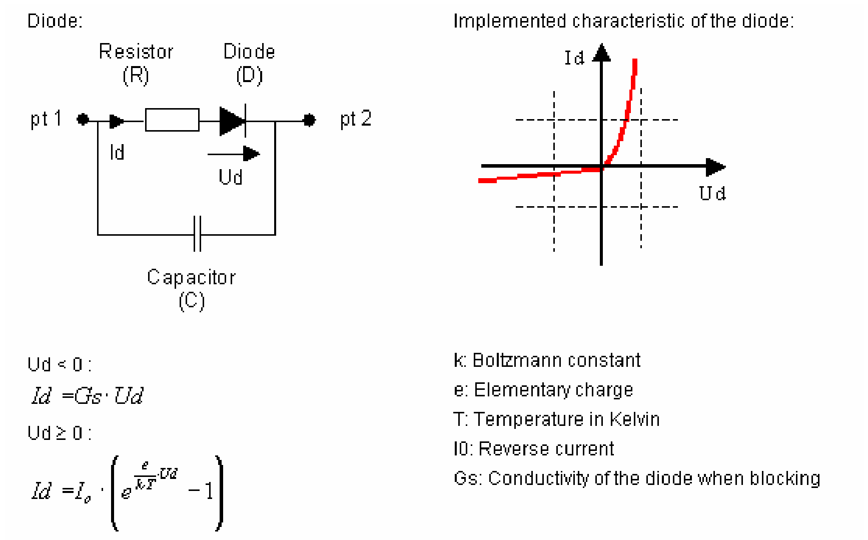

Ud < 0 :

$Id = Gs \cdot Ud$

Ud ≥ 0 :

$Id = I_o \cdot \left(e^{\frac{e}{kT}Ud} - 1 \right)$

k: Boltzmann constant
e: Elementary charge
T: Temperature in Kelvin
I0: Reverse current
Gs: Conductivity of the diode when blocking

Figure 6.13: Diode Model from Microwave Studio [15]

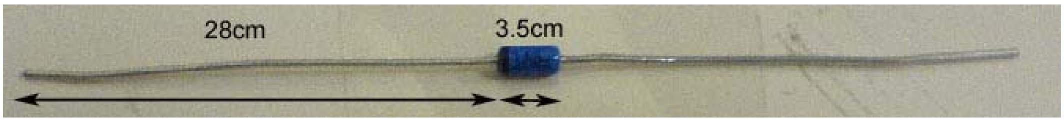

(a) Practical UHF diode

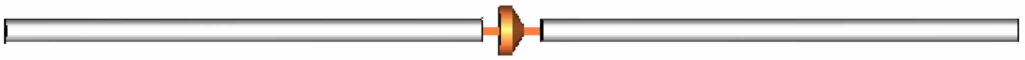

(b) Simulated diode

Figure 6.14: Diode Model (a) Practical UHF diode (b) Simulated diode

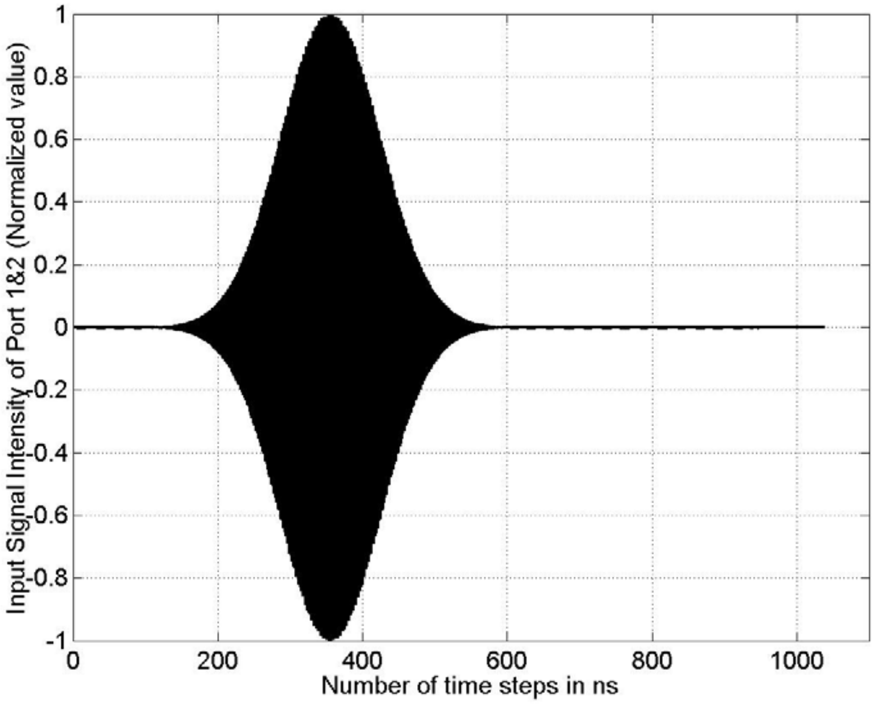

Figure 6.15: Input Signal for Port 1 and Port 2 in time domain (Normalized value)

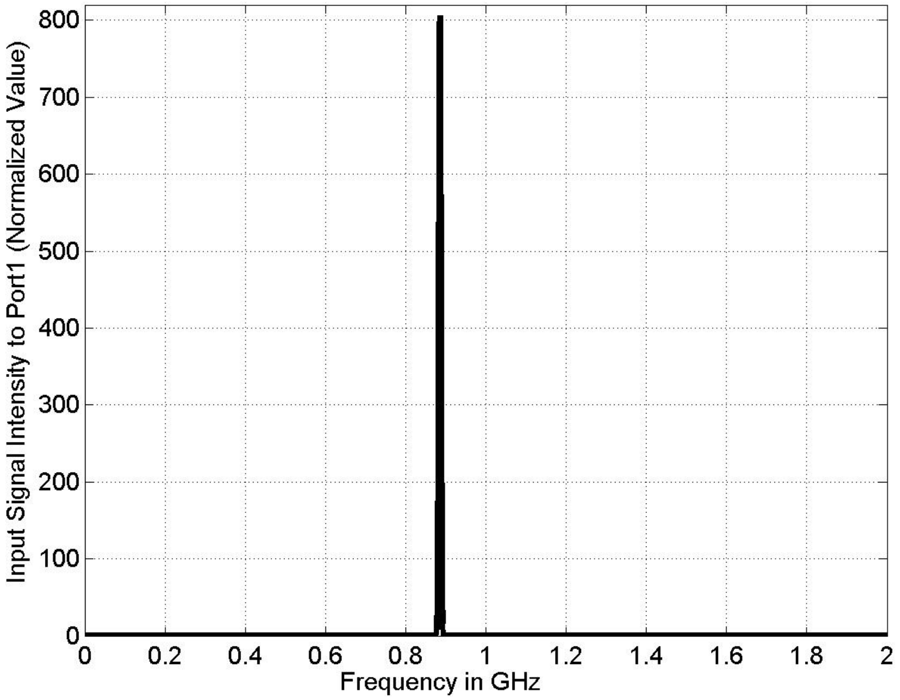

Figure 6.16: Input Signal for Port 1 and Port 2 in Frequency Domain (Normalized value)

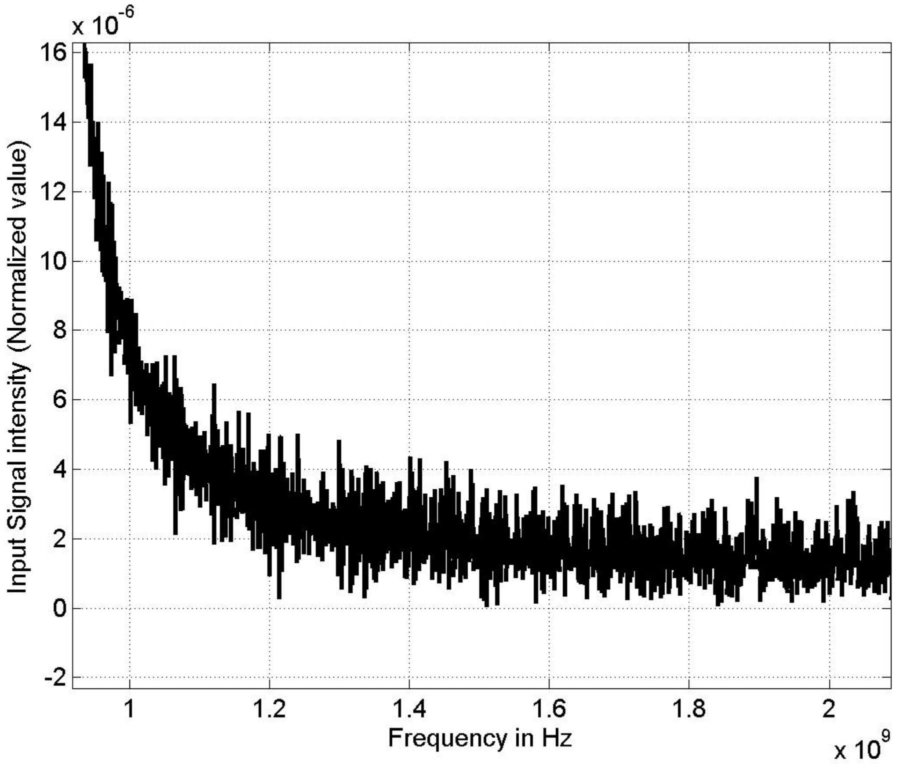

Figure 6.17: Input Signal and Output Signal for Port 1 and Port 2 in Frequency Domain (Enlargement)

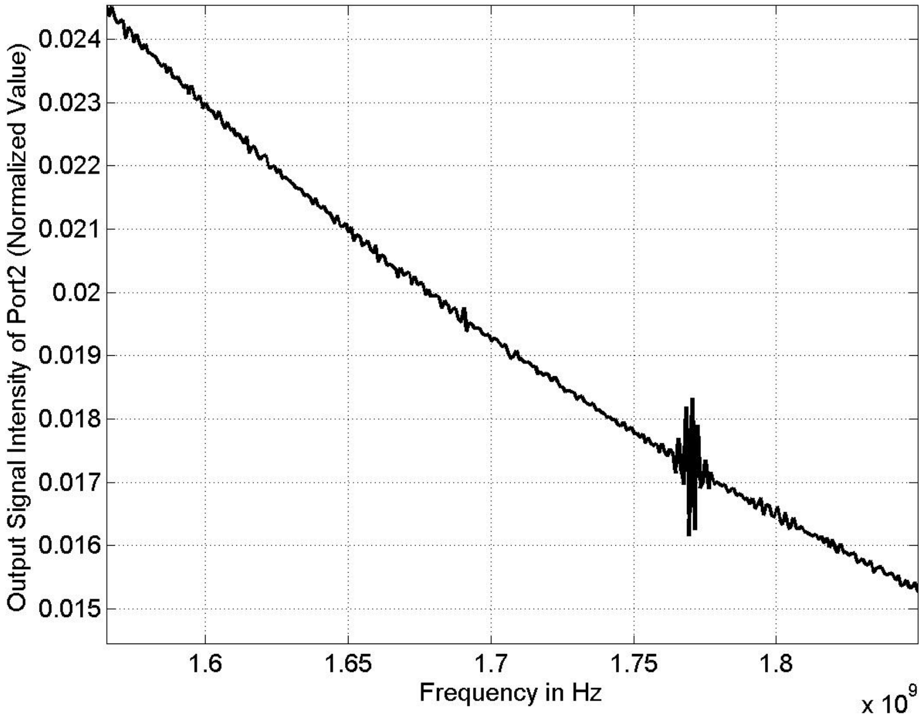

Figure 6.18: Output signal on the receive antenna in Frequency Domain

6.6.2 Testing for variation of the length of diode leads

In this sub-section, the simulation will be conducted to investigate the variation of the second harmonic signal intensity against different lengths of the diode Leads. These leads lengths are considered between 0mm to 28mm and placed into the middle of the dish inside the cavity in which, the orientation direction was kept parallel to the transmit antenna at port 1. As expected, Figure 6.19 illustrates that as the length of the diode leads is reduced, the second harmonic signal strength is decreased. It was observed that the second harmonic signal strength was varied from 2.4 to 0.04 (units) for constant input signal strength of 800 (units: refer to Figure 6.16).

By applying the following formula $\frac{P_{2nd\ harmonic}}{P_{fundamental}} = 10\log 10\left(\frac{0.04}{800}\right)^2 = -86.02dB$, this indicates the minimum requirements of the signal-to-noise ratio that is required to be used for the measurements.

On the other hand, the behaviour of the return loss at output port of the receiver antenna is also been analysed with the variations of the length of diode leads. Figure 6.20 elucidates the S_{22} is about 68 dB when 28mm leads length used, while with the diode without leads, the S_{22} was found around 20dB.

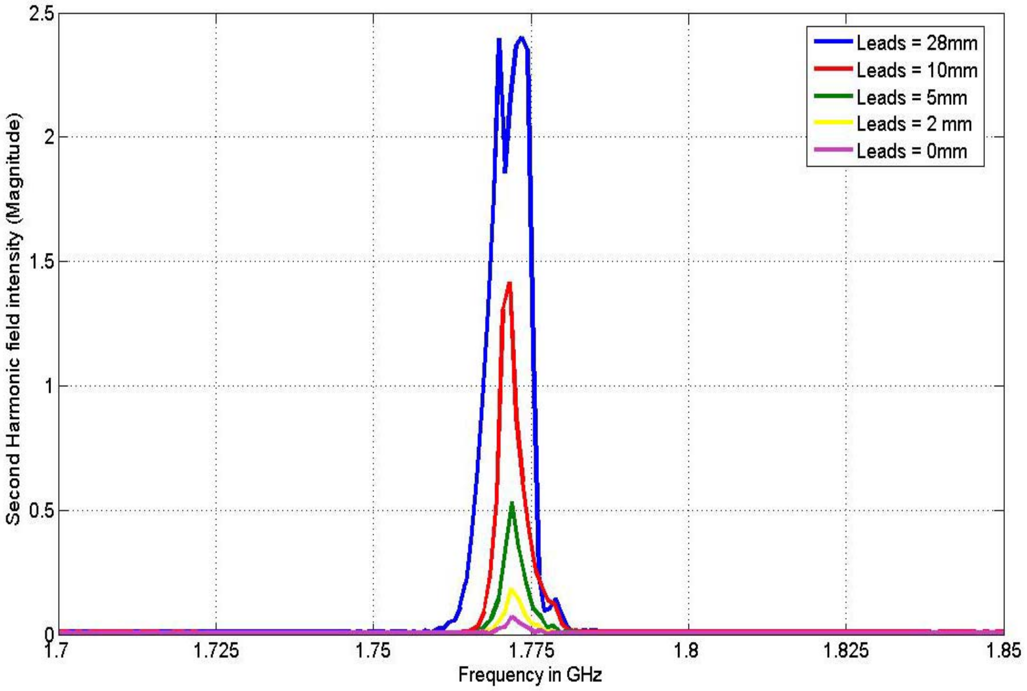

Figure 6.19: Second harmonic signal strength variation with different length of diode leads

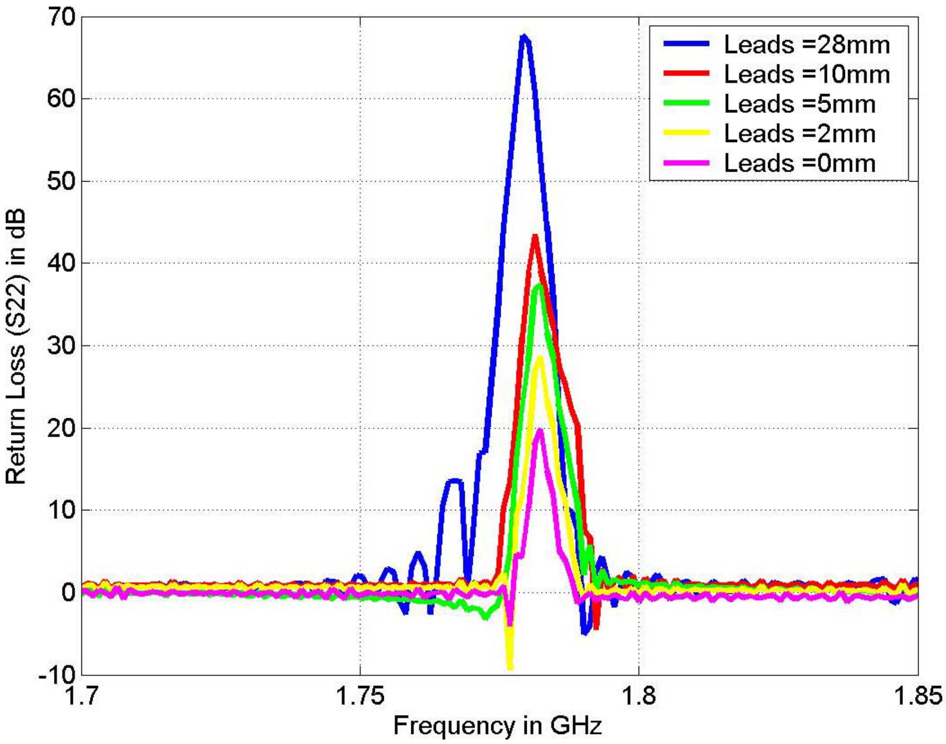

Figure 6.20: Return loss on the output port variation with different length of diode leads

6.7 Proposed Electrical Circuit Model

An efficient way to test the unsymmetrical nonlinear response of biological tissue samples exposed to a 0.9GHz signal is to observe the second harmonic at 1.8GHz in a cavity resonant at the two frequencies. A simple mathematical technique is proposed here to calculate the second harmonic power with known input power.

6.7.1 Summary of method

The procedure of the proposed mathematical model will be demonstrated in the following context. Firstly, the cavity model used in the previous analysis will be implemented. A discrete port or floating port with metal leads of width 1mm which represents the dipole antenna, are placed inside the Petri dish of the cavity and oriented parallel to the transmitted antenna, as depicted in Figure 6.21 and Figure 6.22.

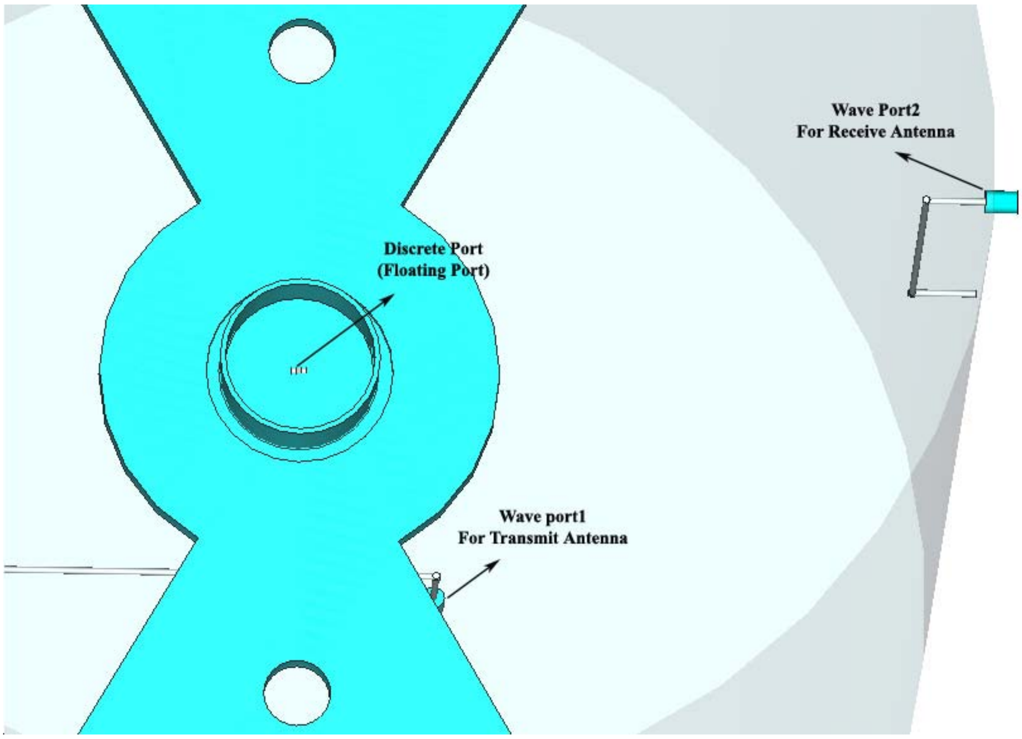

Figure 6.21: Proposed cavity model for mathematical analysis

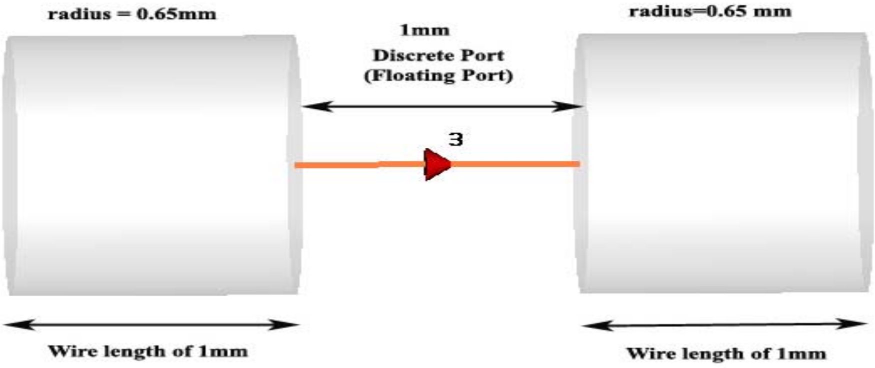

Figure 6.22: Discrete Port Model in the Petri dish of the cavity (Enlargement)

Then, two simulations will be performed separately at frequency of TE_{111} and TE_{113}, in order to extract the 3x3 Z- matrix parameters at both frequencies which is equivalent to the 3-ports network as depicted in Figure 6.23. Once the Z- matrix parameters are obtained at both frequencies, the proposed mathematical model as depicted in Figure 6.24 can be employed. According to Figure 6.24, the input and output ports can equivalently represent the transmitter and the receiver antennas respectively in the cavity, while the nonlinear element can be represented at one port inside the cavity. Hence, the electrical circuit equivalent diode model used is illustrated in Figure 6.25.

From the Figures 6.24 and 6.25, by applying Ohm’s law, the following equation can be stated.

$$\begin{bmatrix} V_1 \\ V_2 \\ V_3 \end{bmatrix} = \begin{bmatrix} Z_{11} & Z_{12} & Z_{13} \\ Z_{21} & Z_{22} & Z_{23} \\ Z_{31} & Z_{32} & Z_{33} \end{bmatrix}_f \begin{bmatrix} I_1 \\ I_2 \\ I_3 \end{bmatrix} \tag{6.4}$$

From Input Port in Figure 6.24:

$$I_1 = \frac{V_i - V_1}{Z_o} \tag{6.5}$$

Where V_i is the input voltage to port1 and Z_o is the characteristic impedance of 50Ω.

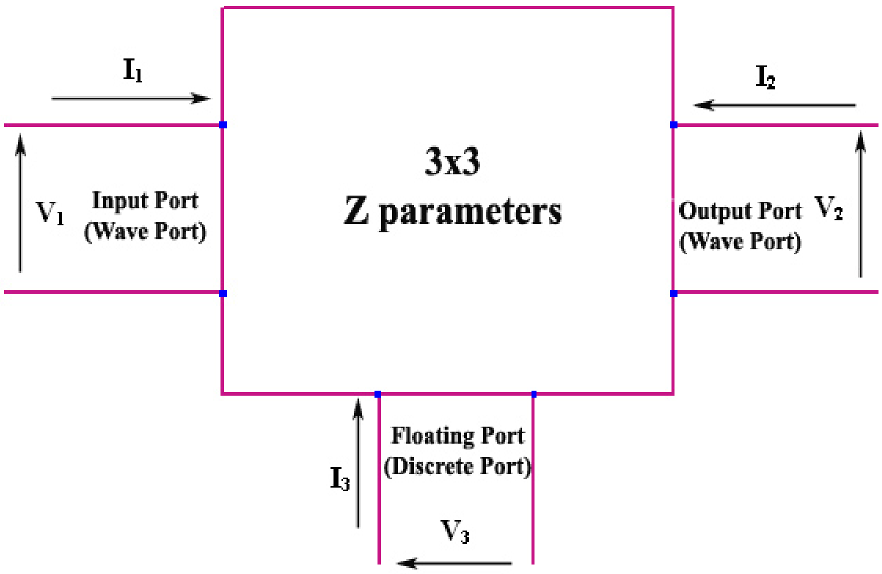

Figure 6.23: Simulated Model in Microwave Studio.

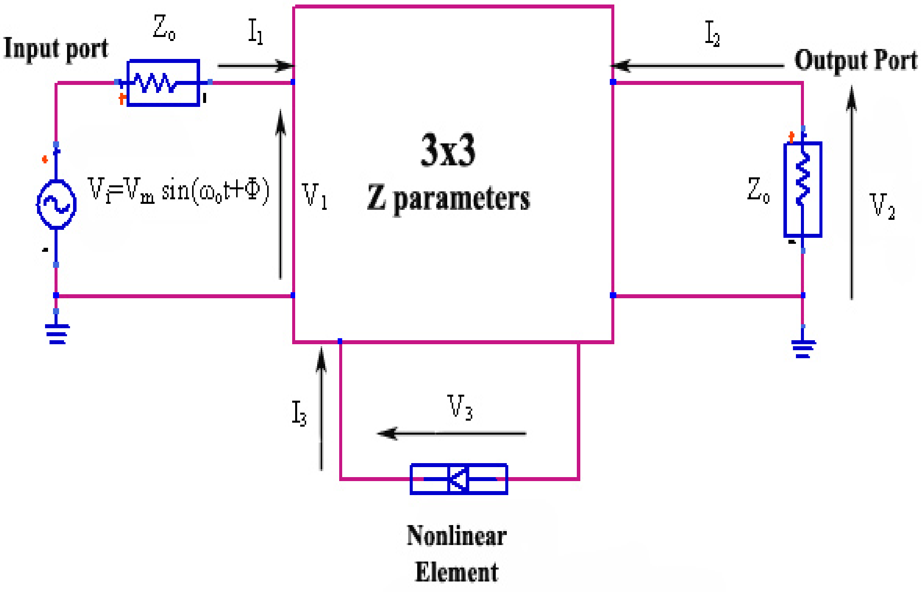

Figure 6.24: Proposed Mathematical Model for TE_{111} mode

From Output Port in Figure 6.24:

$$I_2 = -\frac{V_2}{Z_0} \tag{6.6}$$

From the Diode Model in Figures 6.24 and 6.25:

$$I_3 = I_c + I_d \tag{6.7}$$

Where I_d is the current across the diode and I_c is the current across the capacitor in the diode model as seen in Figure 6.25.

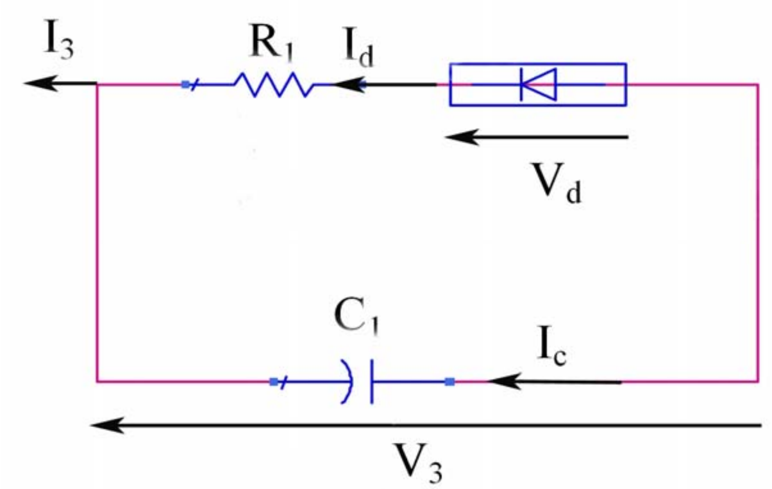

Figure 6.25: Electric circuit model of the nonlinear element in Figure 6.24

From Equation (6.7), I_3 can be further extended to following equation:

$$I_3 = \frac{V_3}{jX_{C1}} + I_d \tag{6.8}$$

Where as

$$I_d = I_o\left(e^{\frac{e}{KT}(V_d)} - 1\right) \tag{6.9}$$

Where e is the Elementary Charge (e=1.60217x10^{-19})

T is the Temperature in Kevin (T=300K)

I$_o$ is the Reserve current (I$_o$=1.0x10^{-14})

k is the Boltzmann Constant (k= 1.3806503x10^{-23})

And since:

$$V_3 = V_d + I_d R_1 \tag{6.10}$$

Substituting the Equations (6.5 to 6.10) into (6.4), the following expression can be obtained:

$$\begin{bmatrix} V_1 \\ V_2 \\ V_d + I_d R_1 \end{bmatrix} = \begin{bmatrix} Z_{11} & Z_{12} & Z_{13} \\ Z_{21} & Z_{22} & Z_{23} \\ Z_{31} & Z_{32} & Z_{33} \end{bmatrix}_{TE_{111}} \begin{bmatrix} \frac{V_i - V_1}{Z_o} \\ -\frac{V_2}{Z_o} \\ \frac{V_d + I_d R_1}{jX_{c1}} + I_d \end{bmatrix} \tag{6.11}$$

Where R$_l$=106.5 and C$_l$=1.5 fF obtained from paper [18]. V$_i$ is the input voltage to Port1.

Since the e, K,T, Io are known parameters, therefore, Equation (6.9) can be simplified as follows:

$$I_d = I_o\left(e^{\frac{e}{KT}(V_d)} - 1\right) = 1.0x10^{-14}\left(e^{38.6815(V_d)} - 1\right) \tag{6.12}$$

By assuming the input voltage and substitute the Z-parameters of TE_{111} into the Equation (6.11), the parameters V_1, V_2 and V_d can be found. Then, the input power of the mathematical model can be computed by using $P_{in} = 0.5\,Re\left(V_1 \times I_1^{\,*}\right)$ (where '*' is the complex conjugate).

Once the V_d is obtained, it can be used as the excitation source to the previous input and output ports, hence, the electrical circuit can be modified as shown in Figure 6.26. Thus the following set of equations can be established as follows:

$$\begin{bmatrix} V_1 \\ V_2 \\ V_3 \end{bmatrix} = \begin{bmatrix} Z_{11} & Z_{12} & Z_{13} \\ Z_{21} & Z_{22} & Z_{23} \\ Z_{31} & Z_{32} & Z_{33} \end{bmatrix}_{TE113} \begin{bmatrix} \dfrac{-V_1}{Z_o} \\ -\dfrac{V_2}{Z_o} \\ \dfrac{V_3 - V_d}{Z_o} \end{bmatrix} \tag{6.13}$$

By substituting the V_d from the solution of equation (6.11) to equation (6.13), V_1 , V_2 and V_3 can be gained. Hence, the output power on port 2 can be calculated by $P_{out} = 0.5 * Re\left(V_2 \times I_2^*\right)$

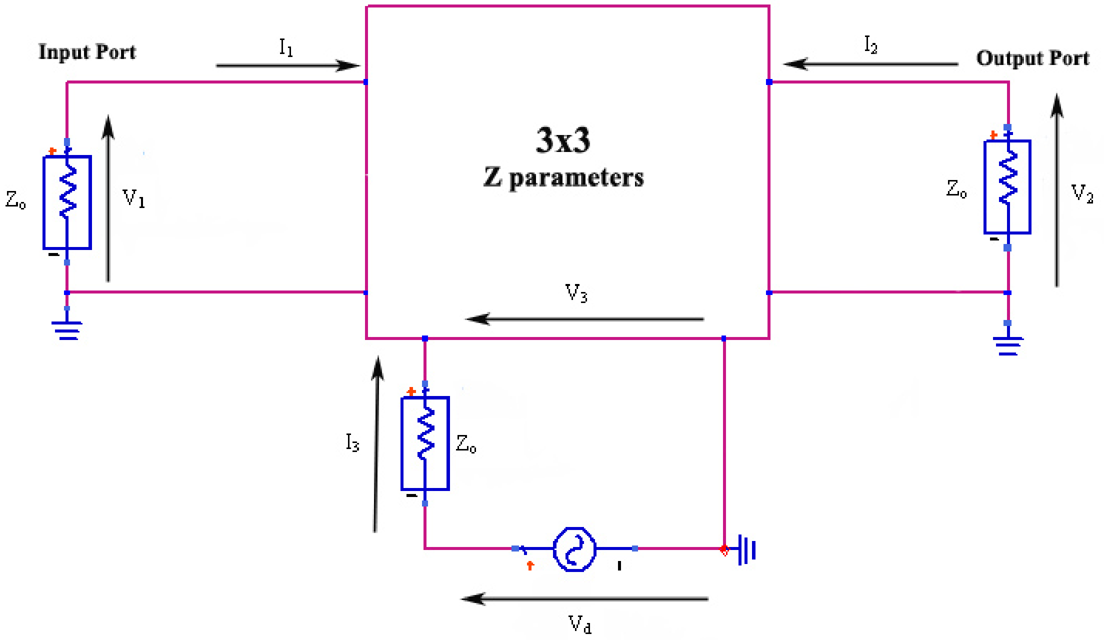

Figure 6.26: Proposed Mathematical Model for TE_{113}

6.7.2 Simulation and Results

Table 6.2 shows the result obtained from the proposed mathematical model presented in the previous section, while Figure 6.27 illustrates the variation of the second harmonic against the input power. These results were computed when each end of the diode is connected to a wire of length 1mm and radius of 0.65mm. It is well known that these particular short leads and unmatched load at port 3 at the present operating frequencies (floating port that describes the inclusion of the active device), the power level of the second harmonic is very low. It can be easily noticed that the generated power level of the second harmonic (at TE_{113}) increases linearly with the input power at TE_{111} mode. In general, the presented results will state the confidence of the proposed method to predict the equivalent nonlinear function of active devices.

Table 6.2: Input power versus Second Harmonic Power

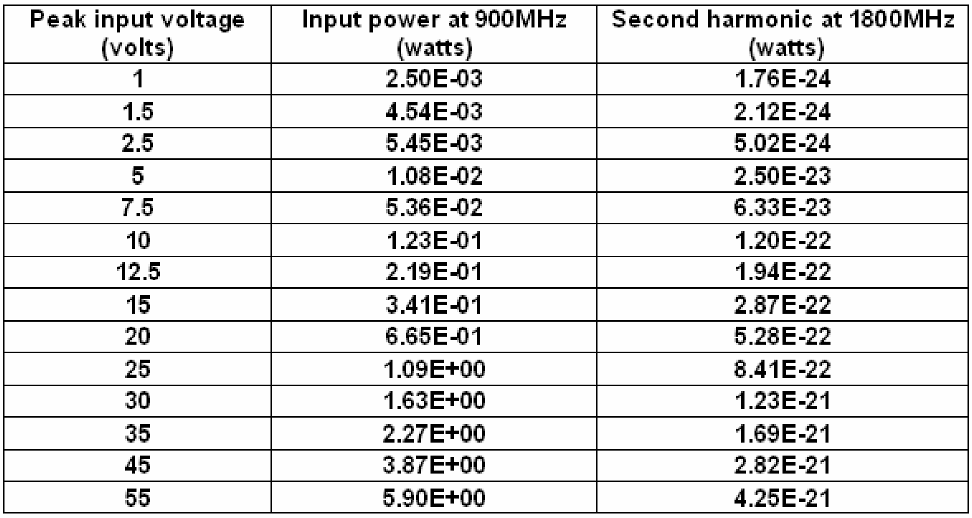

Peak input voltage (volts)	Input power at 900MHz (watts)	Second harmonic at 1800MHz (watts)
1	2.50E-03	1.76E-24
1.5	4.54E-03	2.12E-24
2.5	5.45E-03	5.02E-24
5	1.08E-02	2.50E-23
7.5	5.36E-02	6.33E-23
10	1.23E-01	1.20E-22
12.5	2.19E-01	1.94E-22
15	3.41E-01	2.87E-22
20	6.65E-01	5.28E-22
25	1.09E+00	8.41E-22
30	1.63E+00	1.23E-21
35	2.27E+00	1.69E-21
45	3.87E+00	2.82E-21
55	5.90E+00	4.25E-21

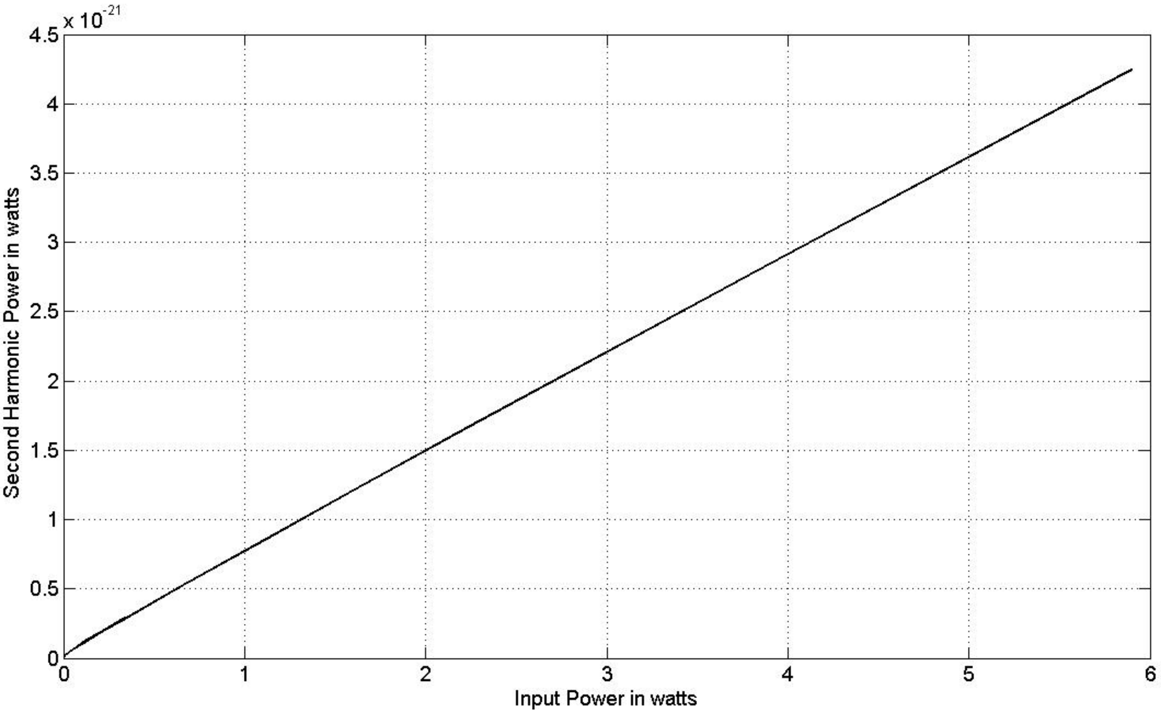

Figure 6.27: Input Power of Port1 versus second harmonic power of Port2

6.8 Biological sample modelling in the cavity

New computer simulation studies were commissioned to investigate on what is the basis for determination of the maximum permissible input signal which can keep the accepted safety thresholds of the sample, in which it must not to be so high to damage the sample under test. By using two different EM software packages (CST Microwave Studio and Agilent HFSS), the field strength in the sample region as function of input power, is computed. Two media samples were considered: air ($\varepsilon_r = 1$, $\sigma = 0$) and generic biological medium ($\varepsilon_r = 50$, $\sigma = 1$ S/m), with the volume 60μl. This 60μl lossy medium is modelled as a cylindrical structure with diameter of 17.5mm and height of 62.36 μm. The results were a little surprising, in showing only a modest difference between air and biological medium, but have been checked and show agreement between the two packages, as reported in Table.6.3.

The International Commission on Non-Ionising Radiation Protection (ICNIRP) limit for SAR is 2 W/kg [19] , in which it has been argued to include a large and poorly quantified safety factor. The National Radiological Protection Board (NRPB) [20] formerly argued that its limit of 10W/kg was more realistic, although that would also include some safety factor and hence it is felt that the option of going up to 100 W/kg should be available to the experiment. Thus we have:

$$SAR = \sigma E^2_{peak}/2\rho$$

Hence: $$E_{peak} = (2\rho.SAR/\sigma)^{0.5}$$

Taking SAR = 100 W/kg again as the upper target, and using reasonable approximations ρ = 1000 kg/m^3 and σ = 1 S/m, we found E_{peak} = 447 V/m. This field strength is considered within the sample, and the value outside could be higher, depending on its orientation. From the SAR calculations, it shows that the induced maximum electric field is about 447V/m when SAR = 100W/kg is considered. This gives indication that the maximum power of order 250mW (from the Table 6.3) is suggested for the experiment.

Table 6.3: Electric Field intensity in the cavity with and without the presence of the biological tissue

			Microwave Studio	HFSS	Microwave Studio	HFSS
			(air)	**(air)**	**Bio.medium**	**Bio.medium**
Voltage(V)	**Power (W)**	**Power(dBm)**	**E-Field (V/m)**	**E-Field (V/m)**	**E-Field (V/m)**	**E-Field (V/m)**
0.2410	0.0005	-3.0103	22.2000	22.7000	19.0000	20.2200
0.2951	0.0008	-1.2494	27.1000	28.7200	23.2000	25.6000
0.3408	0.0010	0.0000	31.3000	32.1000	26.8000	28.6100
0.5388	0.0025	3.9794	49.6000	50.7700	42.4700	45.2400
0.7620	0.0050	6.9897	70.1000	71.8000	60.0200	64.0000
1.0000	0.0086	9.3500	92.0000	94.1600	78.7400	82.0000
1.0776	0.0100	10.0000	99.1000	101.5000	84.8100	88.4000
1.3198	0.0150	11.7609	121.0000	124.0300	103.5600	108.0200
1.5240	0.0200	13.0103	140.0000	143.6000	119.8200	123.0640
1.7039	0.0250	13.9794	157.0000	160.0000	134.3700	137.1100
1.8665	0.0300	14.7712	172.0000	175.8700	147.2000	150.7100
2.1553	0.0400	16.0206	198.0000	203.0000	169.4600	174.2000
2.4097	0.0500	16.9897	222.0000	227.0000	190.0000	194.0000
3.4078	0.1000	20.0000	313.0000	321.0900	269.0000	283.0000
5.3882	0.2500	23.9794	496.0000	507.7000	424.5000	430.5000
7.6201	0.5000	26.9897	701.0000	717.9000	600.0000	620.4000
9.3327	0.7500	28.7506	870.0000	879.3000	750.6000	783.1400
10.7760	1.0000	30.0000	991.0000	1015.0000	849.0000	904.0000

6.9 Measurement

This section is devoted to demonstrate the experimental work for detection the second harmonic. Firstly, the S parameters for port 1 and 2 was carried out using HP Network Analyser 8720B, Anritsu Synthesized Signal Generator MG3632A and Anritsu spectrum Analyser MS2802A, as shown in Figure 6.28. The cavity with height of 272mm and diameter of 248mm, is gold plated aluminum to suppress sources of nonlinearity.

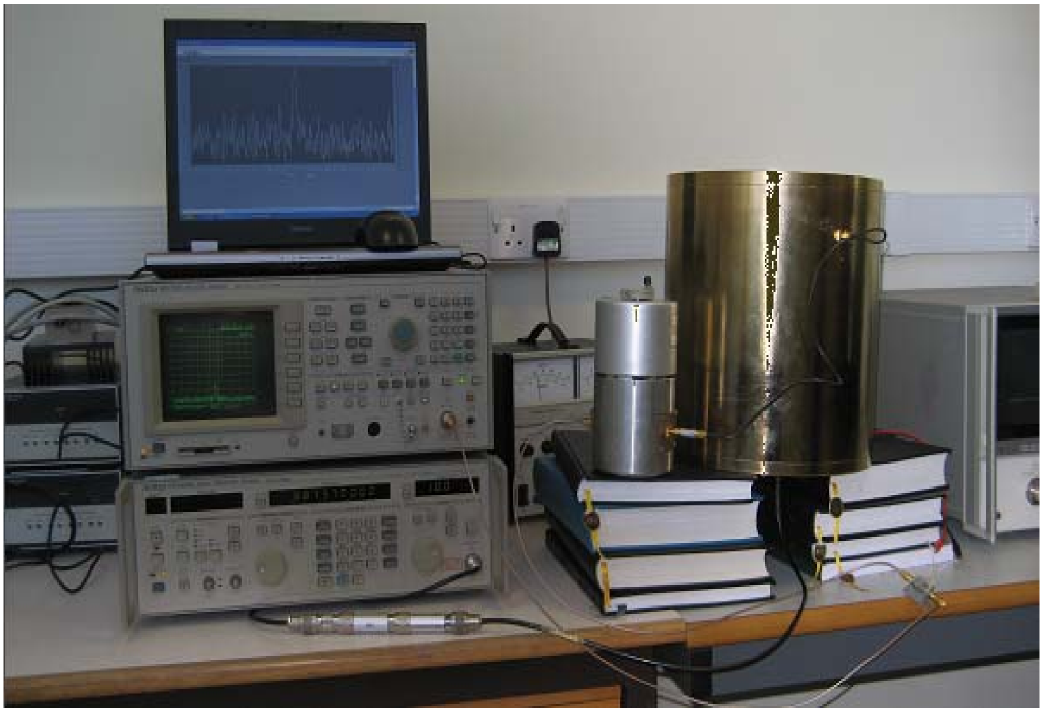

Figure 6.28: Experiment Setup in MSCRC (Mobile and Satellite Research Centre), University of Bradford.

6.9.1 Doubly resonant Cavity

Figure 6.29 depicts the inner geometry of the cavity. As can be observed, a plastic bio-preparation support structure is glued in the centre of the cavity, while the transmitting loop antenna sensor is located at the bottom of the cavity and the receiver loop antenna sensor is mounted on the top side of the cavity in which the position of the maximum TE_{113} field occurs. The size dimensions of the transmitter and receiver sensors are considered to be 6.1cm x 1.4 cm and 2.2cm x 1.5cm respectively. A fine tuning was applied for both sensors to achieve the resonance frequency between 880 MHz and 890 MHz at port 1 and 1760 MHz and 1780 MHz at port 2.

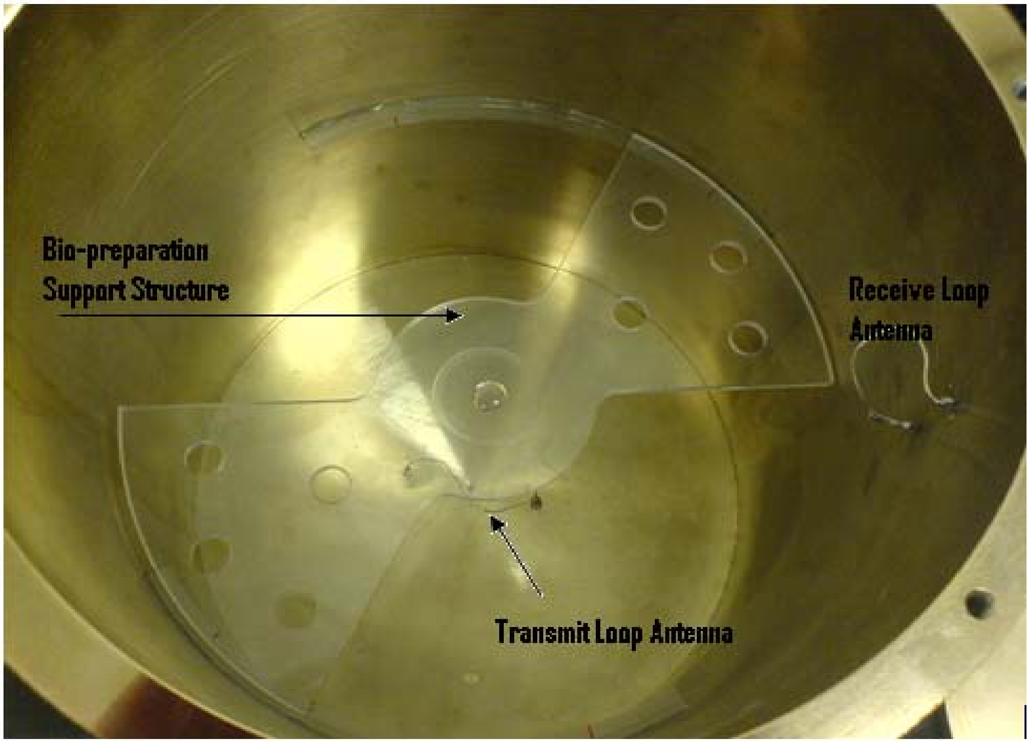

Figure 6.29: Gold plated cylindrical cavity with bio-preparation support structure and two ports sensors.

By doing the fine tuning, the resonance frequency of 0.8883GHz was found, in which a good return loss was obtained at 1.7766 GHz at port 2 as shown in Figure 6.30. This procedure was adjusted again when different loading effects analysis was required such as adding water into the Petri dish inside the cavity; however, it was found that the resonant frequency of both ports shifted around 0.6MHz to the lower frequency band, as illustrated in Figure 6.30.

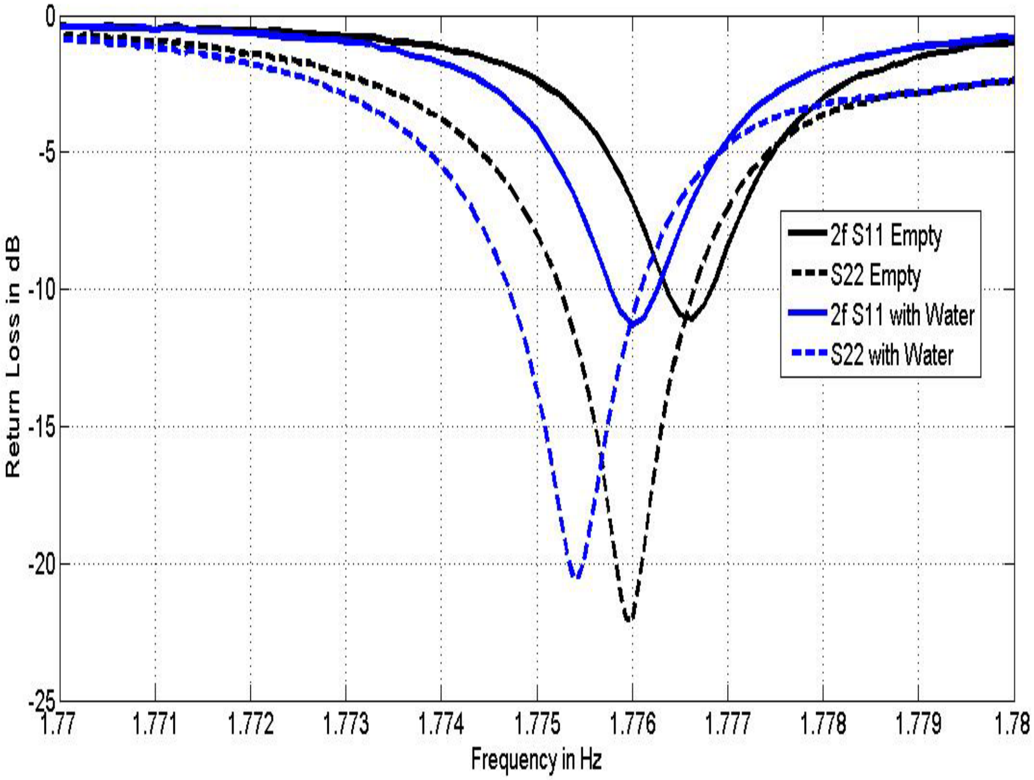

Figure 6.30: The fundamental and second harmonic response of the gold plated cavity

6.9.2 Summary of Methods and Results

The proposed detection system, in principle, will be conducted in the following three phases, these are:

(i) Testing the orientation of the Schottky diode inside the cavity, as illustrated in Figures 6.31 and 6.32.

(ii) Check the sensitivity of the second harmonic corresponding to different length of diode lead, as depicts in Figure 6.33.

(iii) Investigating the effects of non-biological liquids to the diode, as illustrated in Figure 6.34.

The input power is constantly set to 10dBm of all cases of the analysis in phases (i) to (iii).

Figure 6.31: Orientation of the diode parallel to the transmitted antenna.

Figure 6.32: Orientation of the diode orthogonal to the transmitted antenna

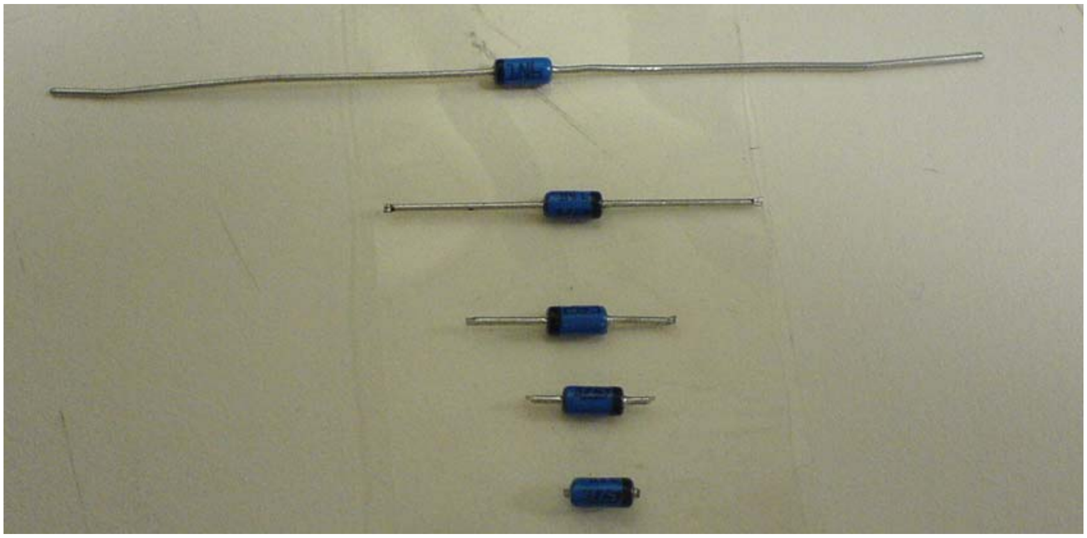

Figure 6.33: UHF diode with different length of leads

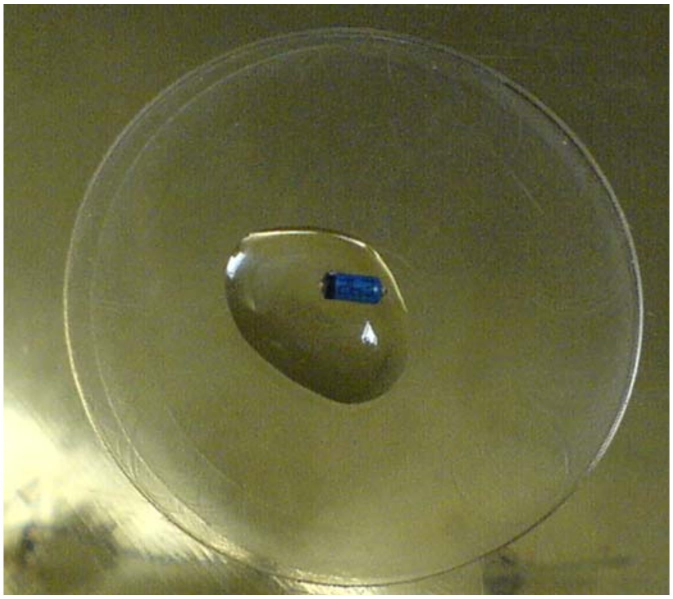

Figure 6.34: UHF diode without leads and loaded with 60µl water

Preliminary experiment is commissioned according to the test bed shown in Figure 6.35. On the input port, Anritsu Synthesized Signal Generator MG3632A is used to generate the input signal to the bottom sensor at 0.8883GHz. Two stages of low pass filters are used to suppress frequencies above 1 GHz that will reduce any effect of generation of the second harmonic products generated by the input generator. On the output port, An Anritsu spectrum Analyser MS2802A is set to display the expected second harmonic frequency component (i.e., twice the fundamental frequency component), at a minimum bandwidth of BW = 1.7766GHz ±100kHz. High pass filter and narrow band pass filter are exploited to ensure at least -60 dB unwanted frequency rejection of the fundamental frequency component.

Two sets of measurements results were observed, the first one, no amplification implemented and the other with two stages power amplifier as shown in Figure 6.35. For phase (i) when the diode is oriented in parallel to the transmitting antenna, as broadly expected, a strong generation of second harmonics was observed on the spectrum analyzer. However, no notice on the existence of the second harmonic was recorded when the orientation of the diode is moved to the position orthogonal to the transmitting sensor. The measurement results are summarized as follows:

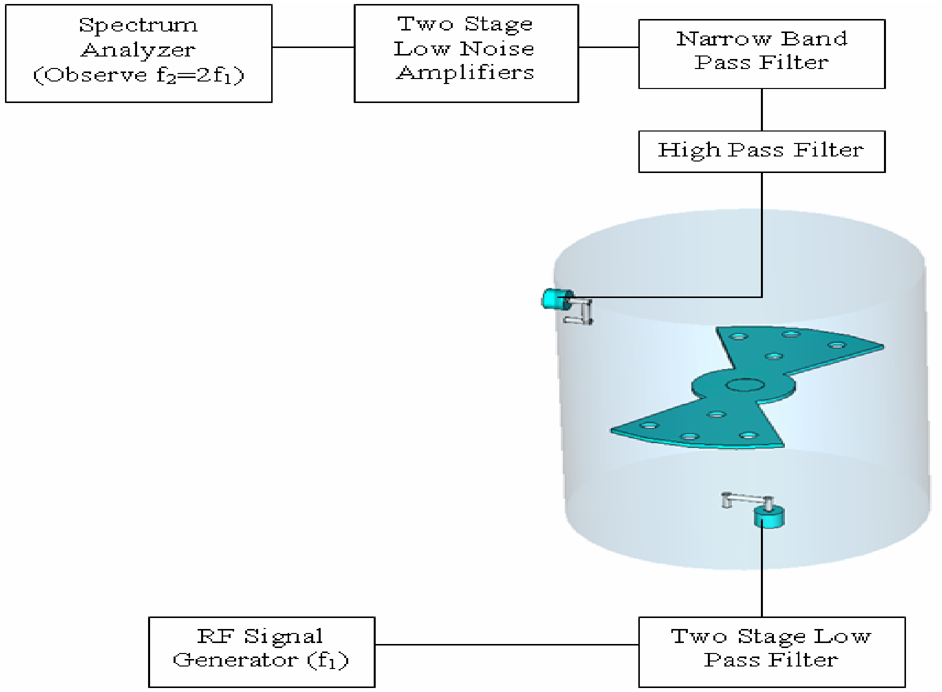

Figure 6.35: Test bed of the experimental setup used for detection the second harmonic.

6.9.2.1: Without the Power Amplifiers:

The experimental results for phases (ii) and (iii) are shown in Figure 6.36. As can be noticed, the minimum noise floor of -115dBm was observed, and as the length of the diode leads gradually reduce from 28mm to 0mm, the second harmonic signal strength is dropped down linearly from -58dBm to -108dBm in which the corresponding difference between the noise floor and second harmonic signal are varied between 57dBm to 7dBm. It is discovered that the generation of the second harmonic by the diode without leads, is indistinguishable with the noise signal.

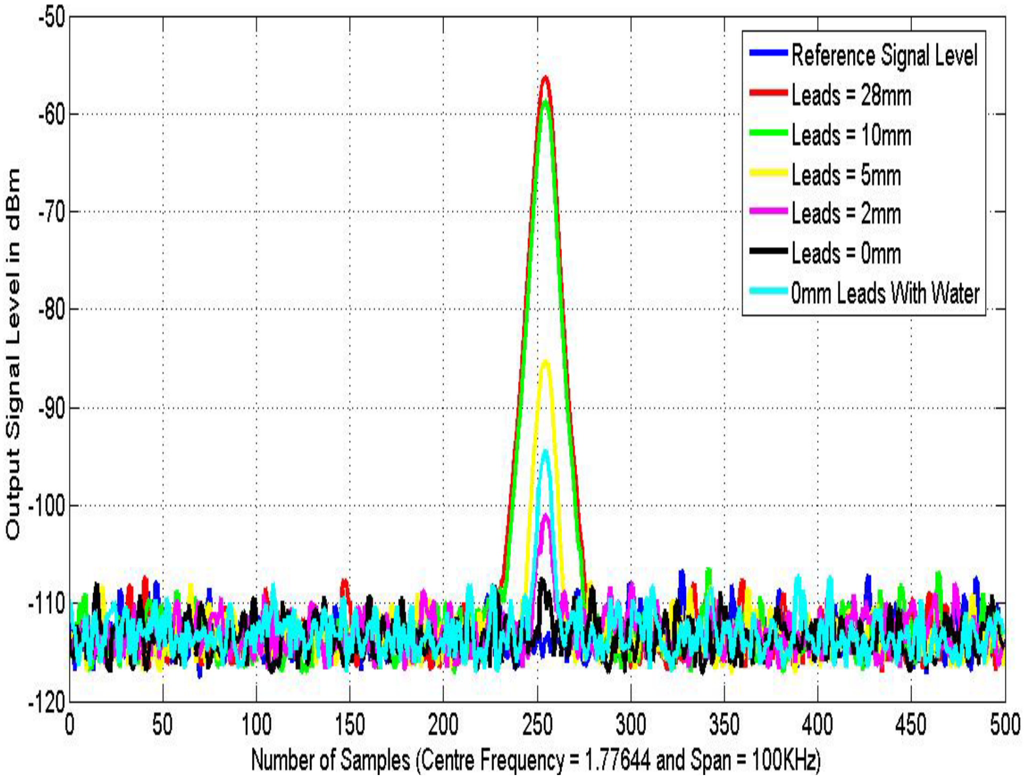

Figure 6.36: Output signal level for detection system without amplification.

Interestingly, when 60µl water is added to the diode without leads, the second harmonic signal was improved from -108dBm to -95dBm i.e., 13dBm improvement in second harmonic power level was noticed.

6.9.2.2. With Power Amplification

In this detection system, two stages power amplifiers were used. The amplifier models are ZRL - 2400 LN and Zel-1724LN enquired from Mini-circuits. Due to these stages, the noise floor of the spectrum analyser was been rose up to -100dBm as elucidated in Figure 6.37. As can be noticed, the second harmonic signal is improved to -62dBm, and when the water was added further increase was achieved by 20dBm (i.e. the power level -42dBm is considered now). This will fully contribute to increase the probability of the expected chances to detect the second harmonic if a biological tissue is considered for test.

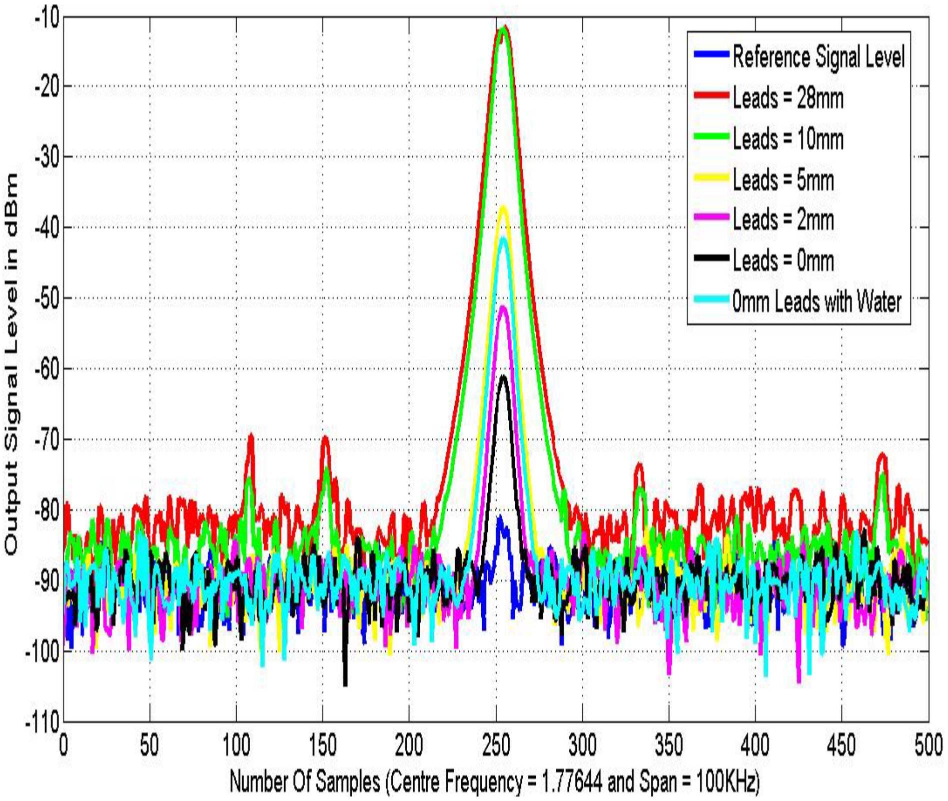

Figure 6.37: Output signal level for detection system with power amplification.

6.10 Conclusions

An efficient way to test the unsymmetrical nonlinear response of biological tissue samples exposed to a 0.9GHz signal is to observe the second harmonic at 1.8GHz in a cavity resonant at the two frequencies. A closed cylindrical cavity model using two rectangular loop antennas for coupling two ports networks was simulated and tested. This also includes loading structure implemented inside the centre of the cavity. The simulated results show that the tuned TE_{113} mode has double the resonant frequency of the TE_{111} mode. The first and second harmonic responses of the cavity due to different loading materials were also demonstrated numerically and experimentally.

Moreover, the level of detectable second harmonic signal from a nonlinear frequency conversion process in the cavity in the presence of known nonlinear diode has been studied. The variations of the second harmonic signal were investigated for different structure orientation of the diode and various diode lead lengths in the cavity. Meanwhile, an electrical circuit model was proposed to calibrate the performance of nonlinear RF energy conversion inside a high quality factor resonant cavity using a known nonlinear loading device. The results from the proposed mathematical model gave a good indication of the input power required to detect the weak second harmonic signal prior to perform the measurement. Hence, this proposed mathematical model will assist in determining the level required of the second harmonic signal: this can be adjusted by supplying the specific input power. On the other hand, the issues on relating signal generator output power to signal strength in the biological sample was also performed. This study will strongly support the requirements of the total power dissipated of the biological samples to estimate the SAR values.

6.11 References

[1] L.J.Challis, "Review Mechanisms for Interaction Between RF Fields and Biological Tissue," *Bioelectromagnetics*, pp. S98-S106, 2005.

[2] S.M.Bawin, R.J.Gavalas, and W.R.Ady, "Effects of modulated very high frequency fields on specified brain rhythms in cats," *Br Res 58:*, pp. 365-384, 1973.

[3] C.F.Blackman, J.A.Elder, C.M.Weil, S.G.Benane, D.C.Eichinger, and D.E.House, "Induction of calcium ion efflux from brain tissue by radio-frequency radiation: Effects of modulation frequency and field strength," *Radio Science 14(6s):*, pp. 93-98, 1979.

[4] W. R. ADEY, "Frequency and power windowing in tissue interactions with weak electromagnetic fields," *Proc. IEEE*, vol. 68, pp. 119-125, 1980.

[5] S.K.Butta, A.Subramaniam, B.Ghosh, and R.Parshad, "Microwave radiation-induced calcium efflux from brain tissue, in vitro," *Bioelectromagnetics*, vol. 6, pp. 1-12, 1984.

[6] B.Lyle, P.Schechter, W.R.Adey, and R.L.Lundak, "Suppression of T-lymphocyte cytotoxicity following exposure to sinusoidally amplitude-modified fields," *Bioelectromagnetics*, vol. 4, pp. 281-292, 1983.

[7] Q.Balzano and A.Sheppard, "RF Nonlinear Interactions in Living Cells –I: Nonequilibrium Thermodynamic Theory," *Bioelectromagnetics*, pp. 473-482, 2003.

[8] Q.Balzano, "RF Nonlinear Interactions in Living Cells-II: Detection Methods for

Spectral Signatures," *Bioelectromagnetics*, pp. 483-488, 2003.

[9] Q.Balzano, "Proposed Test for Detection of Nonlinear Reponses in Biological Preparations Exposed to RF Energy," *Bioelectromagnetics*, pp. 278-287, 2002.

[10] I.Ahmed, P.S.Excell, and R.A.Abd-Alhameed, "Is a rectifying junction essential for demodulation of modulated waveforms in tissue?" *Bioelectromagnetics Society Conference*, pp. 289-290, June 2005.

[11] I.Ahmed, P.S.Excell, and R.A.Abd-Alhameed, "Is a square-law junction essential for demodulation of modulated waveforms in Tissue?" *COST 261-Workshop*, pp. 32-33, 17th-18th Feb 2005.

[12] I.Ahmed, P.S.Excell, and R.A.Abd-Alhameed, "Nonlinear and Demodulation Mechanisms in Biological Tissues," *Proceedings of the Seventh Informatics Workshop for Research Students, University of Bradford, UK*, pp. 115-118, March 2006.

[13] I.Ahmed, P.S.Excell, and R.A.Abd-Alhameed, "Nonlinear and demodulation mechanisms in biological tissues," *Proceedings of the eighth Informatics workshop for research students,University of Bradford, Bradford,UK*, pp. 16-19, 28 June 2007.

[14] D. M. Pozar, "Microwave Engineering," 3rd ed: John Wiley & Sons, Inc., 2005, pp. 14-44.

[15] *CST Microwave Studio*: Germany.

[16] J.X.Zhao, "Numerical dosimetry for cells under millimetre-wave irradiation using Petri dish exposure set-ups," *Phys.Med. Biol.*, vol. 50, pp. 3405-3421, 2005.

[17] G. Emili, A. Schiavoni, F. L. Roselli, and R. Sorrentino, "Computation of electromagnetic field inside a tissue at mobile communications frequencies," *IEEE Trans on MTT*, vol. 51, pp. 178-186, 2003.

[18] Z.Hu, V.T.Ho, and A.A.Rezazadeh, "High Tangential Signal Sensitivity GaAs Planar Doped Barrier Diodes for Microwave/Millimeter-Wave Power Detector Applications," *IEEE MICROWAVE AND WIRELESS COMPONENTS LETTERS*, vol. 15, pp. 150-152, 2005.

[19] ICNIRP, "Guidelines for limiting exposure to time-varying electric, magnetic and electromagnetic fields (up 300 GHz)," *Health Physics*, vol. 56, 1998.

[20] N.R.P.B, "Board statement on restrictions on human exposure to static and time varying electromagnetic fields and radiation," *Documents of the NRPB*, vol. 4, 1993.

Chapter 7

Conclusions and Suggestions for Further Work

7.1 Conclusions

This Chapter summarises the conclusions arising from the earlier Chapters. It also includes a section on the future possibilities arising from this work. The primary target of this presented work is to model the interaction mechanism between the biological cells and electromagnetic field at mobile communication frequency by implementing FDTD numerical method. In microscopic level of modelling biological cells, the computational power required is extremely huge. In order to tackle this problem with affordable computational resources, quasi-static FDTD with floquet periodic boundary conditions and modified Berenger’s PML are proposed to represent an infinite cluster of cells in computational domain.

The main original achievements of the present thesis can be summarised as follows:

- The implementation of FDTD code procedures with Berenger’s PML absorbing boundary condition were demonstrated in chapter 2. It was encompassed the fundamental derivation of time domain finite difference updating equations to solve the Maxwell’s curl equations, discussion of the critical parameters which govern the stability and accuracy of the FDTD algorithm, formulation of incident plane wave source excitations and Berenger’s PML absorbing boundary conditions.

- Based on the circuit theory to derive the relationship between the E and H fields and voltages and current, Chapter 3 extends the FDTD updating equations which are derived from chapter 2, to include the lumped element (resistor, capacitor, inductor and etc.) into the FDTD computational domain. This allows arbitrary microwave circuit to be analysed into the FDTD lattice. In addition, the presence of intrinsic capacitance due to the adjacent cells in FDTD grid can store charge, is also well addressed in this chapter.

- Chapter 4 proposes a frequency scaled FDTD or Quasi-static FDTD approach to modelling the electrical small object which is much smaller than a wavelength. This chapter begins with discussion the incident plane wave characteristic in free space, lossless and lossy media. Then, the Mie series analytical solutions for sphere with arbitrary concentric layers are formulated concisely and systematically. In order to validate the proposed frequency scaled approach, four test cases based on the spherical geometry in different media are carried out. The first two test cases were adopted from paper [1] which analyse the electric field at power line frequency (60Hz) of single layer and multiple layers of conductive sphere in free space. Due to the size of the sphere is negligible compared to wavelength of 60Hz, the FDTD computation can be performed at scaled higher frequency of 20MHz which is still a few tens wavelength larger than the conductive sphere. The analytical solutions are in excellent agreement to the proposed QS-FDTD algorithm. The numerical results give very promising evidence that written FDTD Fortran code is working perfectly. These results motivate this work to further extend to model conductive sphere in lossless and lossy media at mobile frequency. The obtained numerical results from last two test cases again show good agreement to the analytical solution.

➢ Chapter 5 implementing the idea of frequency scaled FDTD from previous chapter incorporate with Floquet periodic boundary conditions and modified PMLs to microdosimetric modelling of bioelectromagnetic interactions at cellular level. In order to include the membrane effect on the biological tissues model in the analysis, the LE-FDTD is exploited to embed the Hodgkin-Huxley cell-membrane model on the surface of the proposed tissue model in the FDTD computational domain. Three different types of the biological tissue are modelled, which are made by a cluster of spherical, cubical and cylindrical cells respectively. Floquet periodic boundary conditions are imposed on the proposed model to imitate the effect of periodic replication of the assemblages. Thus, the analysis of a large structure of cells is made more computationally efficient than the modelling of the entire structure. The total fields of the simulated structures are shown to give reasonable and stable results at 900MHz, 1800MHz and 2450MHz. This leads to the conclusion that the application of the HH model allows cells of arbitrary geometries to be handled and demonstrates the viability of embedding other types of lumped-element model for membrane function. Moreover, use of the Floquet boundary condition enables a non-trivial region of connected biological tissue to be simulated. Such a tool will facilitate deeper investigation of the phenomena in the interaction between EM fields and biological systems at various levels of spatial definition.

- Chapter 6 is devoted to propose a detection system to assist the investigation of whether biological cell exhibit nonlinearity in the radiofrequency (RF) region. An efficient way to test the unsymmetrical nonlinear response of biological tissue samples exposed to a 0.9GHz signal is to observe the second harmonic at 1.8GHz in a high quality cavity resonant at the two frequencies. The presented works are firstly performed by using CST microwave studio software to model a doubly resonant high quality cavity [2]. With the aids of the GUI of the software, the field distribution of the cavity at TE_{111} and TE_{113} modes can be visualised, in order to identify the best location to place the transmit loop antenna, support structure for the bio-preparation and receive loop antenna for better chances of second harmonic detection. The transmitter and receiver antenna sensors were successfully designed to operate at 880-890MHz and 1760-1790 MHz respectively. This will enhance the receiver sensor to receive energy at twice the frequency of the transmit antenna sensor. The cavity was calibrated by verifying the second harmonic generation from a known nonlinear diode. This gave indication on what is the dynamic range required for the practical measurement for detection of the expected second harmonic. Moreover, a proposed circuit model was carried out to more precisely quantify the amount of input power required in the excitation port to generate a detectable second harmonic signal. Finally, an experimental work was implemented and the measured results were compared with the numerical results.

7.2 Overall Conclusions

The combination of quasi-static FDTD, an arbitrarily-oriented lumped element membrane model, the modified Berenger’s absorbing boundary condition and the Floquet periodic boundary condition represent a significant advance in verisimilitude of biological cell modeling. This is because it permits the computationally-efficient FDTD method to model small cell size object with reasonable computing time and accuracy.

The proposed numerical modelling and experimental work for the detection of nonlinear responses in biological cells exposed to RF energy, give the clear procedures on how to perform the nonlinearity test on the biological sample and what precautious have to be taken into consideration. Interestingly, both the numerical and measured results were in good agreement.

7.3 Suggestions for Further Works

Finally, this work can be extended for further research with the following suggestions:

➢ A further work on the electromagnetic field interaction mechanism with biological tissue can be extended to modify the Floquet boundary condition to allow oblique plane wave incidence to excite the proposed model and study the effect of polarization of the incident wave against the field distribution inside the proposed tissue model. This can be done by implementing the proposed techniques in [3-5].

➢ Standard FDTD suffers from staircase error [6] in which a complex geometries can not be accurately modelled. Nonorthogonal curvilinear FDTD algorithm [7] might be employed for future FDTD code that will be able to model the exact cell geometry instead of the spheres, cuboids or cylinders, as described in the present work.

- ➢ The proposed QS-FDTD and Floquet boundary condition can further utilise to develop a fine modelling of a particular portion of the human head or body to precisely investigate the EM interaction mechanism.

- ➢ The presented tissues model only use one FDTD cell to represent the tiny membrane layer of the biological cell. In order to increase accuracy of the model, a further work can be extended to incorporate the sub-gridding algorithm [8] or adaptive meshing technique [9] to increase the mesh cells on the membrane of the cells. This will help to better understanding the field distribution inside the cell membrane.

- ➢ It is very interesting to use the present work to include sub-surface radar application in which breast cancer cells might exist for modelling purposes, to obtain accurate electric field distribution inside the breast tissue.

- ➢ The analysis on the RF interaction mechanism with biological tissue that was performed at mobile frequency at the present work can be expanded to include the EM interaction mechanism at power line operating frequency (i.e., 50Hz or 60Hz) at indoor or outdoor environments.

- ➢ The research work presented here can be easily extended to study the SAR variation values inside the cytoplasm of the cells.

- A further work for the proposed cavity model is to conduct the experimental test with live biological tissue in which the nonlinearity responses can be easily derived.

7.4 References

[1] O.P.Gandhi and J.Chen, "Numerical dosimetry at power-line frequencies using anatomically based models," *Bioelectromagnetics*, vol. 1, pp. 43-60, 1992.

[2] Q.Balzano, "Proposed Test for Detection of Nonlinear Reponses in Biological Preparations Exposed to RF Energy," *Bioelectromagnetics*, pp. 278-287, 2002.

[3] W.L.Ko and R.Mittra, "Implementation of Floquet boundary condition in FDTD for FSS analysis," *Proc. 1993 IEEE Antennas and Propagation Society International Symposium*, vol. 1, pp. 14-17, 1993.

[4] D. T. Prescott and N. V. Shuley, "Extensions to the FDTD Method for the Analysis of Infinitely Periodic Arrays," *IEEE Microwave and Guided Wave Letters*, vol. 4, pp. 352-354, 1994.

[5] P.H.Harms, J.A.Roden, J.G.Maloney, M.P.kesler, E.J.Kuster, and S.D.Gedney, "Numerical analysis of periodic structures using the split-field algorithm," *Proc.*

13th Annual Review of Progress in Applied Computational Electromagnetics, Monterey,CA, pp. 104-111, 1997.

[6] A. Akyurtlu, D. H. Werner, V. Veremey, D. J. Steich, and K. Avdin, "Staircasing errors in FDTD at an air-dielectric interface," *IEEE Microwave Guided Wave Letters*, vol. 9, pp. 444-446, 1999.

[7] J-F.Lee, R.Palendech, and R.Mittra, "Modeling three-dimensional discontinuities in waveguides using nonorthogonal FDTD algorithm," *IEEE Transactions on Microwave Theory and Techniques*, vol. 20, pp. 346-354, 1992.

[8] A.Vaccan, R.Pontalti, C.Malacarne, and L.Cristoforetti, "A robust and efficient subgridding for finite-difference time-domain simulations of Maxwell's equations," *Journal of Computational Physics*, vol. 194, pp. 117-139, 2004.

[9] Y.Liu and C.D.Sarris, "AMR-FDTD: A dynamically adaptive mesh refinement scheme for finite-difference time-domain technique," *IEEE Antenna and Propagation Society International Symposium*, vol. 1A, pp. 134-137, 2005.

Author's Contribution

ARTICLES IN JOURNALS

1. **C.H. See**, R.A. Abd-Alhameed and P.S. Excell, "Computation of Electromagnetic Fields in Assemblages of Biological Cells Using A Modified Finite Difference Time Domain Scheme", Accepted to IEEE Trans. MTT, March 2007
2. **C.H. See**, R.A. Abd-Alhameed and P.S. Excell, "Proposed Circuit Model for Calibration of Nonlinear Responses in Biological Media Exposed to RF Energy", IEEE Trans.MTT, under review, April 2007.

CONFERENCES AND WORSHOPS

1. **C.H. See**, R.A. Abd-Alhameed, I. Ahmed and P.S. Excell "Proposed Circuit Model for Calibration of Nonlinear Responses in Biological Media Exposed to RF Energy", Proceedings of the Seventh Informatics Workshop for Research Students, University of Bradford, UK, 29th of March 2006, pp.163-166.
2. **C.H. See**, R.A. Abd-Alhammed and P.S.Excell, "Computational modelling of electromagnetics of biological cells using lumped elements in quasi-static FDTD", IPEM (Institute of Physics and Engineering in Medicine), 7-9 September 2005, University of Glasgow, pp. 81-82.
3. **C.H See**, R.A. Abd-Alhameed and P.S. Excell, "Application of Time Domain Floquet Boundary Conditions and Berenger's PML for EM analysis of Biological cells", EMC Europe Workshop 2005, Rome, Italy**,** 19-21 September 2005, pp.415-418.
4. **C.H. See**, R.A. Abd-Alhameed and P.S. Excell, "Lumped-Element FDTD Modelling of the Surface Membrane of Biological Cells", Proceedings of the Sixth Informatics Workshop for Research Students, University of Bradford, UK, 23rd of March 2005, pp.153-156.
5. **C.H. See**, R.A. Abd-Alhameed and P.S. Excell, "Electromagnetic Modelling Biological Tissues Equivalent Cluster of Spheres Using LE-FDTD ", Accepted to be published in International Union of Radio Science(URSI) Conference, New Delhi India, October 23-29 2005.
6. **C.H. See**, R.A. Abd-Alhameed and P.S. Excell, "Biological cell modelling using quasi-lumped-element FDTD method", Bioelectromagnetics Society Conf., June 19-24 Dublin, Ireland, 2005, pp.552-555.
7. **C.H. See**, R.A. Abd-Alhameed, M. Mutardi, P.S. Excell and J. Vaul, "Quasi-static FDTD scheme for electrically-small regions in free space and lossless or lossy penetrable media", 5th International Conference in IEE CEM, pp.155-156, April 2004.

8. M. Mutardi, **C.H. See**, R.A. Abd-Alhameed, P.S. Excell and J. Vaul, “Biological cell modeling using Quasi-Static FDTD/Lumped Elements method,” 5th Informatics workshop for research student, University of Bradford, paper. No 27.pp.105-110, March 2004.
9. **C.H. See**, R.A. Abd-Alhameed, P.S. Excell, G. Qasim and J. Vaul, “Biological cell modeling using Quasi-Static FDTD/Lumped Elements method”, 8th IEEE International Multi-topic conference (INMIC 2004) proceedings, NUCES FAST, Lahore, Pakistan, pp.553-559, 24-26 December 2004.
10. **C.H. See**, R.A. Abd-Alhameed, M. Mutardi, P.S. Excell and J. Vaul, “Quasi-static FDTD scheme for electrically-small regions in free space and lossless or lossy penetrable media”, URSI, University of Leeds, Paper No. B6, June 2003.
11. **C. H. See**, R A Abd-Alhameed and P S Excell, “Fields distribution inside biological cells using Quasi-static Finite-Difference Time-Domain”, BA (British Association) Perspectives awards 2003 for young scientists in the North West region, University of Salford, 8-12 Sept, 2003.
12. A.G. Temtam, R.A. Abd-Alhameed, P.S. Excell and **C.H. See**, “Simulation of Antenna design for multiple-input multiple-output (MIMO) wireless communication systems”, URSI national Symposium, commission B fields and Waves, University of Bath, Paper No.2, 5-6 July 2004
13. R. Alias , R.A. Abd-Alhameed, P.S. Excell and **C.H. See**, “Modified Hybrid method between the finite element method and finite difference time domain”, URSI national Symposium, commission B fields and Waves, University of Bath, paper No.1., 5-6 July 2004
14. R.A. Abd-Alhameed, N.T. Ali, P.S. Excell, M.K. Atiya and **C.H. See**. "Beam steering antenna array for mobile base stations", (ref. SSD05-CSP-118) to the Third IEEE International Conference on Conference on Systems, Signals & Devices SSD'05, March in Sousse, Tunisia, 2005.
15. **C. H. See**, R A Abd-Alhameed and P S Excell, “ Design of Folded and Slotted Internal Antenna for 3G IMT-2000 Mobile Handset”, Proceedings of International Union of Radio Science(URSI) Conference, New Delhi India, October 23-29 2005.
16. **C. H. See**, R A Abd-Alhameed, P S Excell, F.Hu and J.G. Gardiner, “Design of a Internal Triple Band Folded Planar Monopole Antenna for Third Generation Mobile Handsets”, WNCG Hosts 2005 Texas Wireless Symposium, University of Texas at Austin (USA), October 26-28, 2005.
17. **C.H. See**, R.A. Abd-Alhameed, P.S. Excell and Y.F.Hu “ Design of Internal Triple-Band Folded Planar Antenna for Third Generation Mobile Handsets”, Proceedings of the Sixth Informatics Workshop for Research Students, University of Bradford, UK, 23th of March 2005, pp.157-160
18. K. Khalil, **C.H. See**, R. Alias, R.A. Abd-Alhameed, P.S. Excell and Y.F. Hu “Reduced-Size Circular-Polarised Microstrip Antennas For Satellite Mobile Communication”, Proceedings of the Sixth Informatics Workshop for Research Students, University of Bradford, UK, 23rd of March 2005, pp.84-87.

19. F.A. Siddiqui, R.A. Abd-Alhammed and **C.H. See**, " Circularly Polarised Microstrip Patch Antenna for Satellite Communications", 9Th IEEE International Multi-topic Conference (INMIC 2005) Proceedings, NUCES FAST, Lahore, Pakistan, 23-25 December 2005, pp.1-3
20. **C.H. See**, A. Adelowokan, R.A. Abd-Alhameed and P.S. Excell "Ultra-Wide Bandwidth Curved Surface Square Planar Monopole Antenna", Proceedings of the Seventh Informatics Workshop for Research Students, University of Bradford, UK, 29th of March 2006, pp.161-162.
21. **C.H. See**, A. Adelowokan, R.A. Abd-Alhameed and P.S. Excell "Circular Polarised Microstrip Patch Antennas with Finite Ground for Satellite Communications", Proceedings of the Seventh Informatics Workshop for Research Students, University of Bradford, UK, 29th of March 2006, pp.115-118.
22. R.A. Abd-Alhameed, K. Khalil, P.S. Excell and **C.H. See**, "Simulation and Measurement of broadband microstrip patch antenna for 3G wireless communications", Twelfth International Conference on Antennas and Propagation, ICAP, Vol 2, pp. 477-480 , 31st March to 3rd April 2003.
23. R.A. Abd-Alhameed, N.T. Ali, P.S. Excell, **C.H. See** and J.G. Gardiner, "Broadband Stripline Fed Microstrip Patch Antennas for 3G Mobile Communication",8th IEEE International Conference on Communication System (ICCS 2002), pp1197-1201, 25 to 28 November 2002.
24. **C.H. See**, R.A. Abd-Alhameed and P.S. Excell, "DESIGN OF DUAL-FREQUENCY PLANAR INVERTED F-L-ANTENNA (PIFLA) FOR WLAN AND SHORT RANGE COMMUNICATION SYSTEMS", In proceeding of the 19th UK URSI Colloquium at Cosenor's- House, the Rutherford Appleton Laboratory, Abingdon, Oxford, UK, 3-4 July 2006.
25. **C.H. See**, R.A. Abd-Alhameed, K. Khalil, P.S. Excell and A.Ali, "REDUCED SIZE CIRCULARLY POLARISED ANTENNAS FOR MOBILE HANDSETS", In proceeding of the 19th UK URSI Colloquium at Cosenor's- House, the Rutherford Appleton Laboratory, Abingdon, Oxford, UK, 3-4 July 2006.
26. D.Zhou, R.A. Abd-Alhameed, **C.H. See**, K. Khalil and P.S Excell, "Adaptive Meshing For Numerical Antenna Design Using Genetic Algorithms", In proceeding of the 19th UK URSI Colloquium at Cosenor's- House, the Rutherford Appleton Laboratory, Abingdon, Oxford, UK, 3-4 July 2006.
27. R.A. Abd-Alhameed, N.T. Ali, **C.H. See**, B. Gizas and P.S. Excell, "Design of broadband slotted ground plane microstrip antenna for 3G communication", IEEE MELECON 2006, May 16-19, Benalmádena (Málaga), Spain, pp.340-343
28. D. Zhou, R.A. Abd-Alhameed, **C.H See**, P.S. Excell and E.A. Amushan, "DESIGN OF QUADRIFILAR HELICAL AND SPIRAL ANTENNAS IN THE PRESENCE OF SATELLITE-MOBILE HANDSETS USING GENETIC ALGORITHMS", Proceedings of European Conference on Antennas and Propagation: EuCAP 2006, Nice France, 6-10-November 2006, paper no: 350529

29. **C.H. See**, R.A. Abd-Alhameed, D. Zhou, P.S. Excell and Y.F. Hu, “A NEW DESIGN OF CIRCULARLY-POLARISED CONICAL-BEAM MICROSTRIP PATCH ANTENNAS USING A GENETIC ALGORITHM”, Proceedings of European Conference on Antennas and Propagation: EuCAP 2006, Nice France, 6-10-November 2006, paper no: 350601
30. **C.H.See,** R.A. Abd-Alhameed, R.S. Zadeh and P.S Excell, “FDTD Subgridding Scheme for Bioelectromagnetics Application”, In proceeding of the URSI Symposium at University of Portsmouth, UK, 2-3 July 2007, pp.11.